Max-Planck-Institut
für Meteorologie

REPORT No. 147

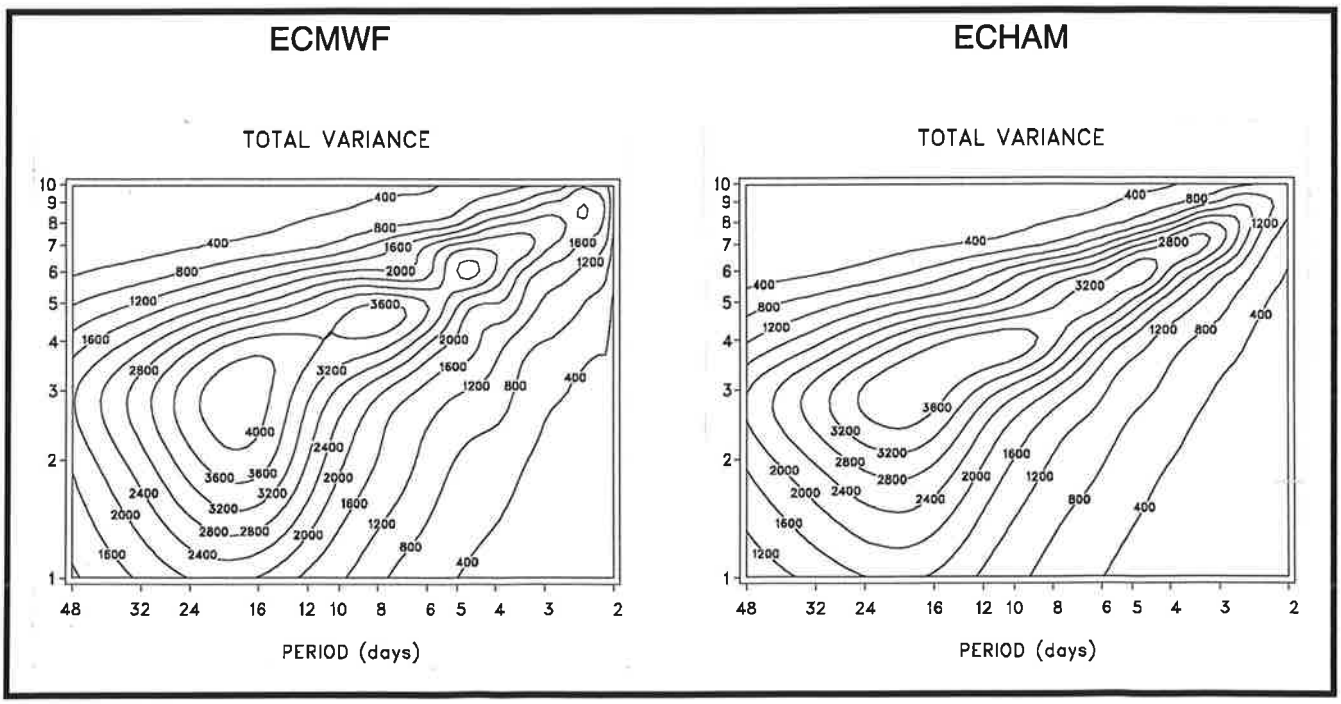

ON THE INTRA-SEASONAL VARIABILITY WITHIN THE EXTRATROPICS IN THE ECHAM3 GENERAL CIRCULATION MODEL

by

WILHELM MAY

HAMBURG, October 1994

AUTHORS:

Wilhelm May

Max-Planck-Institut für Meteorologie
Hamburg, Germany

MAX-PLANCK-INSTITUT
FÜR METEOROLOGIE
BUNDESSTRASSE 55
D-20146 HAMBURG
F.R. GERMANY

Tel.: +49 - (0)40 - 411 73 - 0
Telefax: +49 - (0)40 - 411 73 - 298
E-Mail: <name>@dkrz.d400.de

On the Intra-Seasonal Variability within the Extratropics in the ECHAM3 General Circulation Model

Wilhelm May
Max-Planck-Institute for Meteorology
Hamburg, Germany

ISSN 0937 – 1060

Contents

Abstract

In our study we investigate the intra-seasonal variability in the extratropics as simulated by an atmospheric General Circulation Model (ECHAM3) under different aspects. First we consider the GCM's capability to reproduce the midlatitude variability on intra-seasonal time scales by a comparison with observational data (ECMWF analyses). Secondly we assess the possible influence of Sea Surface Temperatures on the intra-seasonal variability by comparing estimates obtained from different simulations performed with ECHAM3 with varying and fixed SST as boundary forcing.

The intra-seasonal variability as simulated by ECHAM3 is underestimated over most of the Northern Hemisphere. While the contributions of the high-frequency transient fluctuations are reasonably well captured by the model, ECHAM3 fails to reproduce the observed level of low-frequency intra-seasonal variability. This is mainly due to the underestimation of the variability caused by the ultra-long planetary waves in the Northern Hemisphere midlatitudes by the model.

In the Southern Hemisphere midlatitudes, on the other hand, the intra-seasonal variability as simulated by ECHAM3 is generally underestimated in the area north of about 50° southern latitude, but overestimated at higher latitudes. This is the case for the contributions of the high-frequency and the low-frequency transient fluctuations as well. Further, the model indicates a strong tendency for zonal symmetry, in particular with respect to the high-frequency transient fluctuations.

While the two sets of simulations with varying and fixed Sea Surface Temperatures as boundary forcing reveal only small regional differences in the Southern Hemisphere, there is a strong response to be found in the Northern Hemisphere. The contributions of the high-frequency transient fluctuations to the intra-seasonal variability are generally stronger in the simulations with fixed SST. Further, the Pacific storm track is shifted slightly poleward in this set of simulations. For the low-frequency intra-seasonal variability the model gives a strong, but regional response to the interannual variations of the SST.

1 Introduction

Various phenomena on different spatial and temporal scales contribute to the intra-seasonal variability within the extratropics (e.g. Blackmnon, 1976). Baroclinic disturbances such as traveling cyclones with a typical lifetime of a few days affect the day-to-day variability of the atmosphere. Large-scale flow anomalies such as blocking anticyclones or cutoff lows (e.g. Rex, 1950a,b; Blackmon et al., 1986) may last for several weeks. These fluctuations on different scales, however, are influencing each other, in particular the temporal evolution and spatial distribution (e.g. Mullen, 1987).

There has been observational work on various phenomena contributing to the intra-seasonal variability for a long time. In the last decade or so, however, with the increasing importance of atmospheric **G**eneral **C**irculation **M**odels (GCM) there have been some studies dealing with the intra-seasonal variability as simulated by these models. Comparisons of the simulations with observations illustrate the model's capability of simulating the atmospheric variability on intra-seasonal time scales (e.g. Blackmon and Lau, 1980; Dugas and Derome, 1992). Alternatively one may also use suitably formulated atmospheric models to investigate the effect of specific dynamical processes or boundary forcing on the atmospheric intra-seasonal variability (e.g. Held, 1983).

In our study we investigate the intra-seasonal variability in the extratropics as simulated by an atmospheric GCM under several different aspects. First we consider the GCM's capability to reproduce the midlatitude variability on intra-seasonal time scales sufficiently by a comparison with observational data. Secondly we assess the possible influence of **S**ea **S**urface **T**emperatures (SST) on the intra-seasonal variability by comparing estimates obtained from different simulations with varying and fixed SST as boundary forcing. Considering estimates derived from individual simulations, we included different realizations with varying as well as fixed SST in the study, we also assess the natural variability of the extratropical atmosphere.

In section 2 the General Circulation Model is shortly introduced and the observational data are described. The various diagnostics applied to the data are introduced in section 3. Results are discussed in section 4, and a summary (section 5) is given in the end of this report.

2 Data

2.1 Model Data

The simulations were performed with an atmospheric General Circulation Model developed at the Max-Planck-Institute in Hamburg. The model referred to as **ECHAM3** is a spectral model with triangular truncation at wavenumber 42 (T42). It has 19 vertical levels in a hybrid σ-p-coordinate system. The physical parameterization includes radiation, vertical diffusion, gravity wave drag, cumulus convection, stratiform clouds and soil processes. A detailed description of the model and its climatology is given in Roeckner et al. (1992).

We investigate results from several simulations performed with ECHAM3. In five realizations a sequence of observed monthly mean sea surface temperatures for the period September '79 through December '92 is given as boundary forcing, but different atmospheric initial conditions, selected from the control-run of the model, were prescribed. In two other realizations the model was forced by applying the long-term monthly mean SST each year. The SST were averaged over the period January '79 through December '88. The data are available for a period of approximately 14 years at 12 hour intervals for each realization.

2.2 Observational Data

As observational data we use initialized analyses from the **E**uropean **C**entre for **M**edium Range **W**eather **F**orecasts (ECMWF) for the period September '79 through December '92. The data are available once per day and are reduced to T42 triangular truncation for our purposes. The quality of these data, in particular the impact of operational changes in the analysis-forecast system employed at ECMWF, are discussed in Trenberth (1992).

3 Analysis Techniques

3.1 Annual Cycle

In order to investigate the atmospheric variability on intra-seasonal time scales the annual cycle has to be removed from the data. We follow an approach by Lejenäs and Madden (1982) using an analysis of variance method to determine an optimal smoothing in order to represent the annual cycle. Thus we define the annual cycle as the annual

mean plus the first four harmonics.

3.2 Space-Time Spectral Analysis

In order to distinguish the phenomena influencing the atmospheric variability by different spatial and temporal scales we apply a space-time spectral analysis to the 500 hPa geopotential height field. We estimate both one-sided (Pratt, 1976) and two-sided (Hayashi, 1971) frequency spectra. These two methods, however, differ in the way they define the role of standing and zonally propagating fluctuations. These problems are discussed in detail in Pratt (1976).

For a given zonal wavenumber k and frequency ω the two-sided frequency spectrum (E) defines the components of eastward ($+\omega$) and westward ($-\omega$) propagating waves for a frequency band centered at ω

$$E(k, \pm\omega) = \frac{1}{4}[P_\omega(C_k) + P_\omega(S_k)] \pm \frac{1}{2}Q_\omega(C_k, S_k) \tag{1}$$

where P_ω are the power and Q_ω the quadrature spectrum of the cosine- ($C(k)$) and the sine-coefficient ($S(k)$) of the zonal Fourier harmonics. From the cospectrum K_ω we derive the variance from true standing (SR) and from zonally propagating motions (PR) as follows

$$SR(k, \omega) = \sqrt{K_\omega^2(C_k, S_k) + \frac{1}{4}[P_\omega(C_k) - P_\omega(S_k)]^2} \tag{2}$$

and

$$PR(k, \pm\omega) = E(k, \pm\omega) - \frac{1}{2}SR(k, \omega) \tag{3}$$

In Pratt's approach the one-sided **total** (T) variance spectrum is given by the sum of the eastward and westward propagating contributions of (1) as

$$T(k, \omega) = \frac{1}{2}[P_\omega(C_k) + P_\omega(S_k)] \tag{4}$$

The **propagating** variance spectrum is defined as the difference of the eastward and westward contributions

$$PR(k, \omega) = \mid Q_\omega(C_k, S_k) \mid \tag{5}$$

The propagation direction can be determined from the algebraic sign of Q_ω. The **stationary** variance spectrum is defined as in (2). This describes the temporal variability of the amplitude of the stationary waves.

The frequency spectra are estimated for individual seasons. Seasons are defined as slightly overlapping segments of 96 days starting at March 1, June 1, September 1 and December 1, respectively. Before the spectral analysis was done, the residual seasonal mean and the trend were removed from the seasonal segments. To obtain smooth spectral estimators a Tukey-Hanning window with a time lag of 20 days was applied (e.g. Priestley, 1981). This window has a bandwidth of 1/15 cpd with an equivalent number of degrees of freedom of 13.

3.3 Persistent Anomalies

In the extratropics there are recurrent flow anomalies that typically persist between one and several weeks, and thus well beyond the synoptic time scale. Blocking anticyclones are probably the most prominent examples of such features. Following a method applied by Blackmon et al. (1986) we investigate the characteristics of both positive and negative persistent anomalies in the 500 hPa geopotential height field on the Northern and Southern Hemisphere as well.

Starting from time series of anomalies at a given point, which are defined as the deviation from the annual cycle, we obtain a latitudinally scaled anomaly by

$$z'_\phi = z' \frac{sin(45°)}{sin\phi} \tag{6}$$

with the latitude ϕ and the anomaly z'. This normalization is similar to that used in obtaining a geostrophic streamfunction from the geopotential height field. In order to suppress the effect of brief interruptions of an episode, when a persistent anomaly occurs, due to high-frequency transient fluctuations on the statistics we apply a **light low-pass** filter to the anomalies. The filter removes transient fluctuations on time scales shorter than 5 days from the data. The frequency response of the filter is the same as in Blackmon et al. (1986). An anomaly is defined to be **persistent**, if it exceeds a certain value for a minimum number of days. As suggested by Dugas and Derome (1992) we assume a lifetime of at least 9 days for the persistent anomalies on the Northern Hemisphere. For the Southern Hemisphere we assume a shorter life time of at least 5 days, as suggested by Trenberth and Mo (1985). For the magnitude, however, we choose different values for each season derived from estimates of the intra-seasonal variability on time scales longer than 5 days.

3.4 Transient Fluctuations

We estimate the contributions of transient fluctuations to the intra-seasonal variability by computing the transient variances and covariances of selected meteorological variables. Transient fluctuations are defined as the deviation from the annual cycle as described in section 3.1. Using these fluctuations we obtain the transient variances and covariances with respect to the individual seasonal means. These calculations are carried out for unfiltered as well as filtered time series of transient fluctuations.

3.4.1 Spectral Filtering

For the time filtering we use the method introduced by Blackmon (1976), which allows to separate high-frequency fluctuations caused by traveling cyclones, e.g., and low-frequency fluctuations related to blocking highs, cutoff lows or other large-scale phenomena such as transitions between weather regimes.

The time characteristics of the filters applied are chosen on the basis of the results of the wavenumber-frequency analysis, which are discussed in further detail in section 4.1.. For the Northern Hemisphere we follow Blackmon (1976) and define a **band-pass** and a **low-pass** filter retaining transient fluctuations with periods between 2.5 and 6 days and between 10 and 90 days, respectively. The estimates we obtained using a broader band-pass filter from 2 to 10 days show the same characteristic distribution as those we obtained when applying Blackmon's band-pass filter, but the magnitude is enlarged. With regard to the different characteristics of the transient fluctuations in the Southern Hemisphere as compared to the Northern Hemisphere we choose the same band-pass filter, but a different low-pass filter for the Southern Hemisphere containing transient fluctuations on time scales longer than 6 days.

4 Results

4.1 Space-Time Spectral Analysis

In this section we present the variance spectra resulting from the space-time spectral analysis. The estimates give averages over the period of investigation and the zone between latitudes 40° and 70° north and south, respectively. We chose this rather broad area in order to get more robust spectral estimates for the comparison of the estimates derived from the simulations with those from the analyses. The comprehensive presentation for each data set, i.e. the analyses and the two sets of simulations with varying and fixed SST, is double-logarithmic with the period on the abscissa and the

zonal wavenumber ranging from 1 to 10 on the ordinate. The spectral densities were multiplied by wavenumber and frequency. This was done in order to obtain variance conserving spectra and also to emphasize peaks in otherwise red spectra. Each figure contains five panels with the one-sided total, stationary and propagating variance spectra as defined in Equation 4, 2 and 5, but also variance spectra of the westward and eastward propagating waves according to Equation 3. In order to compare the results derived from the different data sets directly we also present figures including the variance spectra for all data sets for different wave regimes. We classify ultra-long (zonal wavenumber 1, 2 and 3), long (wavenumber 4, 5 and 6) and short (wavenumber 7-10) planetary wave regimes. This classification of the planetary wave regimes is motivated by the results of the wavenumber-frequency analysis, where these regimes are generally separated. More common, however, is a classification, where the zonal waves at wavenumber 4 to 9 are grouped to the "synoptic waves". The spectral densities were multiplied by the frequency in this case.

4.1.1 Northern Hemisphere

Figure 4.1.1 shows the variance spectra derived from the ECMWF analyses for the Northern Hemisphere winter. The total spectrum (a) gives a fair amount of variability for all the periods and wavenumbers shown, indicating three prominent regimes. On time scales longer than 10 days, which will be referred to as the low-frequency part of the spectrum, the ultra-long planetary waves at wavenumber 1, 2 and 3 give major contributions to the intra-seasonal variability. The maximum is indicated near 18 days. On time scales shorter than 6 days, the high-frequency part of the spectrum, the variability is mainly caused by the short baroclinic waves at wavenumber 6, 7 and higher. The maximum appears near 5 days. On intermediate time scales between 6 and 10 days the long planetary waves at wavenumber 4 and 5 give major contributions to the intra-seasonal variability. While the variance on intermediate and short time scales is caused mainly by propagating disturbances (c), in the low-frequency part of the spectrum both the propagating and stationary variance (b) contribute to the same extent to the total variance. The ultra-long propagating waves are moving westward (d), whereas the shorter ones travel eastward (e).

During the other seasons (Figs. 4.1.2-4a) the intra-seasonal variability as given in the total variance spectra is considerably reduced on all scales. The three distinct spectral peaks separating the three regimes with strongest variability on long, intermediate and short time scales appear not as pronounced as in winter. Further, maximum contributions to the intra-seasonal variability are caused by transient fluctuations with shorter wavelength on shorter time scales, as indicated by the shift of the spectral peaks to

these scales. In spring (Fig. 4.1.2a), e.g., we find those three spectral peaks, but the variance on intermediate and short time scales is caused by disturbances on smaller spatial scale: on time scales between 5 and 10 days at wavenumber 5 and 6 and on time scales shorter than 5 days for zonal waves 7 and 8. In autumn (Fig. 4.1.4a), on the other hand, the transient fluctuations at wavenumber 4 and 5 cause strong variance on intermediate time scales between 6 and 12 days equal to the estimates in winter, but the activity of the ultra-long waves is considerably reduced. In summer (Fig. 4.1.3a) the total variance spectrum shows enhanced variability in the low-frequency part at wavenumber 4 and 5. In this season the intra-seasonal variability is generally reduced to one third of the estimates observed in winter. The spectra of the propagating waves (Figs. 4.1.1-4c) exhibit the same characteristic seasonal variations as the total variance spectra on intermediate and short time scales. This is also the case for the eastward propagating fluctuations (Figs. 4.1.1-4e), which are typically shorter than the ultra-long waves. On long time scales, where major contributions are caused by the ultra-long traveling waves, the propagating spectra (Figs. 4.1.1-4c) undergo some seasonal variations with respect to the magnitude of their contributions to the intra-seasonal variability. In spring (Fig. 4.1.2c) their magnitude is about two third of the estimate in winter, in autumn (Fig. 4.1.4c) it is approximately one half. In the spectra of the westward propagating waves (Figs. 4.1.1-4d) we find these characteristics even more apparent. The spectra of the stationary waves (Figs. 4.1.1-4b) undergo seasonal variations not only with respect to their magnitude, but also with regard to the prominent scales. In summer (Fig. 4.1.3b) and to a somewhat lesser extent in spring (Fig. 4.1.2b) and autumn (Fig. 4.1.4b) the zonal wavenumber 3 is well pronounced, whereas the ultra-long waves at wavenumber 1 and 2 give major contributions to the intra-seasonal variability in winter. In summer we find relatively large variance on long time scales also at wavenumber 4.

These spectra derived from the ECMWF analyses for the Northern Hemisphere winter are in good agreement with those of Fraedrich and Böttger (1978) and Hansen et al. (1989) using different data. The estimates of the stationary variance in Fraedrich and Böttger (1978), however, are substantially stronger than in this study. This is due to the different approach they use to assess the stationary variance as explained in Hansen et al. (1989). The seasonal variations of the spectra as shown here correspond to the findings of Speth and Madden (1983) for the propagating waves. They, e.g., also observe enhanced variability caused by the westward traveling zonal waves 4 and 5 in summer. The spectra obtained from the ECMWF analyses, however, show enhanced variability at wavenumber 9 and 10 on time scales shorter than 3 days, the high-frequency end of the spectrum. This effect is indicated in the spectra of the stationary waves (Fig. 4.1.1b). In the Southern Hemisphere this effect is even stronger (Fig. 4.1.26b). As the initialized analyses are the result of the analysis-forecast cycle at ECMWF, this is probably an artifact of the analyses. The observational data are processed in a data assimila-

tion procedure, which is affected by the ECMWF forecast model itself. Further, the analysis-forecast cycle is carried out once daily so that inconsistencies occurring in the analyses from day to day may introduce transient variability on these very short time scales.

In the following we present the variance spectra derived from the simulations performed with ECHAM3. We distinguish between simulations with varying (Figs. 4.1.5-8) and fixed (Figs. 4.1.10-13) SST. In the case of varying SST the estimates are presented as averages for five, in the other case for two realizations.

Figure 4.1.5a shows the total variance spectrum derived from the simulations with varying SST for the Northern Hemisphere winter. The model successfully reproduces the general structure we found in the analyses. There is a fair amount of variability on all scales shown, and also the three prominent planetary wave regimes on long, intermediate and short time scales are indicated. They appear, however, not as pronounced as in the analyses (Fig. 4.1.1a), where the spectrum displayes three distinct spectral peaks. To some extent this may be due to the averaging procedure of the five realizations, but also the spectra calculated from individual simulations (Fig. 4.1.9) generally do not exhibit these marked peaks, in particular on intermediate time scales between 6 and 10 days. Only in one simulation (a) this peak is indicated, in two other realizations (b and c) we find contributions in the high-frequency part of the spectrum at periods near 5 and 4 days, respectively. In the low-frequency part of the spectrum, where the ultra-long waves give major contributions to the intra-seasonal variability, the stationary variance (Fig. 4.1.5b) exceeds the variance caused by the propagating disturbances (c). In the propagating variance spectrum the three prominent wave regimes do neither appear as pronounced as in the analyses (Fig. 4.1.1c).

The seasonal variations of the total variance spectra derived from the simulations with varying SST for the Northern Hemisphere (Figs. 4.1.5-8a) are similar to those obtained from the analyses. This means the intra-seasonal variability is considerably weaker than in winter, and maximum contributions are caused by transient fluctuations with shorter wavelength on shorter time scales. Also in the other seasons the spectra derived from the simulations do not show any distinct spectral peaks on intermediate or short time scales. On long time scales the total spectra reveal maximum variance at wavenumber 3 at periods about 16 days in spring (Fig. 4.1.6a) and summer (Fig. 4.1.7a). In autumn (Fig. 4.1.8a) the activity of the ultra-long waves is considerably reduced. Similar seasonal variations appear in the spectra of the propagating waves (Figs. 4.1.5-8c) with those on long time scales traveling westward (Figs. 4.1.5-8d) and those on intermediate and short scales moving eastward (Figs. 4.1.5-8e). The stationary spectra obtained from the simulations (Figs. 4.1.5-8b) are dominated by the contribution at wavenumber

3 in all seasons. The stationary variance is strongest in winter and weakest in summer, in spring its magnitude is larger than in autumn.

In Figures 4.1.10-13 we present the variance spectra derived from the simulations with fixed SST. The general structure of the spectra is similar to the simulations with varying SST, and the seasonal variations correspond to those we found for the other set of simulations. In some seasons, however, typical features of the simulations with fixed SST are indicated in these figures. In winter, e.g., the total (Fig. 4.1.10a) and the propagating (Fig. 4.1.10c) variance are reduced on time scales about 10 days, but enhanced on time scales of 6 or 7 days.

In order to compare the results derived from the different data sets directly we show figures including variance spectra calculated from the analyses and the simulations with varying and fixed SST as well. We distinguish between different planetary wave regimes, i.e. ultra-long (wavenumber 1-3), long (4-6) and short (7-10) waves. Also the contributions of all planetary scale waves (1-10) are included. The spectra obtained from the ECMWF analyses are indicated by the dashed line, those determined from the simulations with varying SST by the heavy and from the simulations with fixed SST by the light solid line.

Figure 4.1.14 gives the total variance spectra for the Northern Hemisphere winter. We find that the intra-seasonal variability is generally underestimated by ECHAM3, in particular the contributions of the ultra-long (1-3) waves, which are prominent on long time scales. The variability caused by the long (4-6) and short baroclinic (7-10) waves, on the other hand, is well captured. The spectra derived from the two sets of simulations are in rather good agreement. On time scales between 8 and 20 days, however, the variance estimated from the simulations with varying SST is larger, on short time scales between 3 and 8 days the variability in the simulations with fixed SST is enhanced. For the stationary variance (Fig. 4.1.15) the estimates from the two sets of simulations are about the same, but generally weaker than in the analyses on all scales. As revealed by the propagating spectra (Fig. 4.1.16), the activity of the ultra-long traveling waves is substantially underestimated in the model in winter, whereas the propagating variance caused by the long waves on time scales between 5 and 10 days and the short baroclinic waves on time scales shorter than 5 days is stronger than in the analyses. The propagating spectra show the enhanced variability caused by the long and short traveling waves on time scales shorter than 8 days in the simulations with fixed SST more clearly.

In the other seasons the total variance spectra (Figs. 4.1.17, 20 and 23) show characteristics similar to those in winter. The intra-seasonal variability is generally underestimated by the model, which is indicated by the spectral estimates including all

planetary waves (1-10). The variability caused by the ultra-long planetary waves in the low-frequency part of the spectrum is closer to the estimates derived from the analyses than in winter. In summer (Fig. 4.1.20) and to some extent in spring (Fig. 4.1.17) estimates obtained from the simulations with varying SST are larger than those from the simulations with fixed SST, in autumn (Fig. 4.1.23) the opposite is true. For the stationary variance (Figs. 4.1.18, 21 and 24) we find the same typical underestimation on all scales as in winter. For the ultra-long planetary waves, however, the estimates of at least one of the simulations are larger than in the analyses, in summer this is the case for the simulations with varying, in the transition seasons for the simulations with fixed SST. The propagating variance spectra reveal that the contributions of the ultra-long traveling waves to the intra-seasonal variability as simulated by ECHAM3 are generally, i.e. on all time scales, in good agreement with the analyses in summer (Fig. 4.1.22) and autumn (Fig. 4.1.25) and on time scales longer than 20 days also in spring (Fig. 4.1.19). The differences between the two sets of simulations in the low-frequency part of the spectrum are similar to those we found in the total and stationary variance spectra. The activity of the long traveling waves (4-6), on the other hand, is stronger in the simulations than in the analyses on intermediate time scales in spring and to some extent in summer.

4.1.2 Southern Hemisphere

Figure 4.1.26 shows the variance spectra derived from the ECMWF analyses for the Southern Hemisphere winter. The total spectrum (a) gives a fair amount of variance for all periods and wavenumbers shown, but different to the Northern Hemisphere (Fig. 4.1.1a) only two prominent planetary wave regimes are pronounced. On time scales shorter than 6 days, i.e. the high-frequency part of the spectrum, the variability is mainly caused by the planetary waves at wavenumber 5, 6 and higher. The maximum appears near 5 days. On time scales between 6 and 16 days the long waves at wavenumber 3 and 4 give major contributions to the intra-seasonal variability. A pronounced maximum at about 10 days is indicated at wavenumber 4. The variance is twice as strong as the estimate we observe on intermediate time scales in the Northern Hemisphere winter (7200 vs. 3600 m^2). The ultra-long waves 1 and 2 contribute about one third less to the intra-seasonal variability than in the Northern Hemisphere. These contrasts are mainly accounted for by the different characteristics of the propagating disturbances in both hemispheres. The propagating variance spectrum (c) exhibits also these two pronounced peaks at wavenumber 4 on intermediate and to some extent also on long time scales and for wave 5 on shorter temporal scales. Distinguishing between westward (d) and eastward moving disturbances (e) the spectra show these features even more clearly. The variance caused by the westward traveling wave 2, e.g., is approximately

one half of the estimate for the other hemisphere (1000 vs. 1800 m^2). The stationary variance spectrum (b) reveals enhanced variability on long time scales at wavenumber 3. The ultra-long waves 1 and 2, on the other hand, do not contribute as much to the stationary variance as in the Northern Hemisphere (Fig. 4.1.1b).

In the other seasons (Figs. 4.1.27-29a) the intra-seasonal variability given in the total variance spectra is considerably reduced on all scales. The prominent wave regime on time scales between 6 and 16 days is shifted to shorter wavelength and shorter time scales. In spring (Fig. 4.1.27a) and autumn (Fig. 4.1.29a) we find this maximum on time scales between 5 and 10 days at wavenumber 5, in summer (Fig. 4.1.28a) for wave 6 at periods between 4 and 8 days. The pronounced spectral peak on short time scales, which the total variance spectrum shows in winter, does not appear in the other seasons. The spectra, however, indicate enhanced variance for waves 6, 7 and 8 on time scales shorter than 5 days in the transition seasons and shorter than 4 days in summer. On intermediate and short time scales the spectra of the propagating waves (Figs. 4.1.26-29c) show the same characteristic seasonal variations as the total spectra. This is also the case for the eastward propagating fluctuations (Figs. 4.1.26-29e). The variance caused by the westward propagating ultra-long waves is pronounced at wavenumber 2 in all seasons except summer, when we find enhanced variability at wavenumber 3 (Fig. 4.1.28d). The stationary variance spectra (Figs. 4.1.26-29b) are dominated by the contributions at wavenumber 3 in all seasons except summer, when wave 4 also shows enhanced variance on long time scales (Fig. 4.1.28b).

The spectra derived from the ECMWF analyses for the Southern Hemisphere are in agreement with the results by Fraedrich and Kietzig (1983) and sea-level pressure power spectra by Mechoso and Hartman (1982). A subperiod of our data from 1979 to 1984 has already been investigated by Hansen et al. (1989) giving essentially the same characteristics as in this study. The contrast between the Northern and Southern Hemisphere seems to be related to the different topography as was pointed out by Hayashi and Golder (1983) in a GCM experiment performed with and without mountains. There are, however, some uncertainties about the ECMWF analyses in the Southern Hemisphere itself. Apart from the effects induced to the analyses by the assimilation procedure and the model in the analysis-forecast cycle, further problems arise due to the sparse data coverage in the Southern Hemisphere. For that reason observations deduced from satellite data are crucial for the analyses. Using satellite data, however, introduces a systematic underestimation of the high-frequency variability caused by short scale planetary waves to the analyses, as the satellite data resolve large scale phenomena to much higher accuracy than those on short scales.

In the following we present the variance spectra derived from the simulations per-

formed with ECHAM3. As the two sets of simulations show the same general characteristics we will discuss here only the results from the simulations with varying SST (Figs. 4.1.30-33). For completeness the results for the simulations with fixed SST, however, are shown in Figures 4.1.34-37.

Figure 4.1.30a shows the total variance spectrum derived from the simulations with varying SST for the Southern Hemisphere winter. Although the general structure, that means the separation of two prominent wave regimes on intermediate and short time scales, is successfully reproduced by the model, the spectrum exhibits a striking difference to the analyses. The variance in both regimes is considerably overestimated in the simulations. The maximum at wavenumber 4 near 10 days, e.g., is twice as strong as in the analyses (14400 vs. 7200 m^2). On other spatial scales the spectral estimates are similar to those observed in the analyses. These discrepancies are mainly accounted for by different characteristics of the propagating planetary waves on intermediate and short time scales (c), which are moving eastward (e). The stationary variance spectrum (b) reveals enhanced variance at wavenumber 3 as we observed also for the analyses.

The seasonal variations of the total variance spectra derived from the simulations for the Southern Hemisphere (Figs. 4.1.30-33a) are substantially different from those found for the analyses. Transient fluctuations on the same spatial and temporal scale account for most of the variance throughout the year. In all seasons we find a spectral peak on short time scales at wavenumber 5 near 5 days and on intermediate and on long time scales between 6 and 16 days at wavenumber 4. The magnitude, however, undergoes some seasonal variations. In summer, e.g., the variance is less than half the value in winter (5600 vs. 14400 m^2). The spectra of the propagating waves (Figs. 4.1.30-33c), in particular those moving eastward (Figs. 4.1.30-33e), exhibit the same kind of seasonal variations. For the westward traveling waves (Figs. 4.1.30-33d) the simulations show the same seasonal variations as the analyses so that the contributions of the westward traveling waves to the intra-seasonal variability are underestimated in the model throughout the year. With respect to the magnitude the stationary variance spectra (Figs. 4.1.30-33b) undergo stronger seasonal changes than observed in the analyses. In summer (Fig. 4.1.32b) the variance is only half as strong as in winter (Fig. 4.1.30b). In all seasons, however, major contributions are caused by the temporal variation of the amplitude of the stationary zonal wave 3.

Figure 4.1.38 shows the total variance spectra for the Southern Hemisphere winter derived from the different data sets distinguishing between different planetary wave regimes. The spectra obtained from the ECMWF analyses are indicated by the dashed line, those determined from the simulations with varying SST by the heavy and from the simulations with fixed SST by the light solid line. We find that the intra-seasonal

variability is generally stronger in the simulations than in the analyses on time scales between 3 and 16 days. This is mainly accounted for by the enhanced contributions of the long planetary waves (4-6) on these time scales. In the low-frequency part of the spectrum the contributions of the ultra-long waves (1-3) are also stronger than in the analyses in winter. The variability caused by the short baroclinic waves (7-10) is of the same magnitude as in the analyses. The spectra derived from the two sets of simulations are in good agreement. The propagating variance spectra (Fig. 4.1.40) indicate that in the simulations the contributions of the traveling waves to the intra-seasonal variability are stronger than in the analyses on all scales. The short baroclinic waves cause enhanced variability at periods shorter than 3 days. For the stationary variance (Fig. 4.1.39), on the other hand, the estimates derived from the simulations are weaker on time scales shorter than 16 days and comparable on longer time scales. On the high-frequency end of the spectrum at periods shorter than 3 days the analyses reveal enhanced variability caused by the baroclinic waves, which is probably an artifact of the data.

In the other seasons the total variance spectra (Figs. 4.1.41, 44 and 47) show different characteristics than in winter. Whereas on time scales shorter than 10 days the intra-seasonal variability is generally stronger in the simulations, it is weaker on longer time scales. The behavior in the low-frequency part of the spectrum, however, is explained by the enhanced activity of both the ultra-long and long waves on these time scales. A typical example for this is given in autumn (Fig. 4.1.47). For the stationary variance (Figs. 4.1.42, 45 and 48) we find in all seasons a typical underestimation in the simulations on all scales, which is also characteristic for the model in the Northern Hemisphere. On intermediate and short time scales the variability caused by the traveling waves (Figs. 4.1.43, 46 and 49) is generally stronger in the simulations in all seasons. On long time scales the contributions of the ultra-long traveling waves are reasonably well reproduced by the model, but longer traveling waves (4-6) do not give any contributions to the intra-seasonal variability on long time scales.

4.2 Persistent Anomalies

In this section we discuss the characteristics of the occurrence of persistent anomalies in the 500 hPa geopotential height field. We distinguish between positive and negative anomalies. The way we define persistent anomalies has been explained in detail in section 3.3. As their lifetime we assume at least 9 days for the Northern and 5 days for the Southern Hemisphere. The thresholds we chose for the different seasons are given in Table 1. The estimates are area averages of the root-mean-square deviation (RMS) of the 500 hPa geopotential height retaining time scales longer than 5 days over the

midlatitudes of each hemisphere. We distinguish between the ECMWF analyses and the individual simulations performed with ECHAM3 with varying (SST...) and fixed (CLI...) SST as well.

NH	MAM	JJA	SON	DJF
ECMWF ANA	86.17	67.01	80.79	100.38
ECHAM CLI1	79.29	59.48	73.29	88.76
ECHAM CLI2	81.20	60.27	73.44	91.77
ECHAM SST1	80.17	61.75	73.83	94.11
ECHAM SST2	80.38	62.39	73.69	91.54
ECHAM SST3	80.07	62.20	72.59	92.42
ECHAM SST4	81.25	62.36	72.58	94.37
ECHAM SST5	81.32	62.33	70.26	91.39

SH	MAM	JJA	SON	DJF
ECMWF ANA	93.01	100.99	93.67	88.63
ECHAM CLI1	81.43	99.80	82.60	69.37
ECHAM CLI2	80.54	99.13	81.85	68.94
ECHAM SST1	82.22	99.54	83.04	71.47
ECHAM SST2	82.90	99.45	83.28	72.51
ECHAM SST3	81.32	101.68	86.78	70.70
ECHAM SST4	84.07	97.84	82.17	71.55
ECHAM SST5	83.59	99.43	84.84	71.56

Table 1. RMS of the 500 hPa geopotential height field retaining time scales between 5 and 90 days in the Northern Hemisphere (NH) and Southern Hemisphere (SH) mid-latitudes obtained from the ECMWF analyses and the various simulations performed with ECHAM3 with varying (SST...) and fixed (CLI...) Sea Surface Temperatures as boundary forcing distinguishing between seasons. Units are m.

In the Northern Hemisphere the ECMWF analyses show strongest intra-seasonal variability on time scales longer than 5 days in winter and weakest in summer. The RMS obtained in spring exceeds the value observed in autumn. In the simulations we find the same seasonal variation, but the estimates derived from the analyses exceed

those obtained from the simulations by 5 to 7 m in all seasons. We do not find any significant difference between the simulations with varying and fixed SST. Also in the Southern Hemisphere the ECMWF analyses show strongest intra-seasonal variability in winter and weakest in summer. The estimates of the RMS are comparable in spring and autumn. We find a stronger seasonal variation in the simulations, as the difference between winter and summer is about 18 m larger than observed. This is accounted for by the fact that the estimates obtained from the simulations are about 18 m smaller than those derived from the analyses for the Southern Hemisphere summer, but are comparable in winter. In spring and autumn the RMS obtained from the analyses exceeds the estimates derived from the simulations by approximately 10 m. There is no significant difference between the simulations with varying and fixed SST.

4.2.1 Northern Hemisphere

Figure 4.2.1a shows the relative occurrence of positive persistent anomalies in the 500 hPa geopotential height field derived from the ECMWF analyses for the entire period of investigation. The number gives the percentage of the time, during which a persistent anomaly was found at a given location. The distribution reveals three centers, where positive persistent anomalies frequently occur. One is located over the eastern Pacific, one over the eastern Atlantic and another one over northern Russia. These coincide with the regions, where observations indicate frequent blocking activity. Long-lived positive anomalies appear rarely over central North America and East Asia. They occur as often in the Pacific region as in the Atlantic sector, but less frequently over northern Russia. Negative persistent anomalies (Fig. 4.2.1b) occur also most frequently in these three regions, but generally not as often as positive ones. In the western Mediterranean, however, the analyses show a relatively high number of negative long-lived anomalies corresponding to the frequent development of cutoff lows in this region. Figure 4.2.1c shows the sum of positive and negative persistent anomalies. The distributions of the relative occurrence of both positive and negative persistent anomalies derived from the ECMWF analyses show the same characteristics as indicated in the results by Blackmon et al. (1986) obtained from about 20 years of NMC analyses for the winter season only. The numbers, however, cannot be compared directly, as Blackmon only shows the number of events, whereas we take also the duration of these events into account.

In the following we investigate the occurrence of persistent anomalies in the simulations performed with ECHAM3. We distinguish between simulations with varying and fixed SST. In the case of varying SST the estimates are averages for five, in the other case for two realizations.

In the simulations with varying SST (Fig. 4.2.2a) we find positive persistent anomalies also most frequently in these three regions mentioned above, but with some different characteristics compared to the distribution obtained from the analyses. In the Pacific sector positive persistent anomalies occur more often in the higher latitudes, in particular over Alaska and the Aleutian Islands. In the Atlantic region the simulations reveal less frequently long-lived anomalies than the analyses, and the maximum west of the British Isles is not pronounced, but extending further northeast over Scandinavia. In addition, positive persistent anomalies occur more often in the Pacific region than in the Atlantic sector. Another maximum, which is not indicated in the analyses, can be found over Baffin Bay between Greenland and Canada. Negative persistent anomalies (Fig. 4.2.2b) occur also most frequently in these three well known regions and, as we observed for the analyses, less frequently than positive ones. Again we find more often long-lived anomalies over Alaska and the Aleutian Islands and less frequently over the eastern Atlantic. In the western Mediterranean ECHAM3 does not indicate any preference of negative rather than positive persistent anomalies. In the distribution of the sum of positive and negative persistent anomalies (Fig. 4.2.2c) these deficiencies of the model even more apparent. The most striking feature is the model's failure to simulate persistent anomalies in the Atlantic region as often as in the Pacific sector.

The distribution of the occurrence of persistent anomalies in the simulations with fixed SST (Fig. 4.2.3c) shows also some characteristics, which are different from the distribution obtained from the analyses. In the Pacific region we observe persistent anomalies more often at high latitudes, but less frequently in the area further south. In the Atlantic sector the distribution reveals a maximum over western Europe extending over Scandinavia. In this set of simulations, however, persistent anomalies occur more often in the Atlantic region than in the Pacific sector. Again we find another maximum over Baffin Bay. These discrepancies are typical for the positive (Fig. 4.2.3a) and negative persistent anomalies (Fig. 4.2.3b) as well. The most striking difference between the simulations with varying and fixed SST is that we find generally less persistent anomalies in the Pacific region for the simulations with fixed SST.

Considering the results obtained from the individual simulations with both varying and fixed SST we can conclude to which extent the characteristic features described in the preceding two paragraphs are typical for the model. Figure 4.2.4 shows the distributions for the sum of positive and negative persistent anomalies derived from the individual simulations. In each of the simulations with varying SST we find long-lived anomalies more often in the Pacific region than in the Atlantic sector. The values over the eastern Pacific exceed those obtained from the analyses (Fig. 4.2.1c) in each realization. The location of the Pacific maximum varies only slightly between individual simulations, and in each simulation we find persistent anomalies over Alaska and the

Aleutian Islands more often than in the analyses. The maximum over Baffin Bay appears also in all simulations, including those with fixed SST. In the Atlantic region, however, the location of the maximum is more variable. In particular the tendency of the frequent occurrence of long-lived anomalies over Scandinavia does not appear in all simulations. In both simulations with fixed SST we find less frequently persistent anomalies over the eastern Pacific than in the simulations with varying SST. There is, however, a clear difference between the two realizations in this region. In one of them the distribution is similar to the analyses, in the other one we find a distinct maximum over Alaska.

The distributions shown so far cover the entire period of investigation of approximately 14 years. In the following we present these distributions distinguishing between seasons in order to conclude how the characteristics of the occurrence of persistent anomalies vary by season. We chose the distributions derived from the simulations with varying SST, which are rather robust, as we combine five individual realizations. Comparing the results between seasons, however, one has to have in mind that different thresholds were chosen for each season (see Table 1). Figure 4.2.5 shows the relative occurrence of positive persistent anomalies for the different seasons. In all seasons we observe those three or, in this case, four centers, where long-lived anomalies frequently occur. These are the regions over the eastern Pacific, the eastern Atlantic and western Europe, northern Russia and, typical for the simulations, Baffin Bay. In all of these regions positive persistent anomalies occur most frequently in winter. In the Pacific sector we find about the same number of long-lived anomalies in spring and autumn, in summer their number is clearly reduced. In autumn the distribution in this region reveals somewhat different characteristics than in the other seasons. The maximum is located further west and persistent anomalies do not occur as often as at higher latitudes over Alaska. In the Atlantic region we find about the same number of long-lived anomalies in all seasons but winter. In spring and winter the maximum is located west of the British Isles, in the other seasons further east, that means downstream, extending over Scandinavia. The maximum over northern Russia is only reduced in summer. In all seasons negative persistent anomalies (Fig. 4.2.6) occur generally not as often as positive ones. The distributions reveal the same seasonal variations we found for the positive anomalies. In the Pacific sector, however, the distribution exhibits more often negative persistent anomalies over the central Pacific in spring than in autumn, when the region with maximum occurrence is located further downstream. Figure 4.2.7 shows the sum of positive and negative persistent anomalies.

In the following we present diagrams giving the relative occurrence of persistent anomalies as a function of longitude. The estimates shown are averages over different zones, which were chosen with respect to the location of the maximum occurrence of

persistent anomalies in the ECMWF analyses. One zone covers the latitudes between 40° and 55°N including the Pacific maximum, the others between 45° and 60°N and between 55° and 70°N the Atlantic maximum and the one over northern Russia, respectively. The average over the zone between 40° and 70°N combines the estimates obtained for these three zones. In addition to the mean value for each data set, i.e. the ECMWF analyses and the two sets of simulations performed with ECHAM3 with varying and fixed SST, the internal variability between the five simulations with varying SST is indicated in the figures. The mean value obtained from the simulations with varying SST is given by the heavy solid line, the light solid lines represent this mean value with the standard deviation of the five individual simulations added and subtracted, respectively. The mean value obtained from the simulations with fixed SST is indicated by long dashes, that derived from the analyses by short dashes.

Figure 4.2.8 shows these average values in the case of positive persistent anomalies for the entire period of investigation exhibiting the features also illustrated in Figures 4.2.1-3. In the Pacific region, e.g., the number of positive persistent anomalies in the simulations with varying SST exceeds the values obtained from the analyses in all zones. In this region we also observe considerably more positive persistent anomalies in the simulations with varying SST than in the simulations with fixed SST in all zones, except for the high latitudes, where about the same number of long-lived anomalies occur. In the Atlantic region we find more frequently positive persistent anomalies in the ECMWF analyses than in the simulations west of 15° western longitude, but not as often further east. The maximum over northern Russia is also stronger in the simulations. The regions of the maximum occurrence of positive persistent anomalies over the western Atlantic and northern Russia appears also clearly separated in the simulations except for the high latitudes, as the model shows enhanced blocking activity over Scandinavia. We find larger variations between individual simulations over the western Atlantic and Europe than in the Pacific region. The sharp decrease of the occurrence of long-lived anomalies east of the maximum over northern Russia at 75°E and east of the maximum in the Pacific sector at about 135°W, however, are in good agreement with the observations and typical for all simulations, as indicated by very small estimates of the internal variability at these longitudes.

Figure 4.2.9 shows the average values for the zone between 40° and 70°N distinguishing between seasons. From this we can conclude to which extent similarities or differences between the two sets of simulations performed with ECHAM3 and the ECMWF analyses are typical for the entire year or rather dominated by a particular season. In the Pacific region, e.g., we find considerably more often positive persistent anomalies than in the analyses in both sets of simulations in spring and autumn, for the simulations with varying SST also in summer. In winter, however, the estimates are in rather good

agreement. In this season the analyses also represent enhanced blocking activity over ther eastern Pacific between 130° eastern longitude and the dateline, a feature that is not indicated in the simulations. In the Pacific region we find also more often positive persistent anomalies in the simulations with varying SST than in those with fixed SST in all seasons but spring. The estimates, however, do not exceed the range of the internal variability. The difference between the analyses and the simulations in the Atlantic region west of 15°W, where the analyses reveal more often long-lived anomalies, can be found in all seasons, but is most pronounced in autumn. In this season the analyses show also the same number of positive persistent anomalies over the Atlantic and northern Russia, whereas in the other seasons the blocking activity is stronger in the Atlantic region. In winter we observe more often positive persistent anomalies in the simulations with fixed SST than in those with varying SST over Europe. In the other seasons the numbers are comparable.

In the Pacific region we find also more often negative persistent anomalies in the simulations with varying SST than in the analyses in all zones (Fig. 4.2.10). The number of negative long-lived anomalies exceeds the values obtained from the simulations with fixed SST, in particular south of 60°N. In the Atlantic region we find more often negative persistent anomalies in the ECMWF analyses than in the simulations west of 15° western longitude, but in the simulations with fixed SST more frequently further east. Over Russia the negative persistent anomalies as obtained from the analyses occur generally further north than the positive ones. In the simulations the regions with maximum occurrence of negative persistent anomalies over the Atlantic and northern Russia are not separated. Negative long-lived anomalies, however, do not occur frequently over northern Russia in all seasons (Fig. 4.2.11). In winter the analyses do not show any enhanced relative occurrence in this region, which is in contrast to the simulations. We observe considerably more often negative long-lived anomalies in both sets of simulations in spring and autumn, in winter also in the simulations with varying SST. Similar to the case of positive anomalies the simulations with fixed SST show more often long-lived negative anomalies over Europe and northern Russia in winter.

In the following we will examine the mean lifetime of persistent anomalies in those three areas over the Pacific, the Atlantic and northern Russia, where they most frequently occur (Fig. 4.2.12a). These regions are indicated by PAC ($40-60$°N and $140-180$°W), ATL ($45-60$°N and 35°W -5°E) and NRU ($55-70$°N and $40-80$°E), respectively. The figures shown here give the relative occurrence of both positive and negative anomalies as a function of their lifetime distinguishing between seasons for the different data sets. The solid line represents the positive and the dashed line the negative anomalies.

In the Pacific region the ECMWF analyses (Fig. 4.2.13) reveal generally more short-lived negative anomalies, but more long-lived positive ones. These two parts are divided at 4 to 5 days, which is about the typical lifetime of extratropical cyclones. In spring, however, there occur somewhat more negative anomalies with a lifetime between 13 and 19 days than positive ones. In the Atlantic region (Fig. 4.2.14) the separation in these two fractions at 4 to 5 days is also typical. In winter, however, when cutoff lows frequently occur in the eastern Atlantic region, the analyses indicate about the same number of long-lived negative and positive anomalies. Over northern Russia (Fig. 4.2.15) we observe the same characteristic separation of negative and positive anomalies with respect to their lifetime, most pronounced in winter.

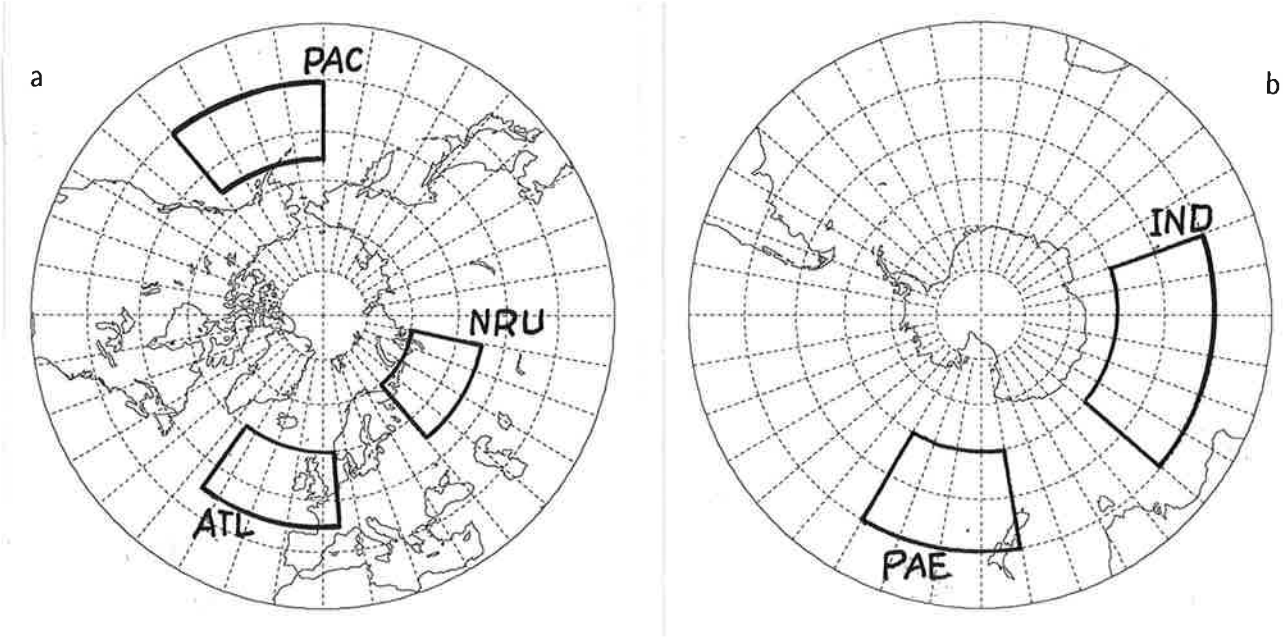

Fig. 4.2.12. Regions where persistent anomalies most frequently occur in the Northern Hemisphere (a) and Southern Hemisphere (b). Anomalies occurring inside these areas have been composited to examine their mean lifetime.

In the Pacific region the model generally shows for both the simulations with varying (Fig. 4.2.16) and fixed SST (Fig. 4.2.19) the same characteristic separation with more short-lived negative anomalies and more long-lived positive ones. These two fractions are divided at a lifetime between 4 and 7 days. For the simulations with varying SST the distribution indicates about the same number of negative and positive anomalies with a lifetime longer than 7 days in winter. This appears to be typical only if we combine the results derived from all five simulations with varying SST. For individual simulations (not shown here) we find some realizations with more positive and some with more negative anomalies that persist for a week or longer. In the Atlantic region we observe more short-lived negative and more long-lived positive anomalies for the simulations (Figs. 4.2.17 and 20) in all seasons but spring. Therefore the model

exhibits some different characteristics than the analyses (Fig. 4.2.14) in winter caused by the model's lack in reproducing cutoff lows in this region sufficiently. Over northern Russia the separation of negative and positive anomalies with respect to their lifetime is reasonably well captured by ECHAM3 (Figs. 4.2.18 and 4.2.21).

4.2.2 Southern Hemisphere

Figure 4.2.22a shows the relative occurrence of positive persistent anomalies in the Southern Hemisphere derived from the ECMWF analyses for the entire period of investigation. The distribution indicates three regions, where positive persistent anomalies frequently occur. One is located in the storm track region over the southern Indian Ocean, another over the South Pacific centered southeast of New Zealand and extending further downstream over the Pacific Ocean. Here the region of maximum occurrence is located approximately 5° closer to the pole than further east. A third region, where long-lived positive anomalies frequently occur, is located over the South Atlantic. There appear two characteristic minima on the edge of Antarctica, one is located near the Greenwich meridian at approximately 70°S and another between 70° and 90°E at about 65°S. In the case of the negative persistent anomalies (Fig. 4.2.22b) the analyses show a similar distribution as for the positive ones. Over the Atlantic, however, the distribution is different. The negative anomalies tend to appear southeast of South America, whereas the positive ones are spread over the entire ocean. There are slightly more positive rather than negative long-lived anomalies over most of the hemisphere. Figure 4.2.22c shows the sum of positive and negative anomalies for the entire period of investigation. The distribution of the relative occurrence of persistent anomalies obtained from the ECMWF analyses is similar to the distribution derived from 8 years of daily analyses from the World Meteorological Centre in Melbourne, Australia, by Trenberth and Mo (1985). In the Southern Hemisphere, however, the results are fairly sensitive to the data used as was pointed out by Lejenäs (1987).

In the following we investigate the occurrence of persistent anomalies in the simulations performed with ECHAM3. We distinguish between the two sets of simulations with varying and fixed SST. In the case of varying SST the estimates give averages for five, in the other case for two realizations.

The distribution of the occurrence of persistent anomalies derived from the simulations with varying SST shows some different characteristics than the analyses. This has to be expected considering the dissimilar distributions of the low-pass filtered RMS of the geopotential height fields, which will be discussed in further detail in section 4.4.1. The simulations with varying SST indicate also three regions, where positive persistent

anomalies frequently occur (Fig. 4.2.23a). We find a maximum in the storm track region, but persistent anomalies occur about one third less frequently than in the analyses in this region. There is no maximum southeast of New Zealand, but long-lived anomalies are found frequently in the region further downstream between 80° and 140°W. Over the South Atlantic the simulations are in general agreement with the analyses, and the minima on the edge of Antarctica are also captured by the model. The distributions of the relative occurrence of negative persistent anomalies obtained from the simulations (Fig. 4.2.23b) are similar to the distributions of positive ones. In addition, the maximum in the storm track region is not pronounced and the simulations indicate a tendency for zonal symmetry instead. There are slightly more positive persistent anomalies rather than negative ones over most of the hemisphere.

The distribution of the occurrence of persistent anomalies obtained from the simulations with fixed SST (Fig. 4.2.24) shows generally the same discrepancies as compared to the analyses as those for the simulations with varying SST. In addition we also observe considerably less frequently positive (Fig. 4.2.24a) and negative (Fig. 4.2.24b) persistent anomalies in the simulations with fixed SST over the South Pacific between 120° western longitude and the dateline. Also in the region southeast of South America there are less frequently long-lived anomalies in the simulations with fixed SST.

Figure 4.2.25 shows the distributions of the sum of positive and negative persistent anomalies obtained from the individual simulations. In each of the simulations we find the same general features as described in the preceding paragraph, although the location of the maxima varies somewhat between different realizations. The maximum in the storm track region, e.g., is substantially underestimated in each simulation and appears also further downstream than in the analyses. Over the South Pacific, on the other hand, in all simulations there are more often persistent anomalies to the west of about 140°W but less frequently further east. In both simulations with fixed SST we find persistent anomalies less frequently than in all simulations with varying SST over the South Pacific in the area between 120°W and the dateline.

In the following we present distributions of the relative occurrence of persistent anomalies derived from the simulations with varying SST distinguishing between seasons. Comparing the results between seasons, however, one has to bear in mind that different thresholds were chosen for each season (see Table 1). Figure 4.2.26 shows the relative occurrence of positive persistent anomalies for the different seasons. We find those three regions, where positive long-lived anomalies occur frequently, in all seasons. These are the storm track region over the southern Indian Ocean and the regions over the southern Pacific and Atlantic Ocean. In all these regions positive persistent anomalies occur most frequently in winter except for the southern Atlantic, where they appear

more often in autumn. The ECMWF analyses (not shown here) display the same feature. In the storm track region we observe about the same number of positive persistent anomalies in all seasons except winter. In summer, however, the maximum is located about 30° further upstream. In this season also the maximum over the southern Pacific is located about 50° further west than in the other seasons. In winter and to some extent in spring we find enhanced blocking activity west of South America centered at 40° southern latitude. The analyses reveal the same feature. In all seasons negative persistent anomalies (Fig. 4.2.27) do not occur as often as positive ones, and the distributions show the same seasonal variations as in the case of positive persistent anomalies.

In the following we present diagrams of the relative occurrence of persistent anomalies as a function of longitude. The estimates are averages over different zones, which were chosen with respect to the location of the maximum occurrence of persistent anomalies. One covers the zone between 40° and 60°S including the maxima in the storm track region and over the Atlantic, the other one between 50° and 70°S according to the maximum in the Pacific sector. The average over the zone between 40° and 70°S combines the estimates obtained for these two zones. In addition to the mean value for each data set, the internal variability between the five simulations with varying SST is indicated in the figures. The mean value obtained from the simulations with varying SST is given by the heavy solid line, the light solid lines represent this mean value with the standard deviation of the five individual simulations added and subtracted, respectively. The mean value obtained from the simulations with fixed SST is indicated by long dashes, that derived from the analyses by short dashes.

Figure 4.2.29 shows these average values in the case of positive persistent anomalies for the entire period of investigation exhibiting the characteristics illustrated in Figures 4.2.22-24 more clearly. In the storm track region over the southern Indian Ocean the ECMWF analyses indicate enhanced blocking activity in the zone between 40° and 60°S, but not at higher latitudes. Over the Pacific we can distinguish two regions, where positive persistent anomalies frequently occur. They are the region southeast of New Zealand and the region in the central Pacific. They are separated near 150° western longitude. In the region southeast of New Zealand long-lived anomalies occur more often in the zone between 40° and 60°S, whereas the maximum over the central Pacific is located closer to the pole. The most striking feature, however, is that there are generally less positive persistent anomalies in the simulations over the Indian and Pacific Ocean, in particular in the zone between 40° and 60°S. The model neither reproduces the enhanced blocking activity in the region southeast of New Zealand sufficiently. In the Atlantic region ECHAM3 reproduces the analysed distribution pretty well, and at high latitudes, i.e. in the zone between 50° and 70°S, we find more persistent anomalies in the simulations. At these latitudes the simulations are generally in better agreement

with the analyses. In the region over the South Pacific between 120° western longitude and the dateline the simulations with varying SST show substantially more long-lived anomalies than those with fixed SST. Although the internal variability between the five simulations with varying SST is particularly large in this region, the estimates obtained from the simulations with fixed SST are well beyond this range. In the other areas the values derived from the two sets of simulations are comparable.

Figure 4.2.30 gives the average values over the zone between 40° and 70°S distinguishing between seasons. In the storm track region we observe about the same number of positive persistent anomalies in the analyses in all seasons. In the Pacific region the two maxima southeast of New Zealand and over the central Pacific are clearly separated only in spring and summer. In winter, on the other hand, there appears only one wide area with frequent blocking activity between 160° eastern and 90° western longitude. In the simulations we find considerably less persistent anomalies in the storm track region in all seasons but winter. In the central Pacific, on the other hand, the simulations with varying SST give numbers comparable to those obtained from the analyses in all seasons but summer, those with fixed SST in spring and summer. In the region southeast of New Zealand ECHAM3 does not produce enough long-lived anomalies throughout the year. The difference between the two sets of simulations in the central Pacific with reduced occurrence of persistent anomalies in the simulations with fixed SST is also typical for all seasons.

In the case of negative persistent anomalies (Fig. 4.2.31) the overall distribution is similar to the distribution we observed for the positive anomalies. The analyses, however, reveal less negative persistent anomalies than positive ones in the storm track region between 40° and 60°S and the two maxima in the Pacific region are not as clearly separated. Negative persistent anomalies also frequently occur over the western Atlantic. In the zone between 40° and 60°S the model reproduces generally not enough long-lived negative anomalies in the storm track region and over the Pacific, but shows good agreement with the analyses over the western Atlantic. Further poleward, i.e. in the zone between 50° and 70°S, the simulations are in better agreement with the analyses in the central Pacific, but there are to often long-lived negative anomalies over the Atlantic. Also in this case the simulations with varying SST indicate more frequently long-lived anomalies than those with fixed SST in the central Pacific, but the discrepancy is reduced compared to the case of the positive anomalies. The seasonal variations of the occurrence of negative persistent anomalies (Fig. 4.2.32) are similar to those found for the positive anomalies, which were already discussed in further detail before.

Figures 4.2.33 and 34 give the relative occurrence of positive and negative anomalies as a function of their lifetime derived from the analyses in two areas, where persistent

anomalies frequently occur (Fig. 4.2.12b). These are the storm track region over the southern Indian Ocean and the area over the Pacific southeast of New Zealand. These regions are indicated by IND (40 – 60°S and 70 – 130°E) and PAE (40 – 60°S and 170 – 210°E), respectively. The solid line represents the positive and the dashed line the negative anomalies. In the storm track region (Fig. 4.2.33) we find more short-lived negative anomalies than positive ones in all seasons but spring. On intermediate time scales there are more positive anomalies, for long-lived anomalies the numbers are hardly distinguishable. In the figures for the Pacific region (Fig. 4.2.24) the curves are close together with generally somewhat less long-lived negative rather than positive anomalies. In autumn this trend is reversed, which may be an effect of the finite sampling time rather than a characteristic feature. In the simulations (not shown here) we could not identify any typical behavior of positive anomalies compared to negative ones with respect to their lifetime.

4.3 Time Mean Zonal Wind

As an example for the time mean climate state of the atmosphere we present maps of the climatological mean of the zonal wind component in this section. We chose the 300 hPa level, which is close to the height of the polar and subtropical jet stream as well.

In winter the ECMWF analyses (Fig. 4.3.1) show several maxima of westerly winds in the Northern Hemisphere. One of them is located over the eastern part of North America and extends over the North Atlantic, another is located at about 30°N extending from northern Africa over India and Japan into the Pacific region. While the maximum over North America is associated with the polar jet stream, the second one represents the core of the subtropical jet stream. Strong westerly winds also appear in these regions in the other seasons, the distribution is, however, altered in strength and shape. They are generally weaker than in winter and maximum values occur further north. In summer, however, the maximum over Japan does not appear, but we observe relatively strong westerlies over the northern Pacific.

In both sets of simulations performed with ECHAM3 (Figs. 4.3.2 and 3) we also find these two regions with strong westerly winds in winter. But here the westerlies are extending further downstream over the central parts of the oceans, in particular in the Pacific region. While the jet core in the Atlantic sector is stronger in the simulations than observed, it is slightly weaker in the Pacific sector. In both regions, however, the simulated westerly winds are stronger than in the analyses in the areas poleward of the jet cores, but weaker further south. The model does not reproduce the jet core over the Arabian Peninsula sufficiently, and the maximum over Japan is expanded upstream into

Asia. In summer the location of the maxima in the simulations is in good agreement with the analyses except for the Pacific region. Whereas the westerlies are too strong over Japan in this season, they are too weak in the central Pacific. In autumn the simulations are in very good agreement with the analyses, but in spring the maximum over the eastern United States is elongated eastward in the simulations. Significant differences between the two sets of simulations with varying and fixed SST with respect to the climatological mean of the zonal wind component are mainly found in the Pacific region. In all seasons but autumn the simulations with varying SST show stronger westerly winds in the area south of the jet core, but weaker ones further poleward.

In the Southern Hemisphere the ECMWF analyses (Fig. 4.3.4) show maximum westerly winds in the zone between 20° and 30°S in winter. Strong westerlies also appear at about 50°S south of Africa. The most striking feature for the Southern Hemisphere winter is the double jet structure in the area near New Zealand. We observe strongest westerly winds exceeding 45 m/s between 20° and 30°S. Further poleward the zonal wind is weaker reaching a minimum of approximately 10 m/s over New Zealand. At about 60°S there is another maximum with westerly winds up to 25 m/s. This characteristic feature appears, though slightly altered, in the other seasons except summer. In this season, on the other hand, the westerly winds in the region southeast of Africa are stronger than during the other seasons.

This characteristic double jet structure south of New Zealand is generally reproduced by ECHAM3 (Figs. 4.3.5 and 6). The maximum of westerly winds in the zone between 20° and 30°S in winter reaches further downstream into the Pacific region. Over the southern oceans, in particular in summer and autumn, the simulations reveal generally weaker westerly winds than the analyses in the zone between 30° and 50° southern latitude, but stronger ones in the regions closer to the pole. Significant differences between the two sets of simulations appear at about 30°S over the eastern Pacific and the Atlantic Ocean, where we find typically stronger westerly winds in the simulations with fixed SST.

The results derived from the ECMWF analyses are in good agreement with the climatologies of the zonal wind component in 200 hPa derived from NMC analyses for the Northern and Australian analyses for the Southern Hemisphere by Speth and Madden (1987), though regional differences appear in the Southern Hemisphere. This, however, may be due to uncertainties in the data itself because of the sparse data coverage in the Southern Hemisphere.

4.4 Transient Fluctuations

In this section we present maps of the contributions of the transient fluctuations to the intra-seasonal variability. The estimates were derived as described in section 3.4 and include the root-mean-square deviation (RMS) of the 500 hPa geopotential height field, the kinetic energy and meridional transport of westerly momentum at 300 hPa, and the meridional transport of sensible heat at 850 hPa. We chose these levels according to observations indicating that the fluxes of momentum are strongest in the upper troposphere just below the level of the jet streams, whereas the heat fluxes are enhanced in the lower troposphere. For each variable we show results derived from unfiltered and band- and low-pass filtered transient fluctuations as well. The band-pass filter retains transient fluctuations with periods between 2.5 and 6 days, whereas the low-pass filter contains fluctuations on longer time scales. Due to the different characteristics of the transient fluctuations in the Northern and Southern Hemisphere (see Figs. 4.1.1 and 26) we chose a low-pass filter keeping transients on time scales between 10 and 90 days for the Northern and between 6 and 90 days for the Southern Hemisphere. In the following the band-pass filtered transients will also be referred to as the high-frequency, the low-pass filtered ones as the low-frequency transients or eddies. The contributions of the band-pass and low-pass filtered transient fluctuations to the intra-seasonal variability exhibit distinctly different patterns because of the different phenomena contributing to the variability on different time scales. While mainly baroclinic disturbances such as traveling cyclones give rise to the high-frequency variability, several phenomena contribute to the extratropical low-frequency variability. Phenomena such as blocking anticyclones and cutoff lows, e.g., lead to large-scale flow anomalies that persist for one or several weeks. Apart from slowly propagating atmospheric waves, the structure of which is basically equivalent barotropic, variations of the stationary ultra-long waves give rise to the low-frequency intra-seasonal variability.

The contributions of the transient fluctuations to the intra-seasonal variability, i.e. the transient variances and covariances, obtained from the ECMWF analyses appear to be noisier than the distributions derived from the simulations. This is not only an effect of the statistical sampling, as the patterns obtained from individual simulations are also smoother than those from the analyses. The fact may rather be accounted for by inconsistencies in the data due to the way the analyses were obtained (see section 4.1.1) or the circumstance that the analyses give more weight to short-scale variations than ECHAM3 because of the higher horizontal resolution.

4.4.1 Geopotential Height

The ECMWF analyses reveal two maxima of the RMS of the 500 hPa geopotential height field obtained from the unfiltered transient fluctuations (Fig. 4.4.1). One is located over the North Pacific near the Aleutian Islands and the other over the North Atlantic centered south of Iceland extending downstream over Scandinavia. We find relatively small values with respect to the zonal mean over the western part of North America and Siberia as well. The intra-seasonal variability is strongest in winter, but the two maxima appear in all seasons though altered in strength and shape. The maximum near the Aleutian Islands, e.g., occurs further south than in winter and is elongated in the zonal direction. The major part of the intra-seasonal variability is caused by the low-frequency transients on time scales longer than 10 days (Fig. 4.4.3) showing the characteristic maxima over the northern Pacific and Atlantic Ocean. Upstream of these maxima the high-frequency transient fluctuations (Fig. 4.4.2) give major contributions to the intra-seasonal variability indicating the regions of the strongest activity of cyclones, the so-called storm tracks, over the Central Pacific and over Labrador extending into the western Atlantic region.

Figure 4.4.4 shows the total, that means estimated from the unfiltered transient fluctuations, RMS field derived from the simulations with varying SST. The maxima over the North Pacific and North Atlantic are pronounced, but compared to the analyses the intra-seasonal variability is generally reduced over most of the hemisphere. This reduction is striking in the Atlantic region, where the RMS is underestimated by approximately 20 m throughout the year. In the Pacific region, on the other hand, the magnitude of the RMS corresponds to the observed estimates, but in contrast to the analyses its center has the same location and shape in spring and autumn as in winter. In the analyses (Fig. 4.4.1) the maximum undergoes some seasonal variations. It is located further south and appears elongated in the zonal direction. Therefore the intra-seasonal variability is generally overestimated in the simulations at high latitudes, in particular over Alaska, but underestimated in the region further south in all seasons but winter. The distribution of the RMS estimated from the low-pass filtered fluctuations (Fig. 4.4.6), which account for most of the intra-seasonal variability, illustrates these deficiencies too. In the Pacific region the intensity of the storm tracks as simulated by ECHAM3 (Fig. 4.4.5) is underestimated by approximately 8 m on its southern side. Further north, on the other hand, the band-pass filtered RMS is stronger than observed. In the Atlantic region the activity of cyclones is generally too weak in the model. In winter, e.g., the maximum values differ by approximately 10 m. In addition, the cyclones as simulated by the model show a tendency to retain their zonal movement, when they approach the continents, rather than turning northeastward as indicated in observations.

The distributions obtained from the simulations with fixed SST (Fig. 4.4.7) show basically the same characteristics as those with varying SST. In the Pacific sector, however, the storm tracks (Fig. 4.4.8) are shifted slightly poleward in this set of simulations. The low-pass filtered RMS (Fig. 4.4.9) reveals enhanced intra-seasonal variability over Alaska and northwestern Canada in winter. This is in agreement with results by Ponater et al. (1990) for an earlier version of the ECHAM model.

In the Southern Hemisphere the ECMWF analyses (Fig. 4.4.10) show several maxima of the RMS of the 500 hPa geopotential height field obtained from the unfiltered fluctuations. One is located over the southern Indian Ocean centered at about 50°S, another one over the South Pacific at about 60° latitude between New Zealand and South America. We find highest values just south of New Zealand in the region, where the double jet structure occurs. A third region with relatively strong intra-seasonal variability appears southeast of South America. We observe the maxima in all seasons, though slightly displaced in meridional direction. In winter the maximum south of New Zealand, e.g., is located $5 - 10°$ further south than in the other seasons. The maximum over the Indian Ocean, however, is placed at about the same latitudes throughout the year. In the Southern Hemisphere the main storm track, which is indicated by the band-pass filtered RMS (Fig. 4.4.11), lies along 50°S over the southern Indian Ocean and is elongated into the Atlantic and Pacific regions. The center is located at about the same latitude throughout the year, but the activity of cyclones is strongest in winter, when the storm track region is also broader than in the other seasons. The maxima of the RMS south of New Zealand and downstream of the tip of South America are mainly caused by the transient fluctuations on time scales longer than 6 days (Fig. 4.4.12). A less pronounced maximum occurs in the storm track region over the Indian Ocean

The results derived from the ECMWF analyses are in good agreement with those of Trenberth (1982) obtained from data originating from the World Meteorological Center in Melbourne, Australia. In the total RMS field he finds three distinct maxima in the southern Indian Ocean, south of New Zealand and southeast of South America in winter and summer as well. Both the magnitude and the seasonal variation are comparable to our estimates. There is also good agreement, if we distinguish between band-pass and low-pass filtered fluctuations, with respect to the location of the storm tracks over the southern Indian Ocean and of the maxima of the low-frequency variability south of New Zealand and southeast of South America. The magnitude, however, cannot be compared directly as Trenberth uses filters with different characteristics.

Figure 4.4.14 shows the band-pass filtered RMS estimated from the simulations with varying SST for the Southern Hemisphere. The model reproduces the main storm track over the southern Indian Ocean, but centered at about 55°S, i.e. 5° further south than

in the analyses. In addition the model shows a strong tendency for zonal symmetry as relatively high values of the band-pass filtered RMS occur over the Atlantic and Pacific Ocean at the corresponding latitudes. As a result in the simulations the band-pass filtered RMS is generally stronger than observed in the zone between 55° and 65°S, but weaker at other latitudes. This deficiency is most pronounced in the Southern Hemisphere summer. With respect to the low-pass filtered RMS the simulations show characteristics quite different from the analyses (Fig. 4.4.15). Throughout the year we find a maximum southwest of South America at about 60°S, which the analyses only show in winter and spring in this region (Fig. 4.4.12). The most important discrepancy is that in the simulations there is no indication of the maximum south of New Zealand. This, however, is surprising as the double jet structure in this region was successfully reproduced by the model. In the simulations with fixed SST (Figs. 4.4.16-18) we find basically the same characteristics as for the other set of simulations.

4.4.2 Kinetic Energy

The distribution of the eddy kinetic energy caused by the band-pass filtered transient fluctuations derived from the ECMWF analyses (Fig. 4.4.20) shows two maxima on the Northern Hemisphere. They are located in the exit regions of the polar jet stream over the northern Atlantic and the subtropical jet stream over the central Pacific and are elongated downstream. Seasonal variations are stronger in the Atlantic region than over the Pacific, where the eddy kinetic energy is comparable for all seasons but summer. In spring and autumn, however, the center over the Pacific is shifted about 5° further poleward than in winter. Maxima of the eddy kinetic energy caused by low-frequency transient fluctuations (Fig. 4.4.21) are located downstream of the storm tracks over the eastern part of the Pacific and Atlantic Ocean extending over the Canadian west coast and western Europe. The eddy kinetic energy is strongest in winter, but only slightly reduced in spring and autumn. The fast and slowly varying transient disturbances contribute to the same extent to the total eddy kinetic energy, which is given in Figure 4.4.19. As a consequence we observe two wide regions with strong eddy kinetic energy extending over the central Pacific and western Canada on one side and the northern Atlantic and western Europe on the other.

In the simulations with varying SST the band-pass filtered eddy kinetic energy (Fig. 4.4.23) is generally underestimated by approximately 20 m^2s^{-2} over most of the Northern Hemisphere midlatitudes. But the maxima are located in the same regions as indicated in the analyses, and the seasonal changes are reasonably reproduced by the model. In winter, however, in the Pacific region the maximum activity of the transient eddies is shifted about 5° further poleward as compared to the analyses. The contri-

butions of the transient fluctuations on time scales longer than 10 days to the eddy kinetic energy (Fig. 4.4.24) are even more severely underestimated in the simulations, in particular in the Atlantic region. Also the general structure is not sufficiently simulated in this sector. While the analyses (Fig. 4.4.21) reveal a pronounced maximum west of the British Isles throughout the year, the simulations do not indicate enhanced eddy activity in this area, but rather a wide area of a comparable amount of eddy kinetic energy extending further downstream over central Europe. This deficiency is especially marked in winter with a reduction of the kinetic energy by more than one third in the region west of Great Britain (160 vs. 110 m^2s^{-2}). The severe underestimation of the eddy kinetic energy on all time scales becomes even more clear from the distribution of the total eddy kinetic energy estimated from the simulations (Fig. 4.4.22).

The distributions obtained from the simulations with fixed SST (Fig. 4.4.25) show basically the same characteristics as in the case of varying SST. For the low-pass filtered RMS (Fig. 4.4.27) we do not find any typical difference between the two sets of simulations appearing in all seasons. In winter and summer, e.g., the low-frequency variability over most of the western hemisphere is stronger in the simulations with varying SST, but it is weaker in spring and autumn. For the eddy kinetic energy caused by the high-frequency transient fluctuations (Fig. 4.4.26), on the other hand, the distributions show a characteristic difference throughout the year. The kinetic energy estimated from the simulations with fixed SST is generally stronger north of the latitude, where the maxima occur, but weaker on the southern side. This feature is most pronounced over the Pacific and Atlantic Ocean in the storm track regions, but is also found over North America, central Europe or East Asia.

In the Southern Hemisphere the transient fluctuations on time scales shorter than 6 days (Fig. 4.4.29) give major contributions to the eddy kinetic energy in the storm track region over the southern Indian Ocean. The maximum is extending into the Atlantic and the Pacific regions with the exception of winter, when relatively weak estimates of the kinetic energy occur southeast of Australia. This feature may be accounted for by the fact that the subtropical jet stream (Fig. 4.3.4) is extending further westward over Australia and the eastern Indian Ocean in this season. Throughout the year the analyses indicate maximum eddy kinetic energy caused by the transient fluctuations on long time scales (Fig. 4.4.30) south of New Zealand, which is just north of the corresponding maximum observed in the RMS field (Fig. 4.4.12). In winter fairly strong values of kinetic energy occur also at about 30°S east of Australia and 40°S west of South America.

The results derived from the ECMWF analyses are in agreement with those by Trenberth (1982), who computed the eddy kinetic energy on the 500 hpa level. In winter, however, he notices a different distribution of the low-pass filtered eddy kinetic energy

in the Pacific region. He observes the maximum south of New Zealand, but only a slight indication of enhanced kinetic energy east of Australia and west of South America. This may be accounted for by a stronger effect of the subtropical jet stream east of Australia at 300 hPa than at the lower level.

Figure 4.4.32 shows the band-pass filtered eddy kinetic energy obtained from the simulations with varying SST. The model generally underestimates the kinetic energy not only in the storm track region, but also at latitudes farther north, i.e. equatorward. This discrepancy is striking in the regions over the southern coast of Australia and New Zealand. Further poleward, on the other hand, the simulations show stronger eddy kinetic energy than the analyses. The underestimation of eddy kinetic energy, in particular in the storm track region, is most severe in the Southern Hemisphere summer. With respect to the low-pass filtered eddy kinetic energy the simulations (Fig. 4.4.33) reveal quite different characteristics than the analyses similar to those we observed in the low-pass filtered RMS field (Fig. 4.4.15). Generally the kinetic energy is severely underestimated over most of the hemisphere, and we find no indication of a maximum south of New Zealand. Instead relatively high estimates occur over the South Pacific at about 60°S. The simulations with fixed SST (Figs. 4.4.34-36) show the same characteristics as the simulations with varying SST.

4.4.3 Meridional Transport of Momentum

Figure 4.4.37 shows the meridional transport of westerly momentum caused by the unfiltered transient fluctuations derived from the ECMWF analyses. Positive values indicate northward, i.e. poleward on the Northern and equatorward in the Southern Hemisphere, and negative values southward fluxes. We find strongest poleward fluxes over North America in the entrance region of the polar jet stream and over northern Africa in the entrance region of the subtropical jet stream. But relatively high values appear also over East Asia and the western Pacific. In the central regions of both the Pacific and Atlantic Ocean the northward transports are generally weak, and westerly momentum is transported southward over the northern oceans. In spring and autumn the fluxes exhibit the same overall structure as in winter, but the fluxes are most intense in winter. In summer the fluxes are generally weak, and only a maximum over Labrador is pronounced. The high-frequency transient fluctuations (Fig. 4.4.38) give rise to distinct dipole patterns in the central part of the Pacific and Atlantic Ocean as well. The fluxes converge at the axes of the storm tracks with poleward fluxes south and equatorward fluxes north of them. The transient fluctuations on short time scales contribute also to the strong northward transports over North America and East Asia. The transient fluctuations on long time scales (Fig. 4.4.39) account for the strong northward

fluxes of westerly momentum over North America and northern Africa, but also in the western Pacific region. In the central regions of the oceans they cause the intense southward fluxes of momentum, in particular in winter, when they reach as far south as 30°N.

Figure 4.4.40 shows the meridional transport of westerly momentum derived from the simulations with varying SST. The distribution reveals some differences with the general structure appearing in the analyses. The most striking feature is that the strong northward fluxes over northern Africa are underestimated in the simulations and that they are located too far downstream, in particular in winter. This is consistent with the misplaced subtropical jet stream in this region (Fig. 4.3.2). But also over eastern North America and East Asia the northward fluxes are underestimated. Over the eastern Pacific and North America we find stronger northward transport of westerly momentum by the high-frequency disturbances (Fig. 4.4.42), in particular in winter. The characteristic dipole structure over the central Pacific is suppressed in the simulations as the northward fluxes south of the storm track are markedly reduced (15 vs. 25 m^2s^{-2}). In the Atlantic region the orientation of the dipole is different to the observed structure. The counterpart of the strong southward fluxes south of Iceland are strong northward fluxes over central Europe and not over western Europe as indicated in the analyses (Fig. 4.4.38). This suggests that ECHAM3 does not simulate the storm tracks over northwestern Europe properly. The different characteristics of the meridional transport by the low-frequency transient fluctuations in the simulations (Fig. 4.4.42) cause the underestimation of the northward fluxes over northern Africa. Over North America, on the other hand, the transports are reasonably well reproduced. Also the southward fluxes of momentum in the central regions of the oceans are captured by the model, though the distribution in the Pacific region is closer to the observed structure.

The distributions obtained from the simulations with fixed SST (Fig. 4.4.43) are similar to those obtained from the simulations with varying SST. For the momentum fluxes due to low-frequency transients (Fig. 4.4.45) we find only regional differences that vary from season to season. For the momentum fluxes caused by the high-frequency transient fluctuations (Fig. 4.4.44), however, we find some typical dissimilarities between the two sets of simulations. In the simulations with fixed SST the northward fluxes of westerly momentum are generally stronger over most of the hemisphere, in particular in the storm track regions over the Pacific and Atlantic Ocean. South of the storm track region we find enhanced northward and on the northern side enhanced southward transports of westerly momentum caused by the high-frequency transient fluctuations.

In the Southern Hemisphere the analyses (Fig. 4.4.46) show poleward transport of westerly momentum nearly everywhere north of 50°S and equatorward fluxes south of this latitude. Maxima occur to the west of the continents, and strongest convergence

is found in the main storm track region over the southern Indian Ocean. The overall structure undergoes no characteristic seasonal variations, but the fluxes are generally strongest in winter. Mainly the high-frequency disturbances (Fig. 4.4.47) accomplish the poleward momentum fluxes over the southern Indian Ocean and the strong convergence of the fluxes at about 55° southern latitude. They contribute also to the enhanced poleward fluxes southwest of Africa. The strong poleward fluxes in the regions upstream of the continents are primarily caused by the transient fluctuations on long time scales (Fig. 4.4.48). The fluxes undergo seasonal changes with respect to their magnitude. In winter, e.g., they are twice as strong as in summer. Our results are in good agreement with those by Trenberth (1982) except for the particular pattern, he noticed, with northward momentum fluxes between Australia and New Zealand. The ECMWF analyses reveal only reduced southward fluxes in this area.

Figure 4.4.50 shows the meridional transport of westerly momentum caused by the band-pass filtered transient fluctuations estimated from the simulations with varying SST. Compared to the analyses and consistent with the weaker storm tracks and their poleward displacement, the simulations reveal weaker poleward momentum fluxes north of the axis of the storm track, but stronger ones further south. This model deficiency is not only typical for the storm track region, but rather for the entire zone between 30° and 60° southern latitude. It is most severe in summer and autumn. The meridional fluxes of westerly momentum caused by low-frequency transient fluctuations (Fig. 4.4.51) show some dissimilarities with the analyses. Generally the analyses reveal stronger poleward momentum fluxes in the midlatitudes and stronger equatorward fluxes at higher latitudes. The enhanced poleward fluxes over the southern coast of Australia and New Zealand are not captured by the model at all. ECHAM3 also fails to reproduce the relatively strong poleward momentum fluxes in the South Pacific between 120° and 150° western longitude that appear in the analyses in all seasons (Fig. 4.4.48). The simulations with fixed SST (Figs. 4.4.52-54) show the same characteristics which we found for the simulations with varying SST.

4.4.4 Meridional Transport of Sensible Heat

Figure 4.4.56 shows the meridional transport of sensible heat by the high-frequency transient disturbances derived from the ECMWF analyses. We find strongest northward fluxes in the main storm track regions over the Pacific and Atlantic Ocean. But the maxima are extending over East Asia and eastern North America reaching over northwestern Canada. Very weak heat fluxes occur over western North America and central Asia. The overall structure shows hardly any seasonal variations with respect to the location of the maxima, but the fluxes are stronger in winter than in spring and autumn,

in particular with regard to the Atlantic storm track. In summer, however, the poleward heat fluxes are markedly reduced, in the Pacific region the maximum is shifted southward of the Aleutian Islands. The transient fluctuations on long time scales (Fig. 4.4.57) cause strong poleward fluxes of sensible heat over the Bering Sea and the Norwegian Sea. Enhanced fluxes occur also over the Canadian Archipelago and central North America. The poleward heat fluxes over the Bering Sea and the Norwegian Sea are strongest in winter, in spring and autumn they are reduced to half the magnitude in winter. Over central North America and the Canadian Archipelago, on the other hand, the poleward heat fluxes are about equal in all seasons but summer. Equatorward heat fluxes arise on the western coast of North America. They are strongest in summer, when the equatorward fluxes in this region are of the same magnitude as the poleward fluxes elsewhere.

Figure 4.4.58 shows the total, that means estimated from the unfiltered transient fluctuations, meridional transport of sensible heat derived from the simulations with varying SST. The distribution is in good agreement with the analyses. The heat fluxes caused by the high-frequency fluctuations (Fig. 4.4.59) are slightly underestimated over most of the hemisphere by the model, but the general structure and also the seasonal variations are successfully reproduced. The distribution of the meridional heat flux caused by the low-frequency fluctuations (Fig. 4.4.60) reveal also a similar structure as in the analyses. The maximum over the Bering Sea, however, is markedly overestimated throughout the year.

Concerning the meridional transport of sensible heat in the lower troposphere the distributions obtained from the simulations with fixed SST (Fig. 4.4.61) are generally closer to those obtained from the simulations with varying SST than in the upper troposphere, that means at the 500 and 300 hPa level. In the preceding sections we have discussed the typical differences between the two sets of simulations. Here we find only small differences. In the simulations with fixed SST the high-frequency fluctuations (Fig. 4.4.62) lead to stronger poleward heat fluxes in the storm track regions over the Pacific and Atlantic Ocean in winter and spring. The strong poleward heat fluxes caused by low-frequency transient fluctuations over the Bering Sea are also stronger in this set of simulations in winter.

In the Southern Hemisphere the poleward fluxes of sensible heat by high-frequency transient disturbances (Fig. 4.4.65) are strongest over the southern Indian Ocean between 30° and 90° eastern longitude. The maxima are extending in the Atlantic and Pacific sector as well. The enhanced poleward heat fluxes southeast of Australia and New Zealand, however, are spinning poleward. This is accounted for by the tendency of storms to turn towards Antarctica, when they pass this region southeast of Australia. The distribution of the heat fluxes by low-frequency eddy activity (Fig. 4.4.66) shows a

characteristic dipole structure near the Andes with equatorward fluxes west and strong poleward fluxes east of the mountain range. The dipole structure appears suppressed in summer. Very strong poleward heat fluxes occur on the coast of southwestern Australia and also downstream of New Zealand. The maximum near the coast of Australia, however, does not show up in winter.

In agreement with the analyses we find strong poleward heat fluxes caused by high-frequency disturbances in the storm track region in the simulations performed with ECHAM3 (Fig. 4.4.68). But another region with enhanced poleward heat fluxes occurs in the South Pacific region between 120° and 180° western longitude. The relatively strong poleward fluxes, which are indicated in the region southeast of Australia and New Zealand in the analyses, however, do not appear in the simulations. As for the analyses the maximum over the South Pacific is located closer to Antarctica than the maximum in the Indian Ocean. Some of the characteristic features of the meridional heat flux by low-frequency eddy activity are captured by the model (Fig. 4.4.69). The dipole pattern near the Andes, however, appears clearly suppressed. We also find the maximum on the southeast coast of Australia in the relevant seasons. But the model fails to reproduce the enhanced poleward heat fluxes just downstream of New Zealand. The distributions obtained from the two sets of simulations do not reveal any typical differences.

5 Summary

In our study we have investigated the intra-seasonal variability in the extratropics as simulated by an atmospheric General Circulation Model (ECHAM3) under different aspects. First we have considered the GCM's capability to reproduce the midlatitude variability on intra-seasonal time scales by a comparison with observational data (ECMWF analyses). Secondly we have assessed the possible influence of Sea Surface Temperatures on the intra-seasonal variability by comparing estimates obtained from different simulations performed with ECHAM3 with varying and fixed SST as boundary forcing.

As shown in the results of the space-time spectral analysis, ECHAM3 successfully reproduces the general structure of the intra-seasonal variability in the Northern Hemisphere midlatitudes. There are three prominent planetary wave regimes indicated in the spectra. On time scales longer than 10 days, the low-frequency part of the spectrum, the ultra-long planetary waves at zonal wavenumber 1, 2 and 3 give major contributions to the intra-seasonal variability. On time scales shorter than 6 days, the high-frequency

part of the spectrum, the variability is mainly caused by the short baroclinic waves at wavenumber 6, 7 and higher. A third regime on intermediate time scales between 6 and 10 days, which is caused by the long planetary waves at wavenumber 4 and 5, however, does not appear as pronounced in the simulations as in the analyses. Also the seasonal variation of the intra-seasonal variability is captured by ECHAM3. Its magnitude is strongest in winter and considerably reduced in the other seasons. Also the intra-seasonal variability is caused by transient fluctuations with shorter wavelength on shorter time scales.

In the simulations, however, the low-frequency variability caused by the ultra-long planetary waves is severely underestimated. This deficiency is mainly due to the considerable underestimation of the variance induced by the ultra-long propagating waves on these time scales. The variance caused by the stationary waves, on the other hand, is underestimated by ECHAM3 on all time scales, but not as severe as for the propagating waves. In the high-frequency part of the spectrum the estimates of the variance obtained from the simulations are close to those obtained from the analyses.

There are characteristic differences between the spectra obtained from the two sets of simulations performed with ECHAM3 with varying and fixed SST as boundary forcing. On time scales shorter than 6 days the variance obtained from the simulations with fixed SST exceeds the variance derived from the simulations with varying SST. This effect is caused by the enhanced activity of the propagating waves in the case of fixed SST, in particular at wavenumber 6 and higher. In the low-frequency part, on the other hand, the spectra do not reveal any systematic difference between the two sets of simulations. In spring and autumn, e.g., the low-frequency variability is stronger for the simulations with fixed SST, in summer, however, for the simulations with varying SST.

The spectra obtained for the Southern Hemisphere midlatitudes reveal a quite different structure than for the Northern Hemisphere. There are only two prominent wave regimes indicated rather than three in the Northern Hemisphere. On time scales shorter than 6 days the variability is mainly caused by the planetary waves at wavenumber 5, 6 and higher. On time scales between 6 and 16 days, on the other hand, the long waves at wavenumber 3 and 4 give major contributions to the intra-seasonal variability. The contributions of the ultra-long waves 1 and 2 to the intra-seasonal variability are not as strong as in the Northern Hemisphere. These contrasts are mainly accounted for by the different characteristics of the propagating disturbances in both hemispheres. The intra-seasonal variability undergoes some seasonal variation. It is strongest in winter and considerably reduced in the other seasons. Also the prominent wave regime on time scales between 6 and 16 days is shifted to shorter wavelength and shorter time scales.

Although the general structure of the intra-seasonal variability in the Southern Hemisphere midlatitudes, that means the separation of the two prominent wave regimes on intermediate and short time scales, is successfully reproduced by ECHAM3, the spectra obtained from the simulations exhibit a striking difference to the ECMWF analyses. The variance in both regimes is considerably overestimated in the simulations. On other scales, in particular on time scales longer than 10 days for the long planetary waves at wavenumber 4 and 5, the intra-seasonal variability is significantly underestimated by the model. These discrepancies are mainly accounted for by the different characteristics of the propagating waves on these scales. The variance induced by the stationary waves is underestimated by ECHAM3 on all time scales, which is also characteristic for the Northern Hemisphere. The seasonal variation of the intra-seasonal variability obtained from the simulations, however, differs from the variation observed for the ECMWF analyses. Transient fluctuations on the same spatial and temporal scale account for most of the variance throughout the year. Only the magnitude undergoes a seasonal variation, the variance is strongest in winter and considerably reduced in the other seasons. In the Southern Hemisphere the spectra do not reveal any characteristic difference between the two sets of simulations with varying and fixed SST.

Some of the typical features described in the preceding paragraphs can also be found in maps of the contributions of the transient fluctuations to the intra-seasonal variability. The estimates have been derived from unfiltered and filtered time series as well. The time characteristics of the filters have been chosen on the basis of the results of the wavenumber-frequency analysis. The band-pass filter retains the high-frequency fluctuations on time scales between 2.5 and 6 days and the low-pass filter fluctuations on time scales between 10 and 90 days for the Northern Hemisphere and between 6 and 90 days for the Southern Hemisphere.

As shown in the maps of the RMS of the geopotential height field derived from the unfiltered time series, the intra-seasonal variability as simulated by ECHAM3 is underestimated over most of the Northern Hemisphere, in particular in the Pacific and Atlantic region. Over Alaska and Kamchatka, on the other hand, the intra-seasonal variability is enhanced in the simulations. This is mainly due to the contributions of the low-frequency transient fluctuations. The contributions of the high-frequency or band-pass filtered fluctuations, which indicate the storm tracks, are in better agreement with the ECMWF analyses. In the Atlantic region, however, the strength of the storm track is generally underestimated by the model. In the Pacific region, on the other hand, the strength of the storm track is reduced on the southern side, but enhanced on the northern side of the axis. Further, the cyclones as simulated by the model show a tendency to retain their zonal movement, when they approach the continents, rather than turning northeastward as indicated in observations.

In the simulations with fixed SST the band-pass filtered RMS is stronger than in the simulations with varying SST over most of the Northern Hemisphere. Further, the Pacific storm track is shifted slightly poleward in this set of simulations. The contributions of the low-frequency transient fluctuations indicate significant differences between the two sets of simulations mainly at higher latitudes. In spring and autumn the distributions reveal enhanced variability on time scales longer than 10 days over most of the Northern Hemisphere in the simulations with fixed SST, in summer and winter in the case of varying SST. The largest difference appears in winter, when the intra-seasonal variability is considerably enhanced over northwestern Canada in the simulations with varying SST.

In the Southern Hemisphere the intra-seasonal variability as simulated by ECHAM3 is generally underestimated north of about 50° southern latitude, but overestimated at higher latitudes. The main storm track over the southern Indian Ocean, e.g., is located 5° further south than indicated in the ECMWF analyses. Further, the distribution of the band-pass filtered RMS reveals a strong tendency for zonal symmetry in the Southern Hemisphere midlatitudes. The contributions of the low-frequency fluctuations show a different pattern than in the analyses in the Pacific region. In the simulations there is no indication of a maximum of the low-pass filtered RMS south of New Zealand, which has been observed in the analyses. The simulations, on the other hand, show enhanced variability in the area southwest of South America. The distributions obtained from the two sets of simulations with varying and fixed SST reveal only small regional differences in the Southern Hemisphere midlatitudes.

A major part of the intra-seasonal variability on long time scales is induced by recurrent flow anomalies such as blocking anticyclones and cutoff lows that typically persist between one and several weeks. In agreement with the ECMWF analyses the simulations performed with ECHAM3 indicate three centers in the Northern Hemisphere, where persistent anomalies frequently occur. One is located over the eastern Pacific, one over the eastern Atlantic and another one over northern Russia. Another center, which the analyses do not reveal, is found over Baffin Bay. In the simulations, however, persistent anomalies occur more often at high latitudes, in particular over Alaska and the Aleutian Islands. Over the Atlantic, on the other hand, long-lived anomalies occur less frequently than observed and the maximum west of the British Isles, which is indicated in the analyses, is not pronounced. Also the model does not reproduce the frequent occurrence of cutoff lows in the Mediterranean. While the analyses show about the same number of persistent anomalies in the Pacific and Atlantic region, the model generates more long-lived anomalies in the Pacific than in the Atlantic region, if the model was forced by varying SST. In the case of fixed SST the opposite is true. This feature reflects the main difference between the two sets of simulations. In the Pacific

region persistent anomalies occur more often in simulations with varying SST, whereas in the Atlantic region the numbers of long-lived anomalies are comparable for the two sets of simulations.

In the Southern Hemisphere the distributions obtained from the ECMWF analyses indicate three regions, where persistent anomalies frequently occur. One is located in the storm track region over the southern Indian Ocean, another over the South Pacific centered southeast of New Zealand and extending further downstream over the Pacific Ocean. The third region is found over the South Atlantic. The distributions obtained from the simulations, however, show some different characteristics consistent with the dissimilar patterns of the low-frequency variability in the Southern Hemisphere. The model reproduces the center in the storm track region, but persistent anomalies occur about one third less frequently than in the analyses in this region. There is no maximum indicated southeast of New Zealand, but long-lived anomalies are found more frequently in the region further downstream. Over the South Atlantic the simulations are in general agreement with the analyses. The two sets of simulations reveal significant differences in the Pacific region. Over the South Pacific between 120° western longitude and the dateline and also in the region southeast of South America persistent anomalies occur more often in the simulations with varying SST.

As an example for the time mean climate state of the atmosphere we have investigated the climatological mean of the zonal wind component. The maps show that ECHAM3 reproduces the maxima of westerly winds over the eastern part of North America and over Asia, which represent the core of the polar jet stream and the subtropical jet stream, respectively. But the westerlies are extending further downstream over the central parts of the oceans than observed in the analyses. Further, the jet core as simulated by the model is stronger than in the analyses in the Atlantic region, but slightly weaker in the Pacific sector. In both regions, however, the simulations reveal stronger westerly winds in the areas poleward of the jet cores, but weaker ones further south. Besides, the model fails to reproduce the subtropical jet stream over the Arabian Peninsula sufficiently. Significant differences between the two sets of simulations with varying and fixed SST with respect to the climatological mean of the zonal wind component are mainly found in the Pacific region. The simulations with varying SST reveal stronger westerly winds in the area south of the jet core, but weaker ones further poleward.

ECHAM3 reproduces also the characteristic double jet structure south of New Zealand realistically. But the simulations reveal weaker westerly winds than the ECMWF analyses in the zone between 30° and 50° southern latitude, but stronger ones further poleward. The simulations with fixed SST show considerably stronger westerly winds at

about 30°S over the eastern Pacific and the Atlantic than the simulations with varying SST.

The maps of the meridional transport of westerly momentum caused by the transient fluctuations reveal some differences between the simulations and the analyses, which to some extent are due to the different characteristics of the jet streams as simulated by ECHAM3 and given by the ECMWF analyses. The strong northward fluxes of westerly momentum over northern Africa, e.g., cannot be found in the simulations. Further, the characteristic dipole structure induced by the high-frequency fluctuations with poleward fluxes south of the axes of the storm tracks and equatorward fluxes north of them is suppressed over the central Pacific. This is mainly accounted for by the reduced northward fluxes of momentum south of the Pacific storm track in the simulations. In the Atlantic region the orientation of the dipole is different to the observed structure. The counterpart of the strong southward fluxes south of Iceland are strong northward fluxes over central Europe and not over western Europe as indicated in the analyses.

In the simulations with fixed SST the meridional fluxes of momentum caused by the high-frequency simulations are generally stronger than in the simulations with varying SST over most of the Northern Hemisphere. With respect to the transports caused by the low-frequency fluctuations there are regional differences between the two sets of simulations, which vary by season.

In the Southern Hemisphere the simulations reveal weaker poleward fluxes of westerly momentum caused by the high-frequency fluctuations north of the axis of the main storm track over the southern Indian Ocean, but stronger ones further south. This is consistent with the weaker storm track and its poleward displacement compared to the ECMWF analyses. This deficiency of the model, however, is not only typical for the storm track region, but rather for the entire Southern Hemisphere midlatitudes. The momentum fluxes caused by the low-frequency fluctuations show also some dissimilarities with the analyses. The analyses reveal stronger poleward fluxes in the midlatitudes and stronger equatorward fluxes at higher latitudes. The enhanced poleward fluxes over the southern coast of Australia and New Zealand, which are indicated in the analyses, are not captured by the model. ECHAM3 also fails to reproduce the relatively strong poleward momentum fluxes in the central part of the South Pacific.

With regard to the meridional transport of sensible heat in the lower troposphere the simulations are in good agreement with the ECMWF analyses in the Northern Hemisphere. The only marked difference is the overestimation of the strong poleward heat fluxes over the Bering Sea by the model. In the simulations with fixed SST the heat fluxes caused by the high-frequency fluctuations are generally stronger than in the sim-

ulations with fixed SST in the storm track regions.

In the Southern Hemisphere, however, also the distribution of the meridional transport of sensible heat as simulated by ECHAM3 shows some differences with the analyses. The model fails to reproduce the enhanced poleward heat fluxes caused by the low-frequency fluctuations just downstream of New Zealand. Further, the characteristic dipole structure near the Andes with equatorward heat fluxes west and strong poleward fluxes east of the mountain range appears suppressed in the simulations.

To summarize, the intra-seasonal variability as simulated by ECHAM3 is underestimated over most of the Northern Hemisphere. While the contributions of the high-frequency transient fluctuations are reasonably well captured by the model, ECHAM3 fails to reproduce the observed level of low-frequency intra-seasonal variability. This is mainly due to the underestimation of the variability caused by the ultra-long planetary waves in the Northern Hemisphere midlatitudes by the model.

In the Southern Hemisphere midlatitudes, on the other hand, the intra-seasonal variability as simulated by ECHAM3 is generally underestimated in the area north of about 50° southern latitude, but overestimated at higher latitudes. This is the case for the contributions of the high-frequency and the low-frequency transient fluctuations as well. Further, the model indicates a strong tendency for zonal symmetry, in particular with respect to the high-frequency transient fluctuations.

While the two sets of simulations with varying and fixed SST as boundary forcing reveal only small regional differences in the Southern Hemisphere, there is a strong response to be found in the Northern Hemisphere. The contributions of the high-frequency transient fluctuations to the intra-seasonal variability are generally stronger in the simulations with fixed SST. Further, the Pacific storm track is shifted slightly poleward in this set of simulations. For the low-frequency intra-seasonal variability the model gives a strong, but regional response to the interannual variations of the SST.

Acknowledgments

I would like to thank Dr. Lennart Bengtsson for valuable discussions and Dr. Lydia Dümenil for editorial advice. I would also like to thank Dipl.-Phys. Monika Esch and Dipl.-Ing. Uwe Schulzweida, who performed the simulations with ECHAM3. The ECMWF analyses were used with permission of the German Weather Service.

References

Blackmon, M. L., 1976: A Climatological Spectral Study of the 500 mb Geopotential Height of the Northern Hemisphere. *J. Atmos. Sci.*, **33**, 1607-1623.

Blackmon, M. L., and N.-C. Lau, 1980: Regional Characteristics of the Northern Hemisphere Wintertime Circulation: A Comparison of the Simulation of a GFDL General Circulation Model with Observations. *J. Atmos. Sci.*, **37**, 497-514.

Blackmon, M. L., S. L. Mullen, and G. T. Bates, 1986: The Climatology of Blocking Events in a Perpetual January Simulation of a Spectral General Circulation Model. *J. Atmos. Sci.*, **43**, 1379-1405.

Dugas, B., and J. Derome, 1992: On the Climatology of Persistent Circulation Anomalies in the Atmosphere and in a General Circulation Model. *Atmosphere-Ocean*, **30**, 339-361.

Fraedrich, K., and H. Böttger, 1978: A Wavenumber-Frequency Analysis of the 500 mb Geopotential Height at 50°N. *J. Atmos. Sci.*, **35**, 745-750.

Fraedrich, K., and E. Kietzig, 1983: Statistical Analysis and Wavenumber-Frequency Spectra of the 500 mb Geopotential along 50°S. *J. Atmos. Sci.*, **40**, 1037-1045.

Hansen, A. R., A. Sutera, and D. E. Venne, 1989: An Examination of Midlatitude Power Spectra: Evidence for Standing Variance and the Signature of El Niño. *Tellus*, **41a**, 371-384.

Hayashi, Y., 1971: A Generalized Method of Resolving Disturbances into Progressive and Retrogressive Waves by Space Fourier and Time Spectral Analysis. *J. Meteor. Soc. Japan*, **49**, 125-128.

Hayashi, Y., and D. Golder, 1983: Transient Planetary Waves Simulated by GFDL Spectral General Circulation Models. Part I: Effects of Mountains. *J. Atmos. Sci.*, **40**, 941-950.

Held, I. M., 1983: Stationary and Quasi-Stationary Eddies in the Extratropical Troposphere: Theory. *Large-Scale Dynamical Processes in the Atmosphere*, edited by B. Hoskins, and R. Pearce, Academic Press, London, 397 pp.

Lejenäs, H., 1987: A Comparative Study of Southern Hemisphere Blocking during the Global Weather Experiment. *Q. J. R. Meteor. Soc.*, **113**, 181-188.

Lejenäs, H., and R. A. Madden, 1982: *The Annual Variation of the Large Scale 500 mb and Sea Level Pressure Fields.* Report from the Department of Meteorology, University of Stockholm and the International Meteorological Institute in Stockholm, DM-35, 36 pp.

Mechoso, C. R., and D. L. Hartmann, 1982: An Observational Study of Traveling Planetary Waves in the Southern Hemisphere. *J. Atmos. Sci.*, **39**, 1921-1935.

Mullen, S. L., 1987: Transient Eddy Forcing of Blocking Flows. *J. Atmos. Sci.*, **44**, 3-22.

Ponater, M., E. Kirk, and U. Schlese, 1990: GCM-Simulated Transient Variability in the Northern Hemisphere Extratropics and its Sensitivity to Sea Surface Temperature Variation. *Beitr. Phys. Atmosph.*, **63**, 189-204.

Pratt, R. W., 1976: The Interpretation of Space-Time Spectral Quantities. *J. Atmos. Sci.*, **33**, 1060-1066.

Priestley, M. B., 1981: *Spectral Analysis and Time Series.* Academic Press, London, 890 pp.

Rex, D. F., 1950a: Blocking Action in the Middle Troposphere and its Effect upon Regional Climate (I). An Aeorological Study of Blocking Action. *Tellus*, **3**, 196-211.

Rex, D. F., 1950b: Blocking Action in the Middle Troposphere and its Effect upon Regional Climate (II). The Climatology of Blocking. *Tellus*, **3**, 275-301.

Roeckner, E., K. Arpe, L. Bengtsson, S. Brinkop, L. Dümenil, M. Esch, E. Kirk, F. Lunkeit, M. Ponater, B. Rockel, R. Sausen, U. Schlese, S. Schubert, and M. Windelband, 1992: *Simulation of the Present-Day Climate with the ECHAM Model: Impact of Model Physics and Resolution.* MPI Report, 93, 172 pp.

Speth, P., and R. A. Madden, 1983: Space-Time Spectral Analyses of Northern Hemisphere Geopotential Heights. *J. Atmos. Sci.*, **40**, 1086-1100.

Speth, P., and R. A. Madden, 1987: The Observed General Circulation of the Atmosphere. *Landolt-Börnstein Meteorology, Volume 4a: Thermodynamical and Dynamical Structures of the Global Atmosphere*, edited by G. Fischer, Springer Verlag, Berlin, 491 pp.

Trenberth, K. E., 1982: Seasonality in Southern Hemisphere Eddy Statistics at 500 mb. *J. Atmos. Sci.*, **39**, 2507-2520.

Trenberth, K. E., 1992: *Global Analyses from ECMWF and Atlas of 1000 to 10 mb Circulation Statistics.* NCAR Technical Note, NCAR/TN-373+STR, 191 pp.

Trenberth, K. E., and K. C. Mo, 1985: Blocking on the Southern Hemisphere. *Mon. Wea. Rev.*, **113**, 3-21.

List of Figures

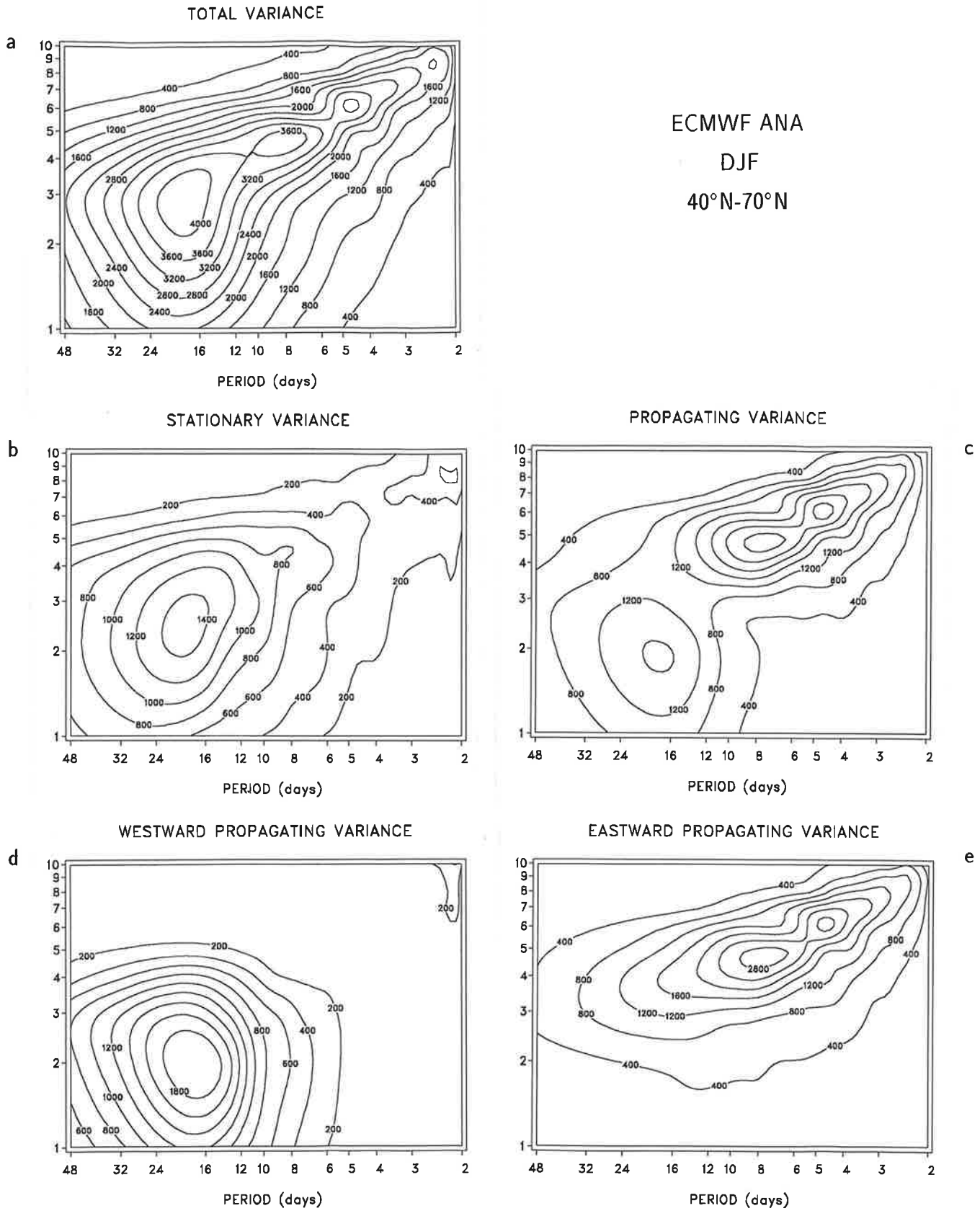

Fig. 4.1.1. Spectrum of the 500 hPa geopotential height for local winter in 40°N-70°N obtained from the ECMWF analyses for the total (a), the stationary (b), the propagating (c), the westward propagating (d) and the eastward propagating (e) variance. The spectral estimates are multiplied by wavenumber and frequency. Units are m^2, the contour interval is 400 m^2 for the total, propagating and the eastward propagating variance, 200 m^2 for the stationary and westward propagating variance. The zonal wavenumber is given on the ordinate.

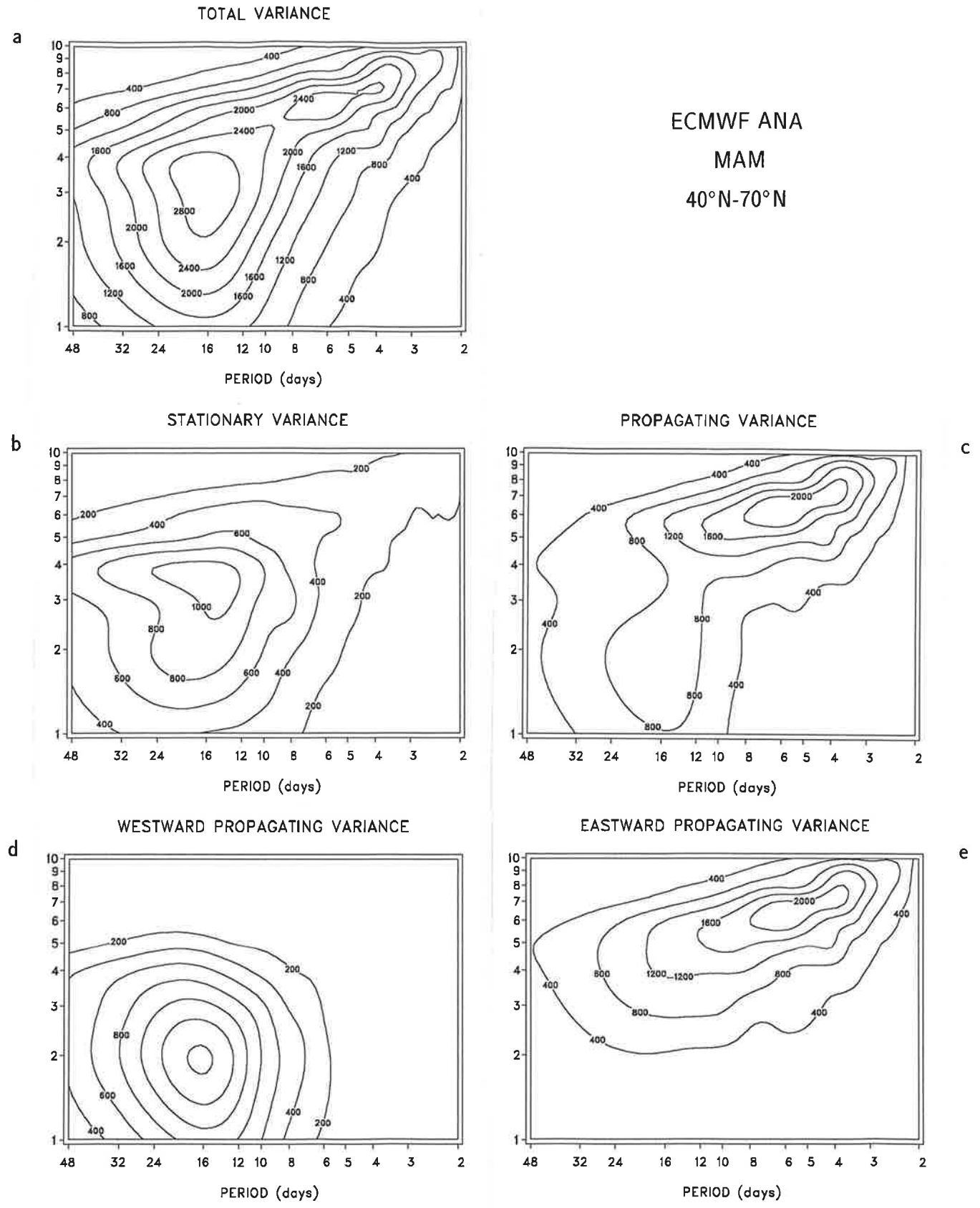

Fig. 4.1.2. As Fig. 4.1.1 but for local spring.

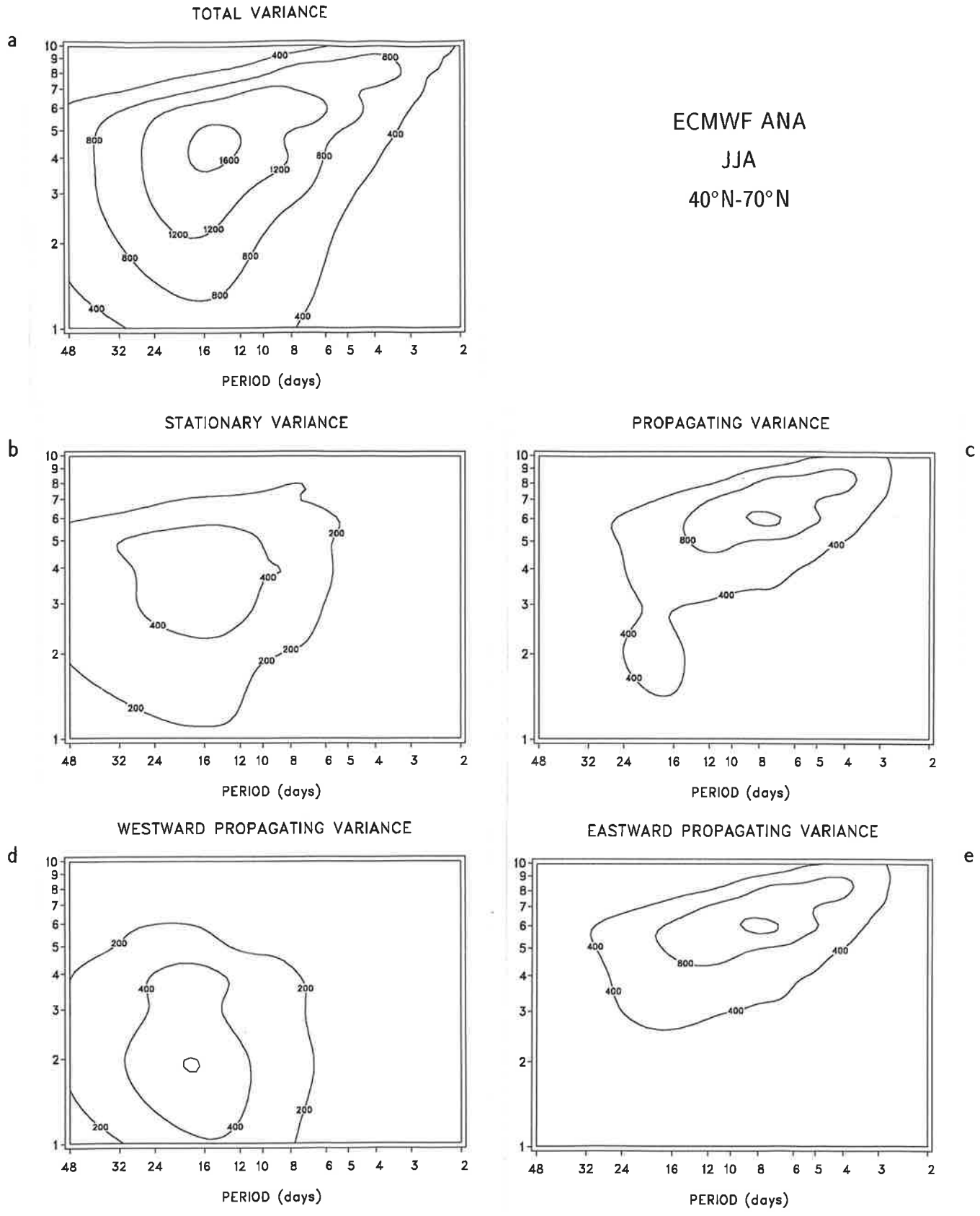

Fig. 4.1.3. As Fig. 4.1.1 but for local summer.

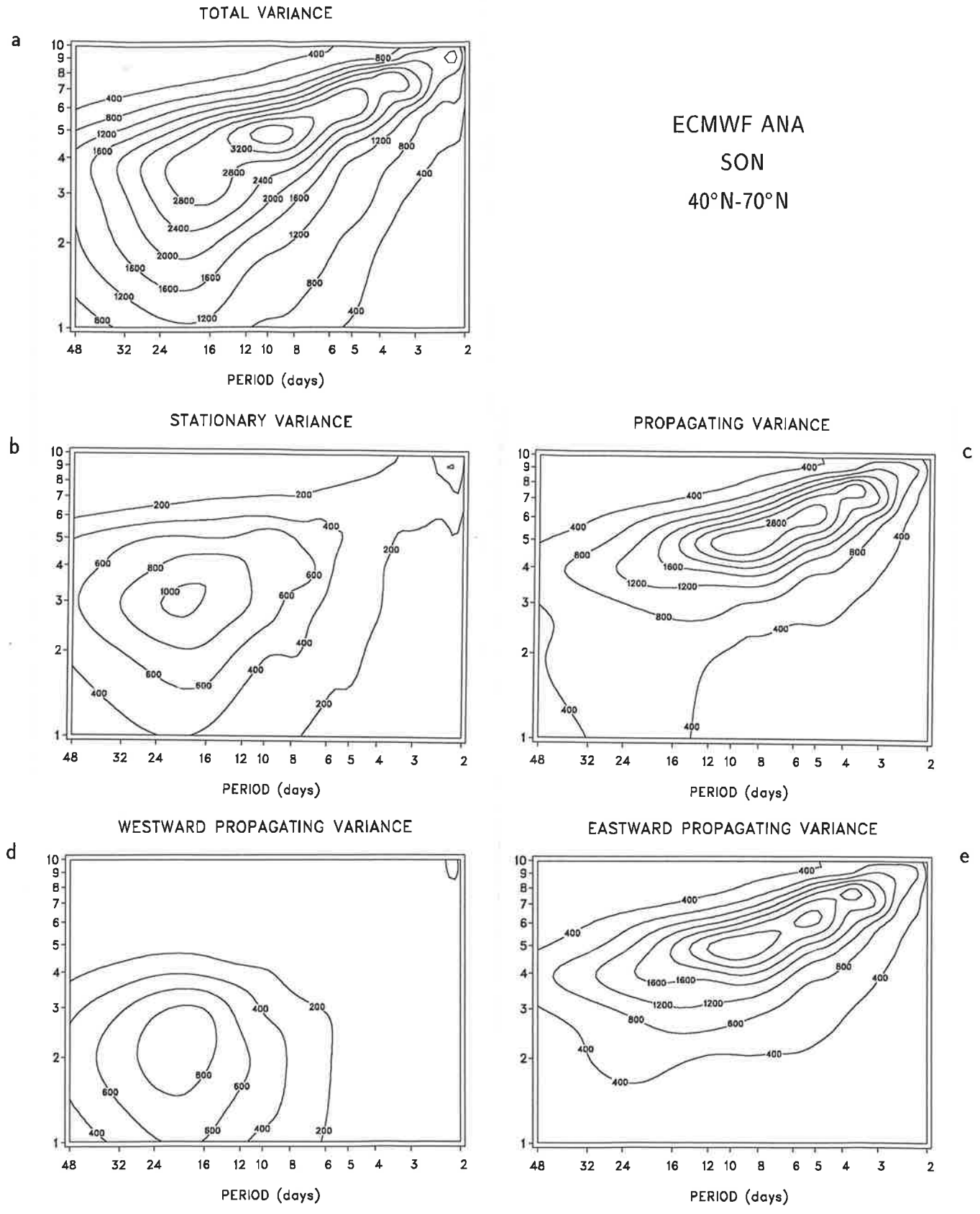

Fig. 4.1.4. As Fig. 4.1.1 but for local autumn.

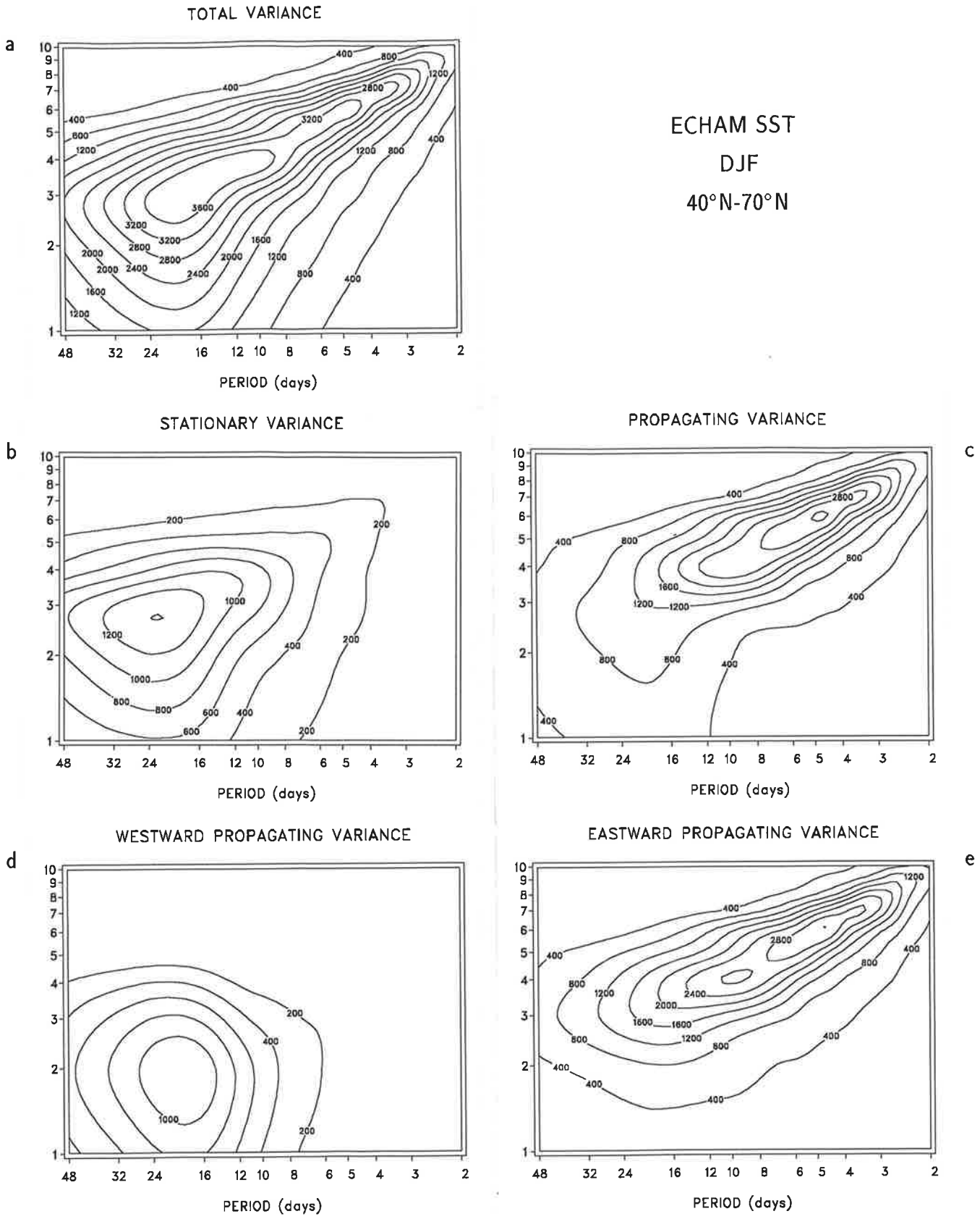

Fig. 4.1.5. As Fig. 4.1.1 but for the spectrum obtained from the simulations performed with ECHAM3 with varying Sea Surface Temperatures as boundary forcing.

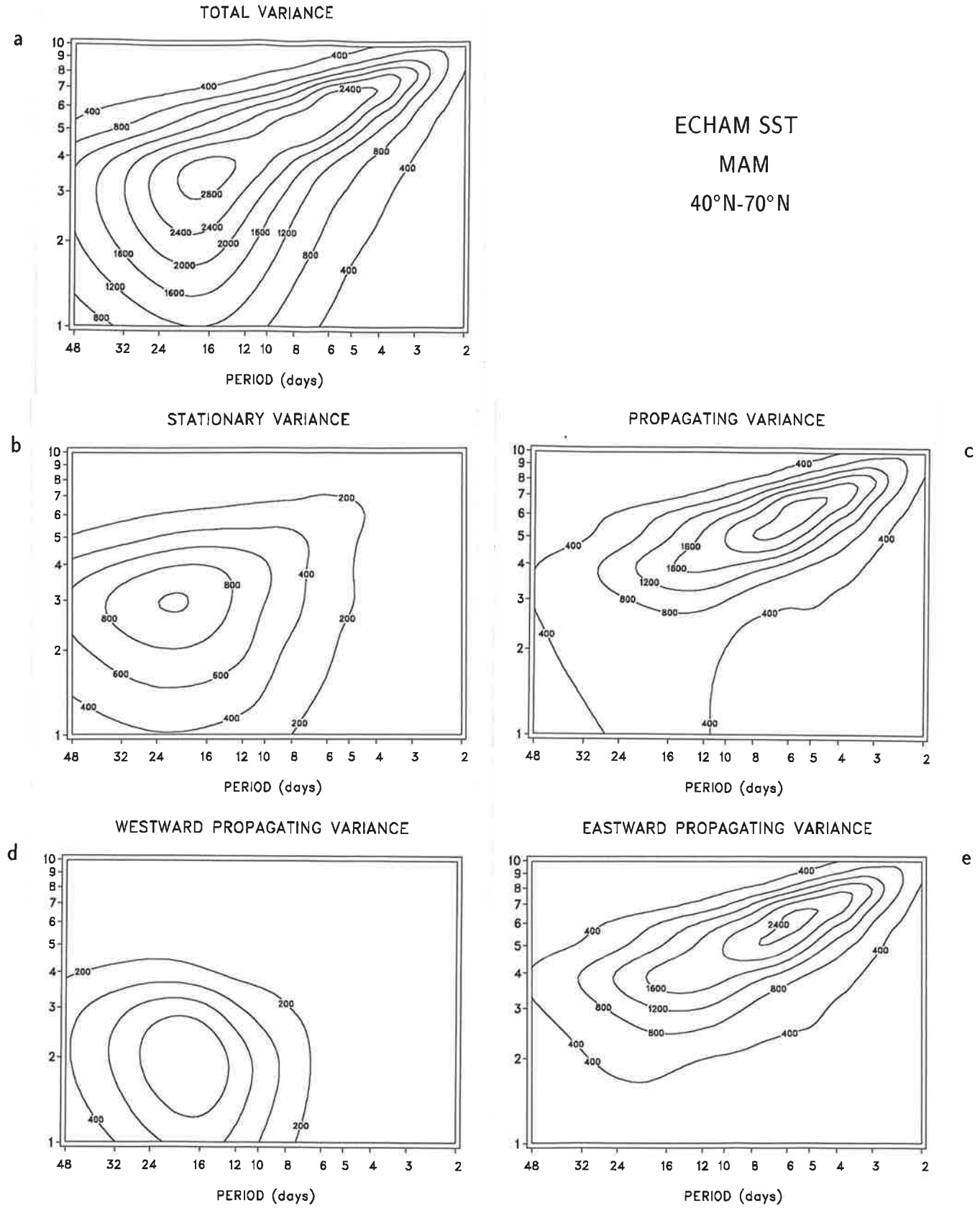

Fig. 4.1.6. As Fig. 4.1.5 but for local spring.

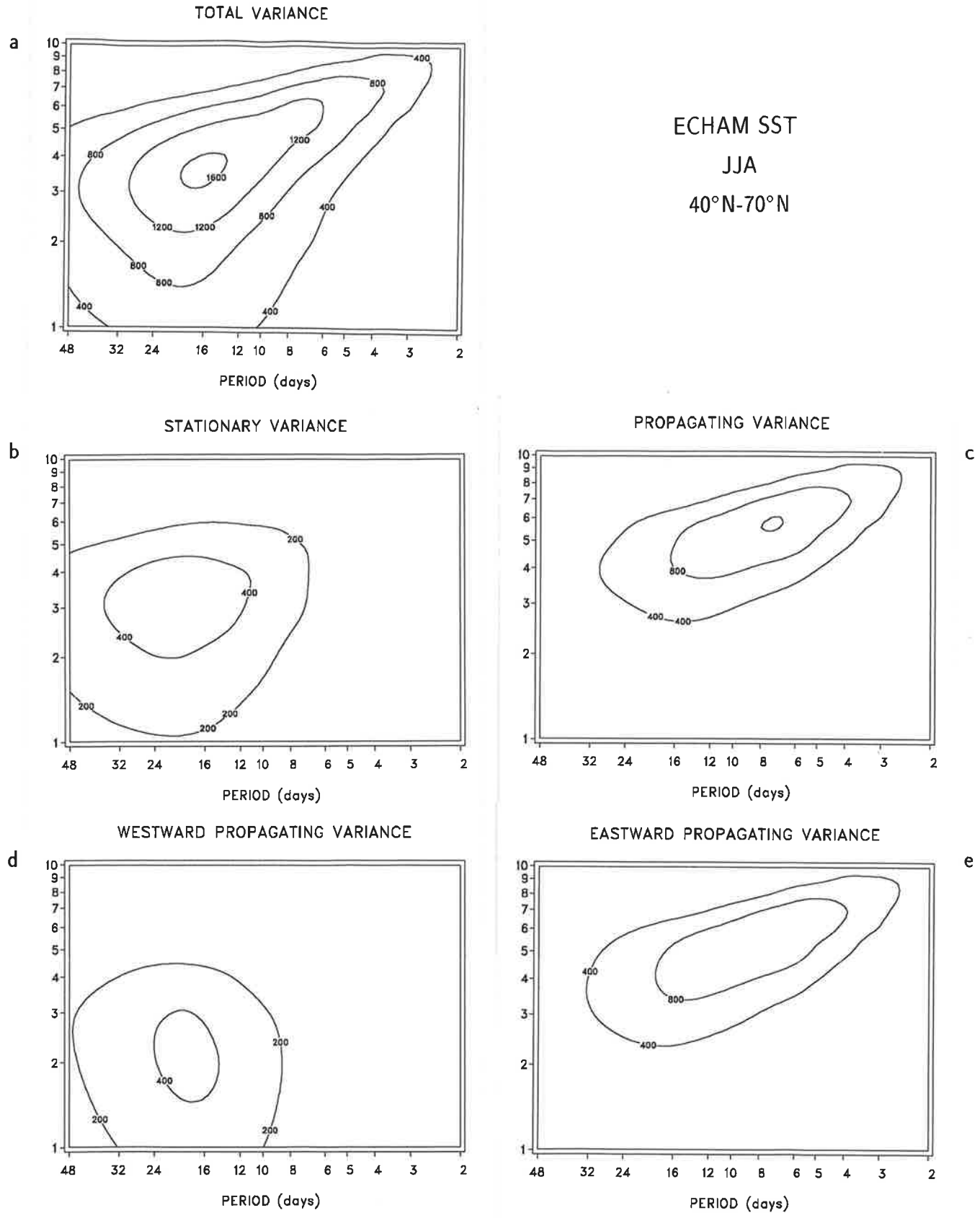

Fig. 4.1.7. As Fig. 4.1.5 but for local summer.

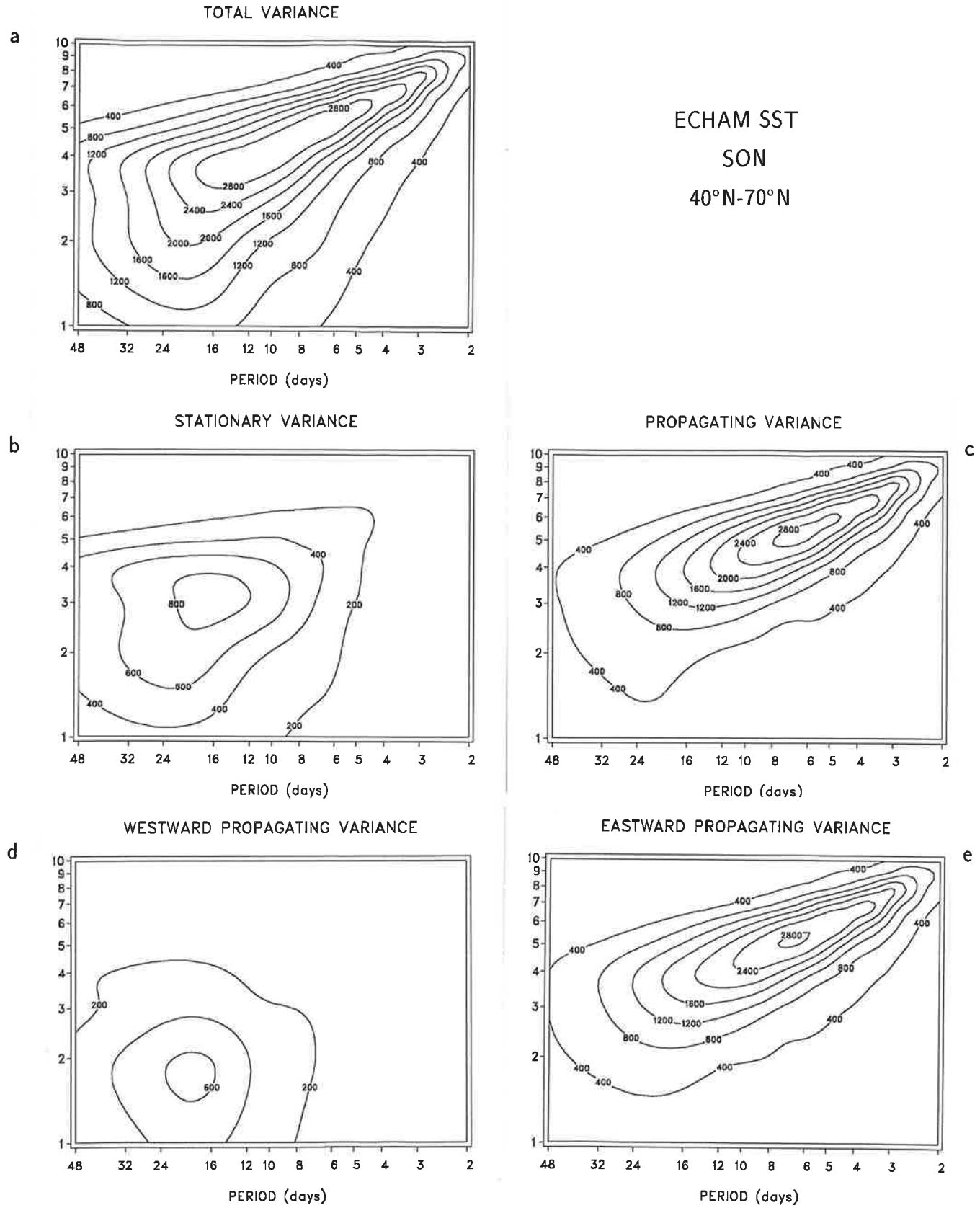

Fig. 4.1.8. As Fig. 4.1.5 but for local autumn.

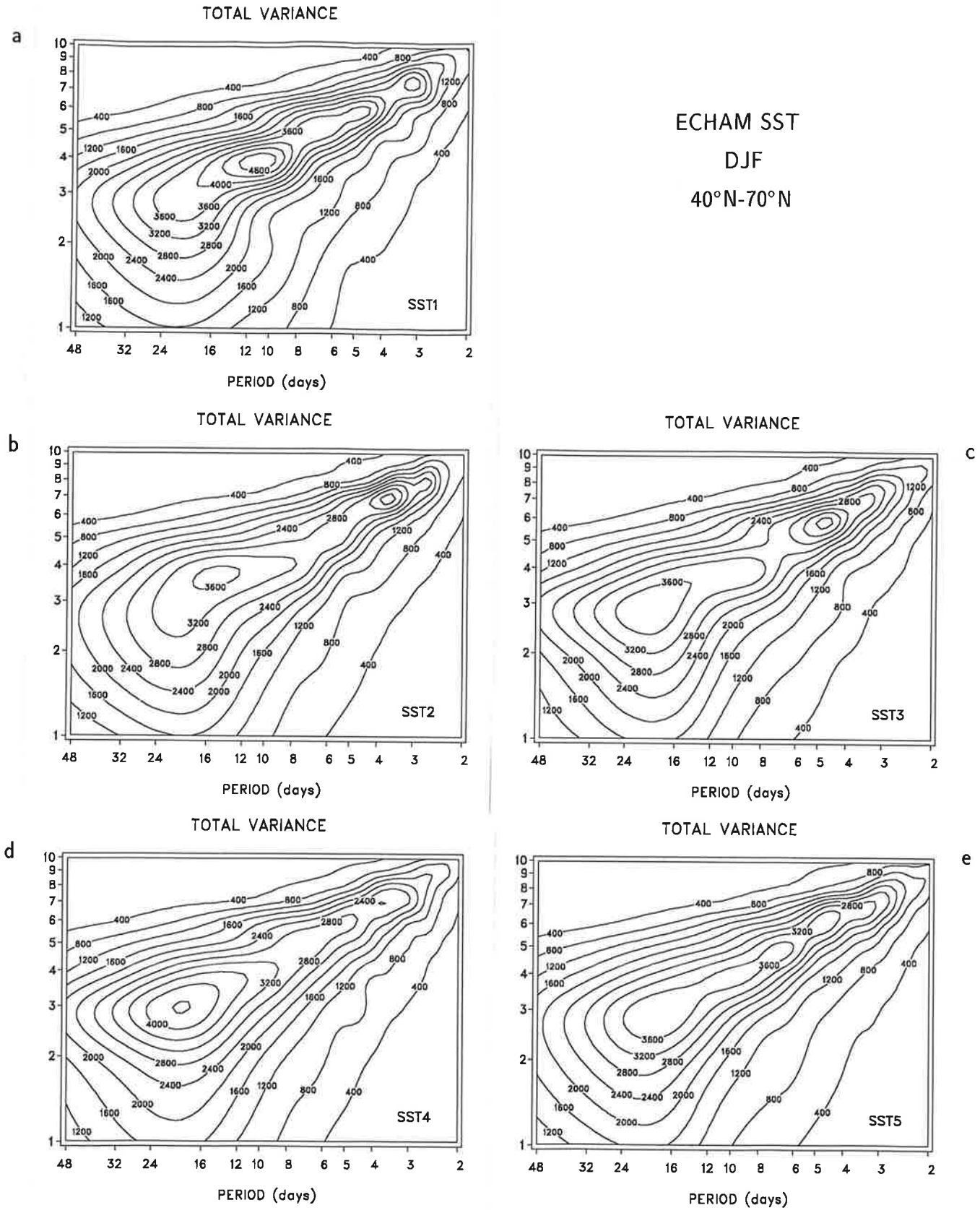

Fig. 4.1.9. Total variance spectrum of the 500 hPa geopotential height for local winter in 40°N-70°N obtained from the individual simulations performed with ECHAM3 with varying Sea Surface Temperatures as boundary forcing. The spectral estimates are multiplied by wavenumber and frequency. Units are m^2, the contour interval is 400 m^2. The zonal wavenumber is given on the ordinate.

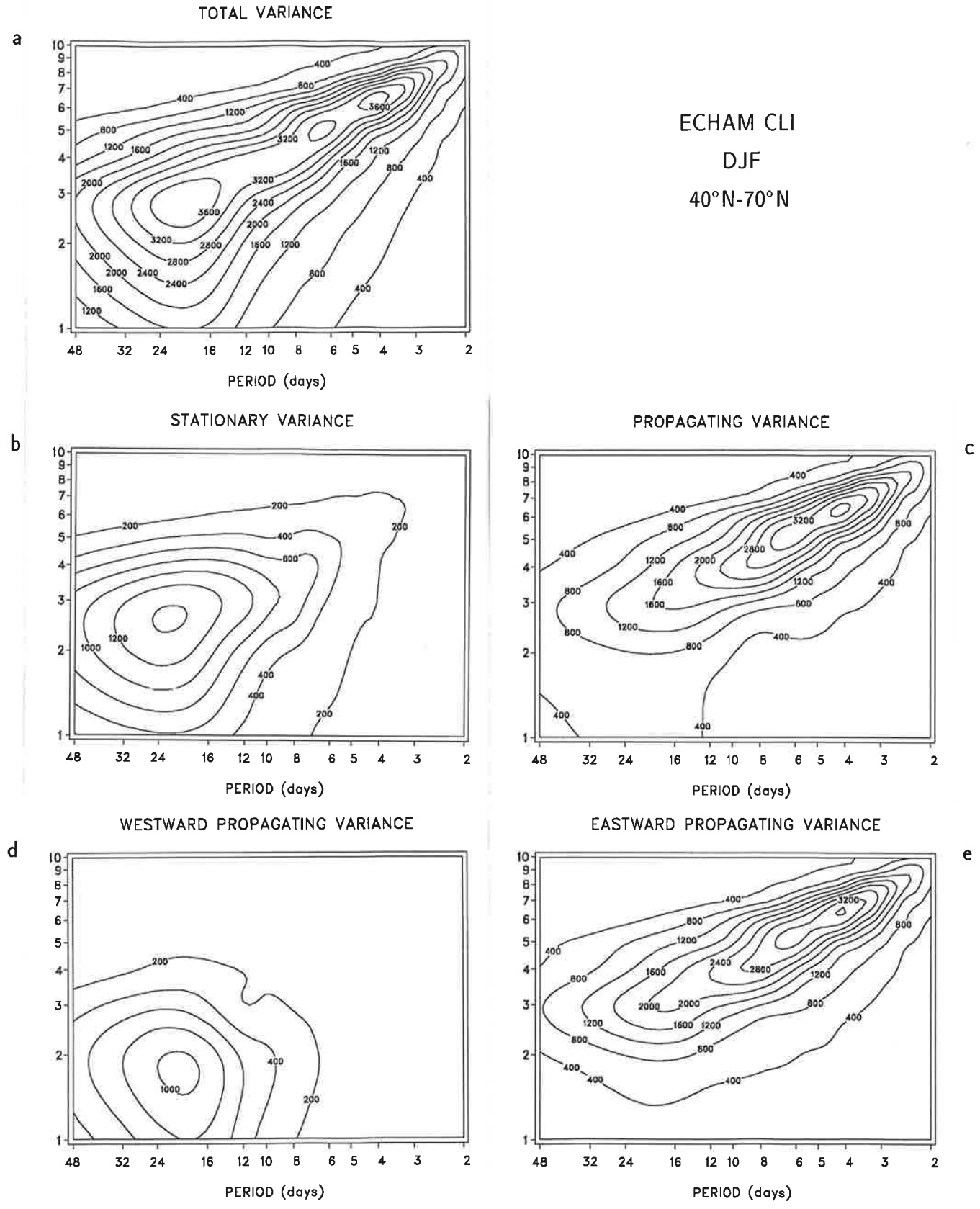

Fig. 4.1.10. As Fig. 4.1.1 but for the spectrum obtained from the simulations performed with ECHAM3 with fixed Sea Surface Temperatures as boundary forcing.

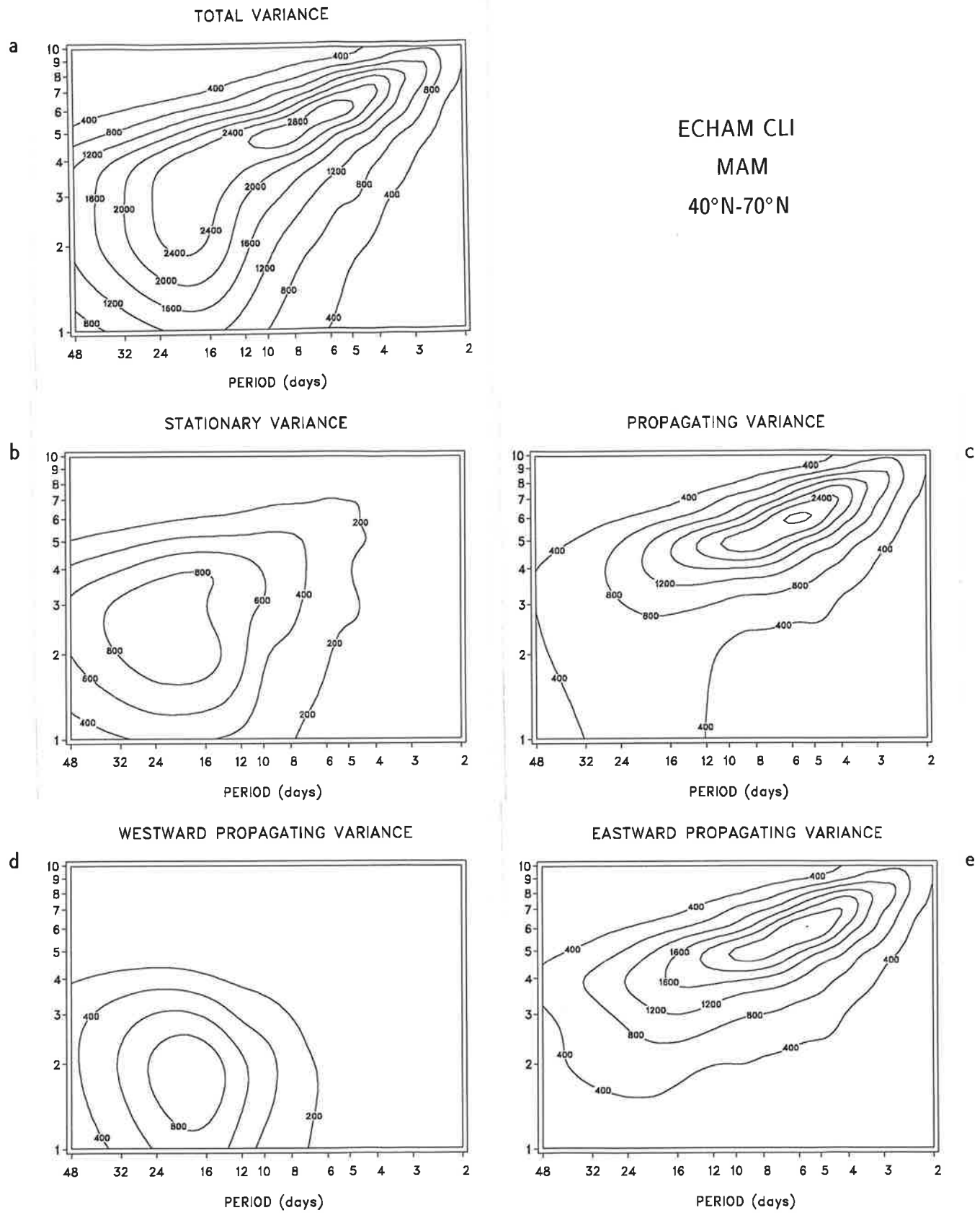

Fig. 4.1.11. As Fig. 4.1.10 but for local spring.

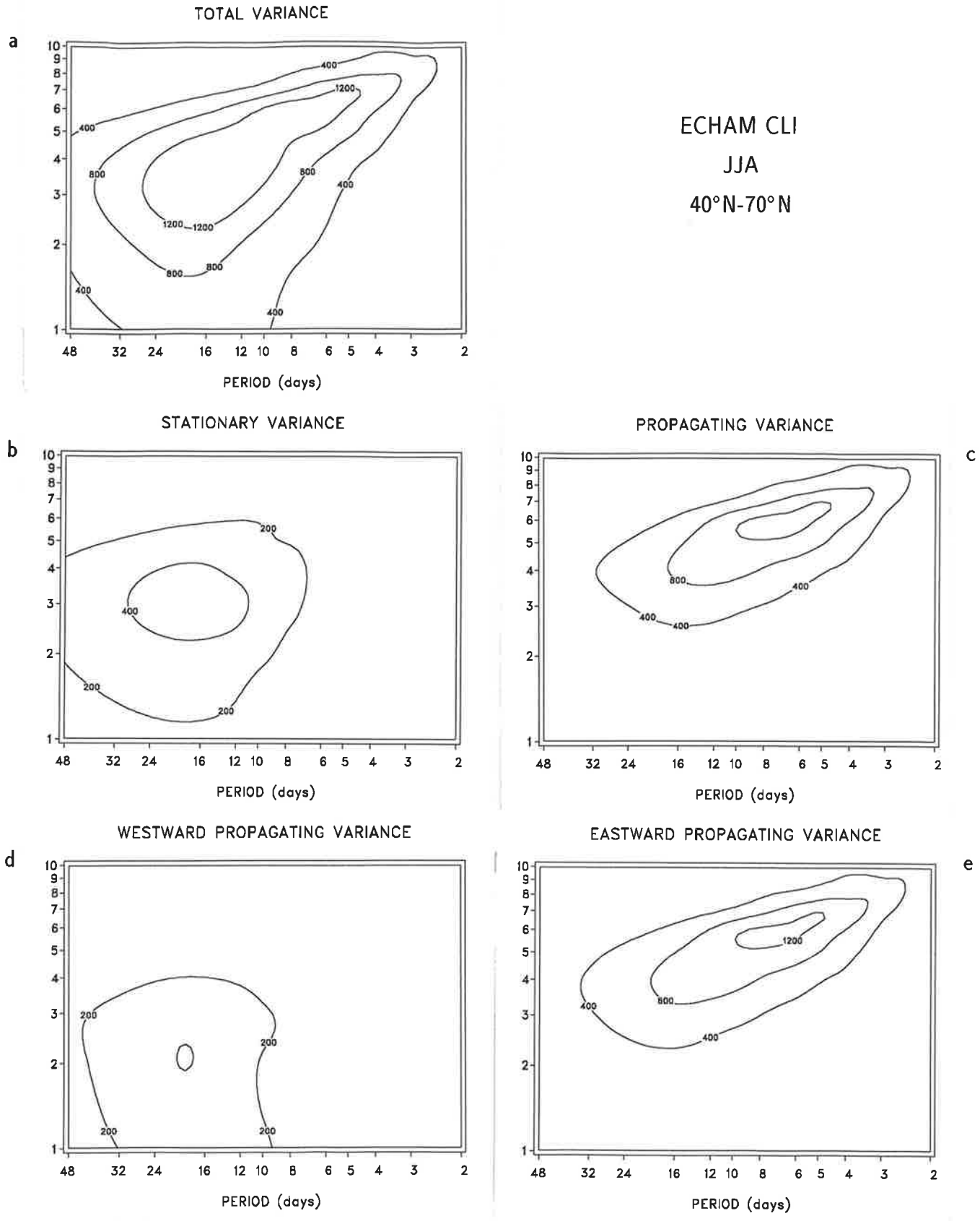

Fig. 4.1.12. As Fig. 4.1.10 but for local summer.

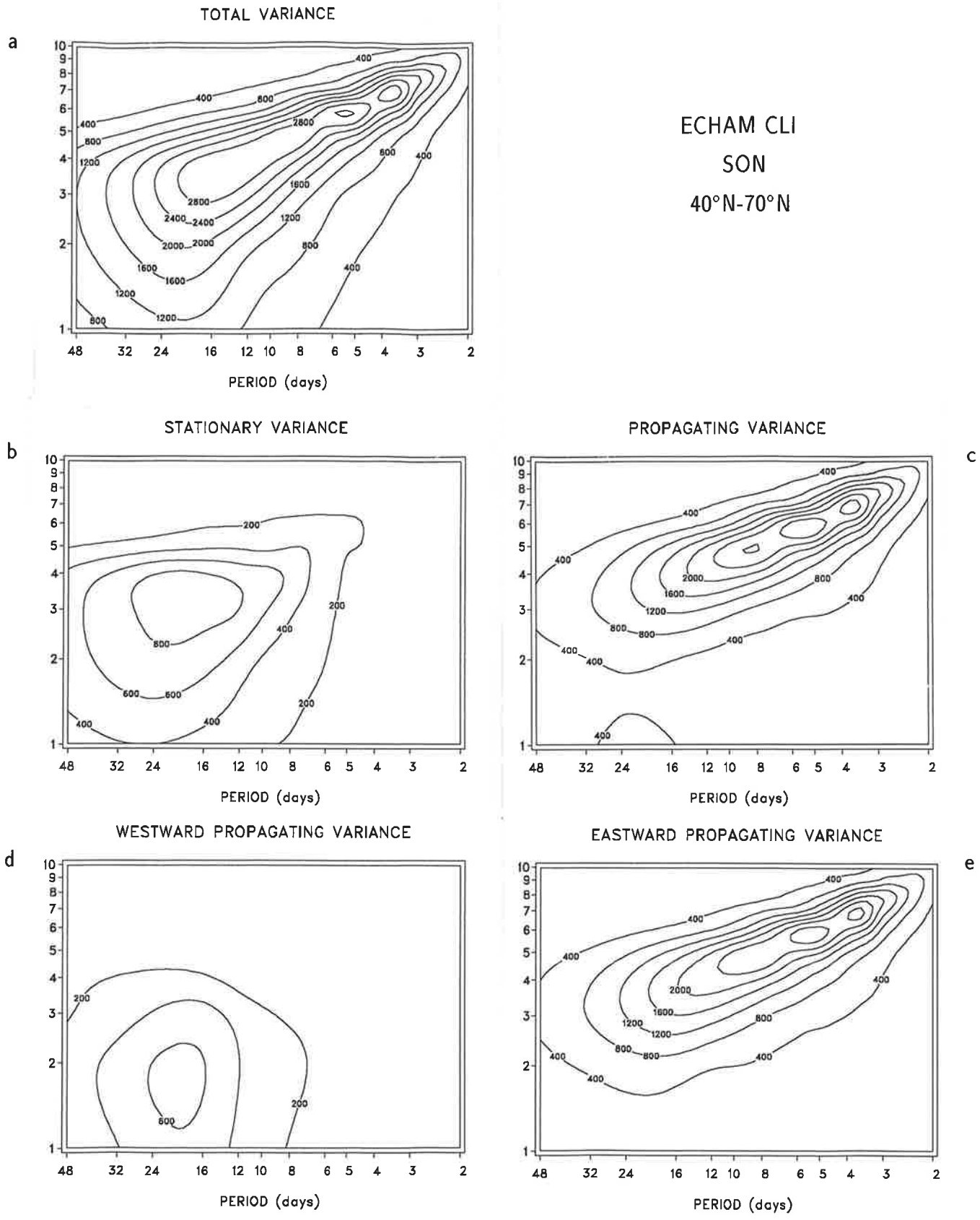

Fig. 4.1.13. As Fig. 4.1.10 but for local autumn.

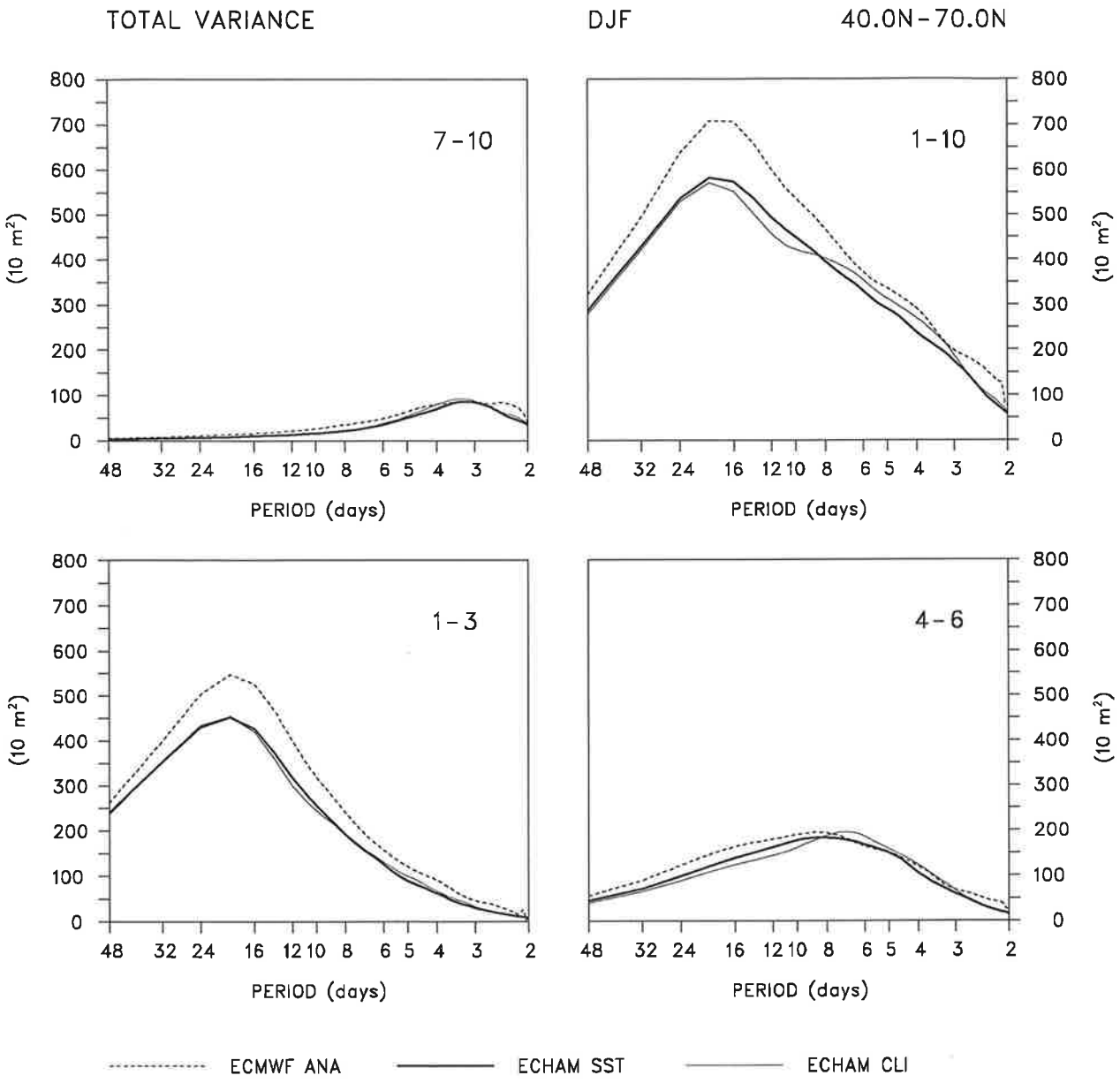

Fig. 4.1.14. Total variance spectrum of the 500 hPa geopotential height for local winter in 40°N-70°N obtained from the ECMWF analyses and the two sets of simulations performed with ECHAM3 for different planetary wave regimes: ultra-long (1-3), long (4-6), short (7-10) and all (1-10) planetary scale waves. The spectral estimates are multiplied by frequency. The spectra obtained from the analyses are indicated by the dashed line, those derived from the simulations with varying SST by the heavy and from the simulations with fixed SST by the light solid line.

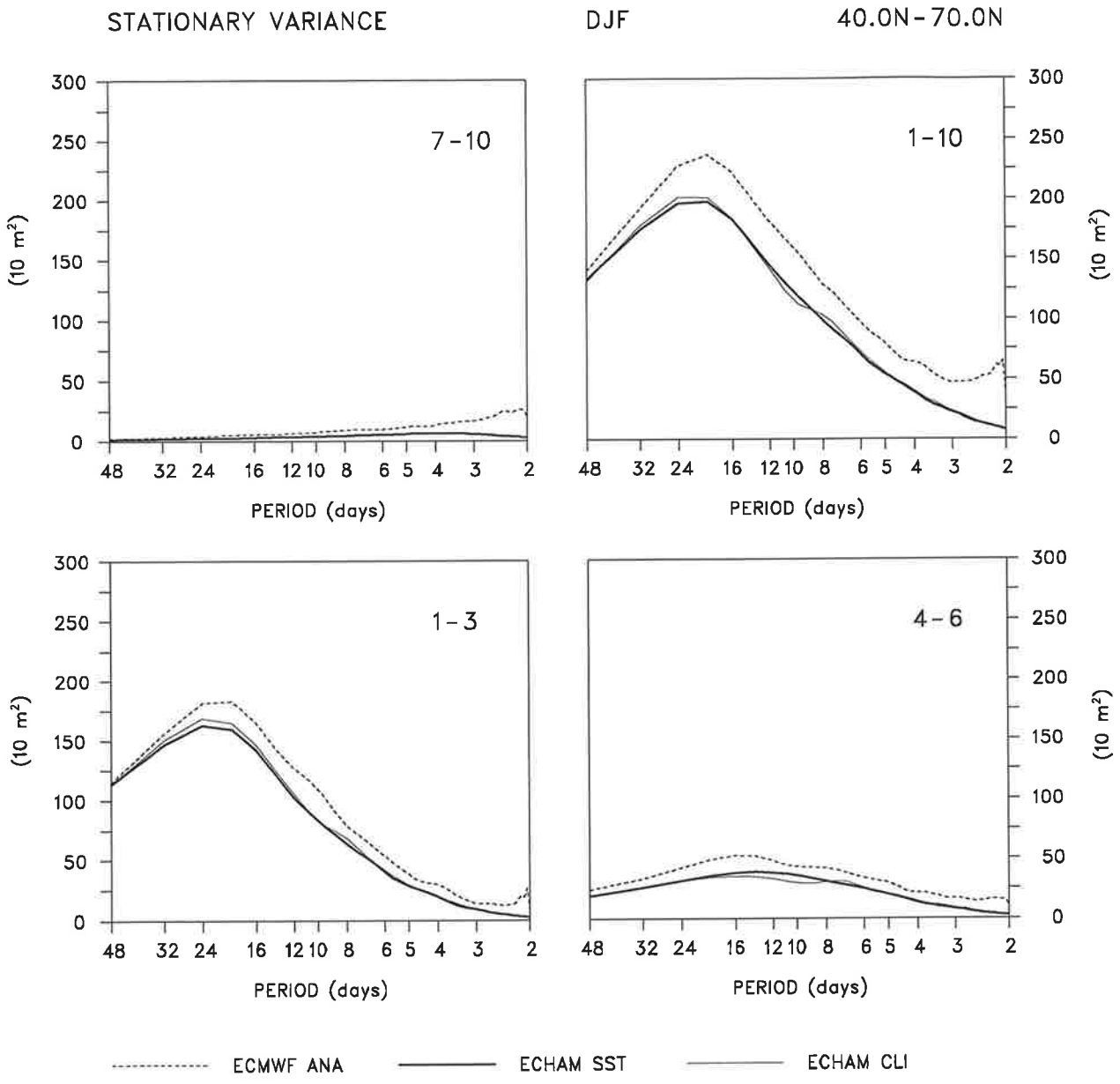

Fig. 4.1.15. As Fig. 4.1.14 but for the stationary variance spectrum.

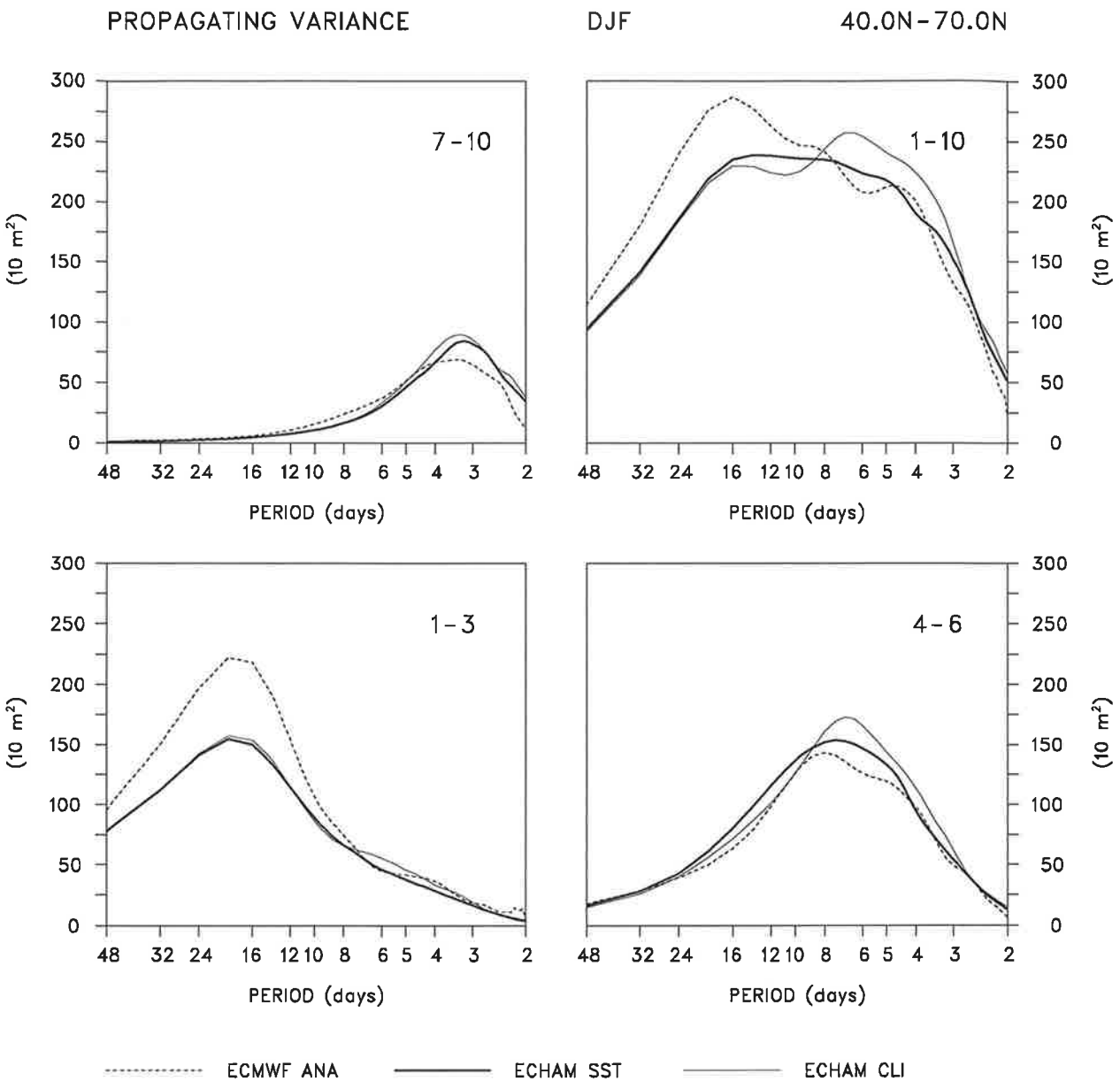

Fig. 4.1.16. As Fig. 4.1.14 but for the propagating variance spectrum.

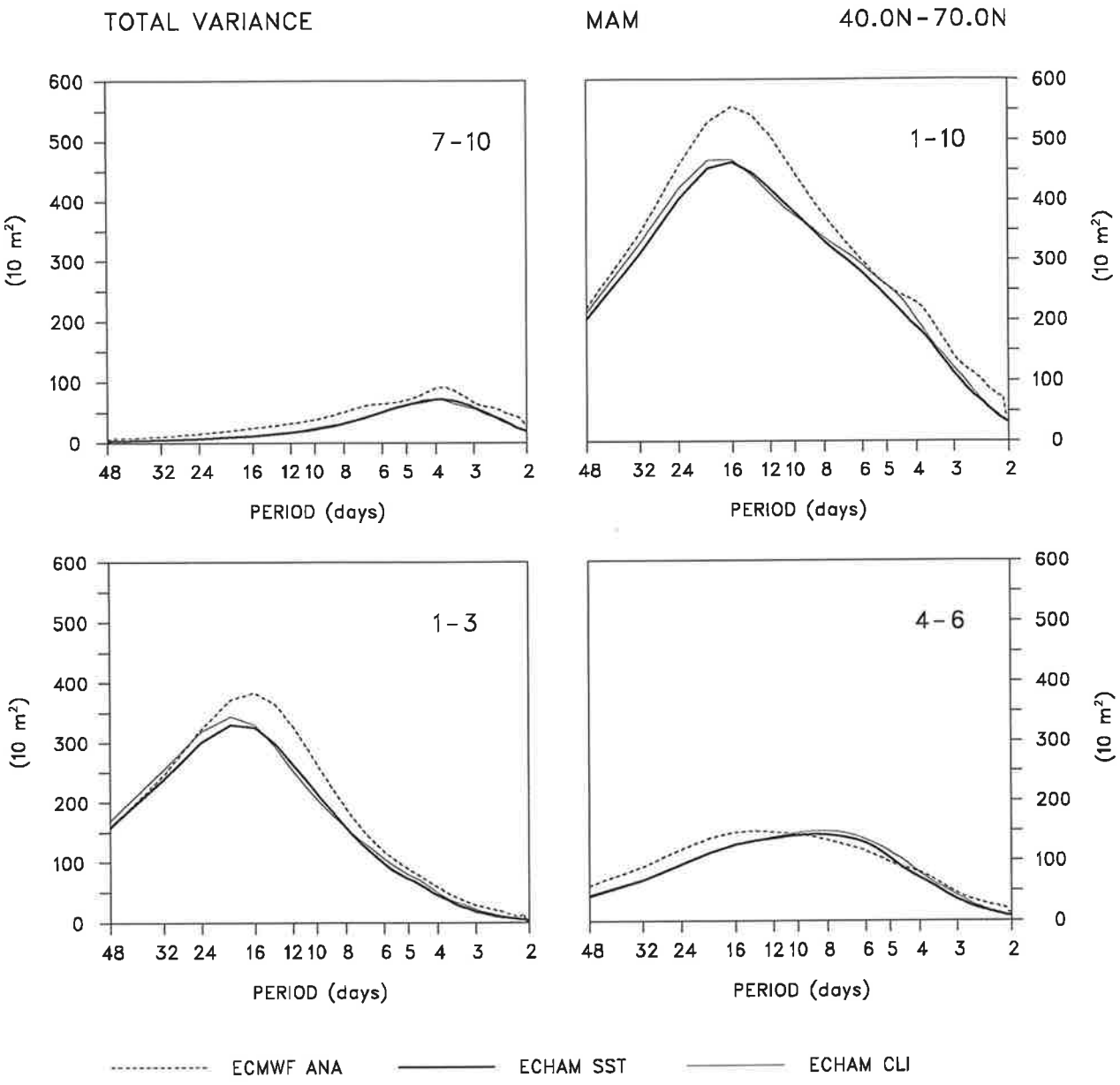

Fig. 4.1.17. As Fig. 4.1.14 but for local spring.

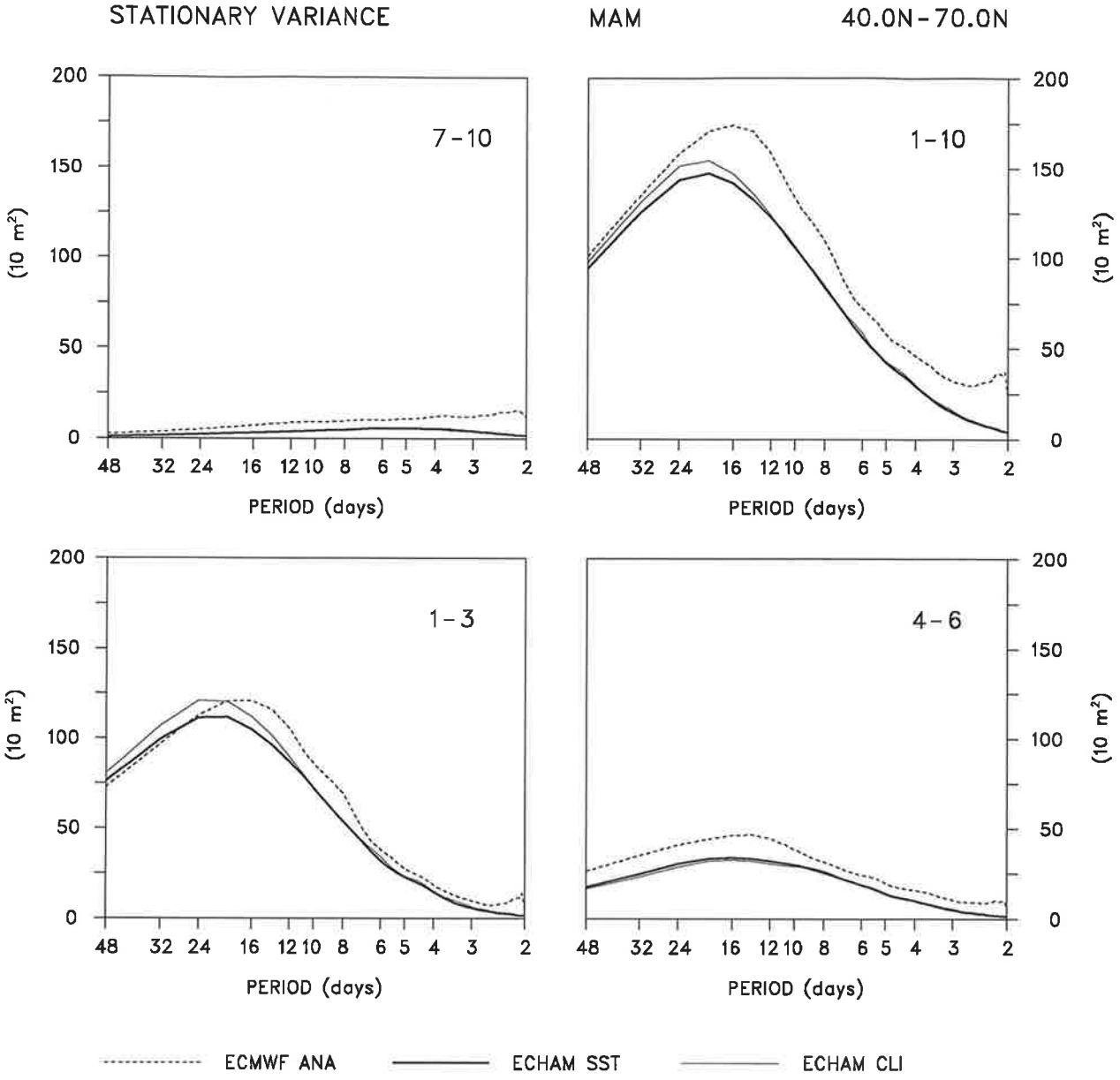

Fig. 4.1.18. As Fig. 4.1.17 but for the stationary variance spectrum.

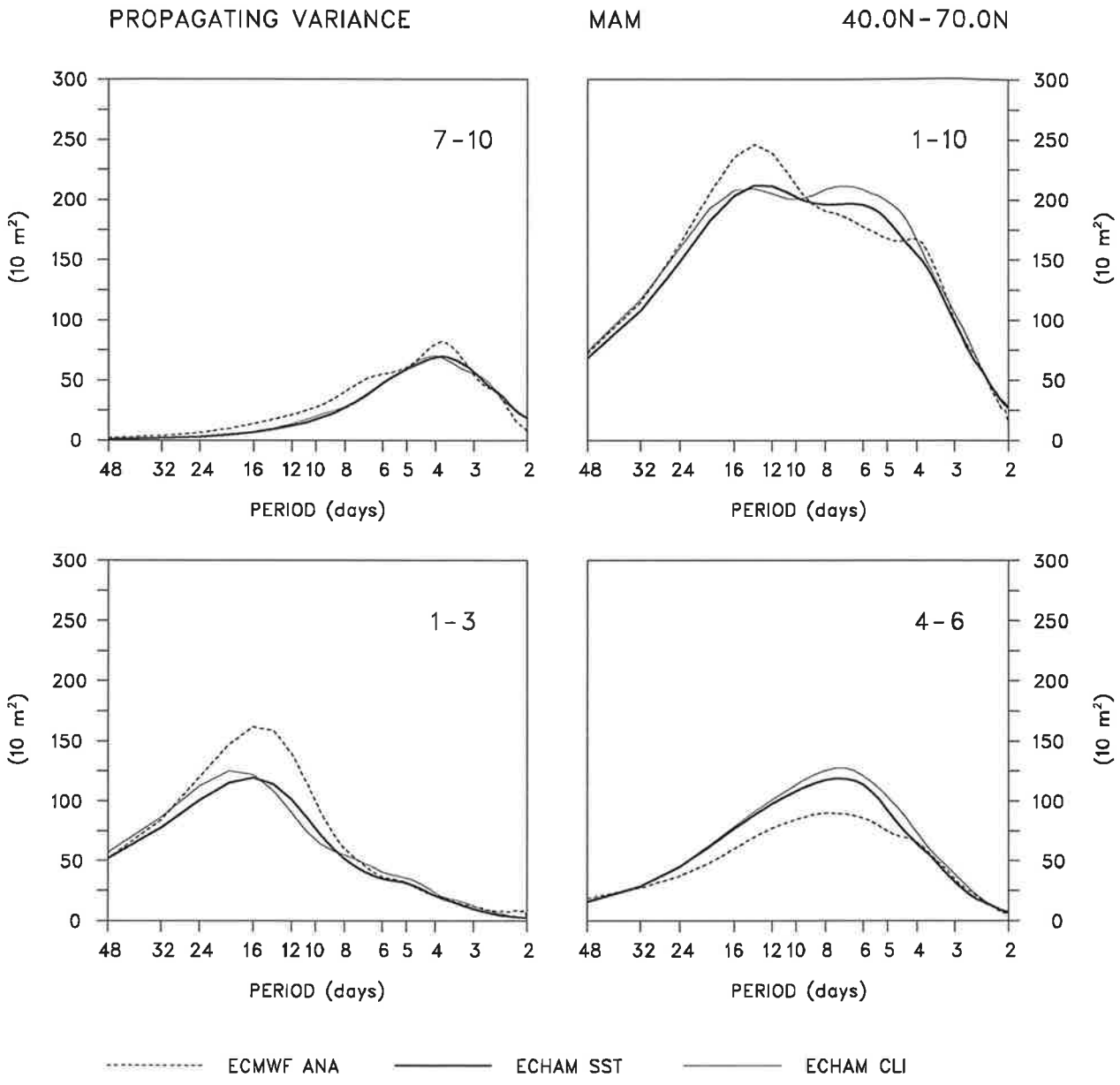

Fig. 4.1.19. As Fig. 4.1.17 but for the propagating variance spectrum.

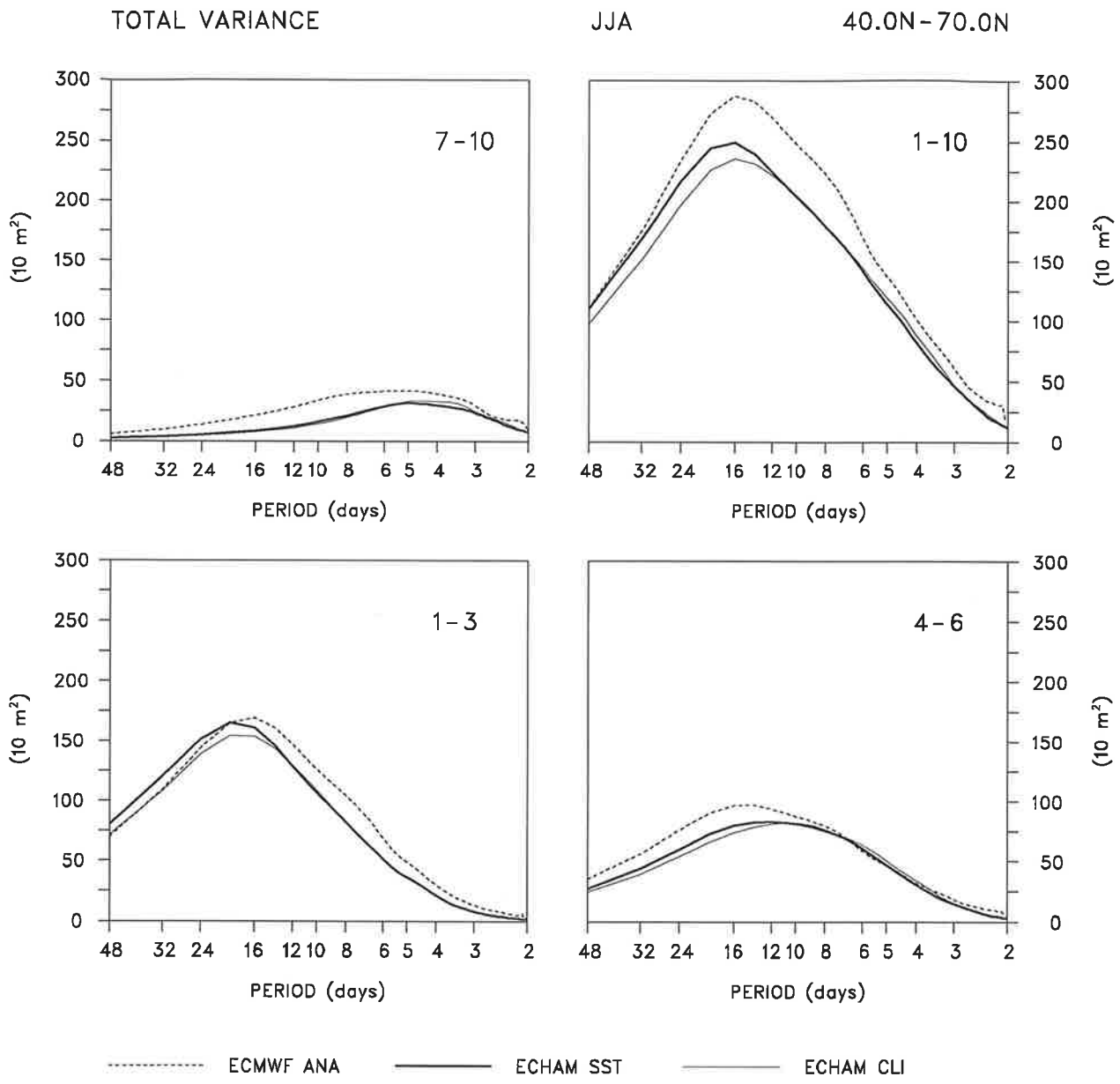

Fig. 4.1.20. As Fig. 4.1.14 but for local summer.

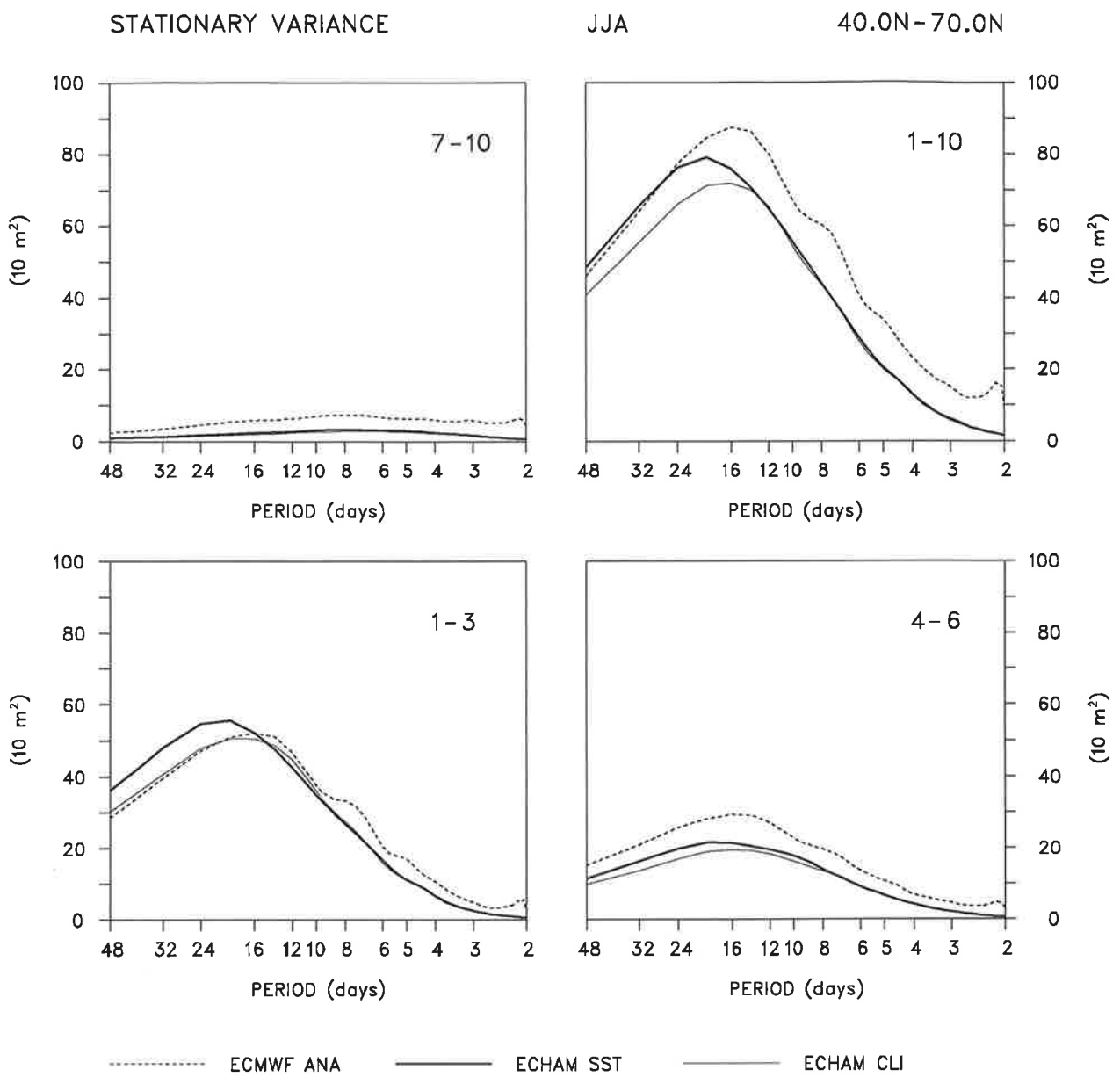

Fig. 4.1.21. As Fig. 4.1.20 but for the stationary variance spectrum.

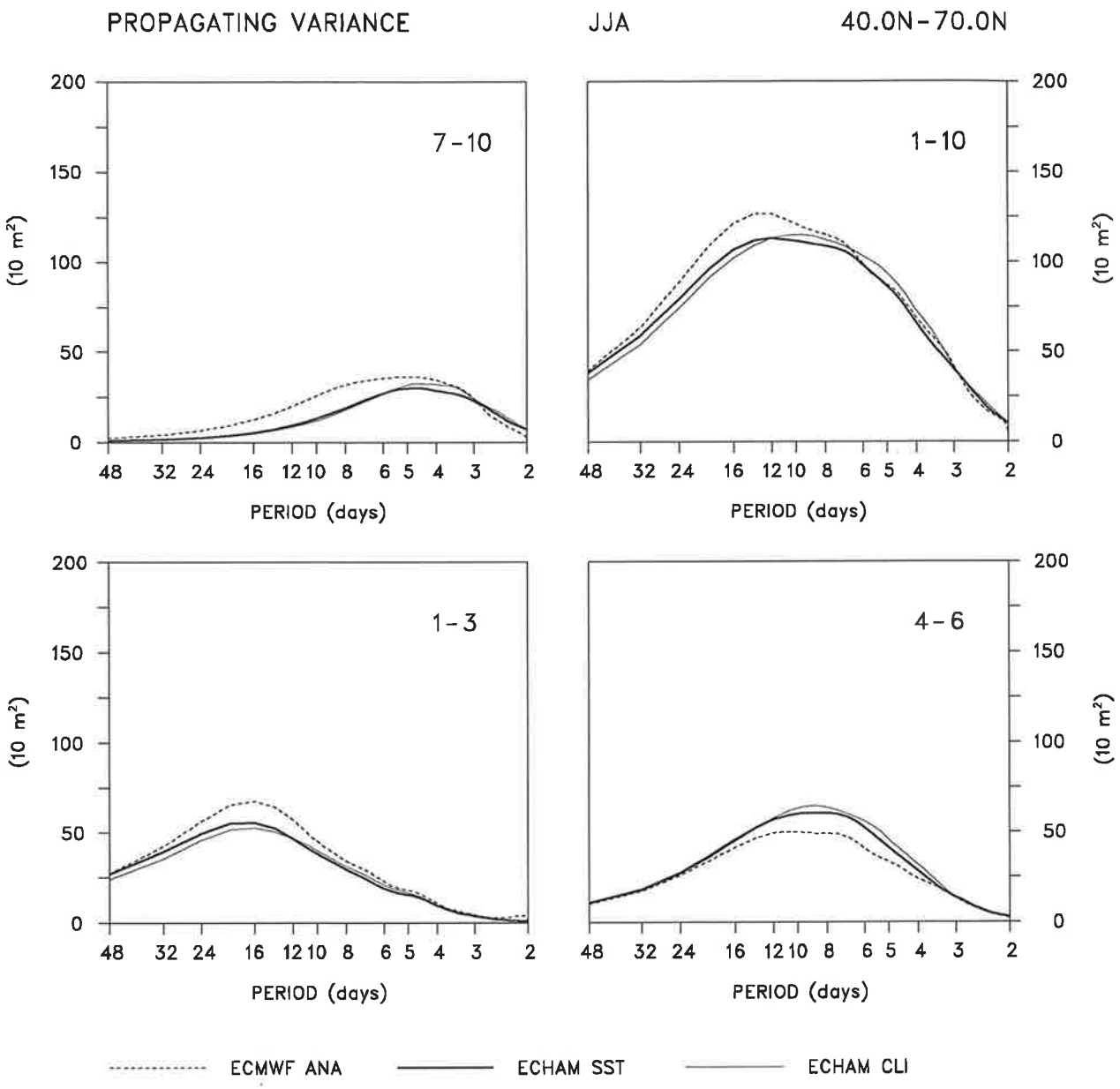

Fig. 4.1.22. As Fig. 4.1.20 but for the propagating variance spectrum.

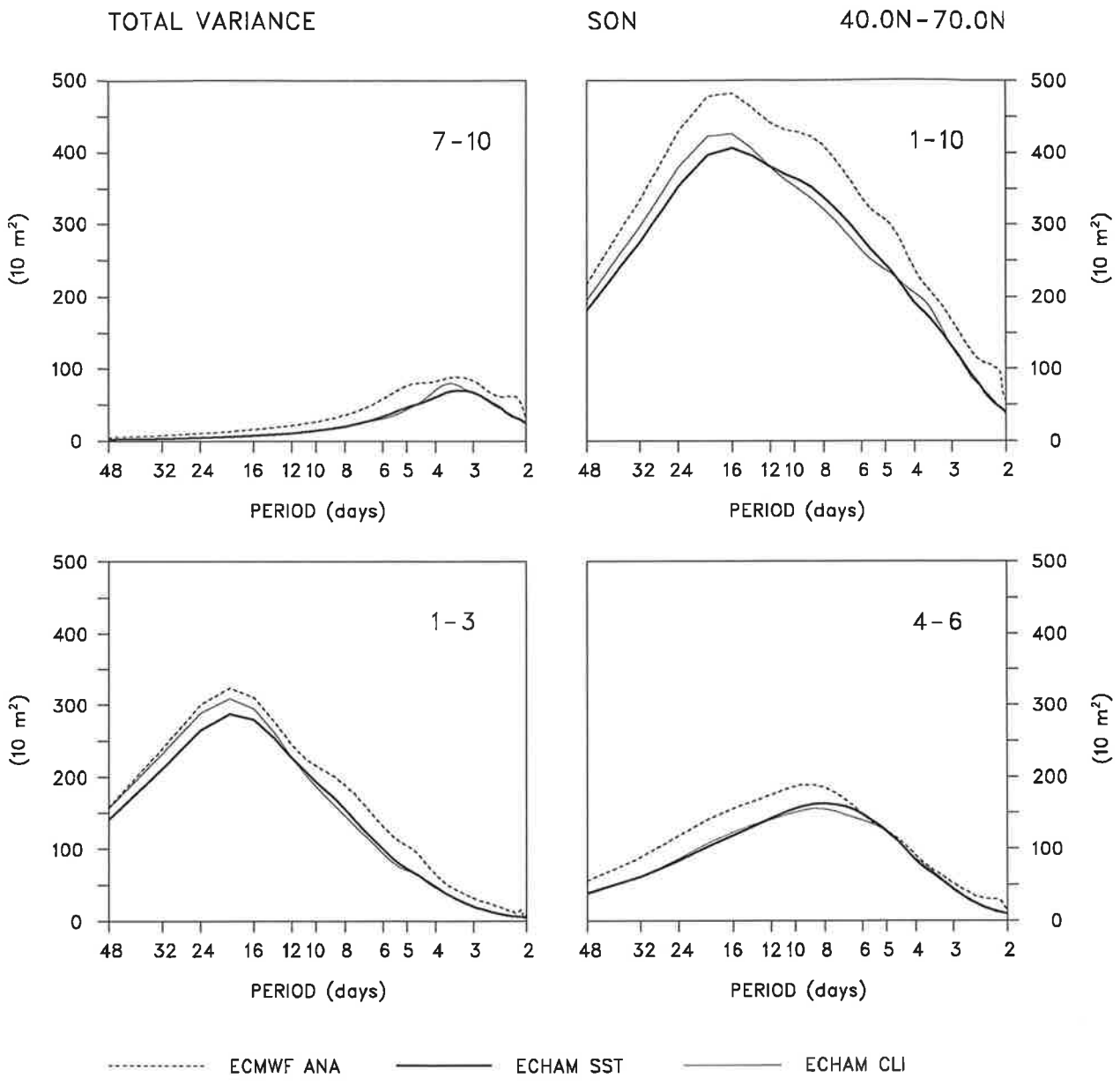

Fig. 4.1.23. As Fig. 4.1.14 but for local autumn.

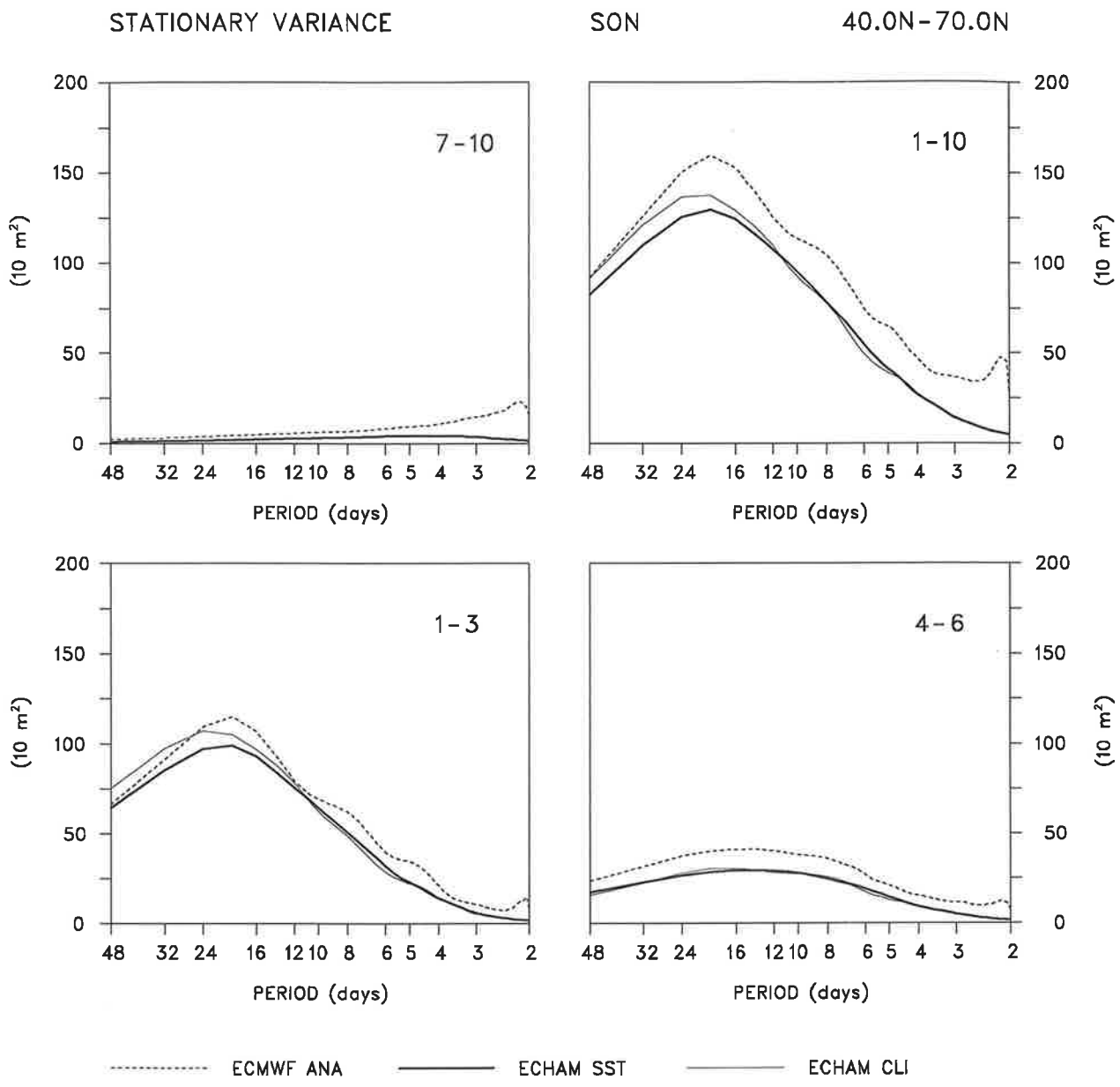

Fig. 4.1.24. As Fig. 4.1.23 but for the stationary variance spectrum.

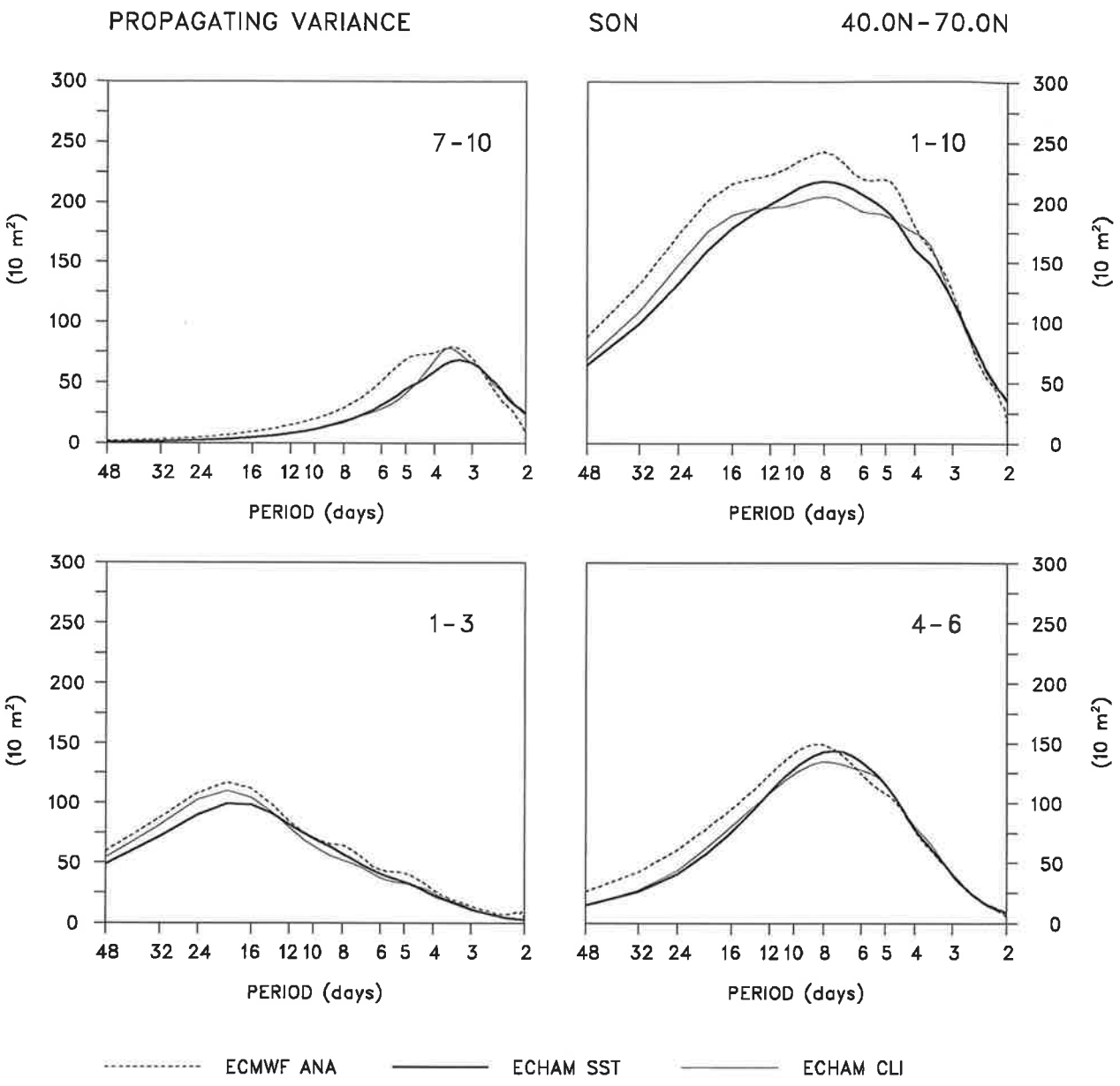

Fig. 4.1.25. As Fig. 4.1.23 but for the propagating variance spectrum.

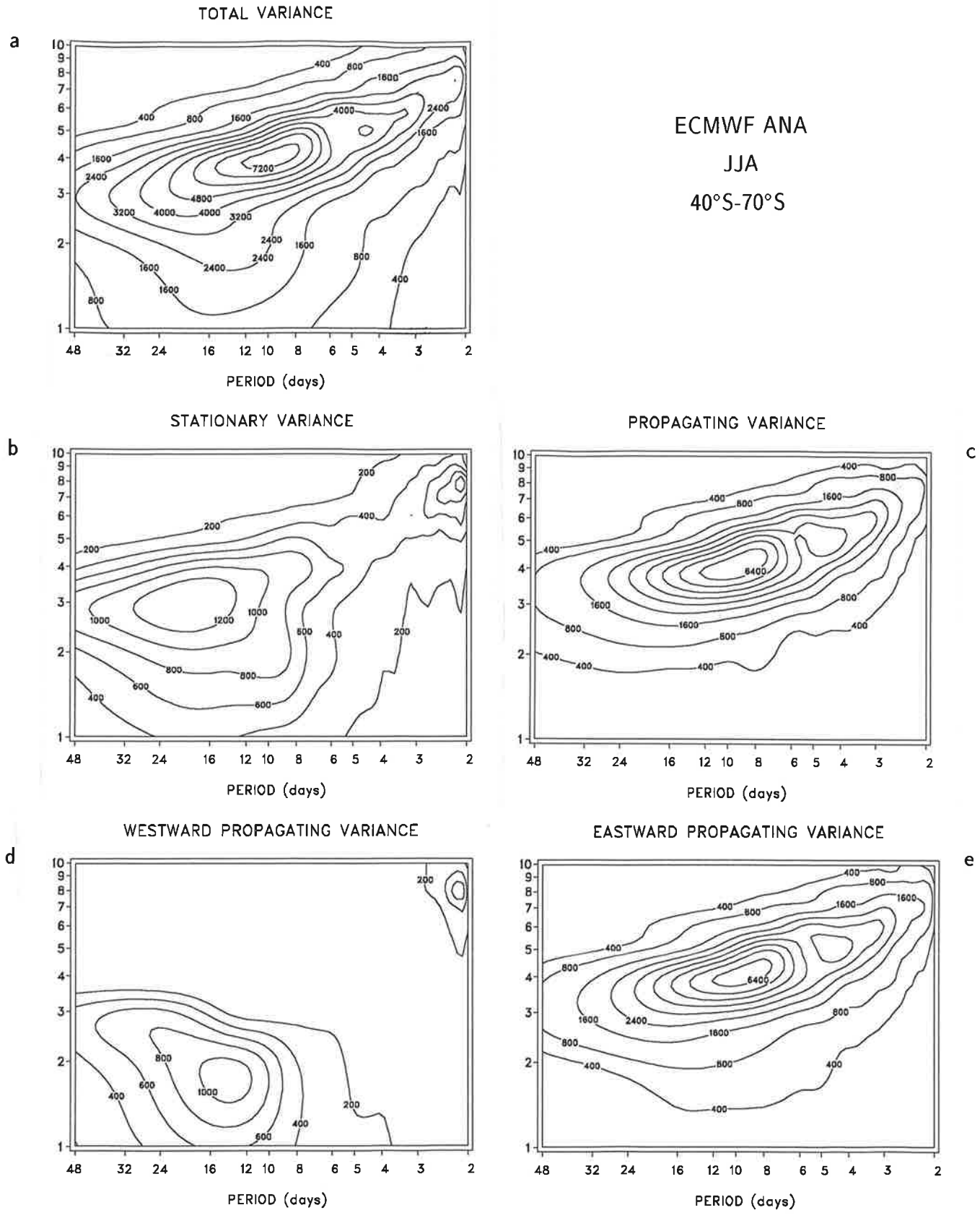

Fig. 4.1.26. Spectrum of the 500 hPa geopotential height for local winter in 40°S-70°S obtained from the ECMWF analyses for the total (a), the stationary (b), the propagating (c), the westward propagating (d) and the eastward propagating (e) variance. The spectral estimates are multiplied by wavenumber and frequency. Units are m^2, the contour interval is 800 m^2 for the total, propagating and the eastward propagating variance, 400 m^2 for the stationary and westward propagating variance. The 400 m^2 and the 200 m^2 contour line, respectively, are indicated as well. The zonal wavenumber is given on the ordinate.

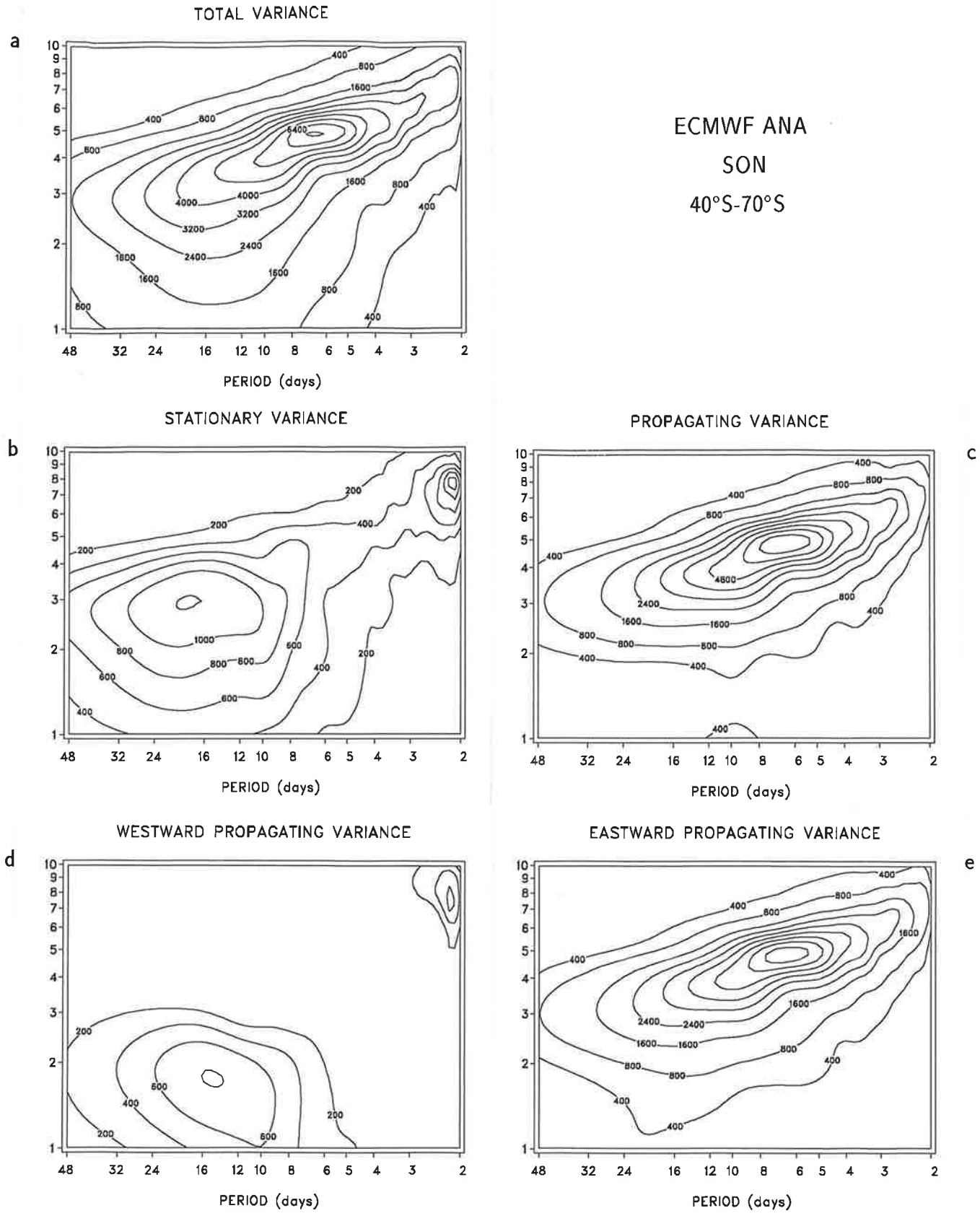

Fig. 4.1.27. As Fig. 4.1.26 but for local spring.

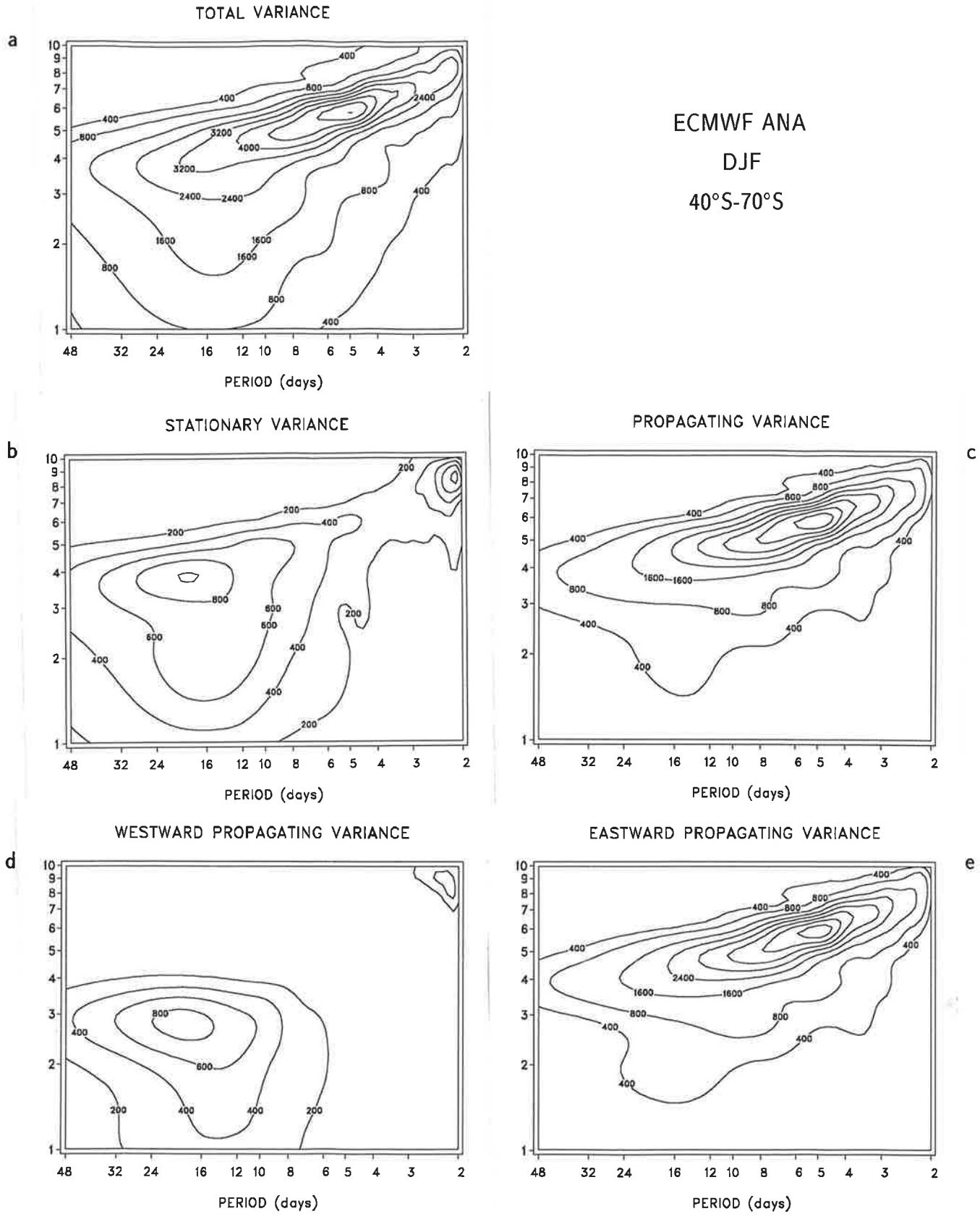

Fig. 4.1.28. As Fig. 4.1.26 but for local summer.

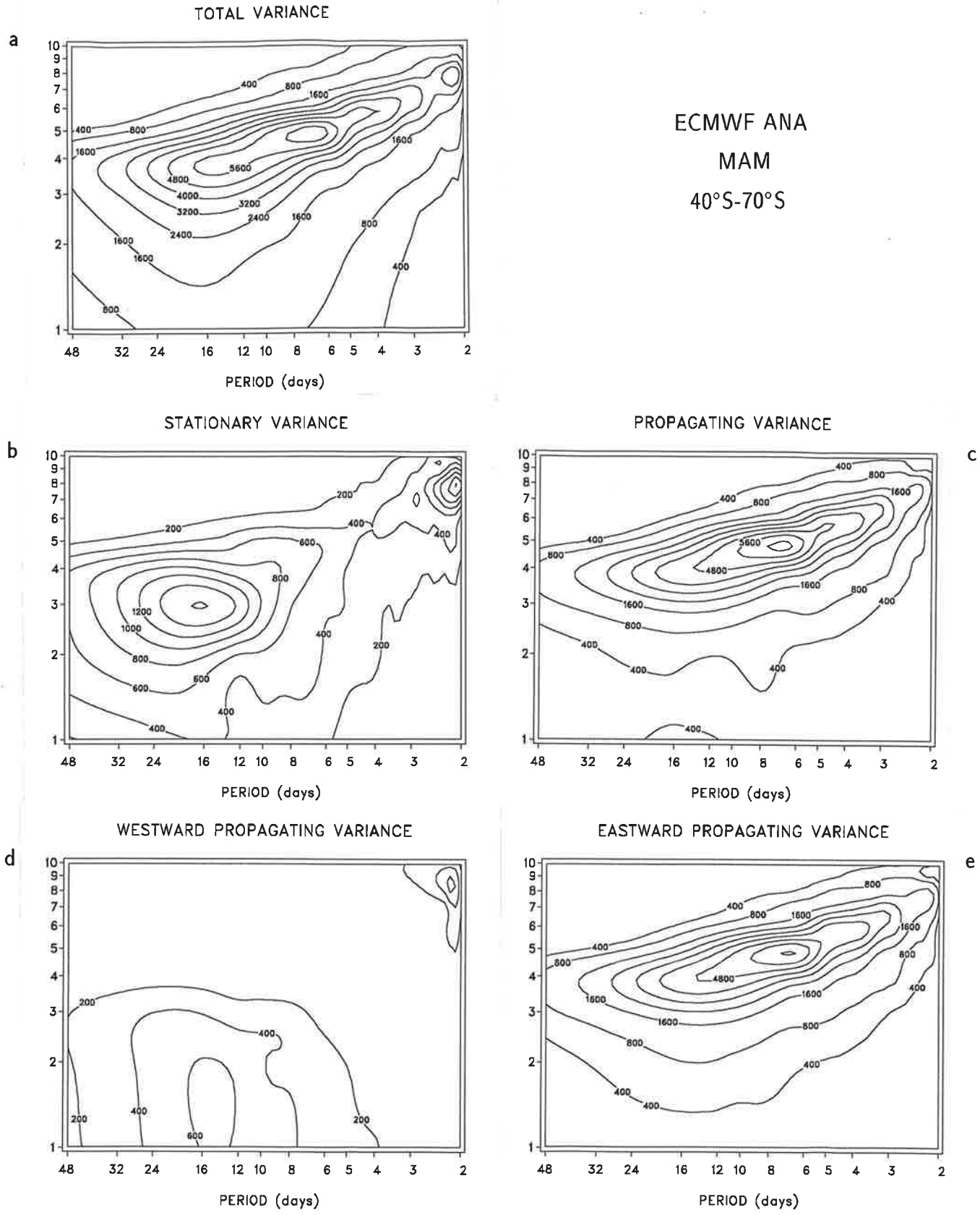

Fig. 4.1.29. As Fig. 4.1.26 but for local autumn.

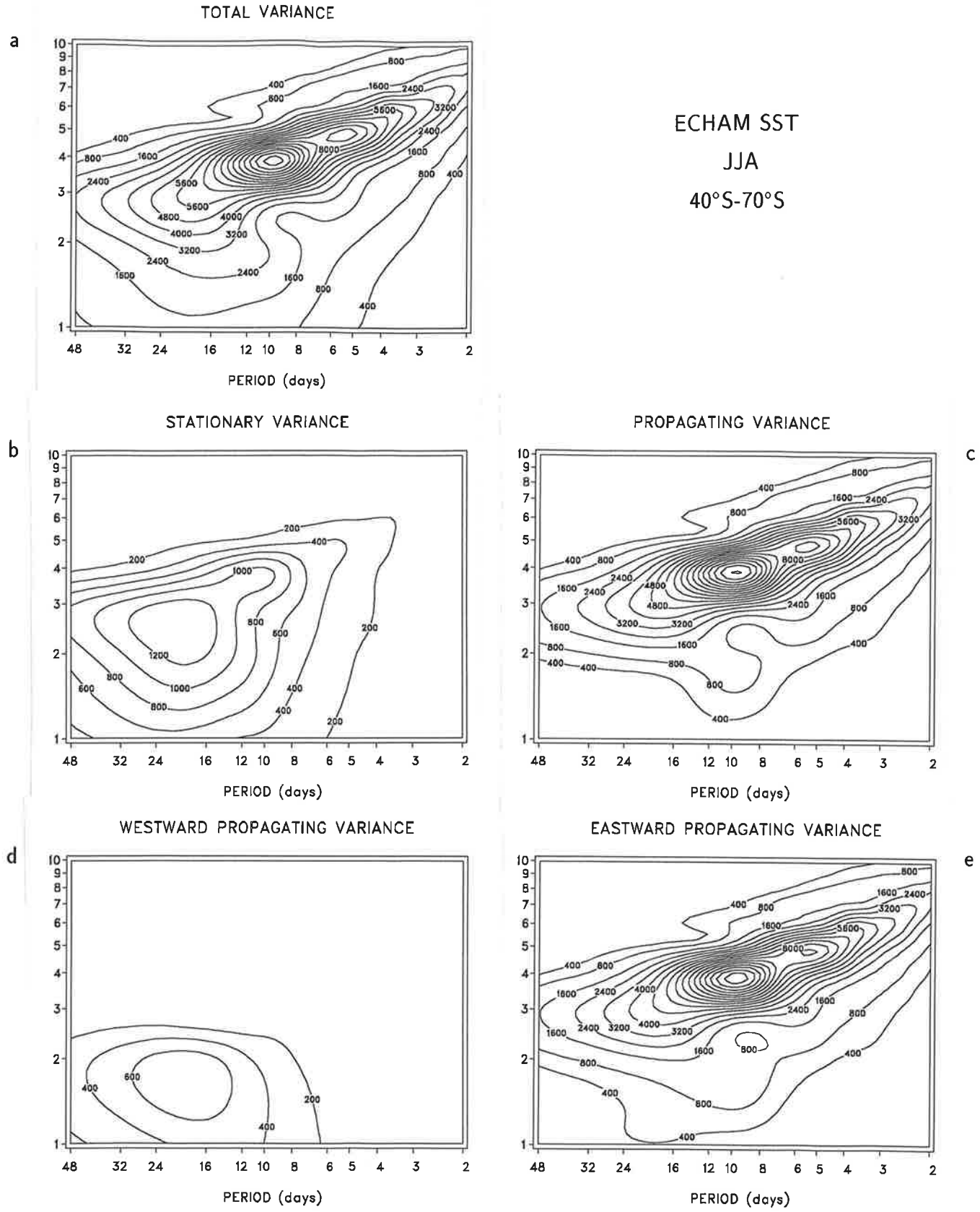

Fig. 4.1.30. As Fig. 4.1.26 but for the spectrum obtained from the simulations performed with ECHAM3 with varying Sea Surface Temperatures as boundary forcing.

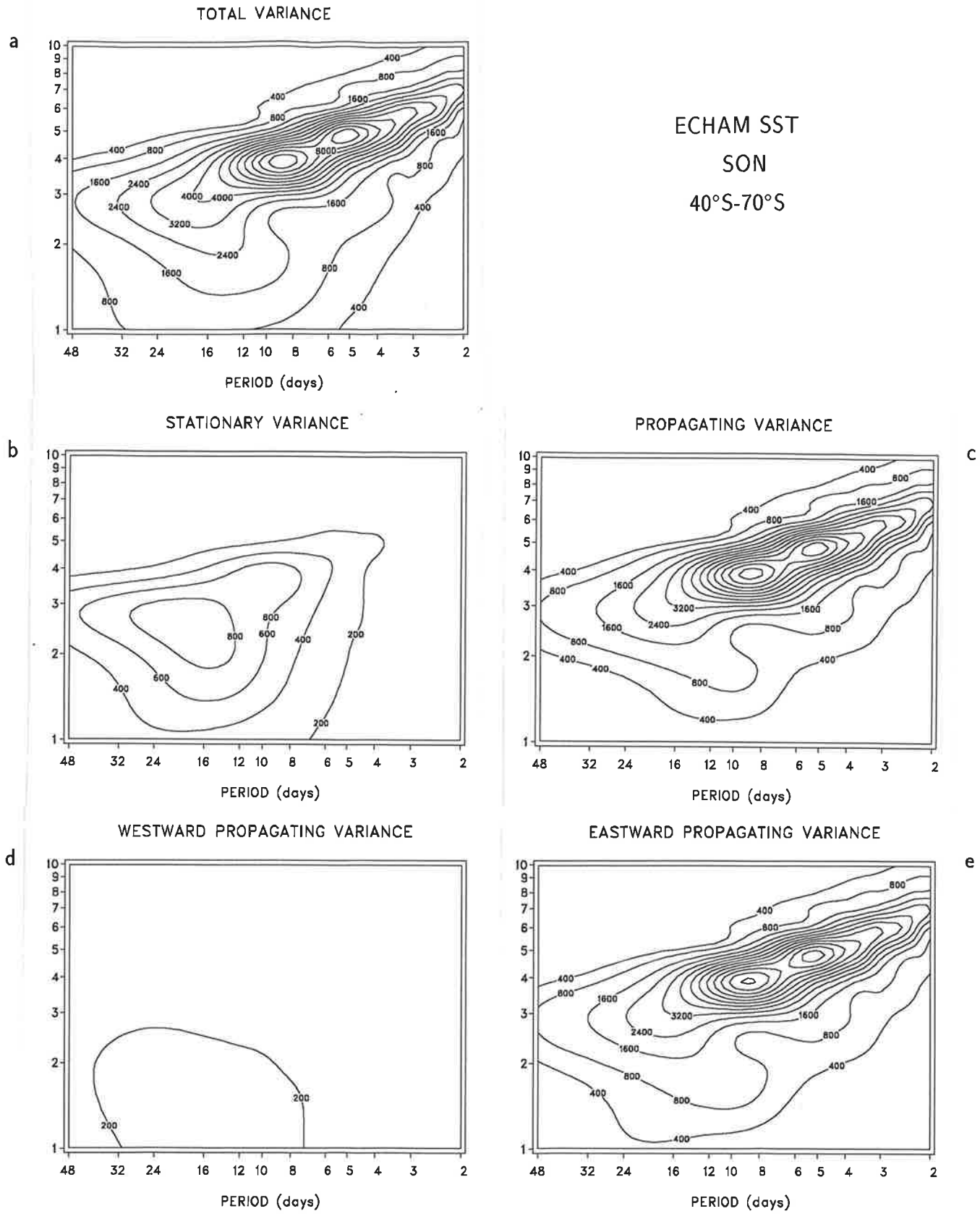

Fig. 4.1.31. As Fig. 4.1.30 but for local spring.

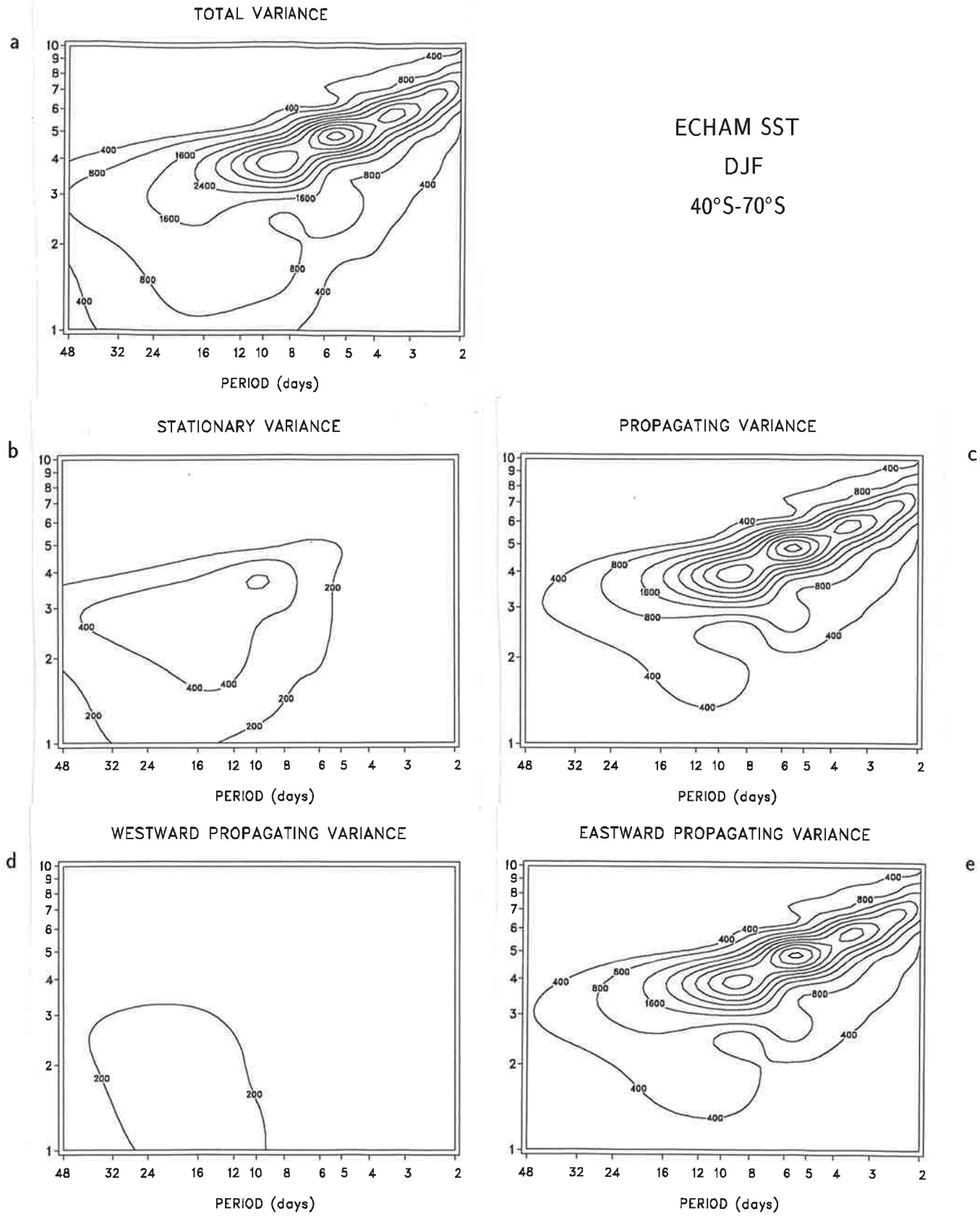

Fig. 4.1.32. As Fig. 4.1.30 but for local summer.

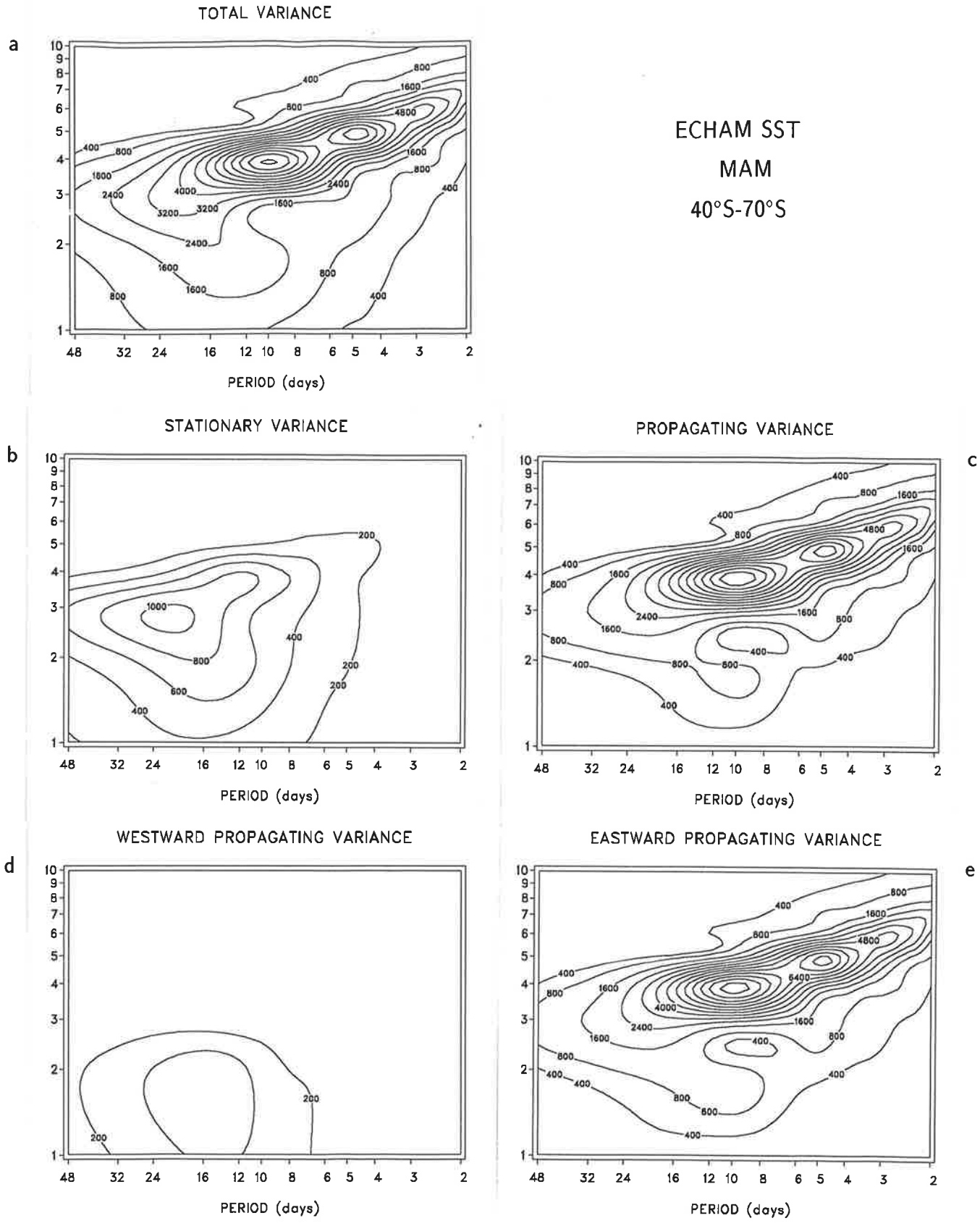

Fig. 4.1.33. As Fig. 4.1.30 but for local autumn.

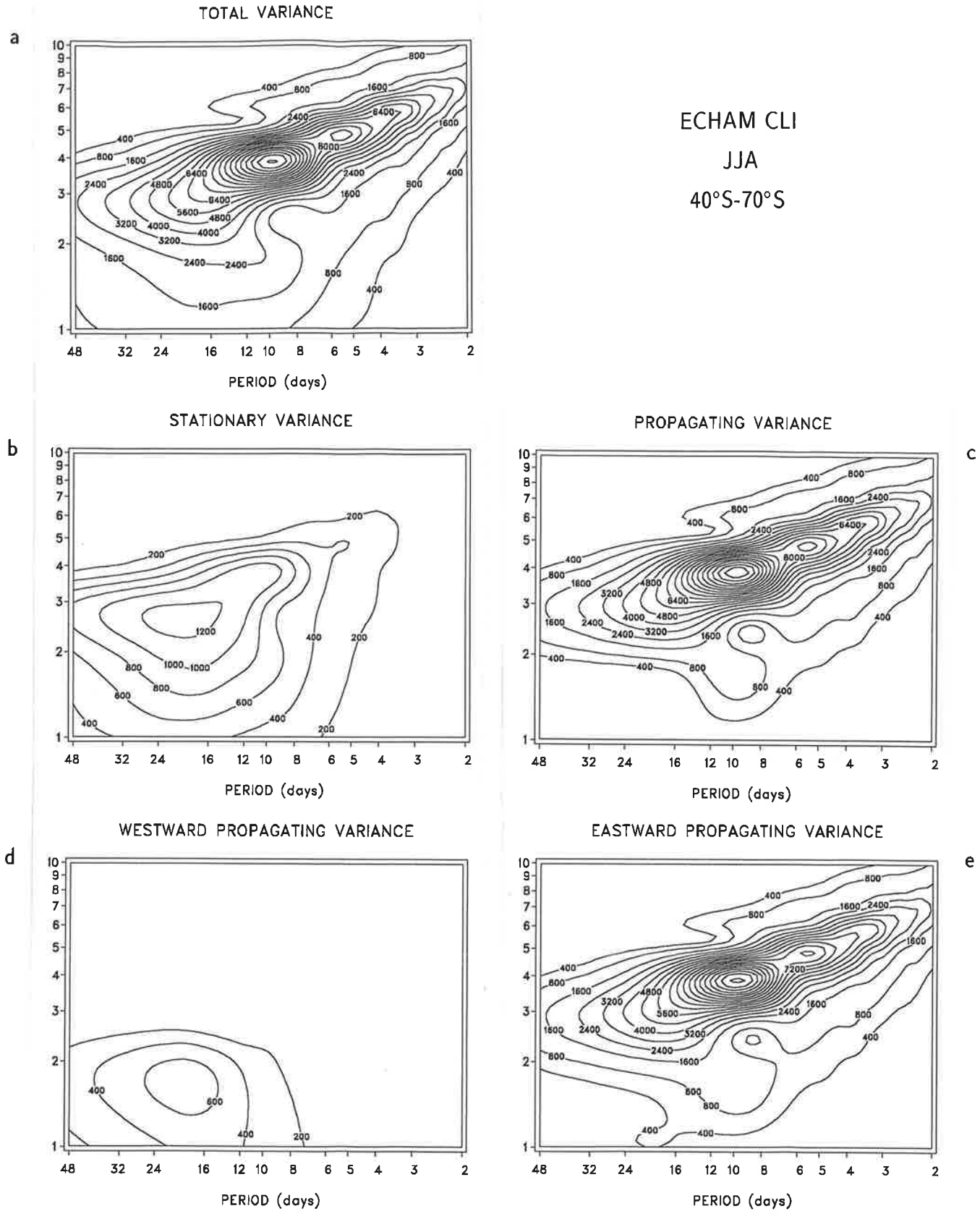

Fig. 4.1.34. As Fig. 4.1.26 but for the spectrum obtained from the simulations performed with ECHAM3 with fixed Sea Surface Temperatures as boundary forcing.

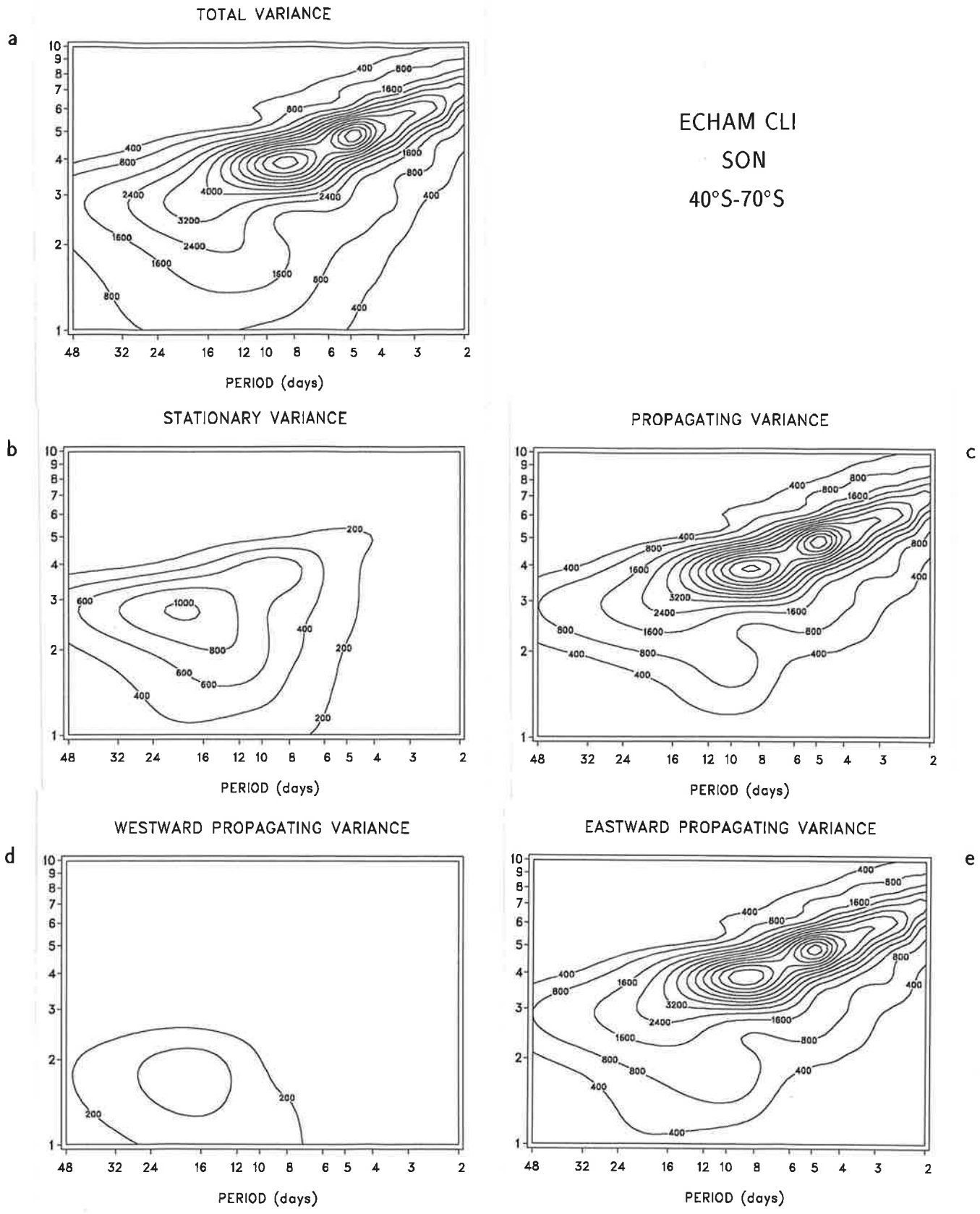

Fig. 4.1.35. As Fig. 4.1.34 but for local spring.

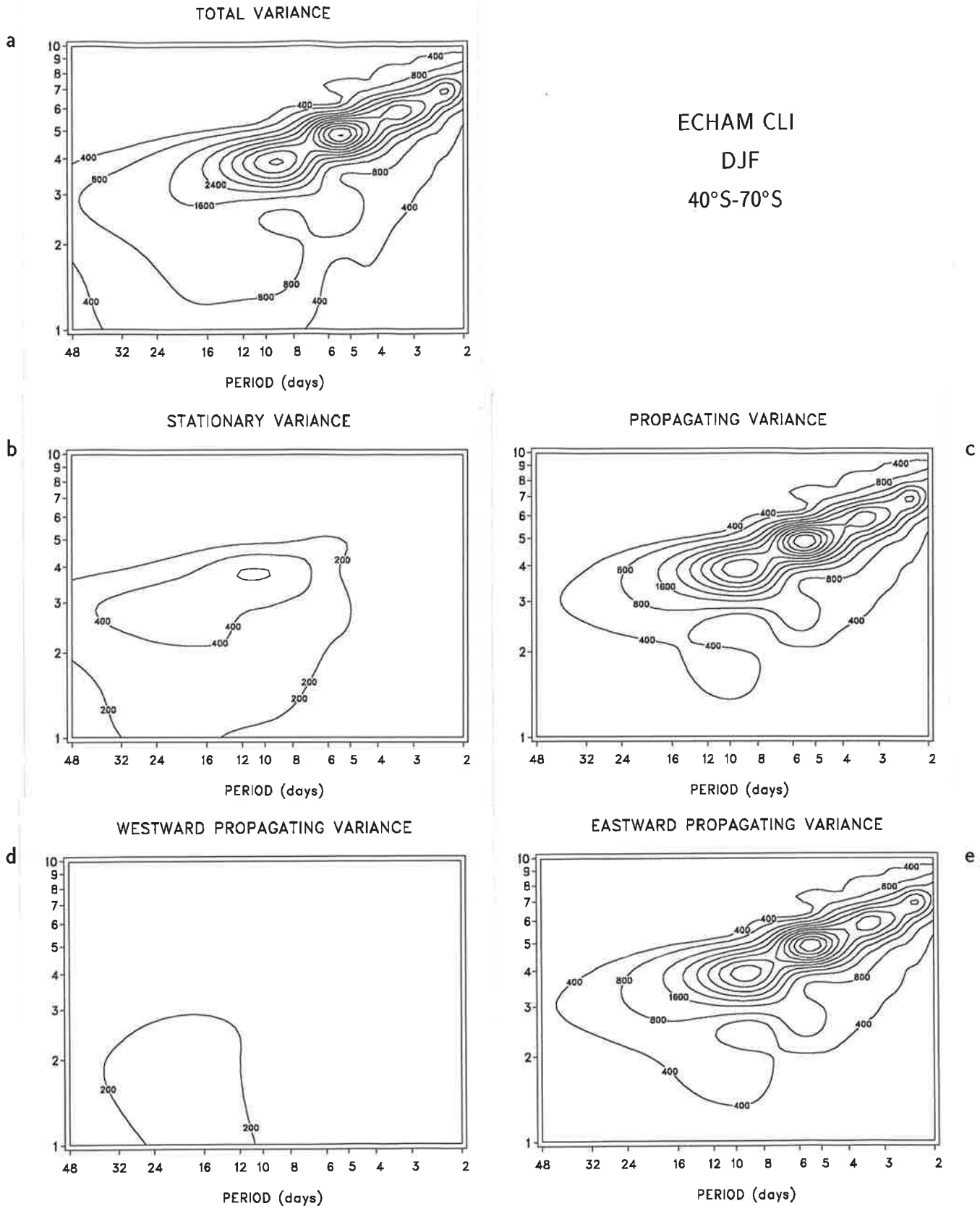

Fig. 4.1.36. As Fig. 4.1.34 but for local summer.

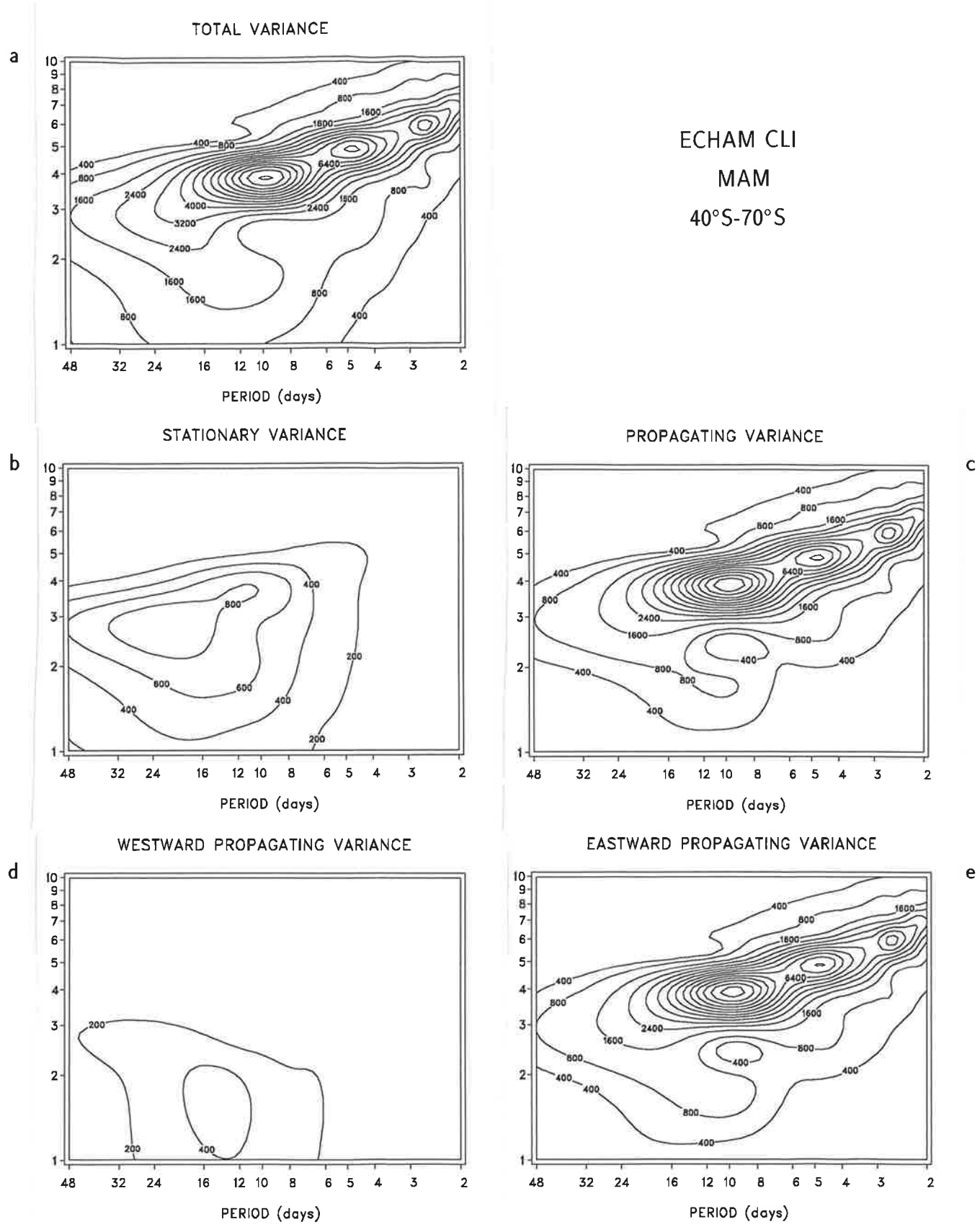

Fig. 4.1.37. As Fig. 4.1.34 but for local autumn.

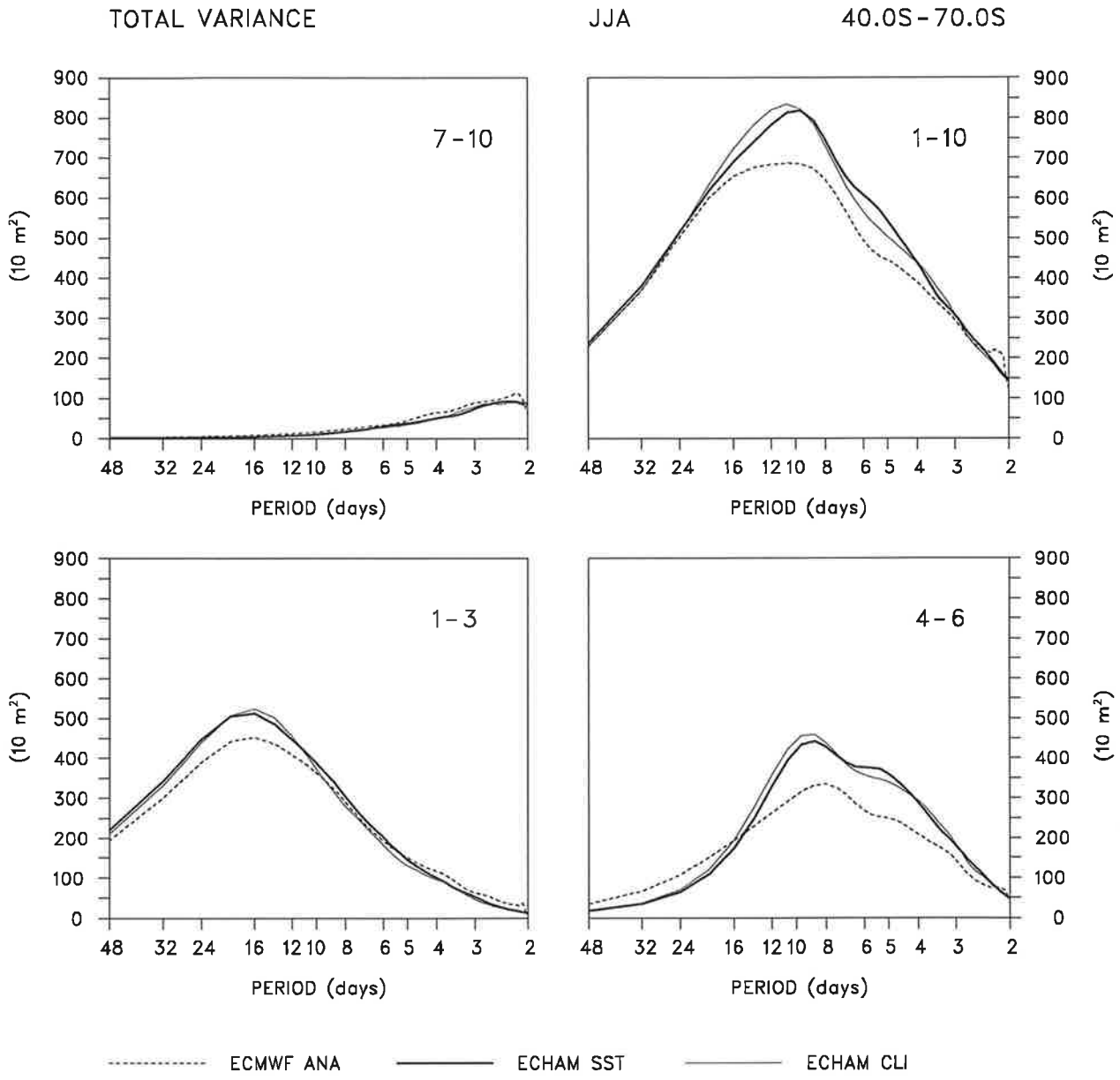

Fig. 4.1.38. Total variance spectrum of the 500 hPa geopotential height for local winter in 40°S-70°S obtained from the ECMWF analyses and the two sets of simulations performed with ECHAM3 for different planetary wave regimes: ultra-long (1-3), long (4-6), short (7-10) and all (1-10) planetary scale waves. The spectral estimates are multiplied by frequency. The spectra obtained from the analyses are indicated by the dashed line, those derived from the simulations with varying SST by the heavy and from the simulations with fixed SST by the light solid line.

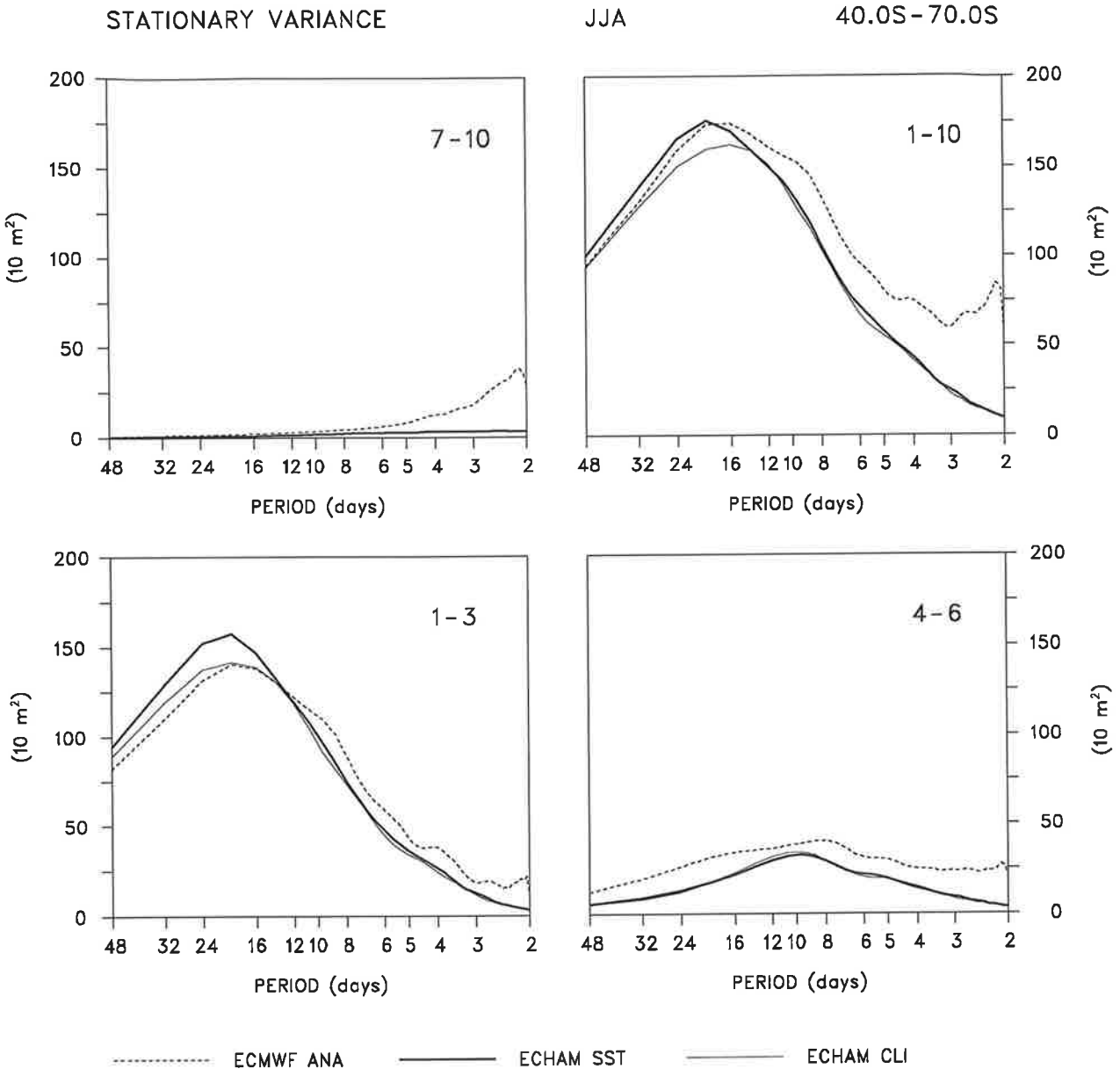

Fig. 4.1.39. As Fig. 4.1.38 but for the stationary variance spectrum.

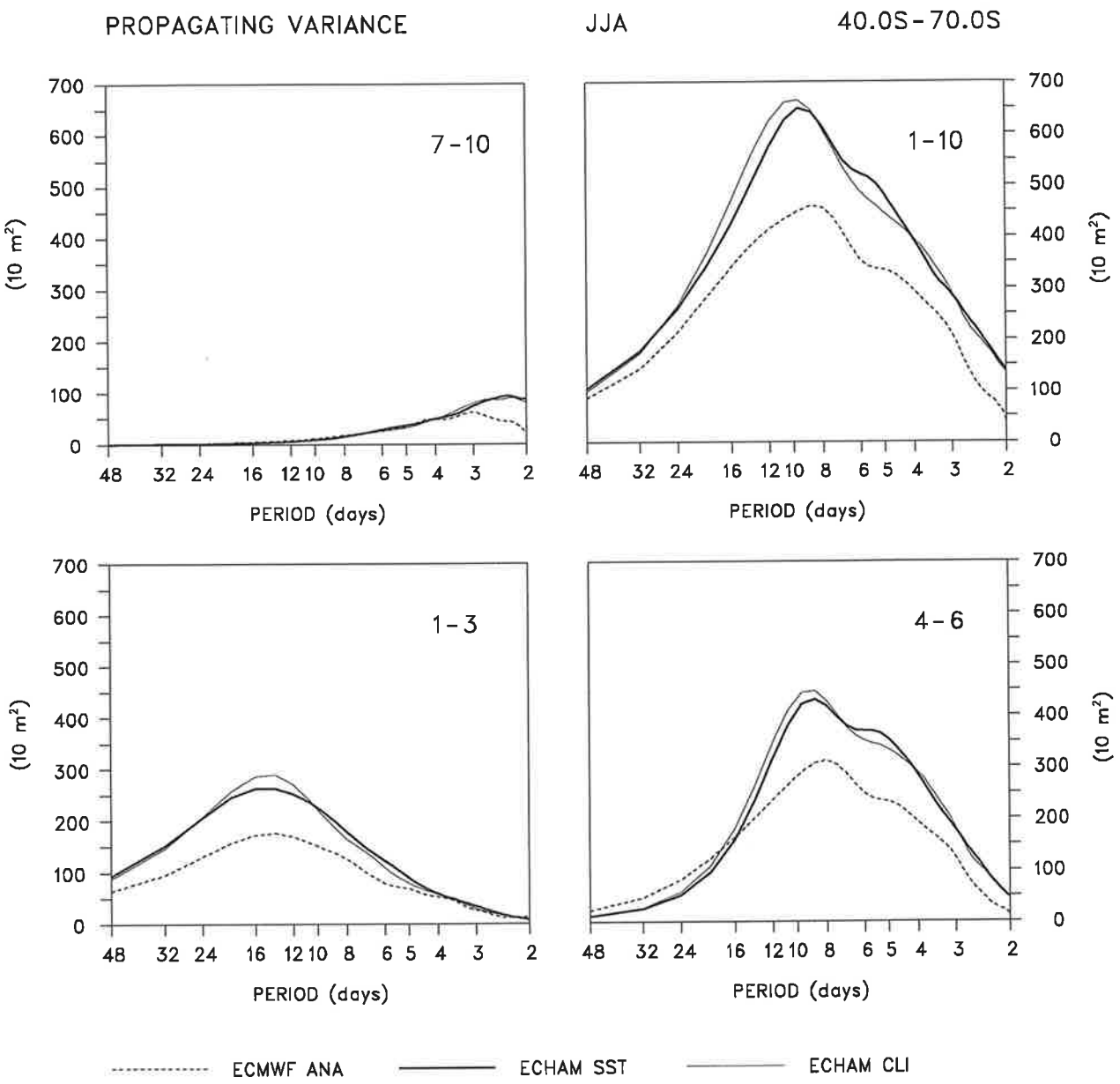

Fig. 4.1.40. As Fig. 4.1.38 but for the propagating variance spectrum.

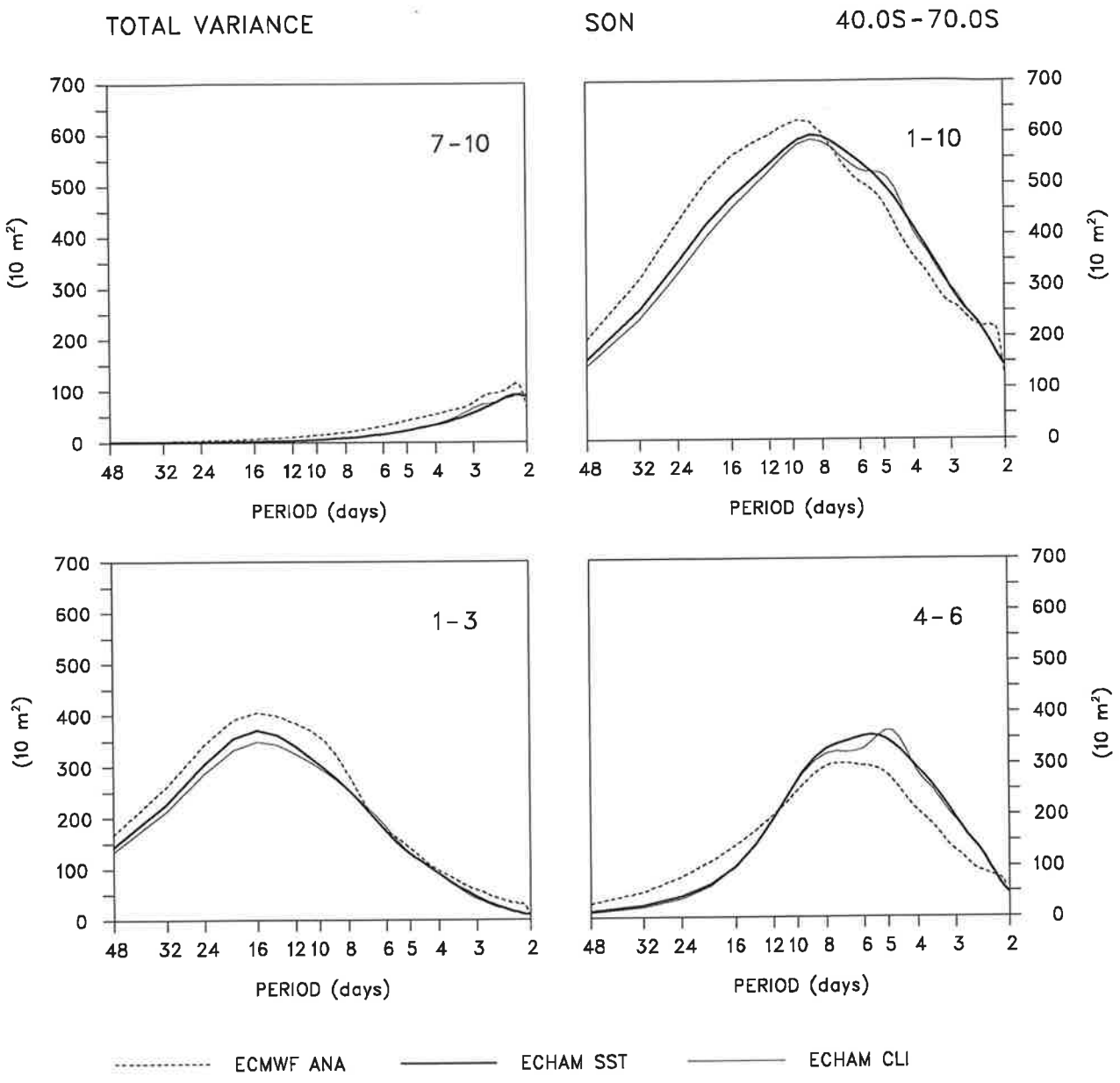

Fig. 4.1.41. As Fig. 4.1.38 but for local spring.

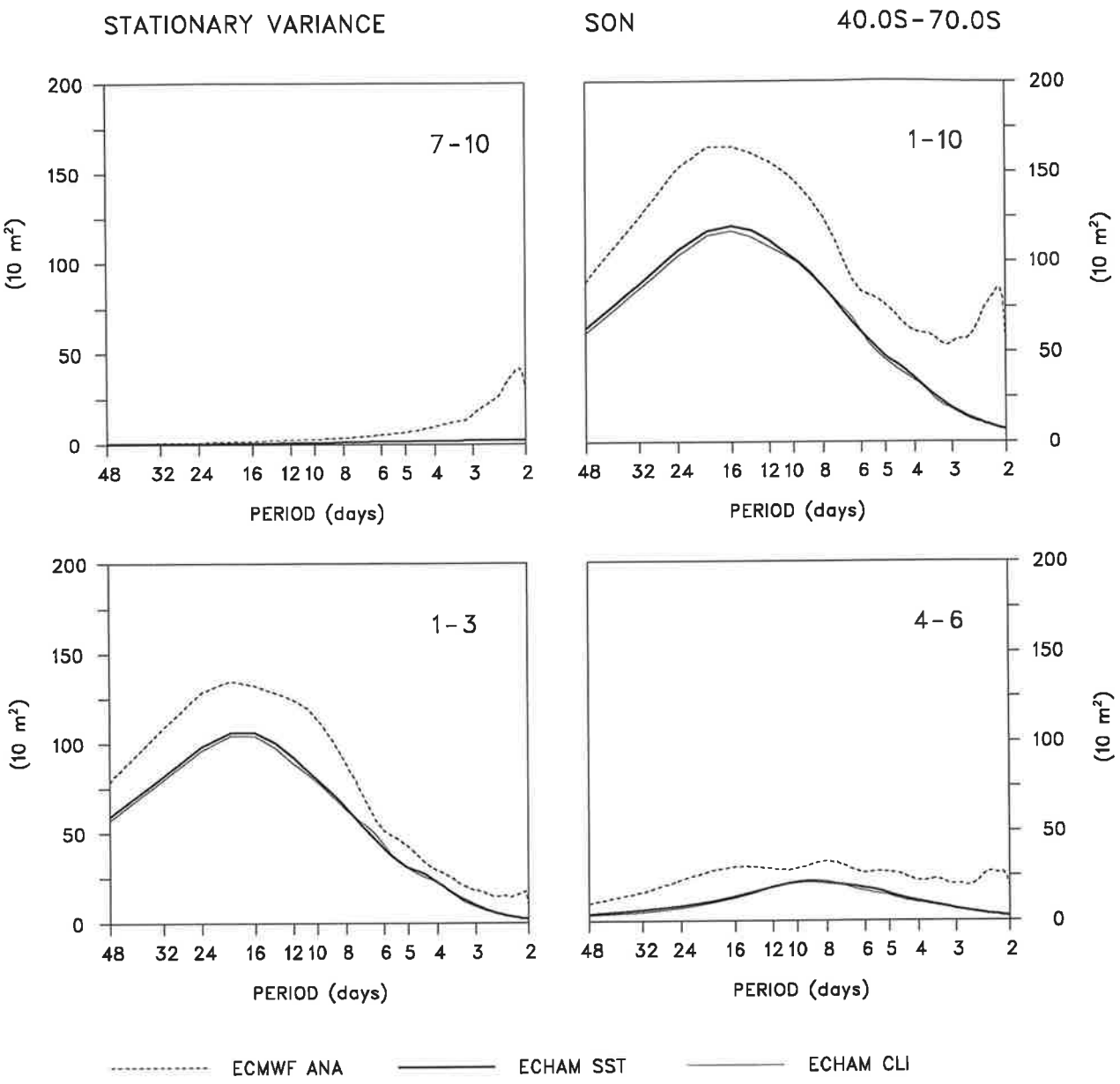

Fig. 4.1.42. As Fig. 4.1.41 but for the stationary variance spectrum.

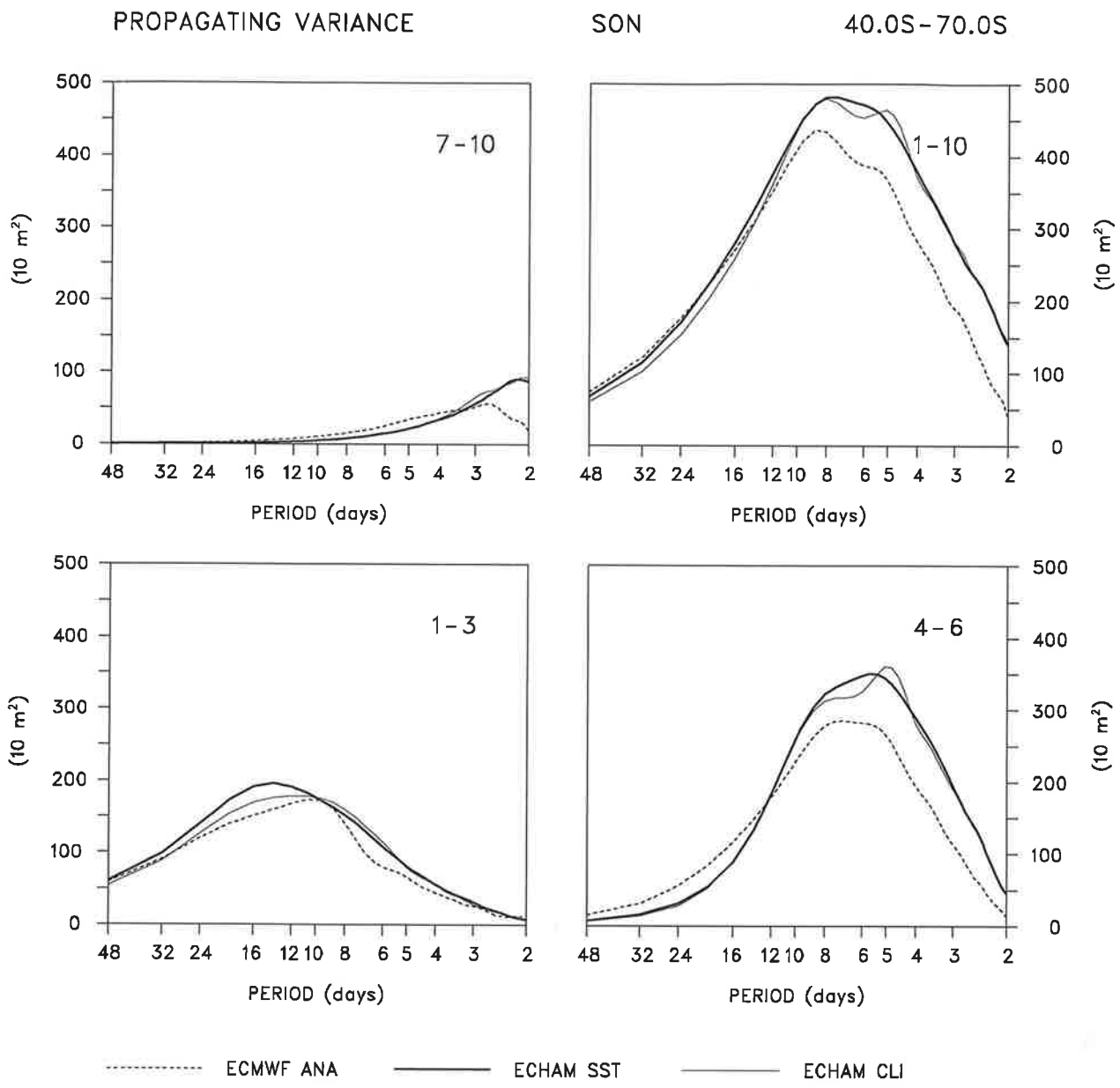

Fig. 4.1.43. As Fig. 4.1.41 but for the propagating variance spectrum.

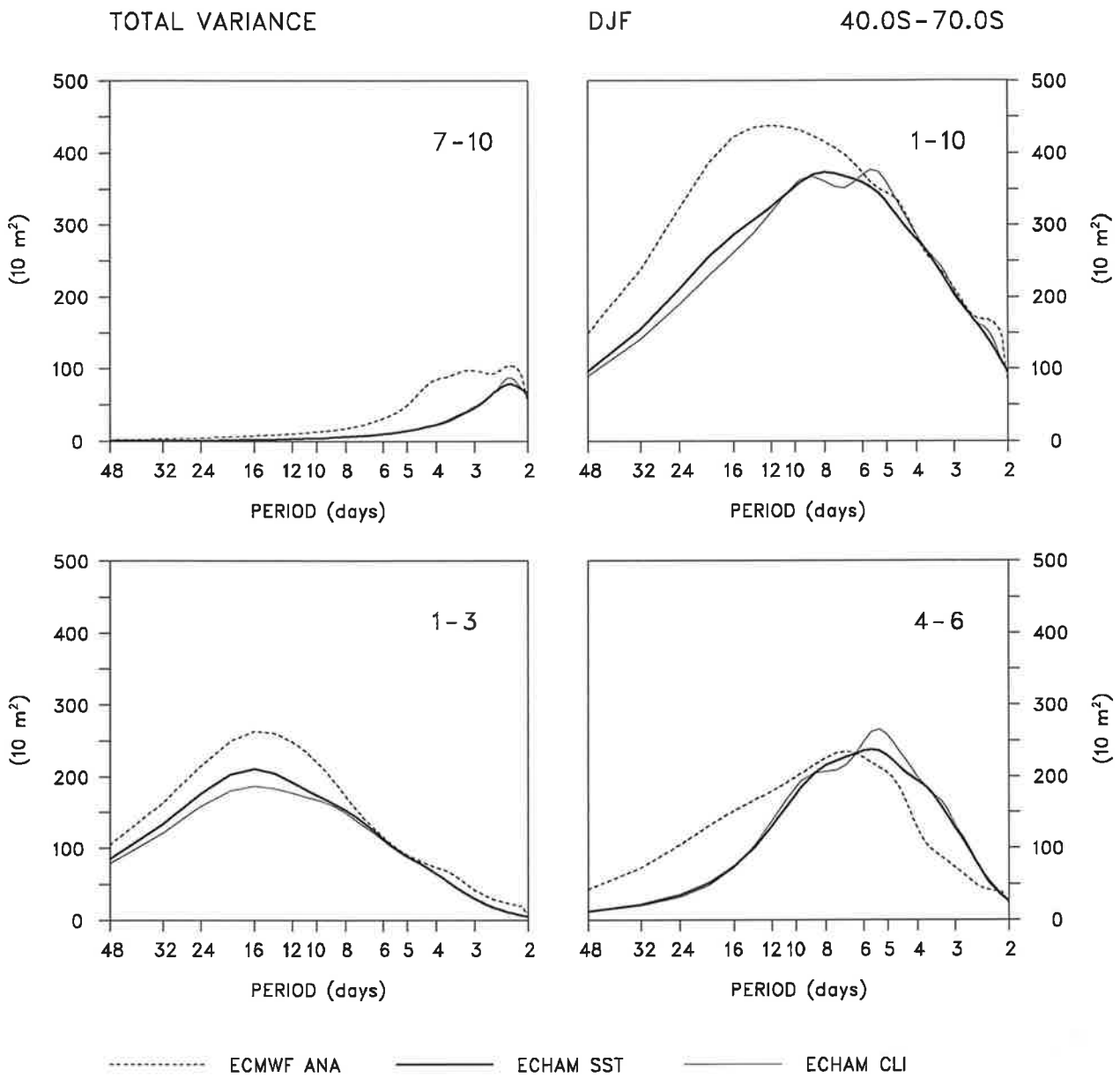

Fig. 4.1.44. As Fig. 4.1.38 but for local summer.

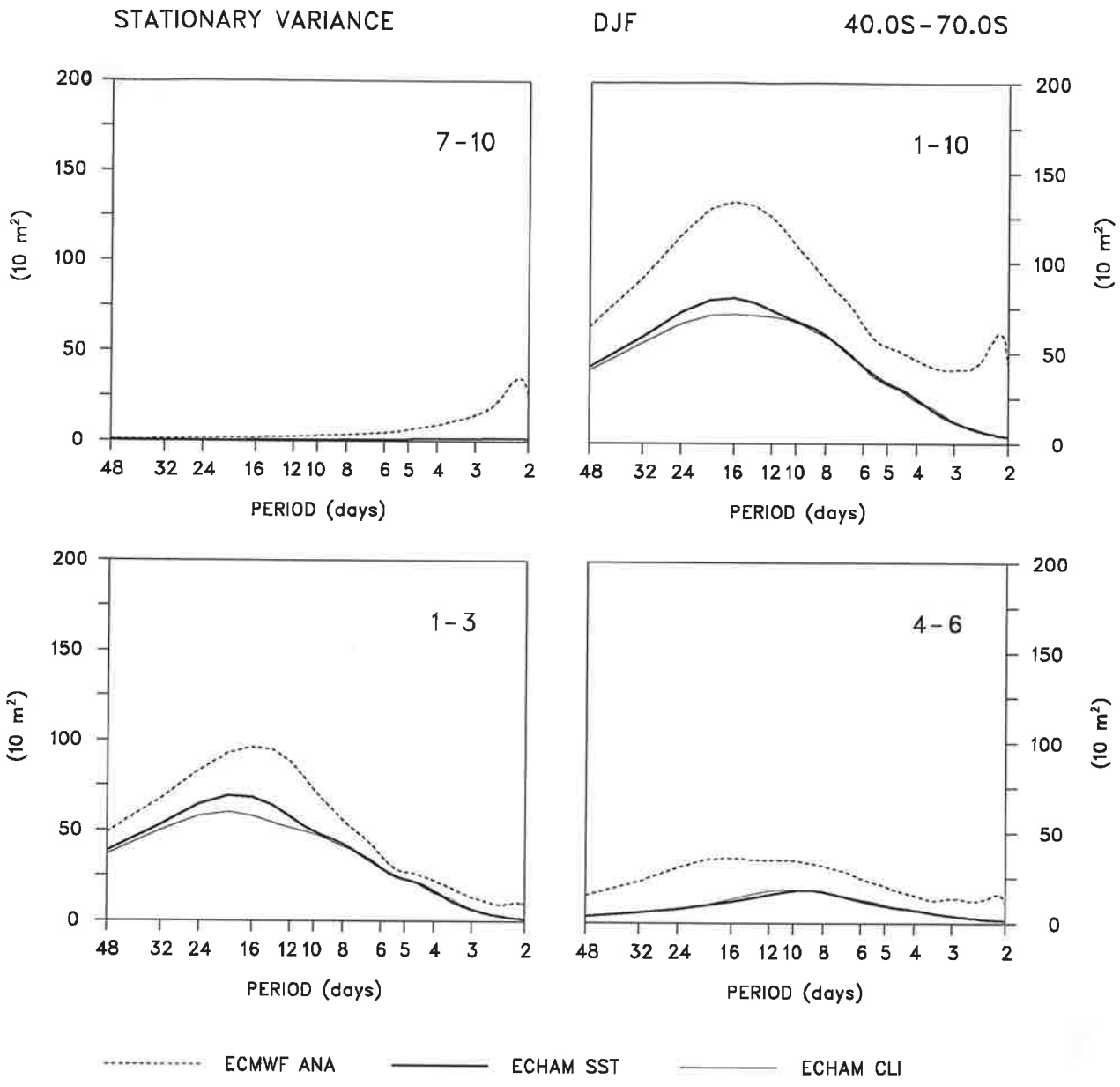

Fig. 4.1.45. As Fig. 4.1.44 but for the stationary variance spectrum.

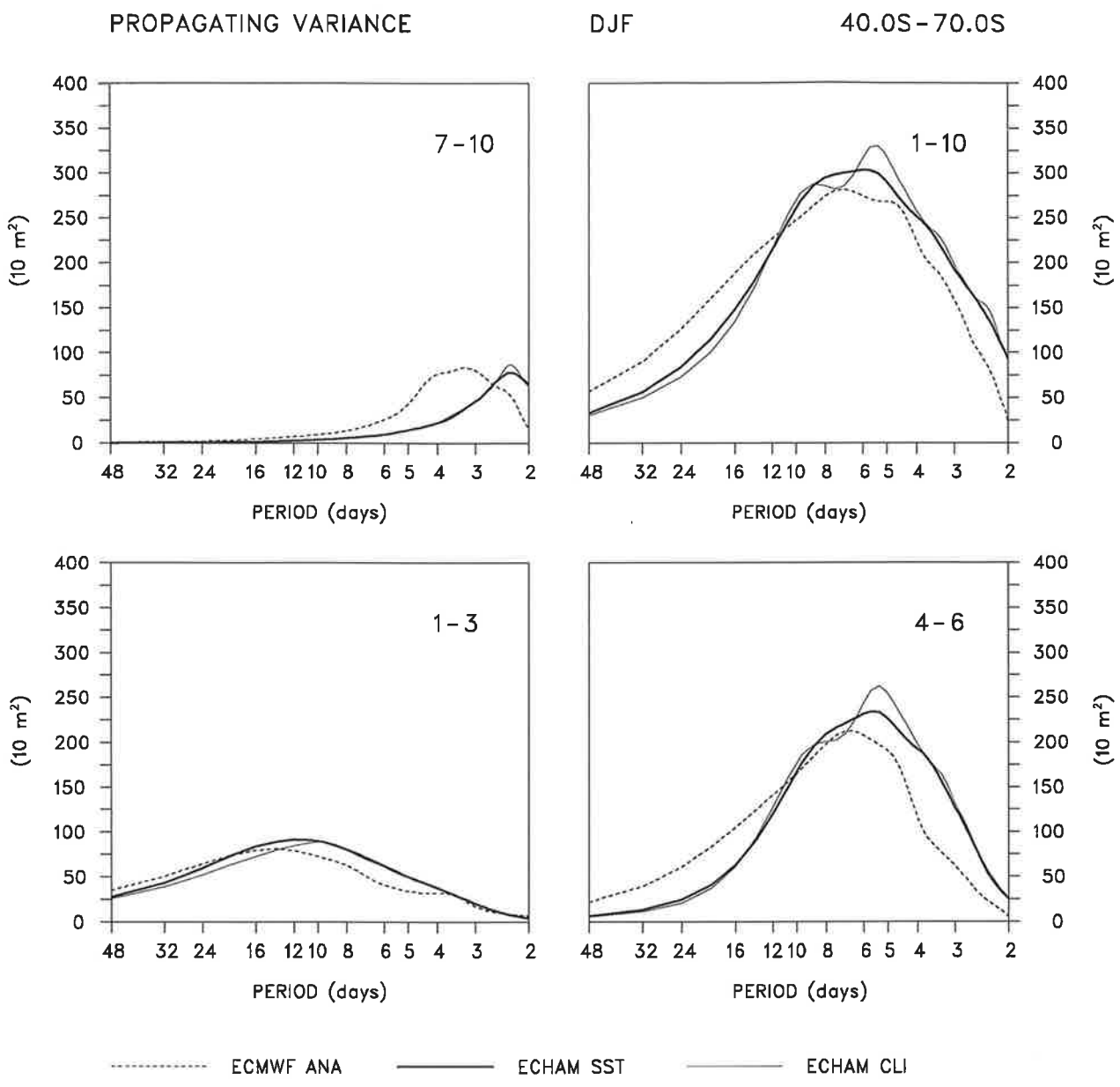

Fig. 4.1.46. As Fig. 4.1.44 but for the propagating variance spectrum.

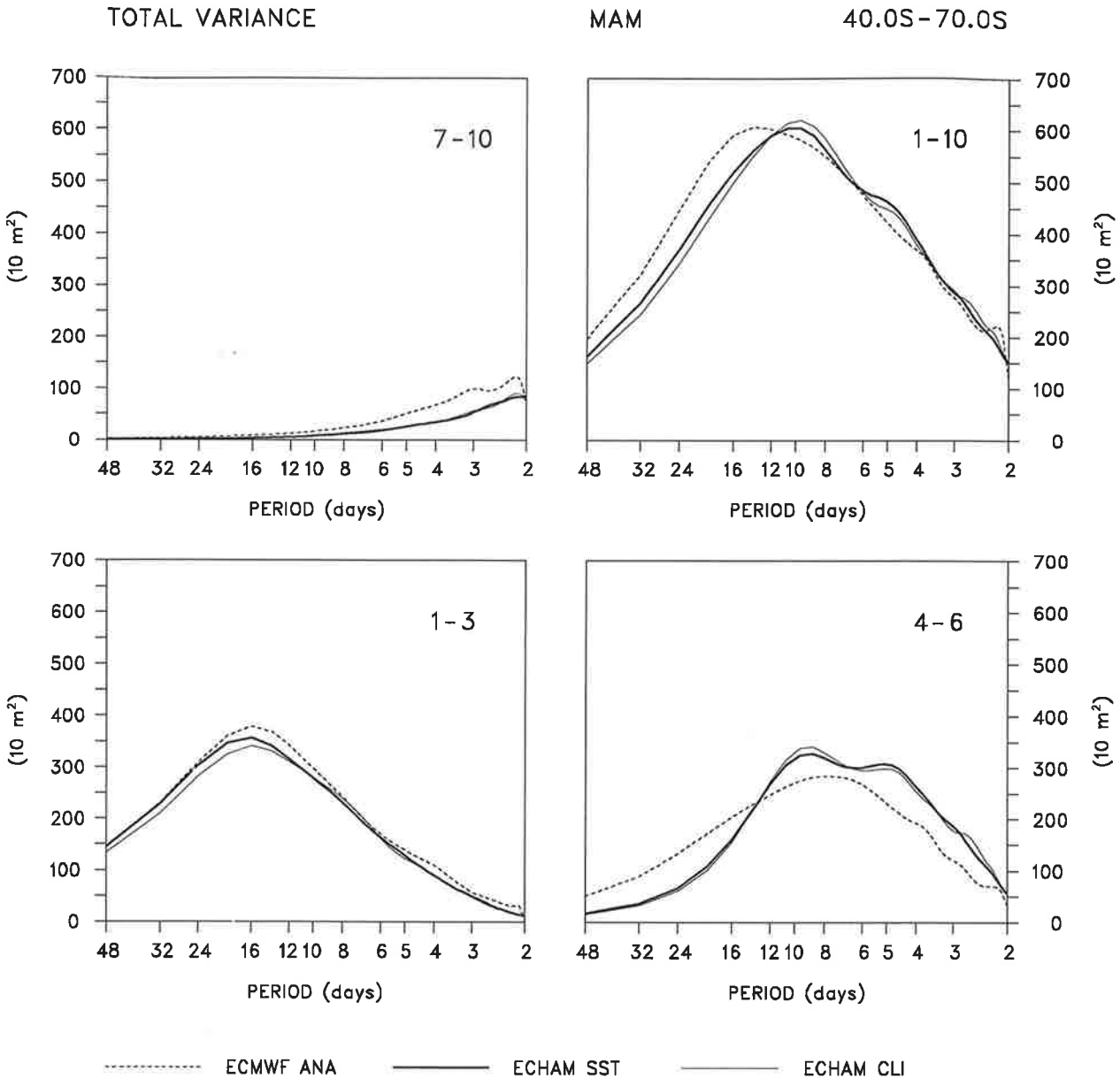

Fig. 4.1.47. As Fig. 4.1.38 but for local autumn.

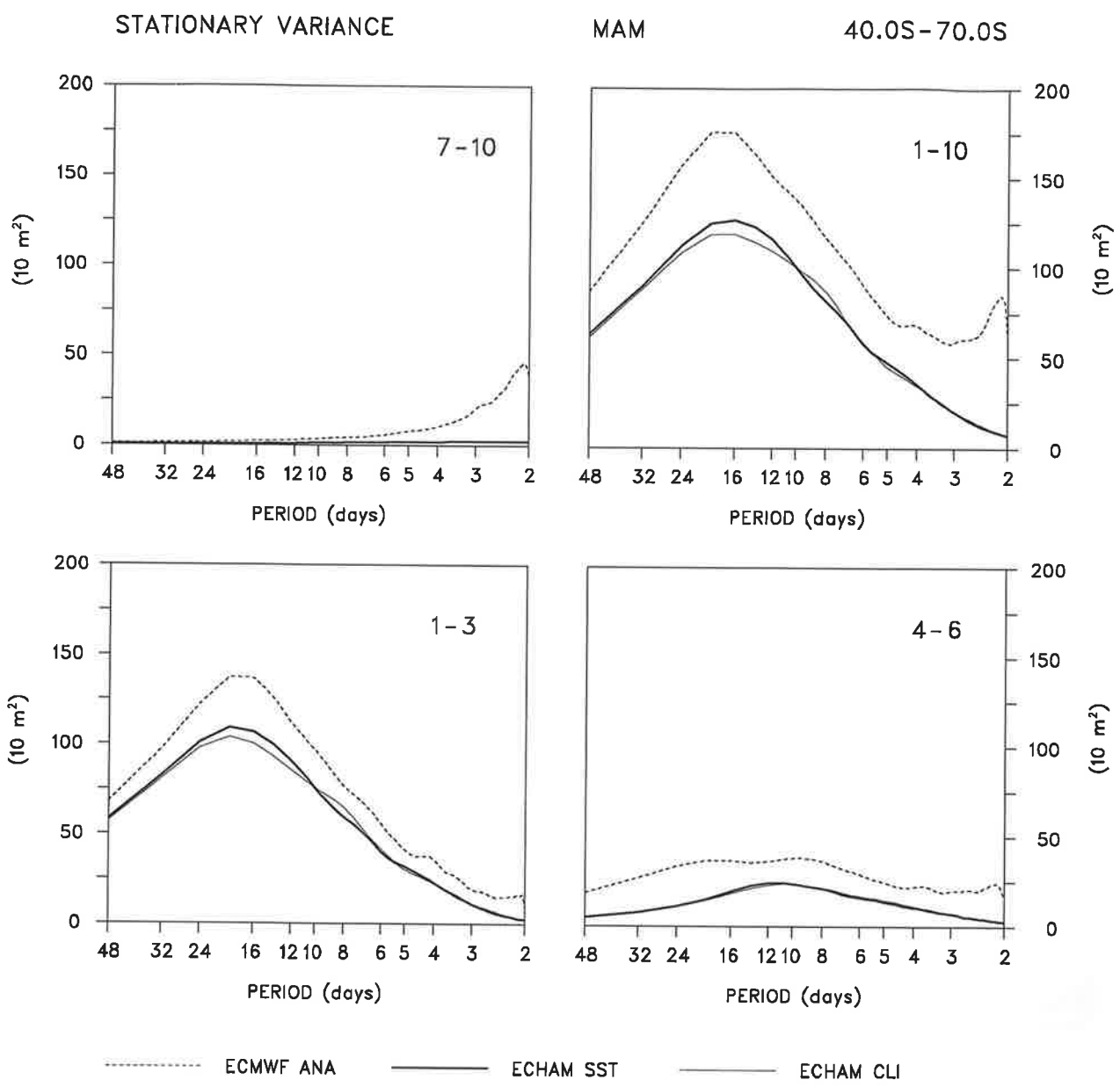

Fig. 4.1.48. As Fig. 4.1.47 but for the stationary variance spectrum.

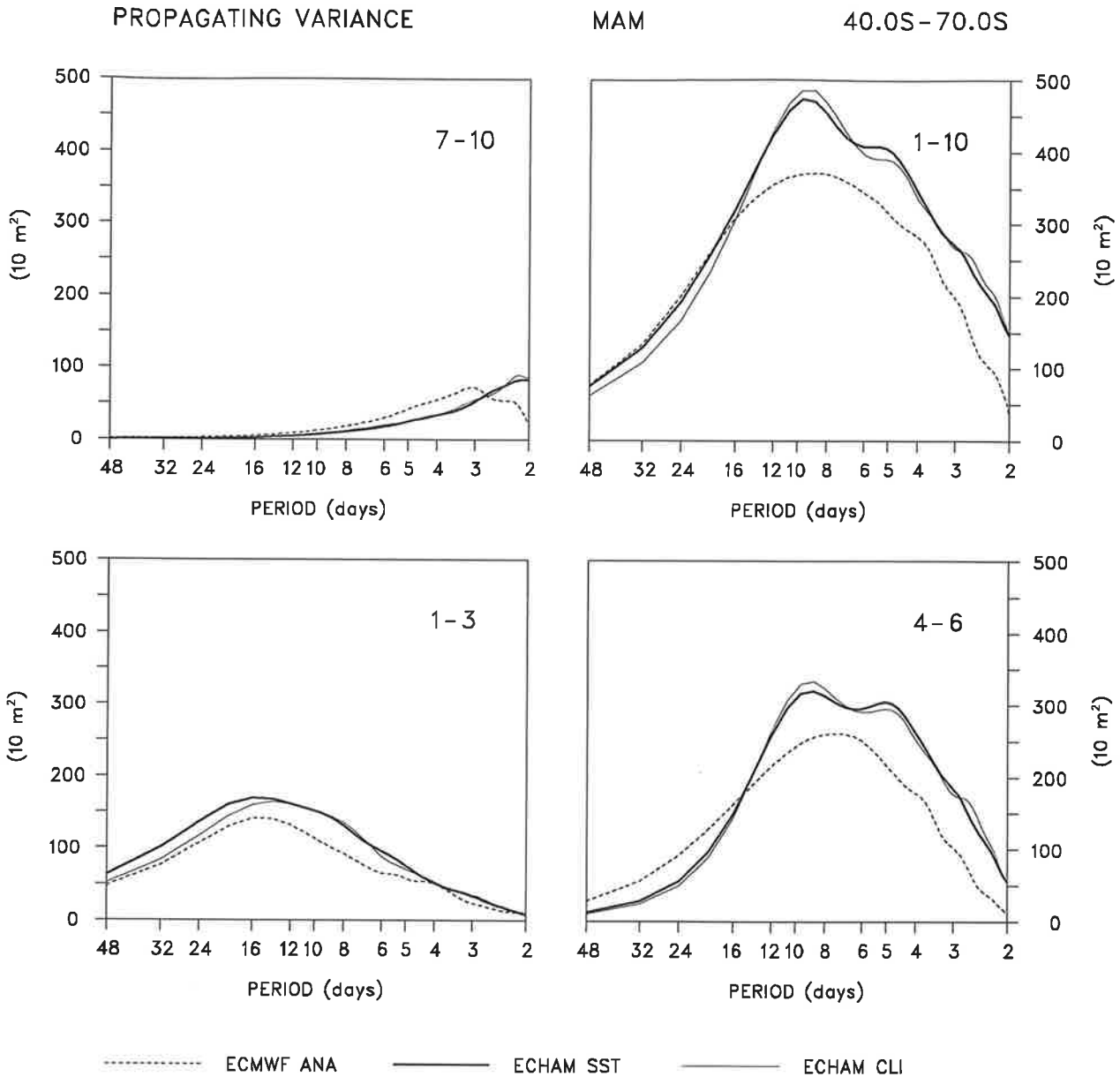

Fig. 4.1.49. As Fig. 4.1.47 but for the propagating variance spectrum.

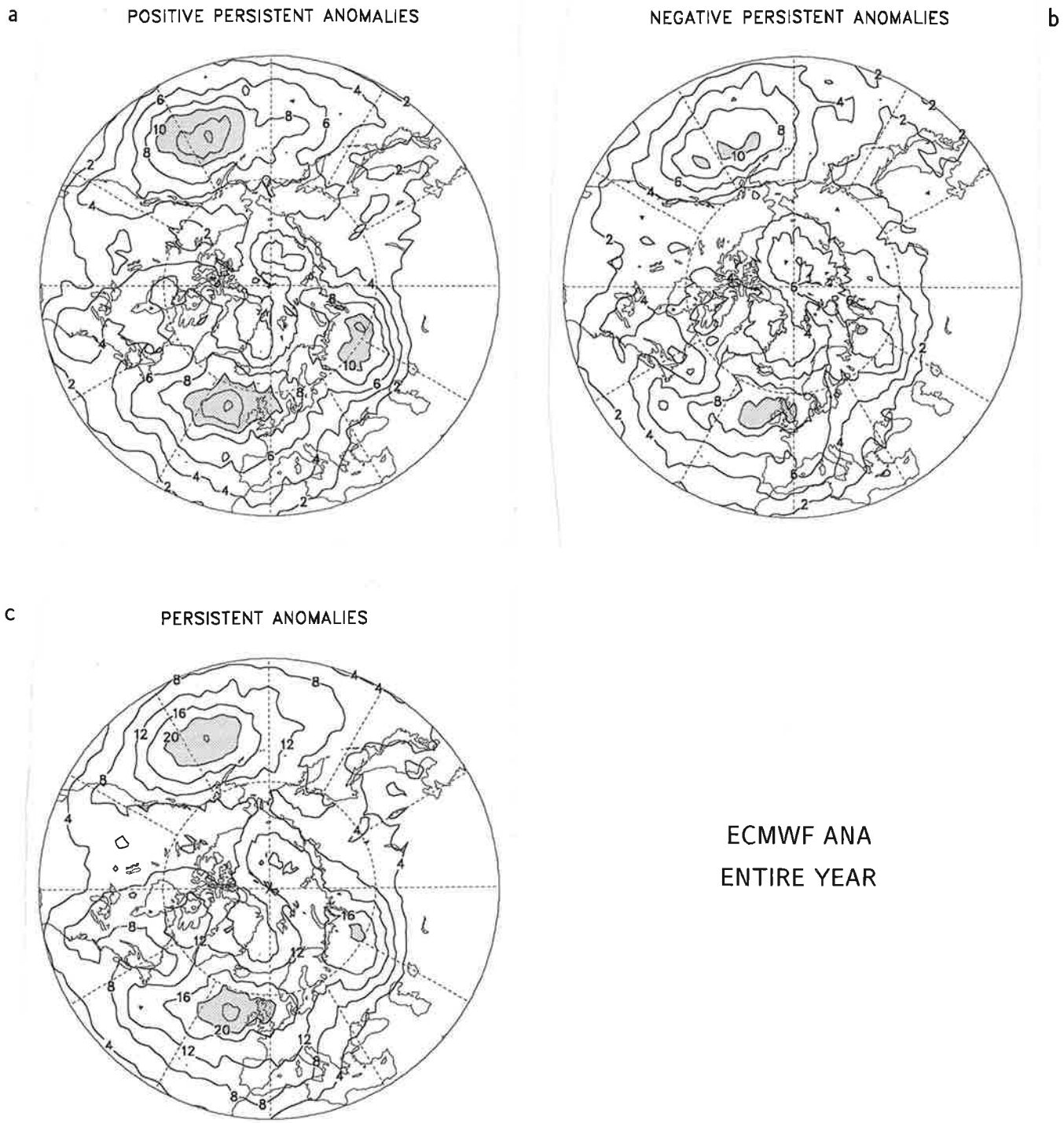

Fig. 4.2.1. Relative occurrence of persistent anomalies in the 500 hPa geopotential height field obtained from the ECMWF analyses for the positive (a), the negative (b) and the sum of postive and negative (c) persistent anomalies. Units are %, the contour interval is 2% for the positive and negative persistent anomalies, 4% for the sum of positive and negative persistent anomalies. Values higher than 10% and higher than 20%, respectively, are indicated by stippling.

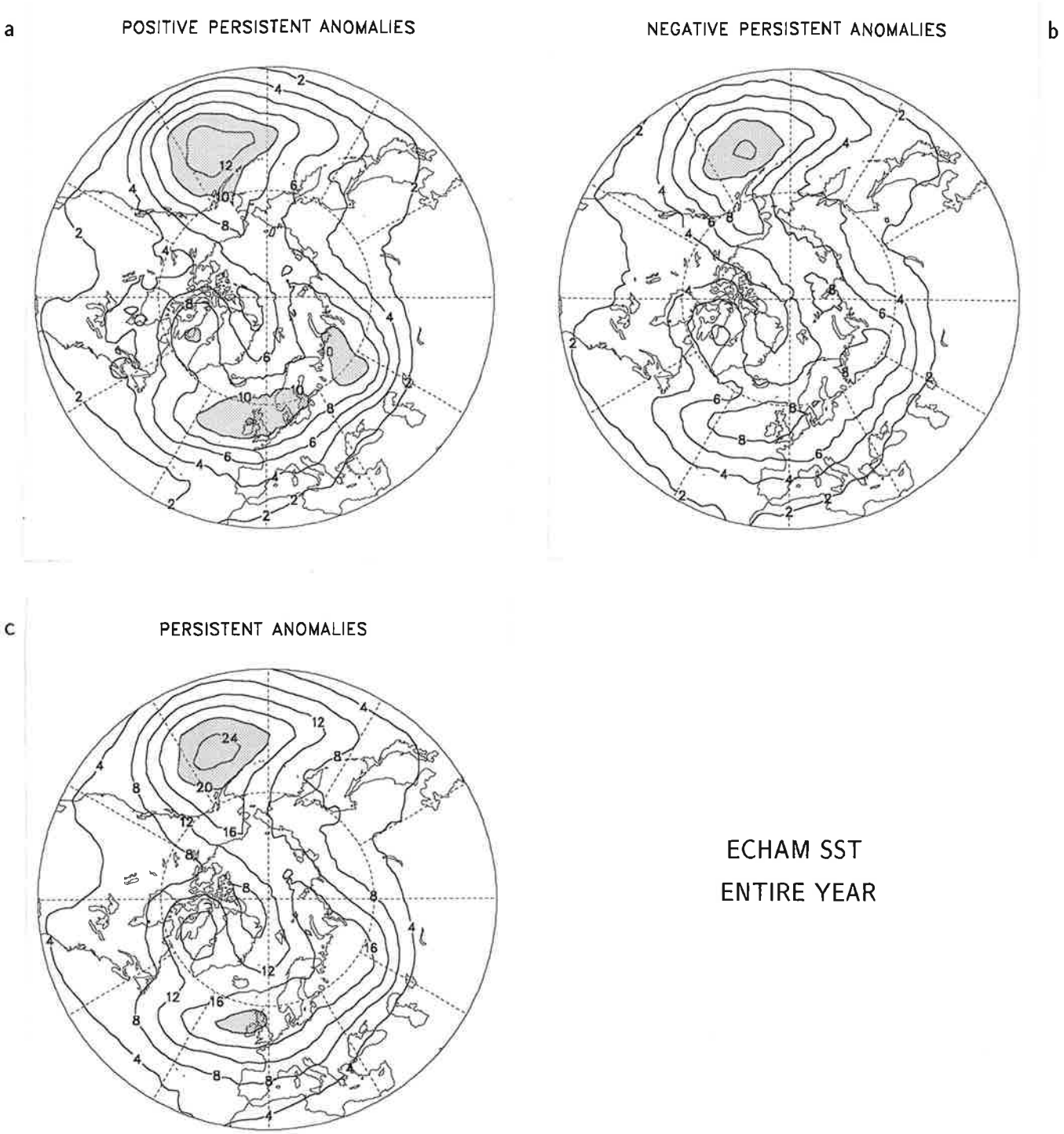

Fig. 4.2.2. As Fig. 4.2.1 but for the simulations performed with ECHAM3 with varying Sea Surface Temperatures as boundary forcing.

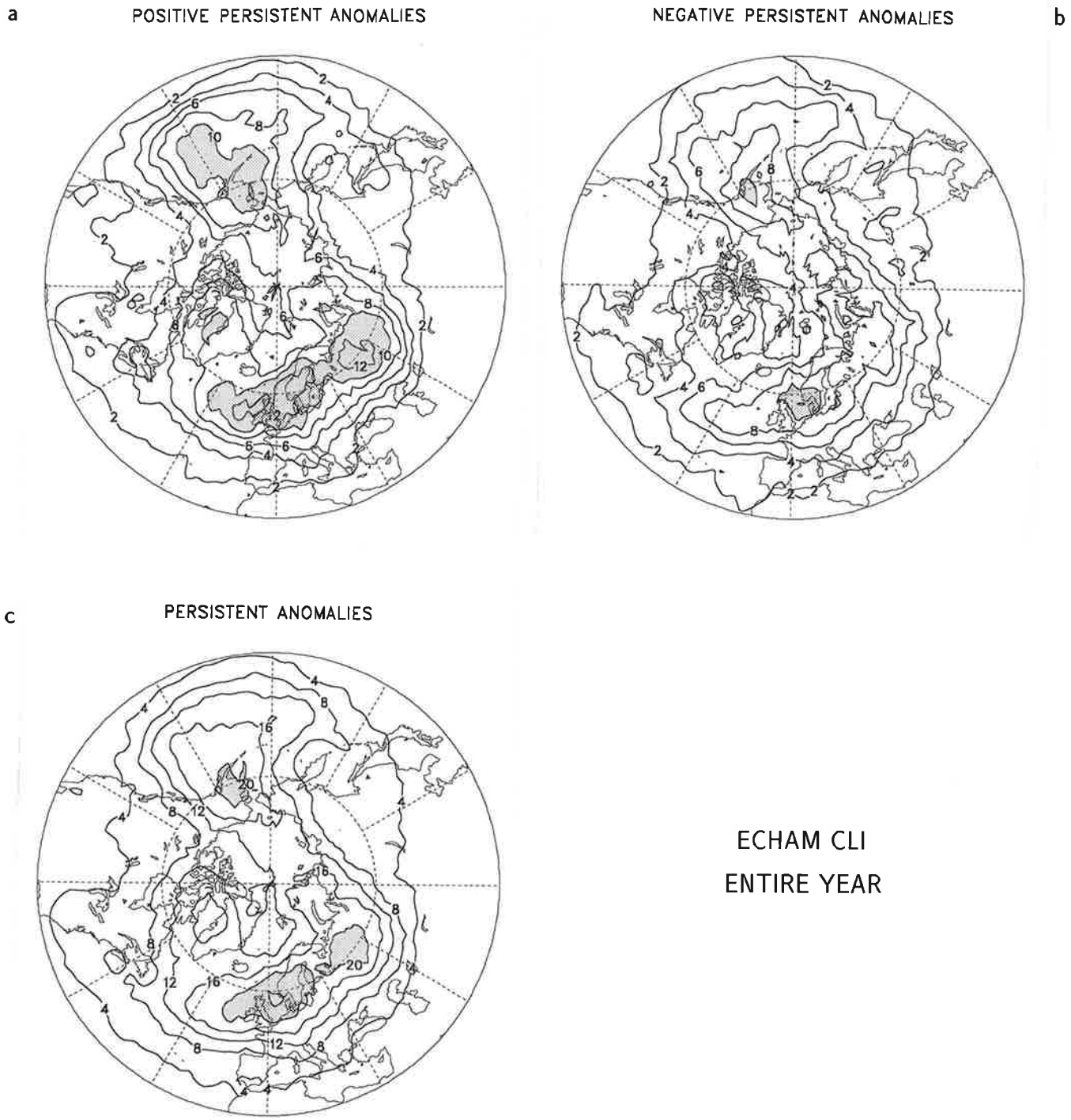

Fig. 4.2.3. As Fig. 4.2.1 but for the simulations performed with ECHAM3 with fixed Sea Surface Temperatures as boundary forcing.

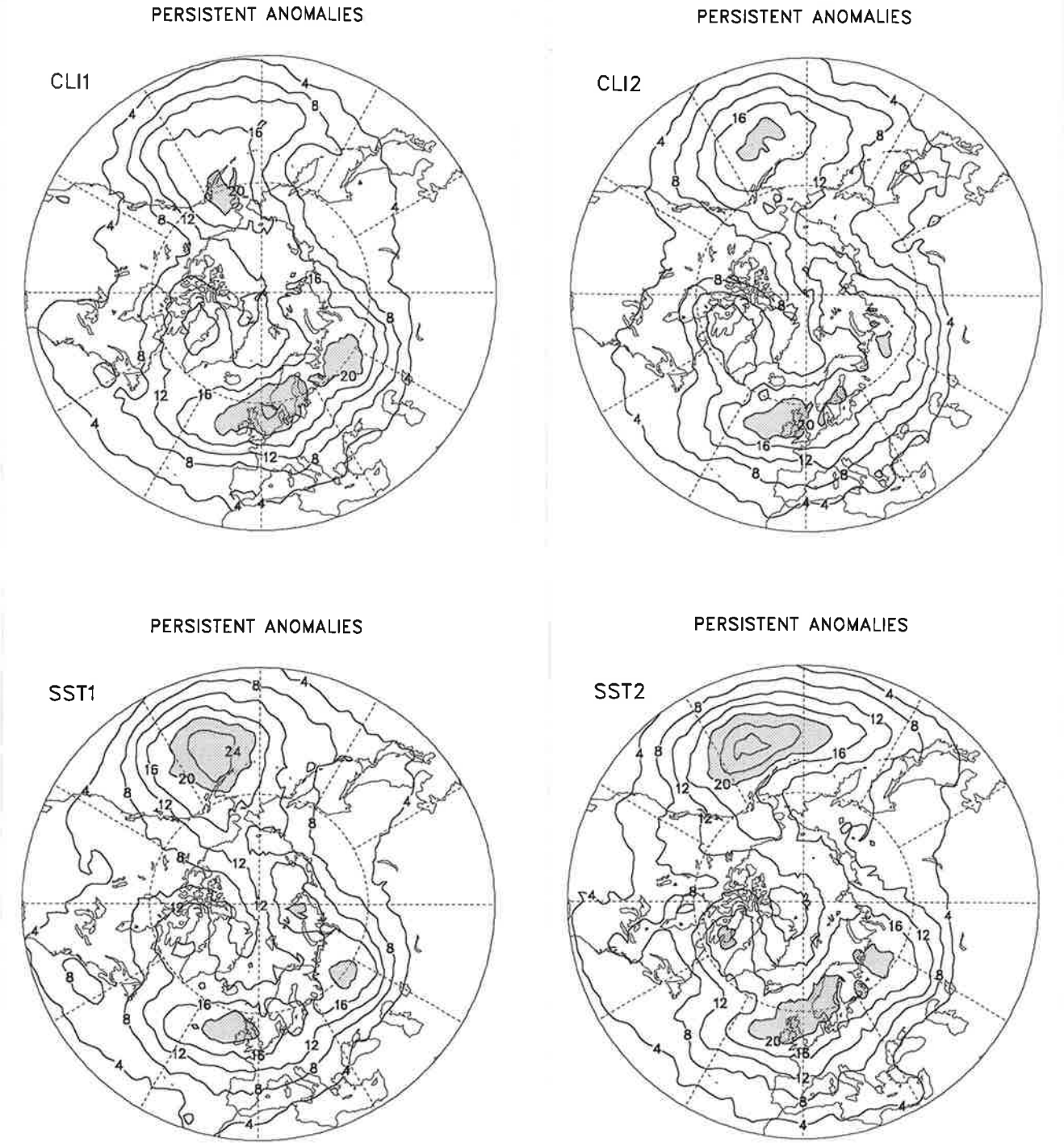

Fig. 4.2.4. Relative occurrence of persistent anomalies in the 500 hPa geopotential height field (sum of positive and negative persistent anomalies) obtained from the individual simulations performed with ECHAM3 with varying Sea Surface Temperatures (SST...) and fixed Sea Surface Temperatures (CLI...) as boundary forcing. Units are %, the contour interval is 4%. Values higher than 20% are indicated by stippling.

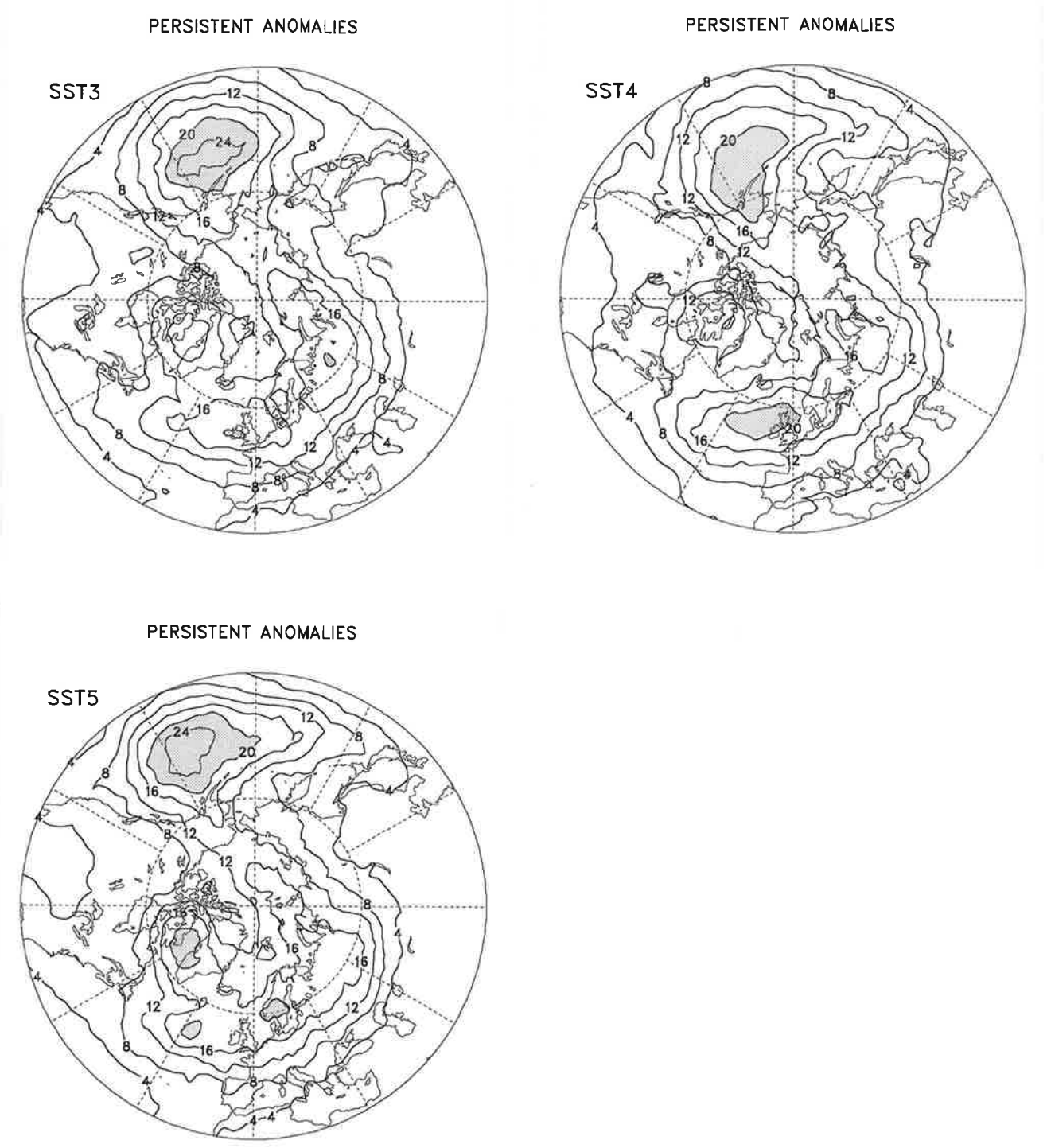

Fig. 4.2.4. Relative occurrence of persistent anomalies in the 500 hPa geopotential height field (sum of positive and negative persistent anomalies) obtained from the individual simulations performed with ECHAM3 with varying Sea Surface Temperatures (SST...) and fixed Sea Surface Temperatures (CLI...) as boundary forcing. Units are %, the contour interval is 4%. Values higher than 20% are indicated by stippling.

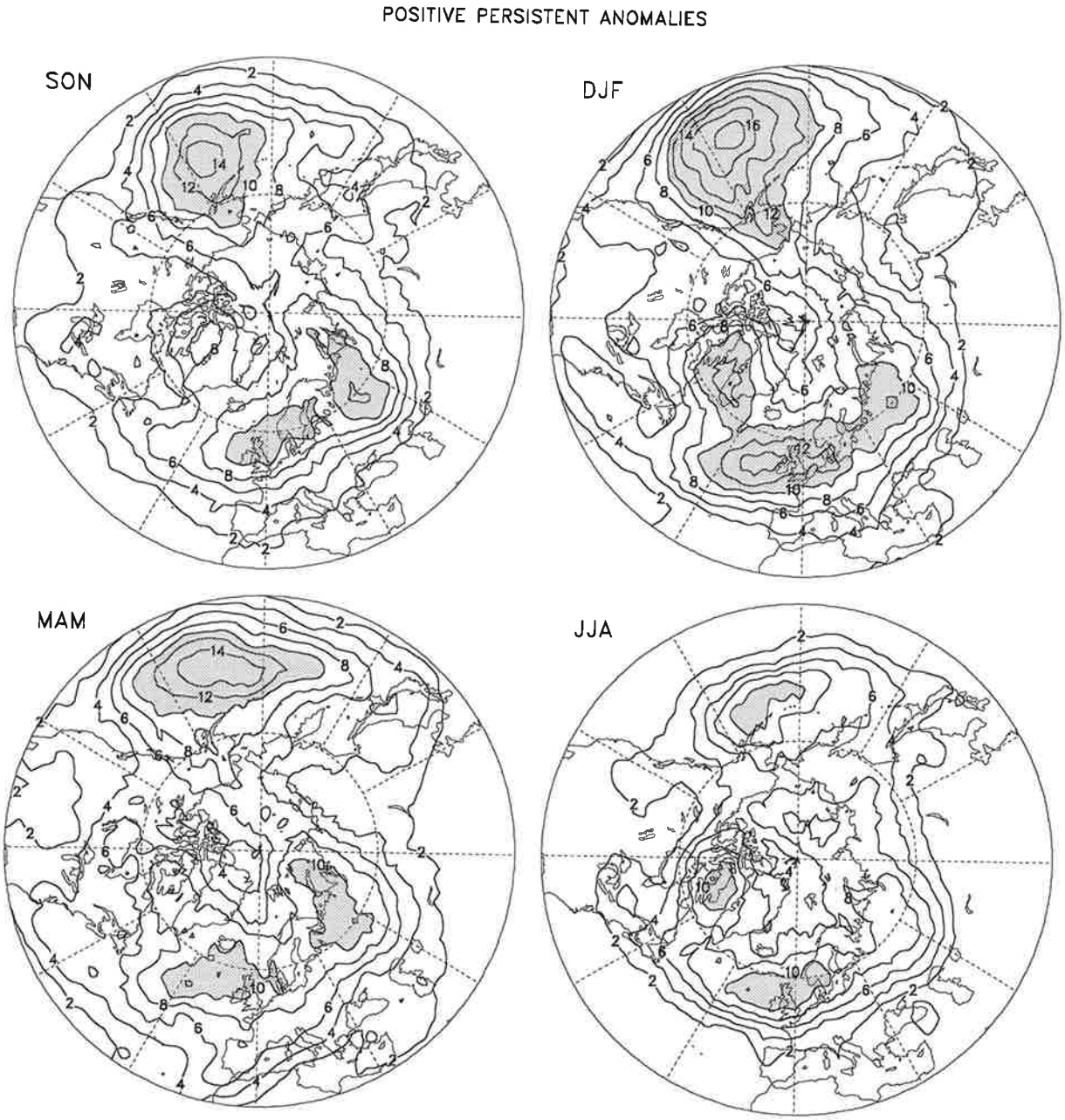

Fig. 4.2.5. Relative occurrence of positive persistent anomalies in the 500 hPa geopotential height field obtained from the simulations with varying Sea Surface Temperatures distinguishing between seasons. Units are %, the contour interval is 2%. Values higher than 10% are indicated by stippling.

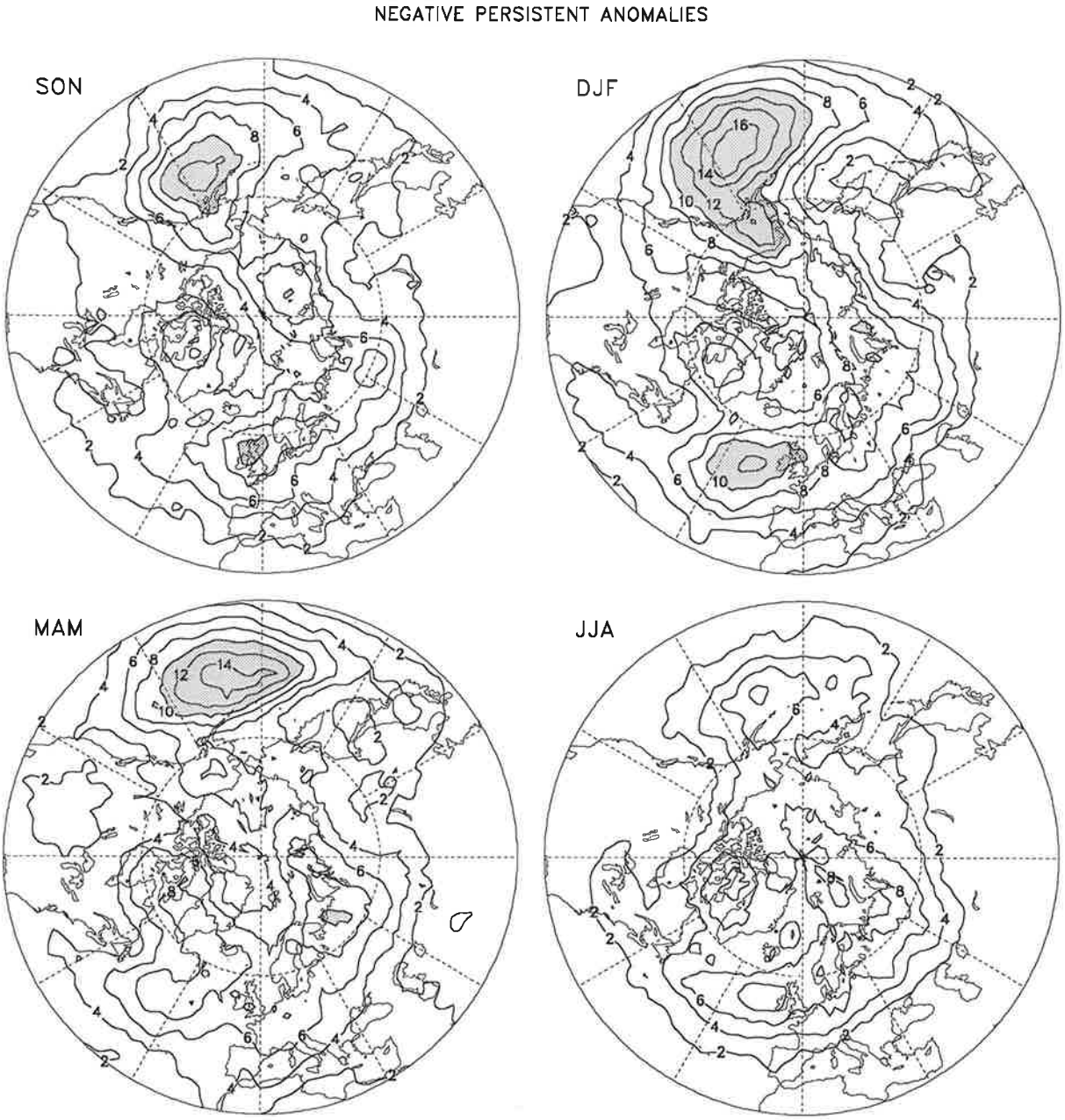

Fig. 4.2.6. As Fig. 4.2.5 but for the negative persistent anomalies.

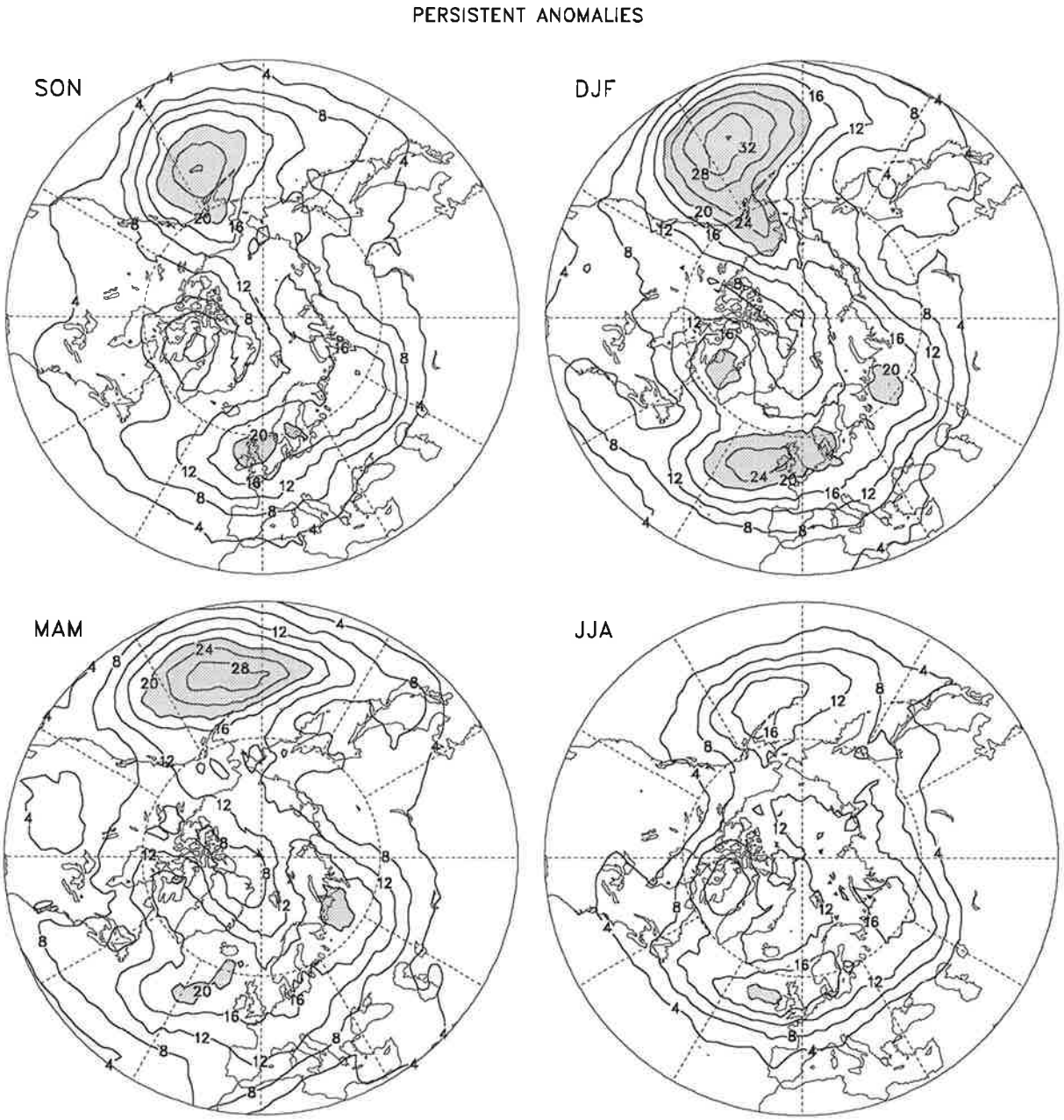

Fig. 4.2.7. As Fig. 4.2.5 but for the sum of positive and negative persistent anomalies. The contour interval is 4%, values higher than 20% are indicated by stippling.

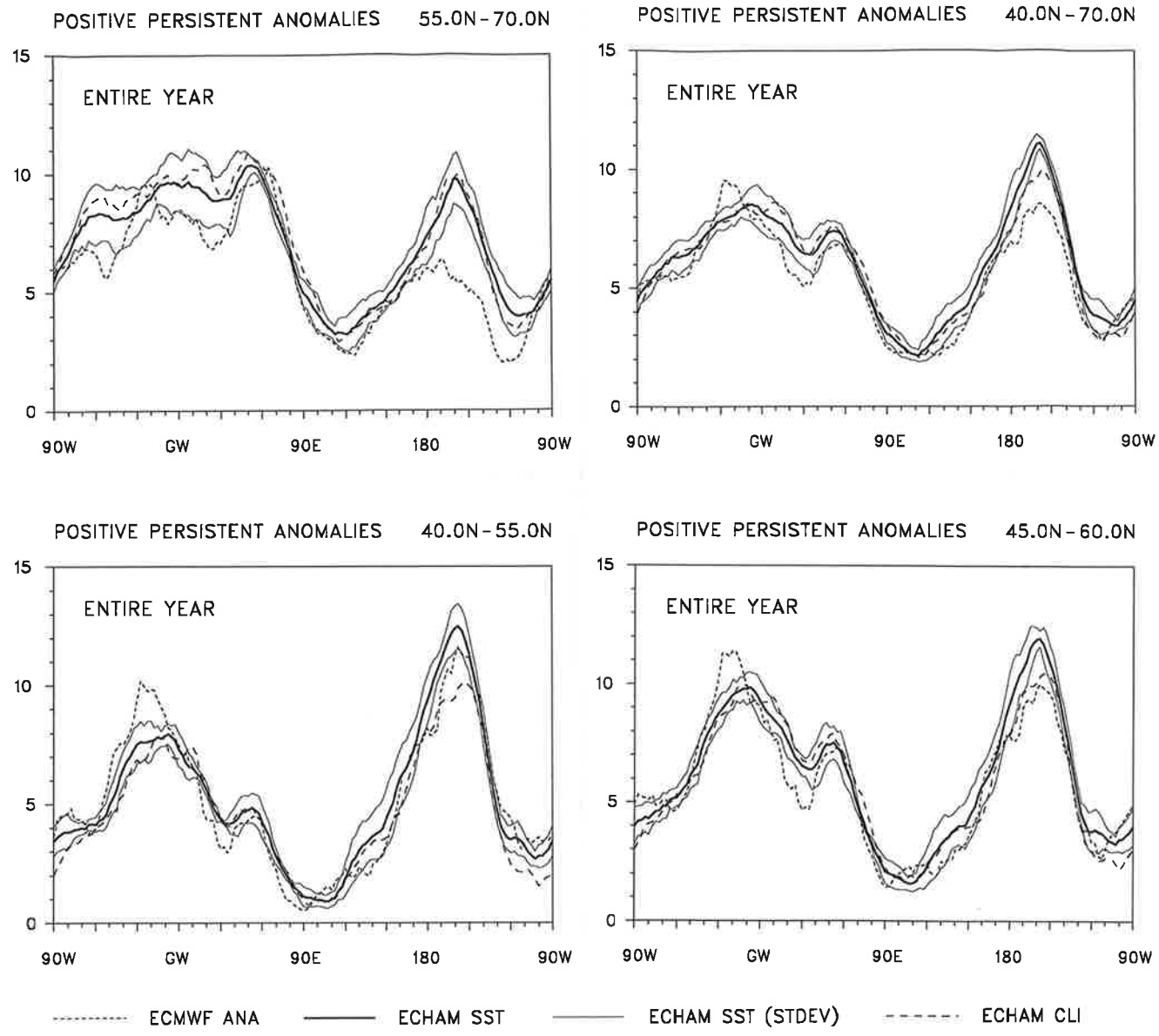

Fig. 4.2.8. Relative occurrence of positive persistent anomalies in the 500 hPa geopotential height field obtained from the the ECMWF analyses and the two sets of simulations performed with ECHAM3 as a function of longitude for different zones. The mean value obtained from the simulations with varying Sea Surface Temperatures is given by the heavy solid line, the light solid lines represent this mean value with the standard deviation of the five individual simulations added and subtracted, respectively. The mean value obtained from the simulations with fixed Sea Surface Temperatures is indicated by long dashes, that derived from the analyses by short dashes. Units are %.

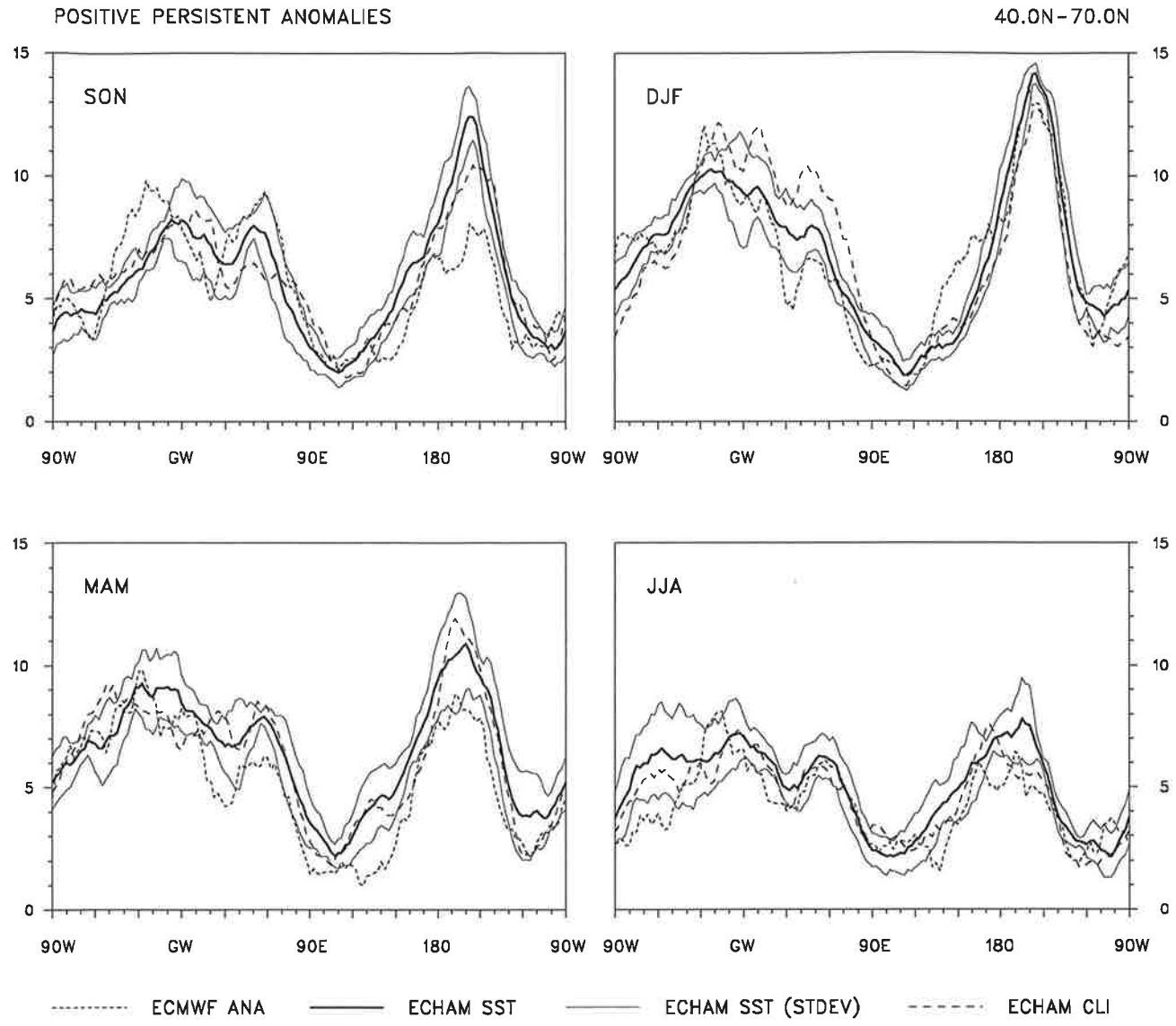

Fig. 4.2.9. As Fig. 4.2.8 for the zone beteeen 40° and 70°N distinguishing between seasons.

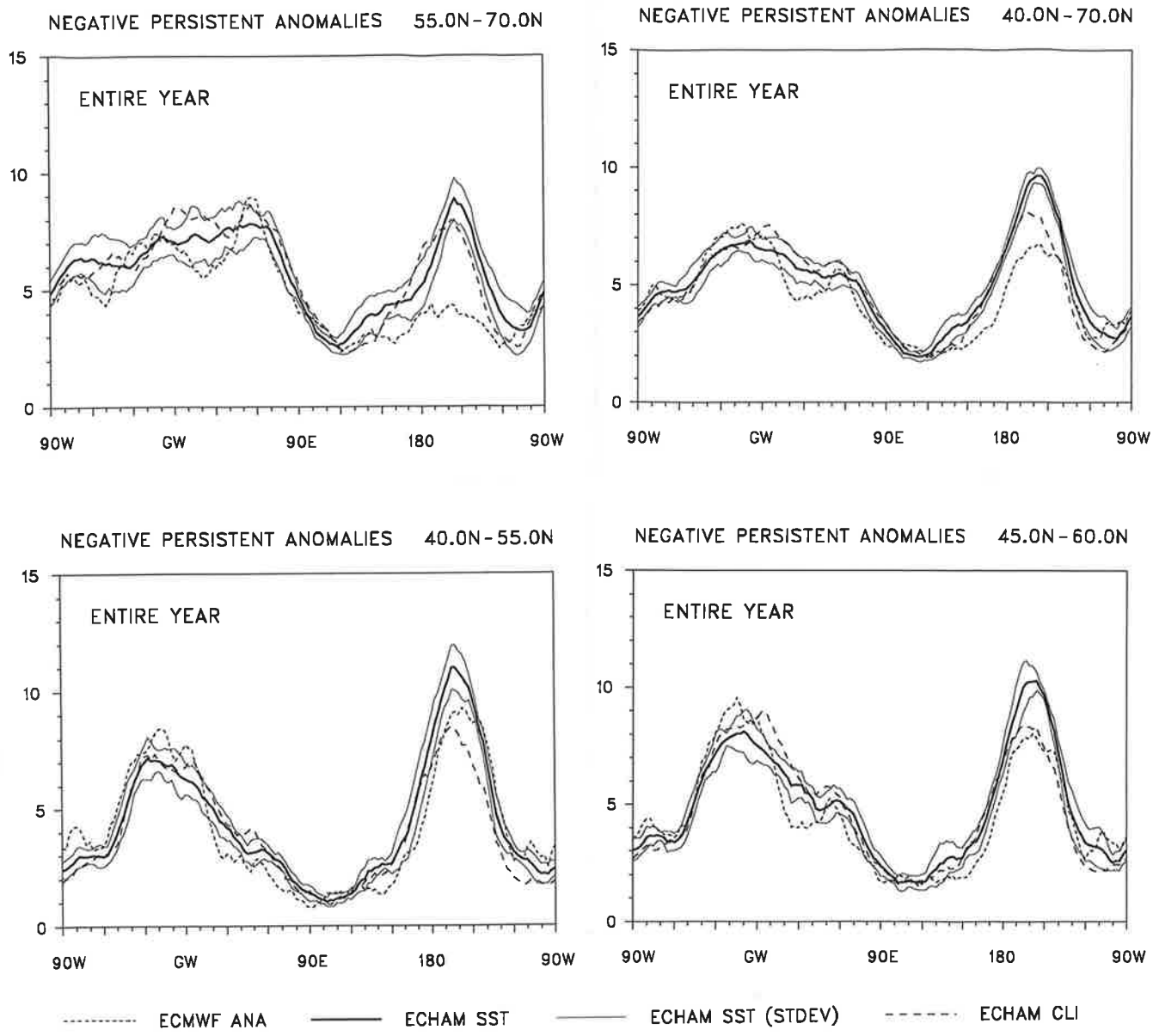

Fig. 4.2.10. As Fig. 4.2.8 but for the negative persistent anomalies.

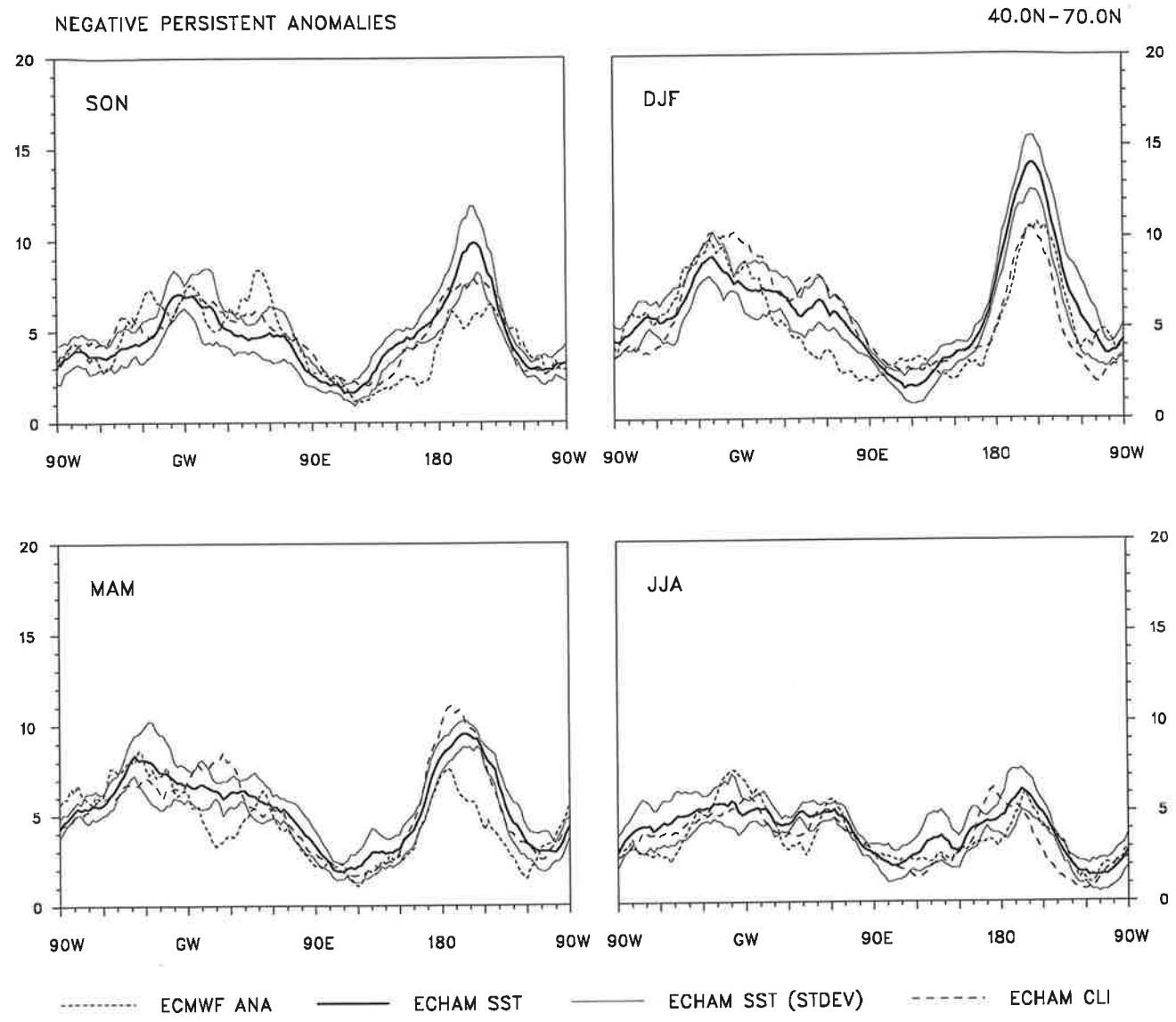

Fig. 4.2.11. As Fig. 4.2.10 for the zone beteeen 40° and 70°N distinguishing between seasons.

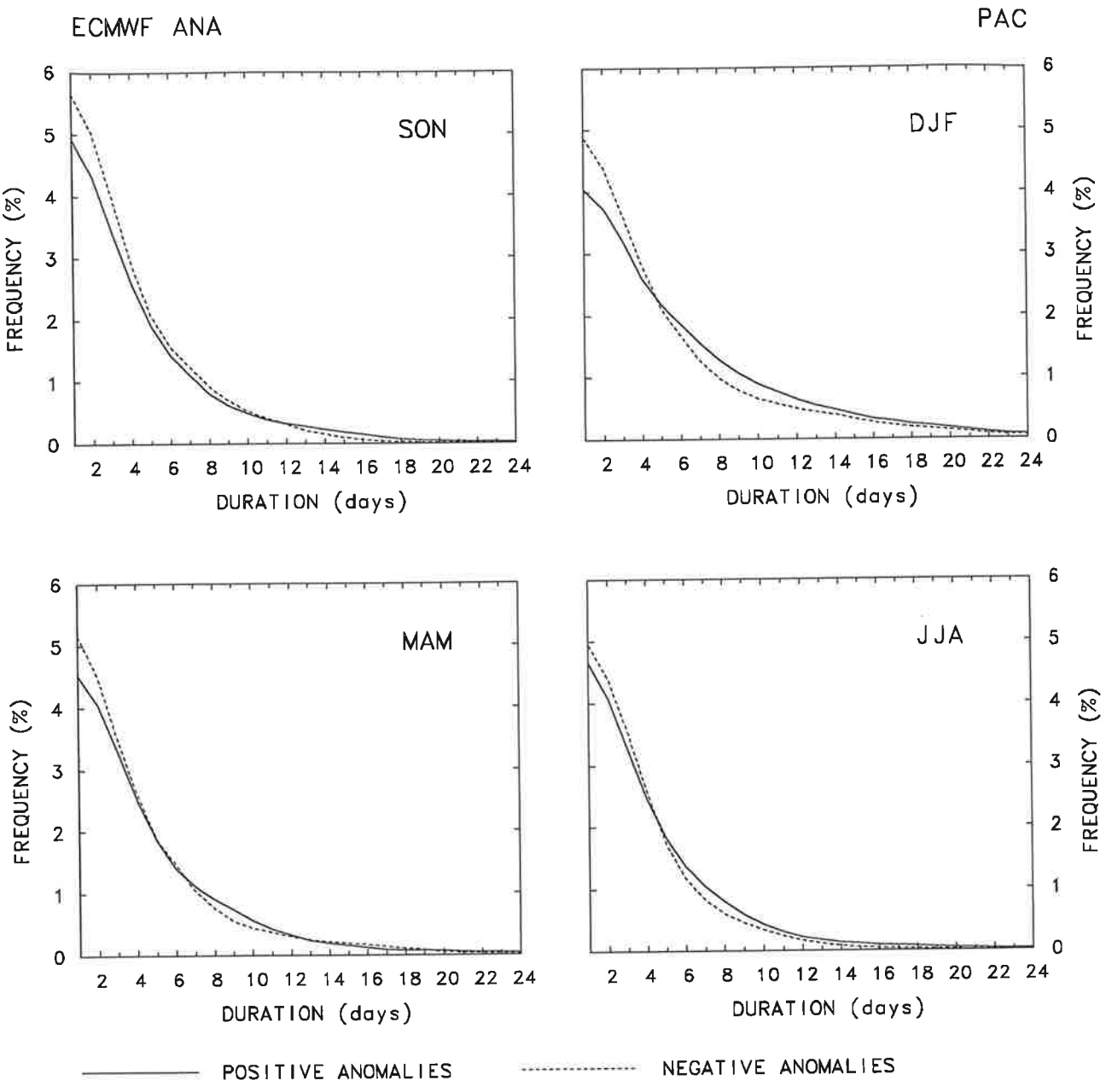

Fig. 4.2.13. Relative occurrence of anomalies in the 500 hPa geopotential height field obtained from the the ECMWF analyses as a function of their lifetime for the Pacific region (see text for details) distinguishing between seasons. The solid line represents the positive and the dashed line the negative anomalies.

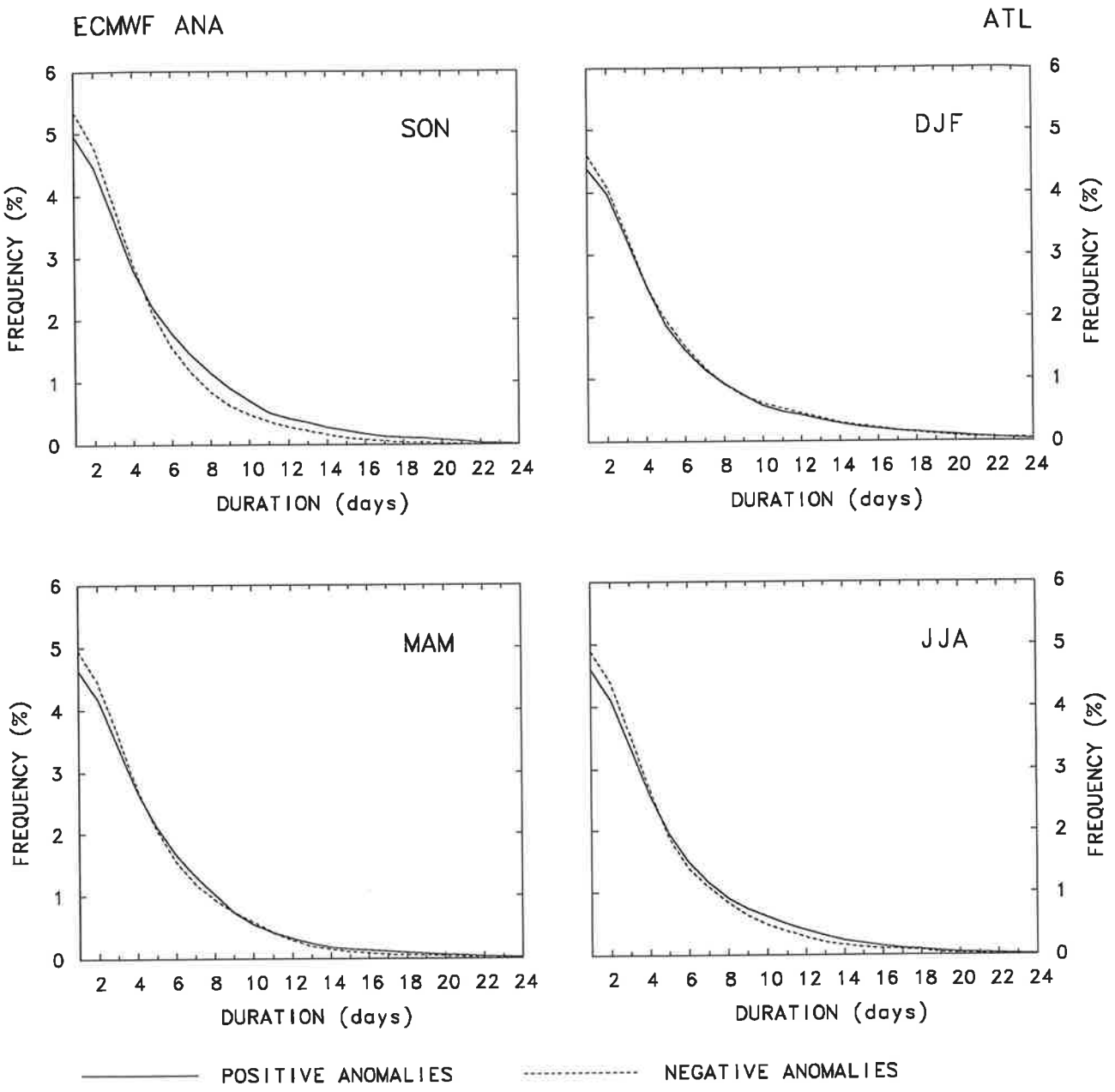

Fig. 4.2.14. As Fig. 4.2.13 but for the Atlantic region.

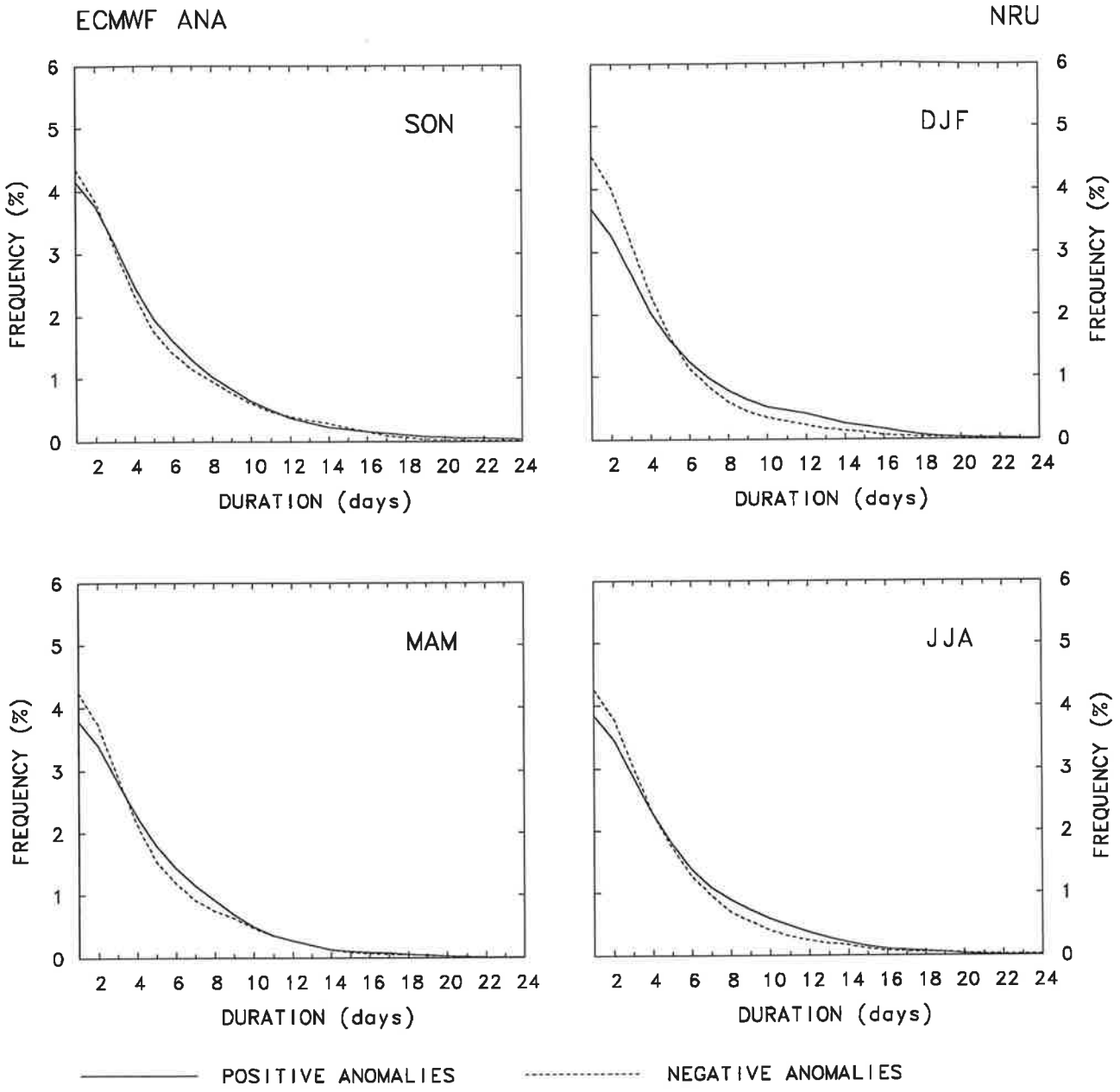

Fig. 4.2.15. As Fig. 4.2.13 but for northern Russia.

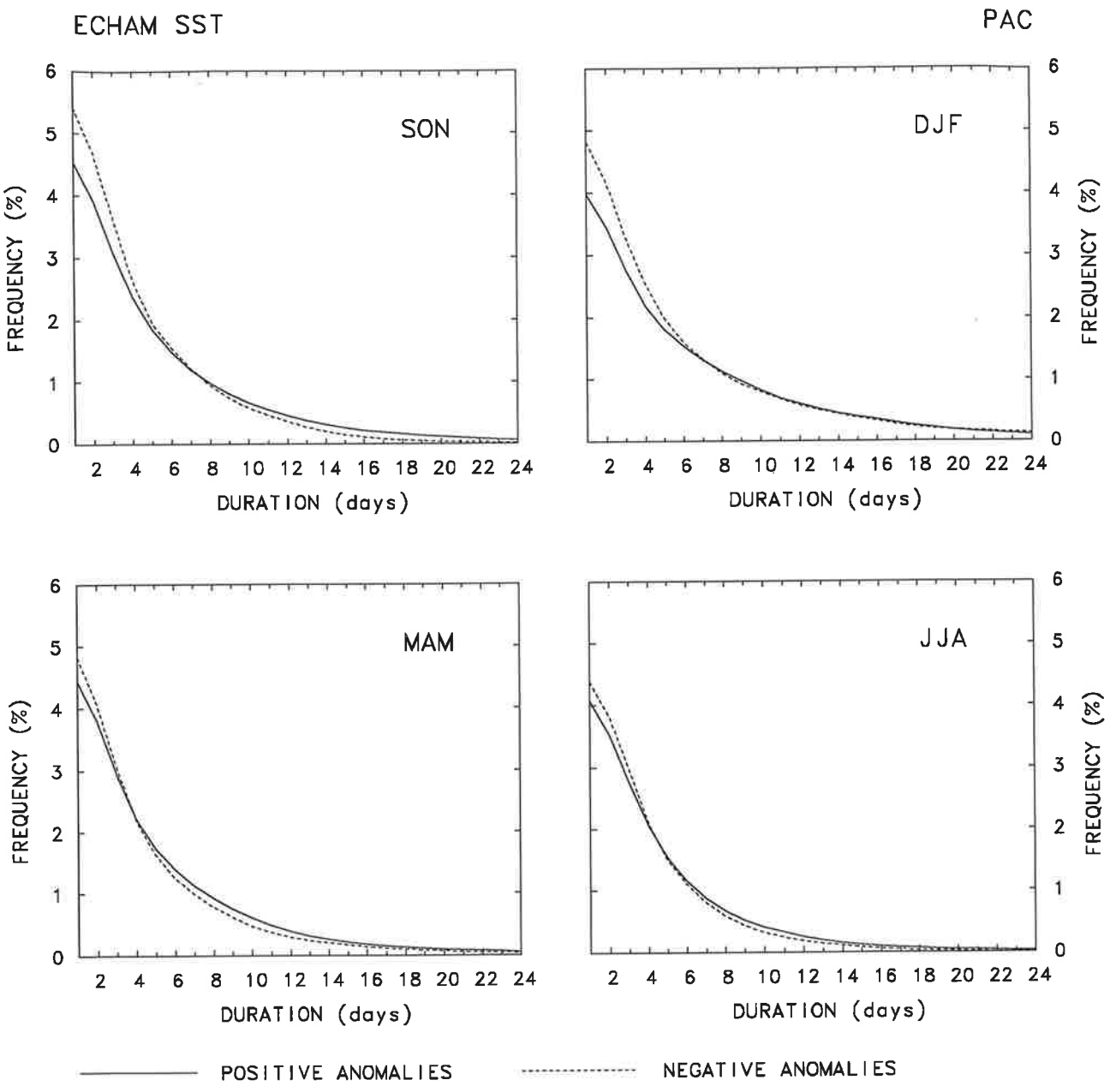

Fig. 4.2.16. As Fig. 4.2.13 but for the simulations performed with ECHAM3 with varying Sea Surface Temperatures as boundary forcing.

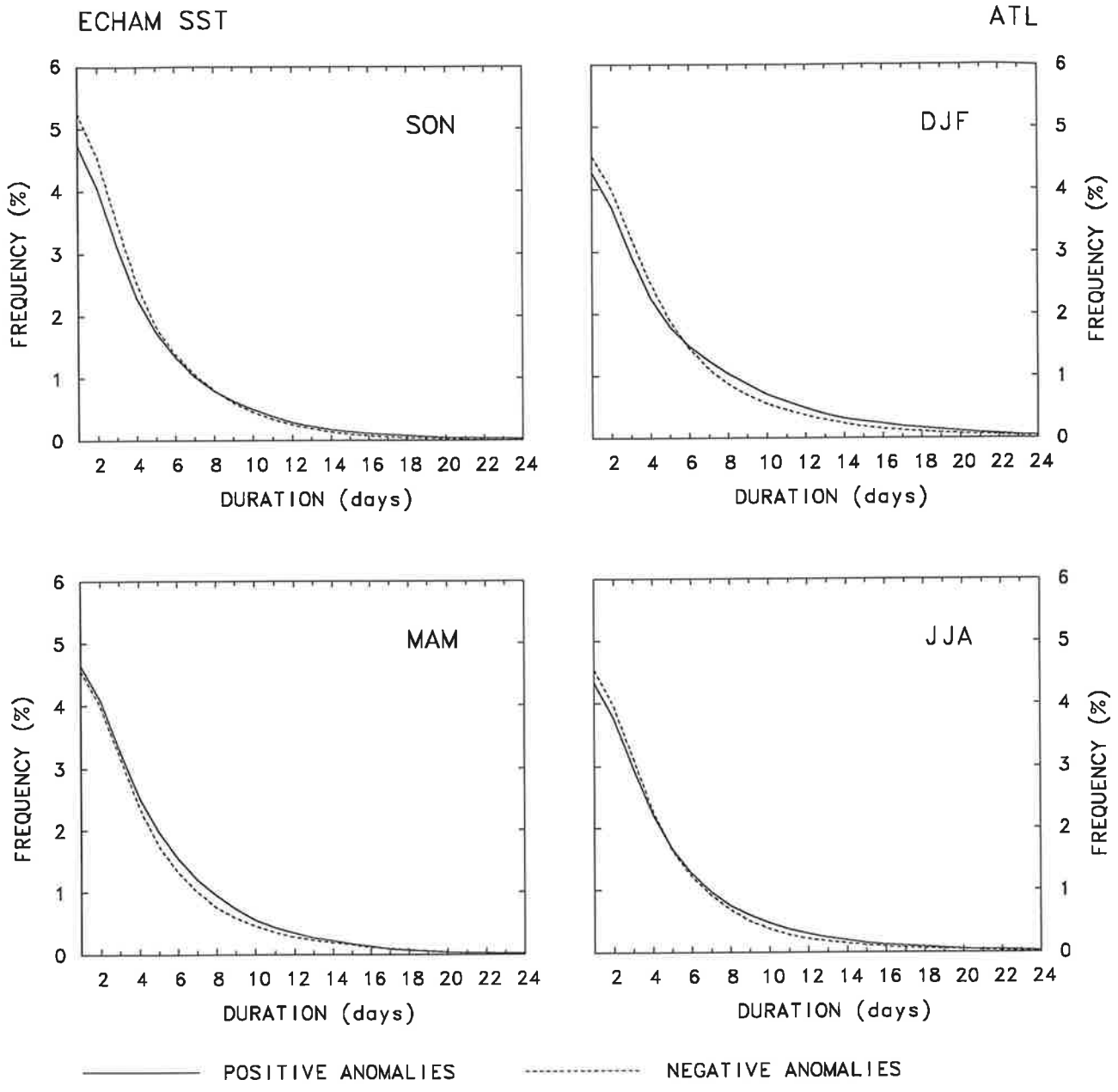

Fig. 4.2.17. As Fig. 4.2.16 but for the Atlantic region.

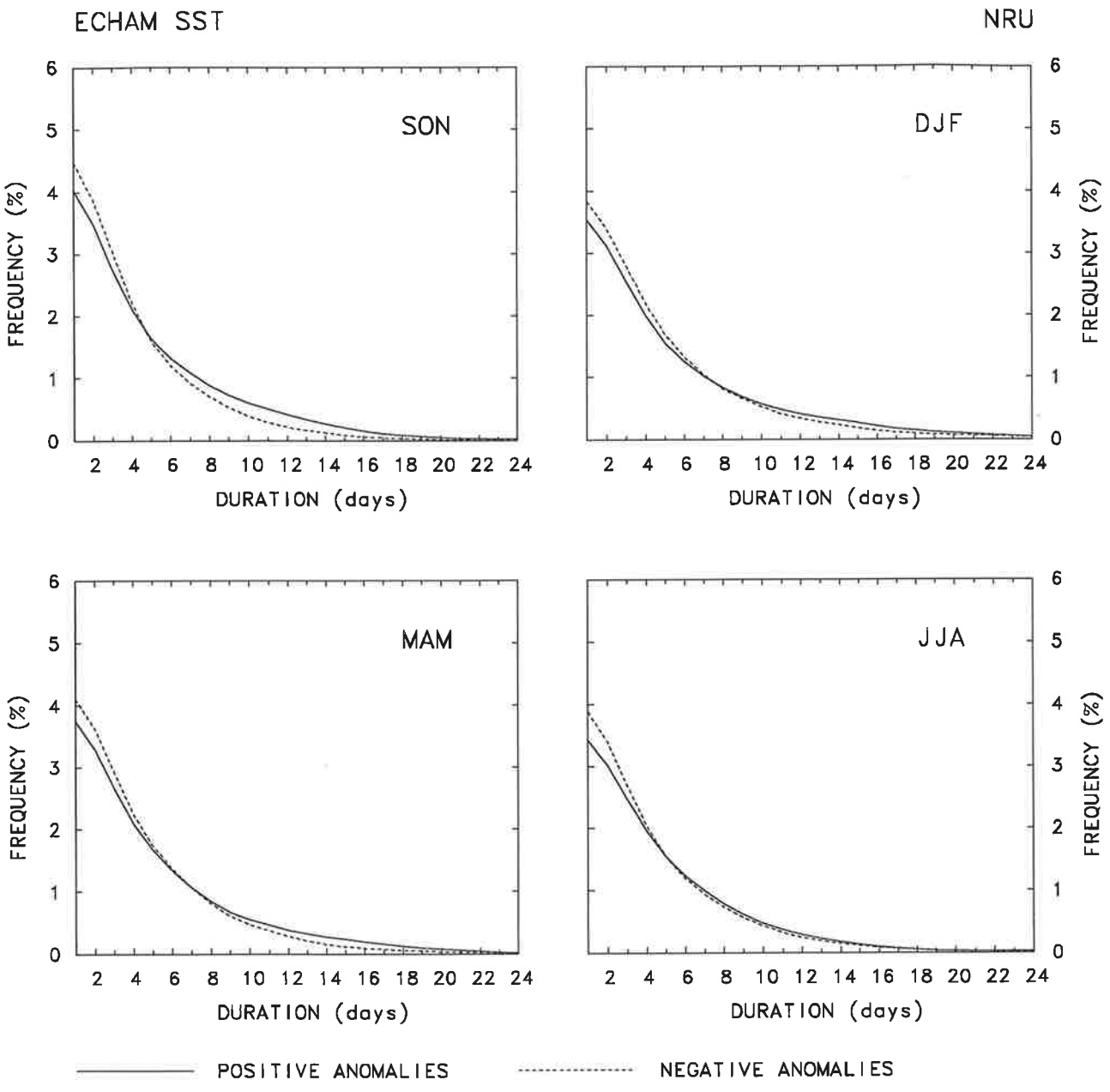

Fig. 4.2.18. As Fig. 4.2.16 but for northern Russia.

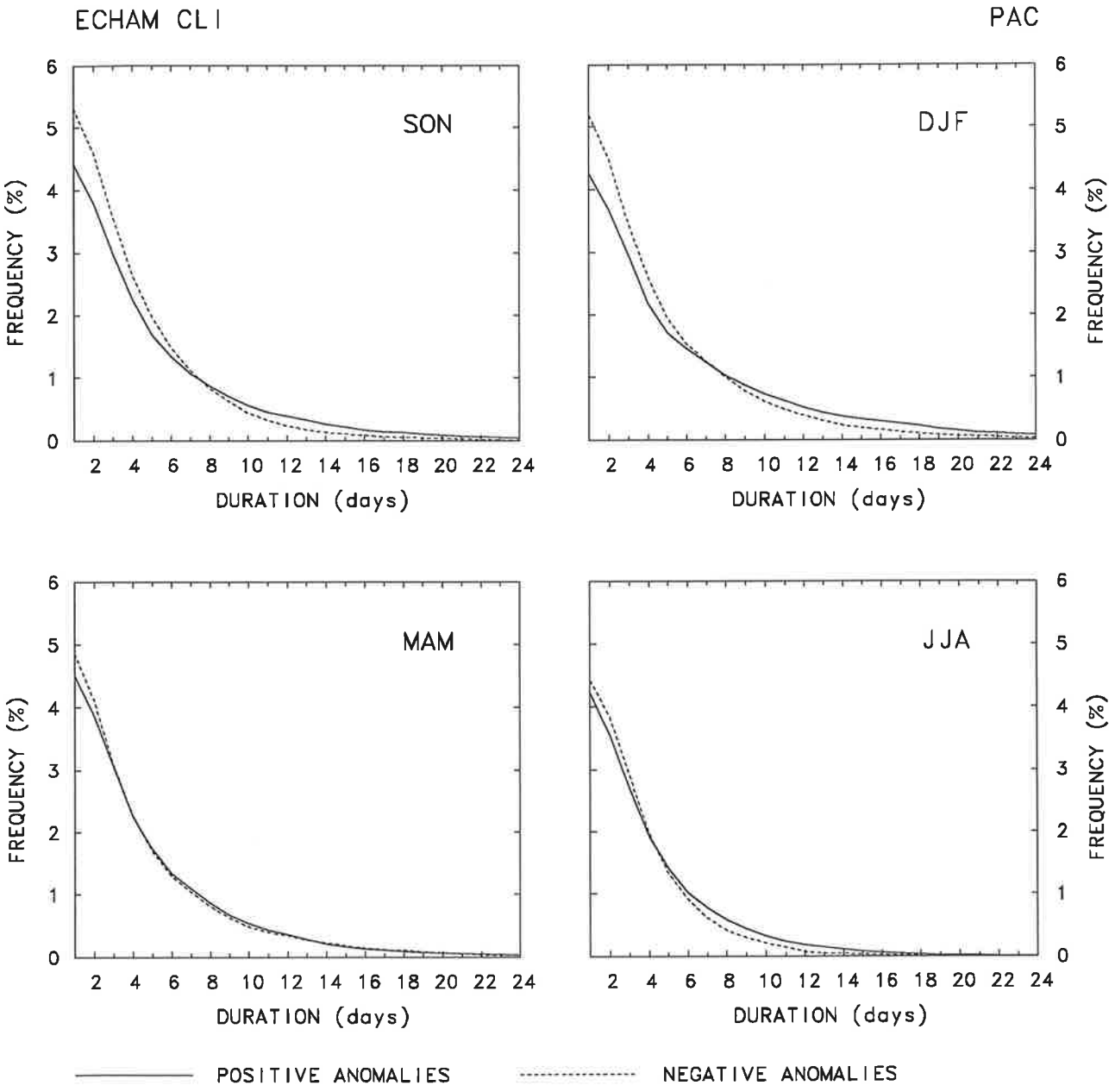

Fig. 4.2.19. As Fig. 4.2.13 but for the simulations performed with ECHAM3 with fixed Sea Surface Temperatures as boundary forcing.

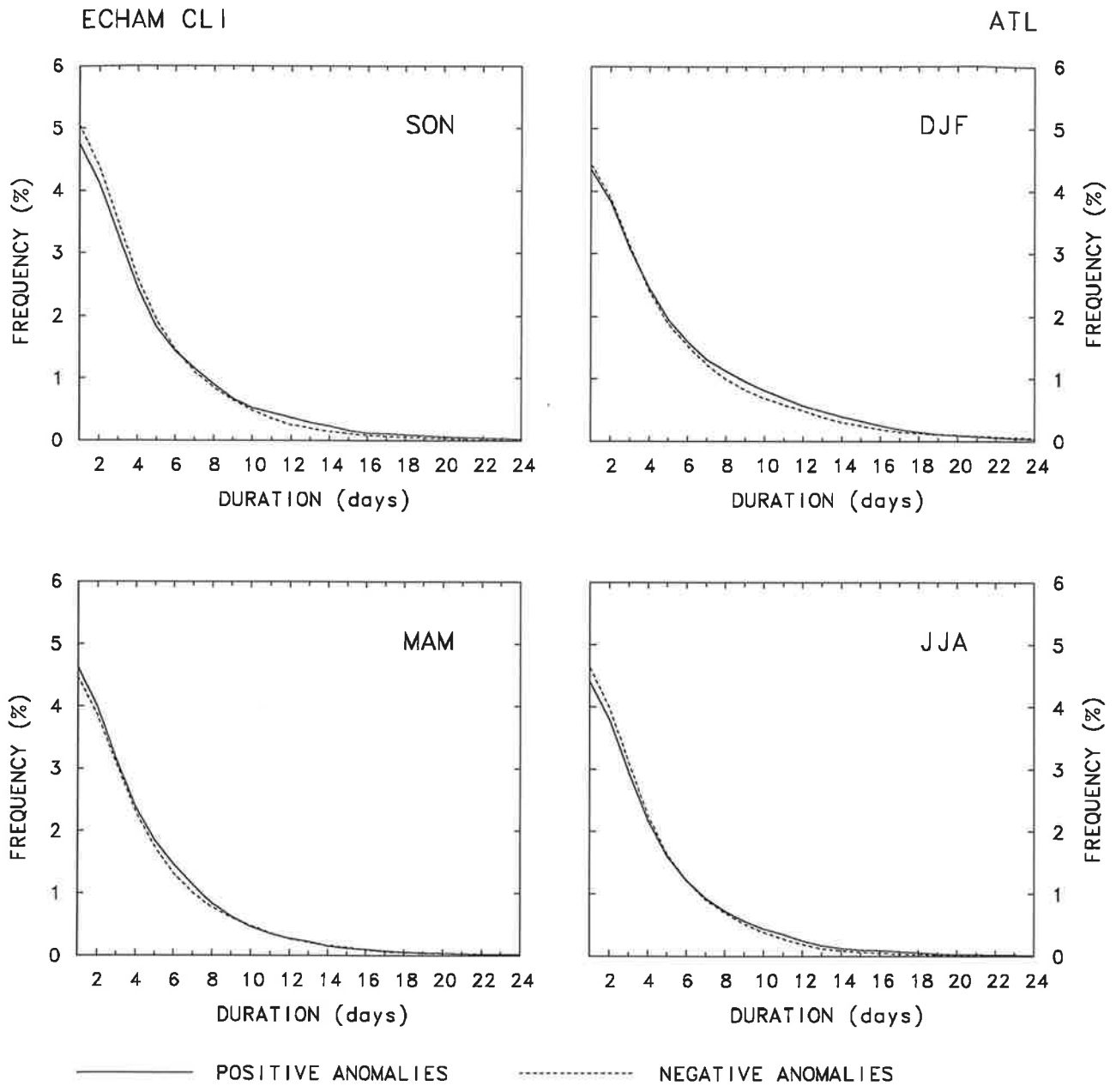

Fig. 4.2.20. As Fig. 4.2.19 but for the Atlantic region.

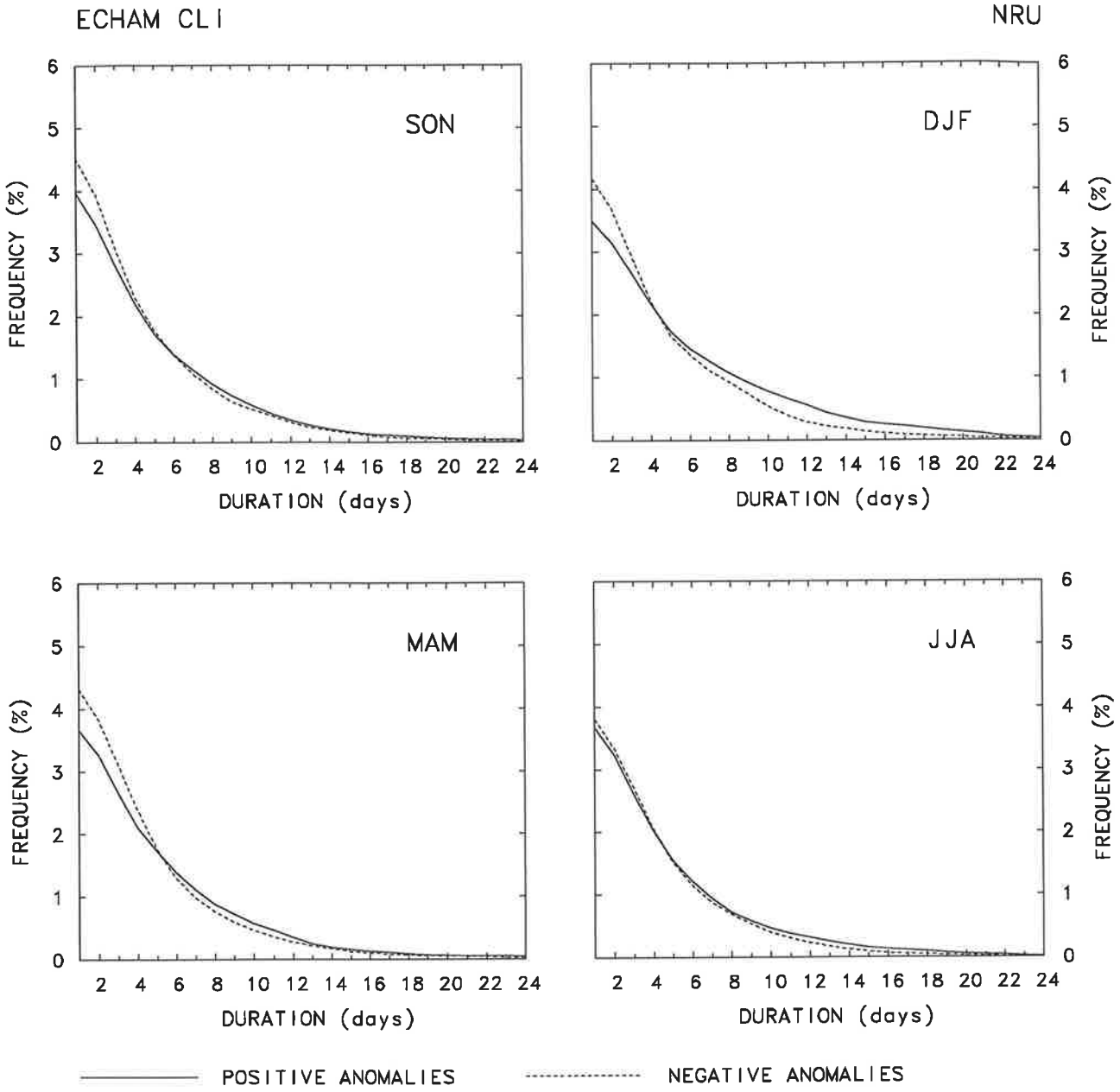

Fig. 4.2.21. As Fig. 4.2.19 but for northern Russia.

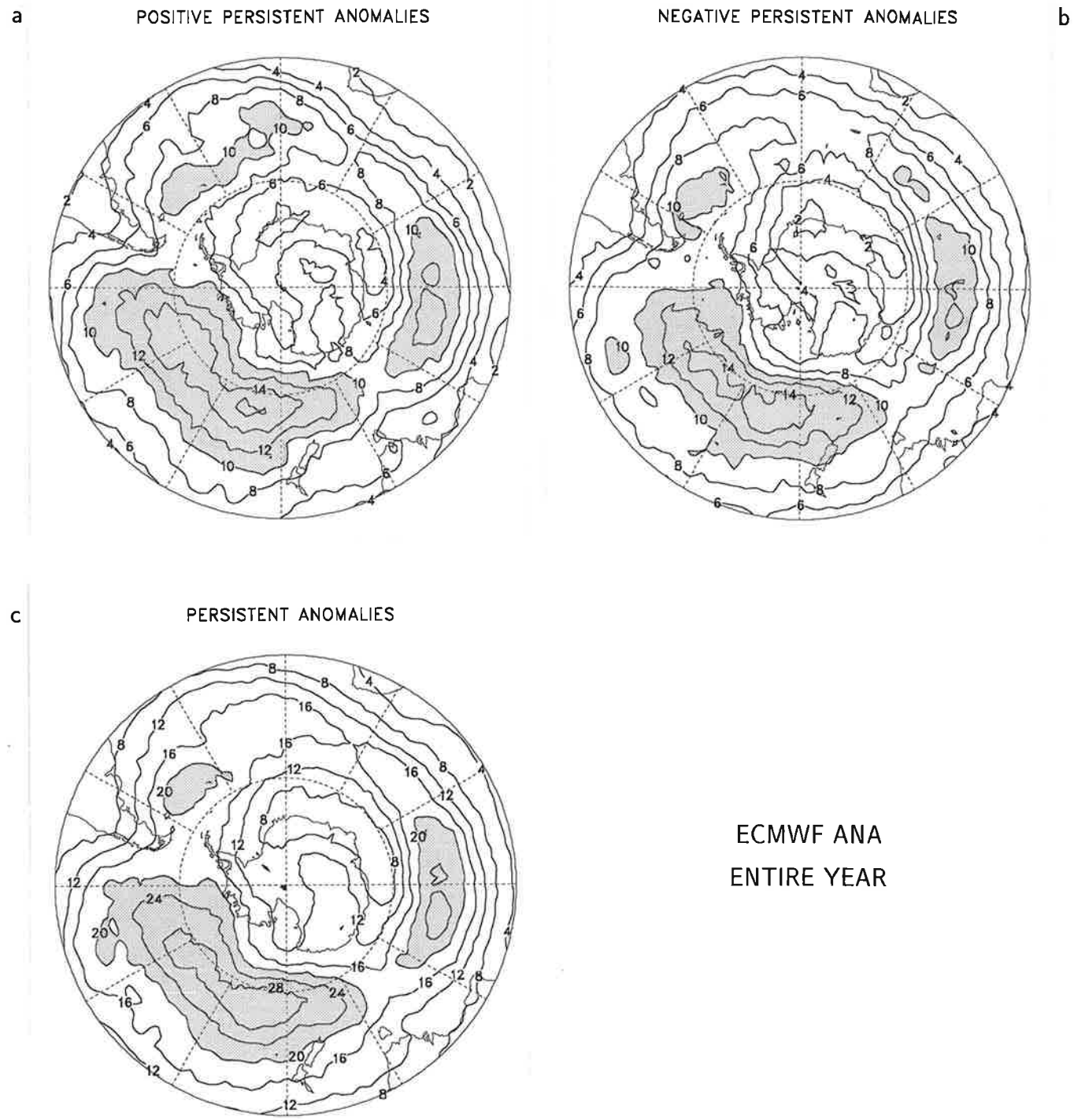

Fig. 4.2.22. Relative occurrence of persistent anomalies in the 500 hPa geopotential height field obtained from the ECMWF analyses for the positive (a), the negative (b) and the sum of postive and negative (c) persistent anomalies. Units are %, the contour interval is 2% for the positive and negative persistent anomalies, 4% for the sum of positive and negative persistent anomalies. Values higher than 10% and higher than 20%, respectively, are indicated by stippling.

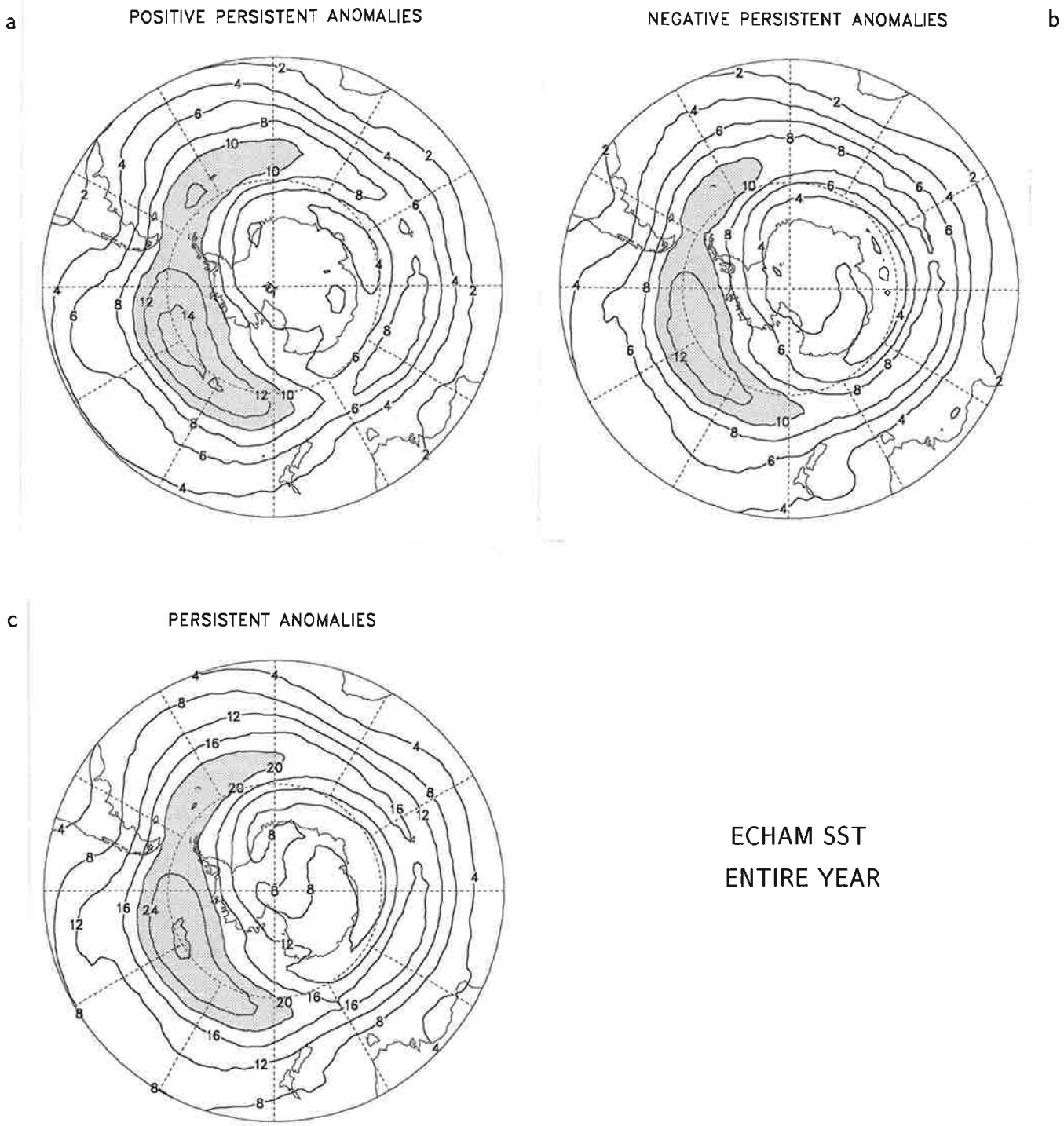

Fig. 4.2.23. As Fig. 4.2.22 but for the simulations performed with ECHAM3 with varying Sea Surface Temperatures as boundary forcing.

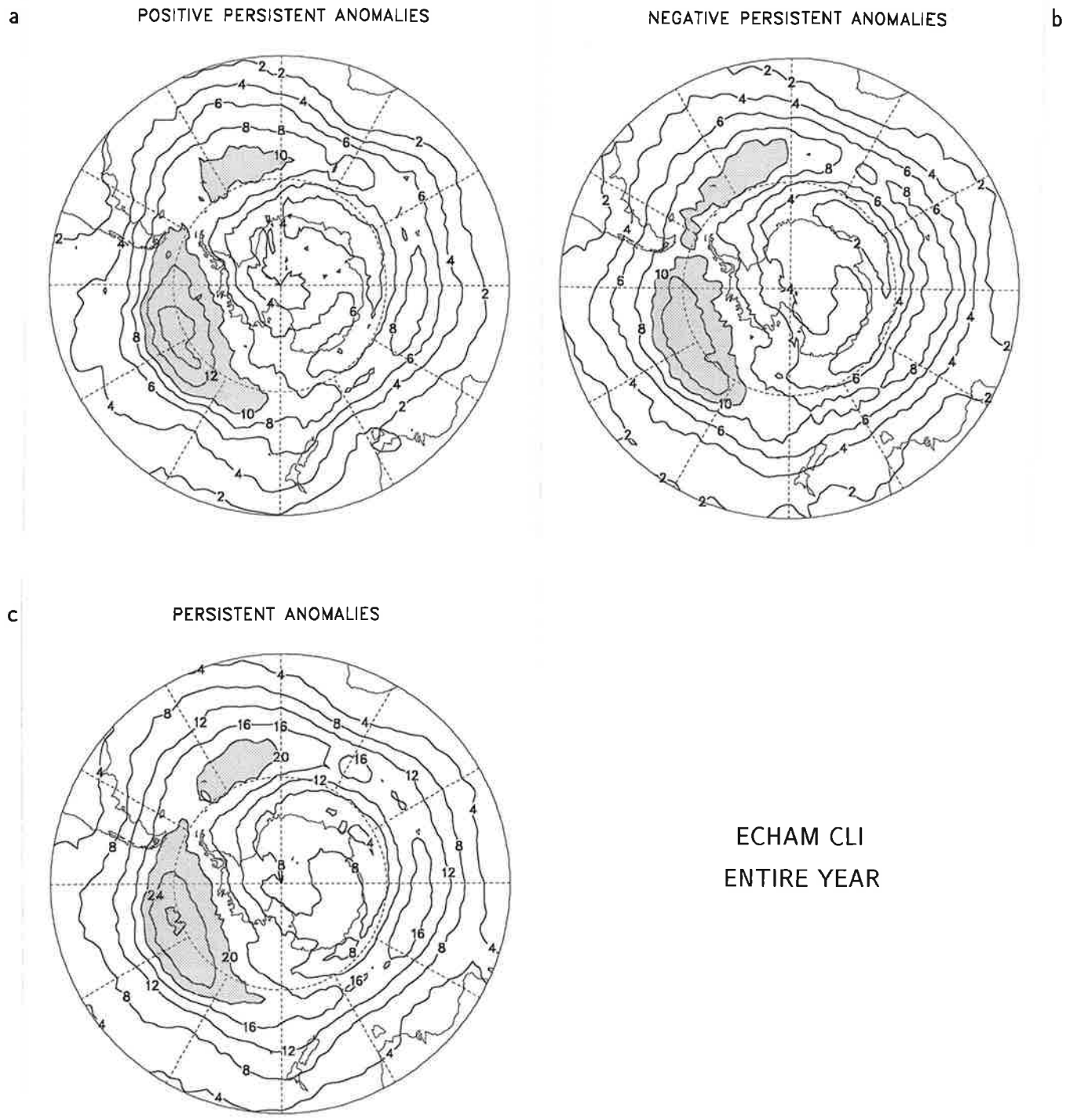

Fig. 4.2.24. As Fig. 4.2.22 but for the simulations performed with ECHAM3 with fixed Sea Surface Temperatures as boundary forcing.

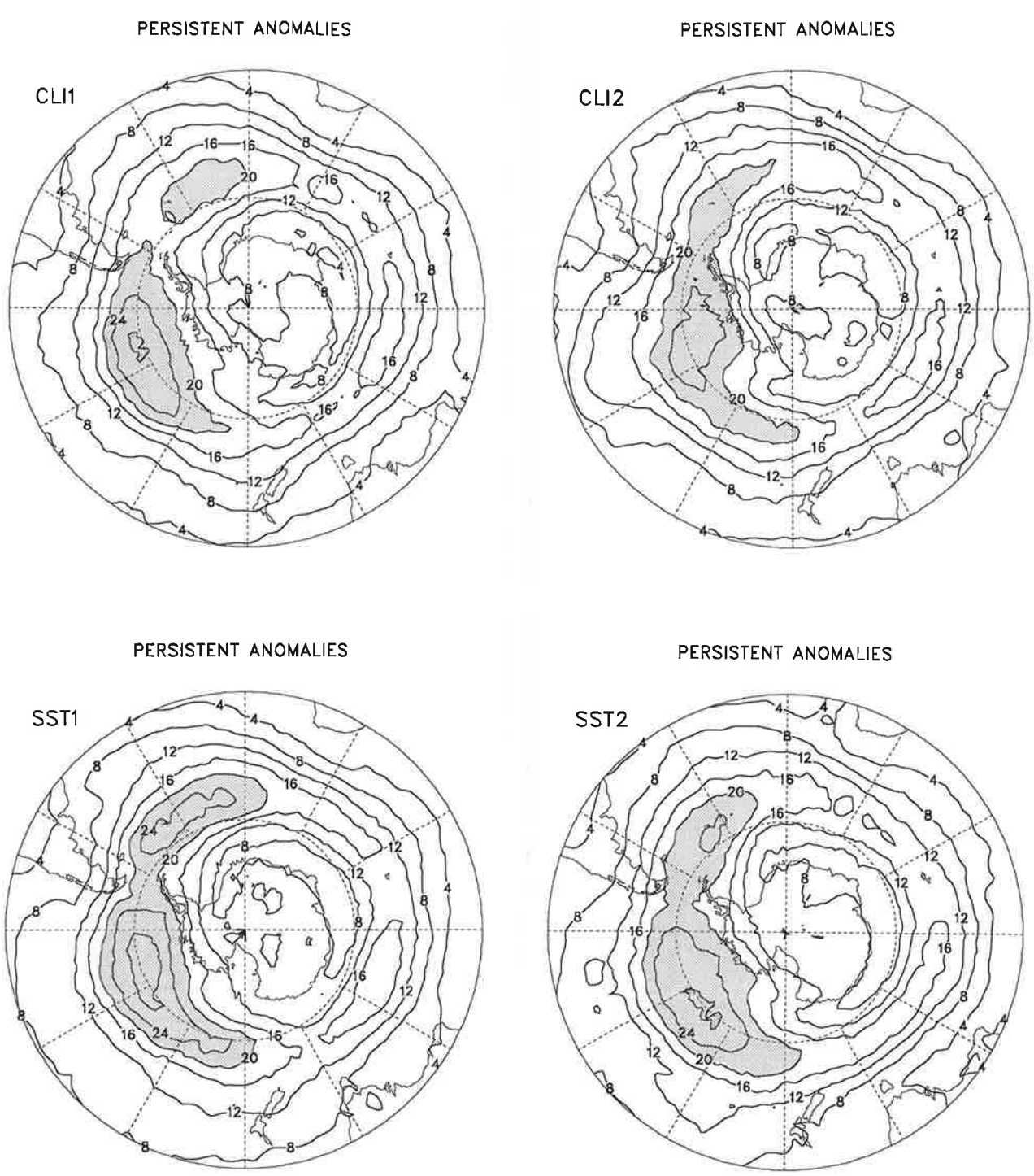

Fig. 4.2.25. Relative occurrence of persistent anomalies in the 500 hPa geopotential height field (sum of positive and negative persistent anomalies) obtained from the individual simulations performed with ECHAM3 with varying Sea Surface Temperatures (SST...) and fixed Sea Surface Temperatures (CLI...) as boundary forcing. Units are %, the contour interval is 4%. Values higher than 20% are indicated by stippling.

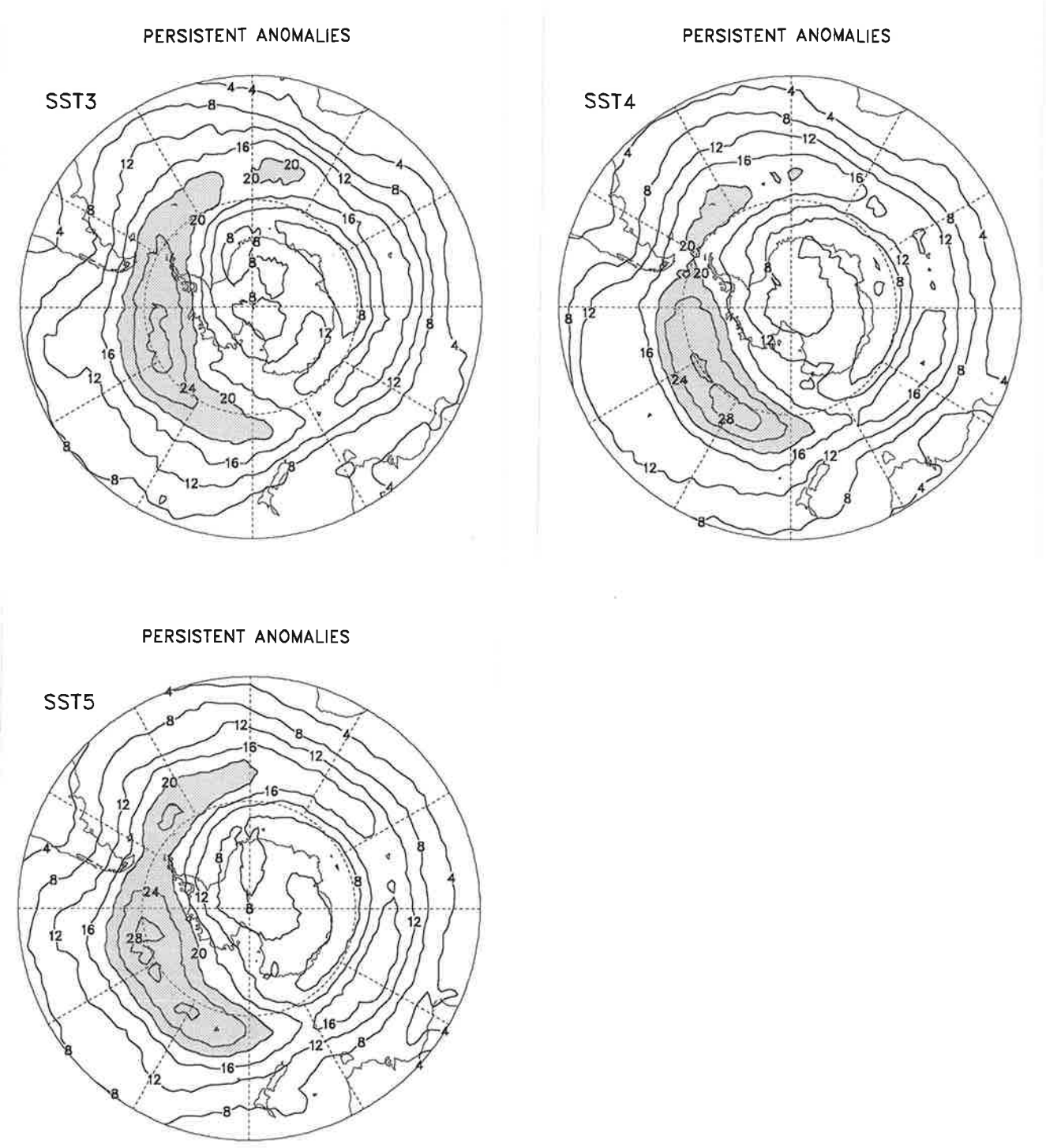

Fig. 4.2.25. Relative occurrence of persistent anomalies in the 500 hPa geopotential height field (sum of positive and negative persistent anomalies) obtained from the individual simulations performed with ECHAM3 with varying Sea Surface Temperatures (SST...) and fixed Sea Surface Temperatures (CLI...) as boundary forcing. Units are %, the contour interval is 4%. Values higher than 20% are indicated by stippling.

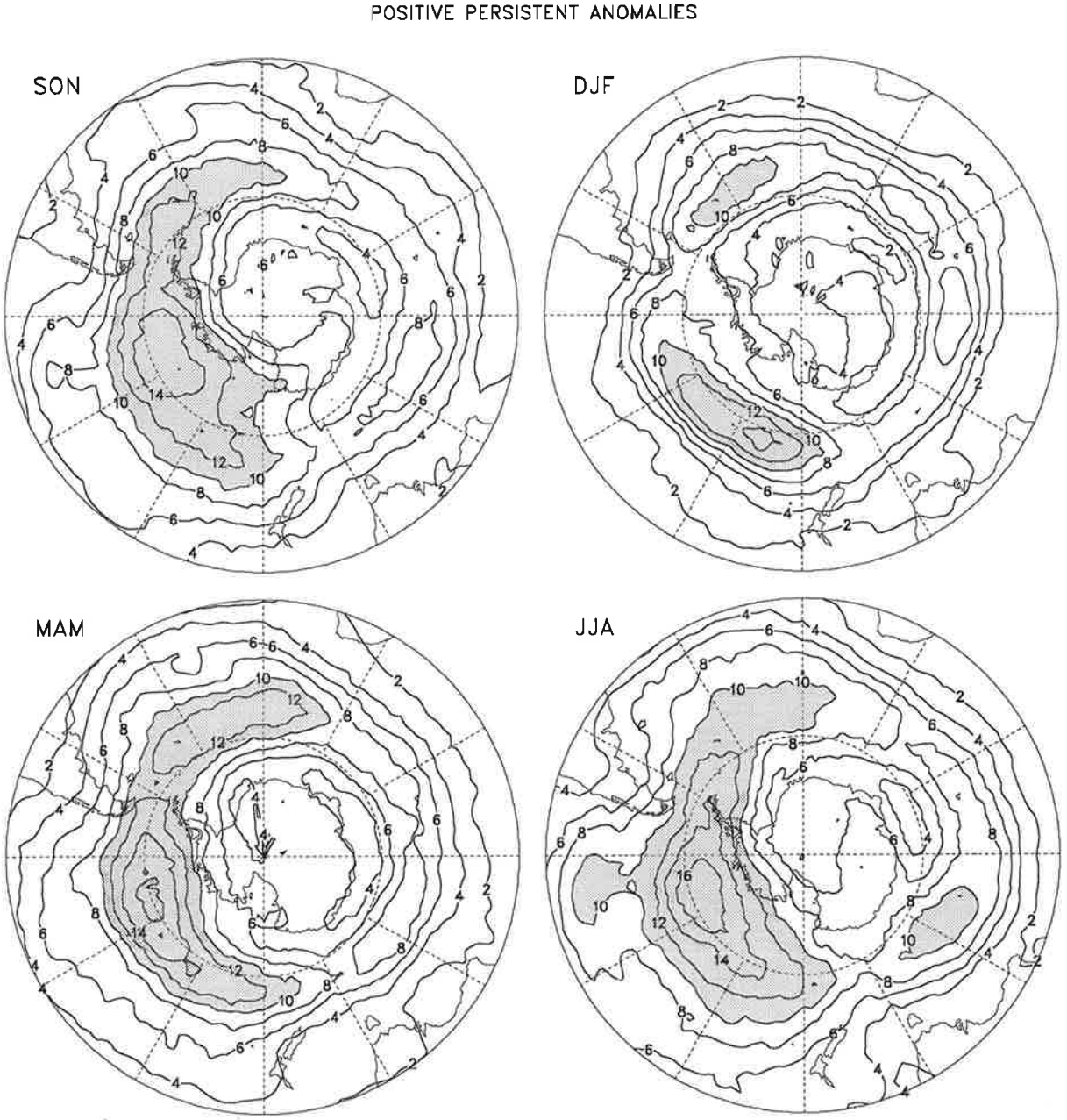

Fig. 4.2.26. Relative occurrence of positive persistent anomalies in the 500 hPa geopotential height field obtained from the simulations with varying Sea Surface Temperatures distinguishing between seasons. Units are %, the contour interval is 2%. Values higher than 10% are indicated by stippling.

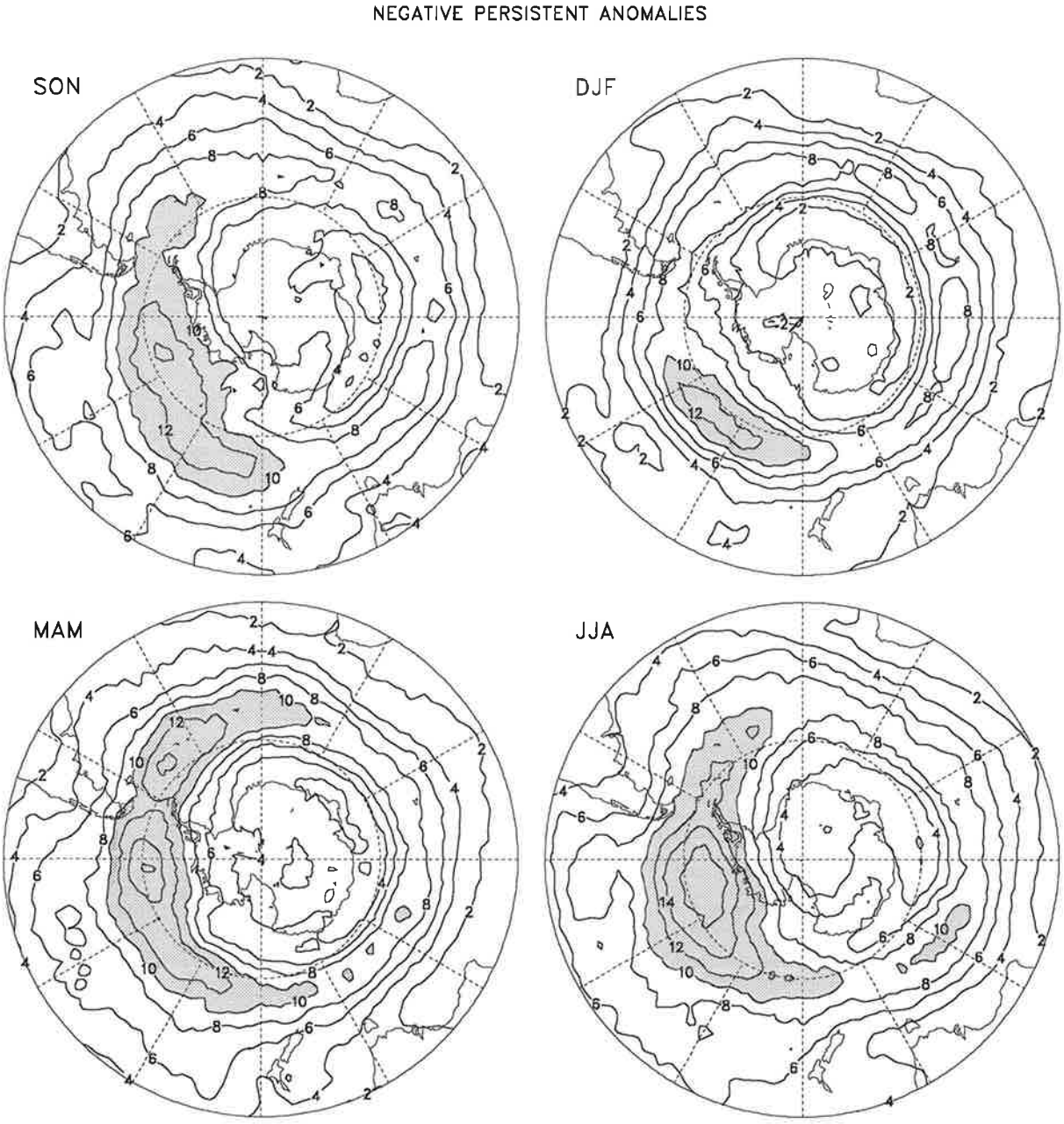

Fig. 4.2.27. As Fig. 4.2.26 but for the negative persistent anomalies.

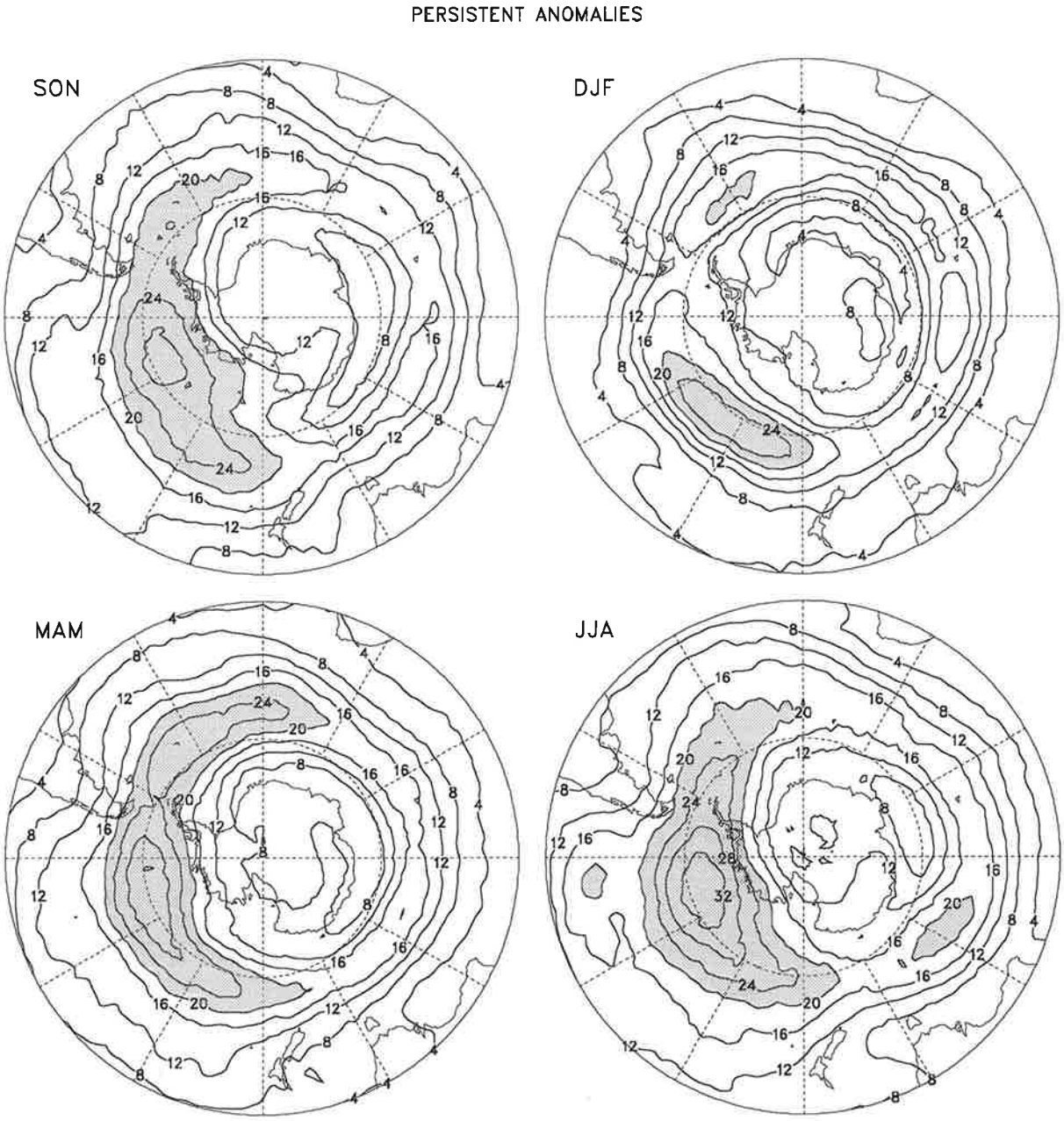

Fig. 4.2.28. As Fig. 4.2.26 but for the sum of positive and negative persistent anomalies. The contour interval is 4%, values higher than 20% are indicated by stippling.

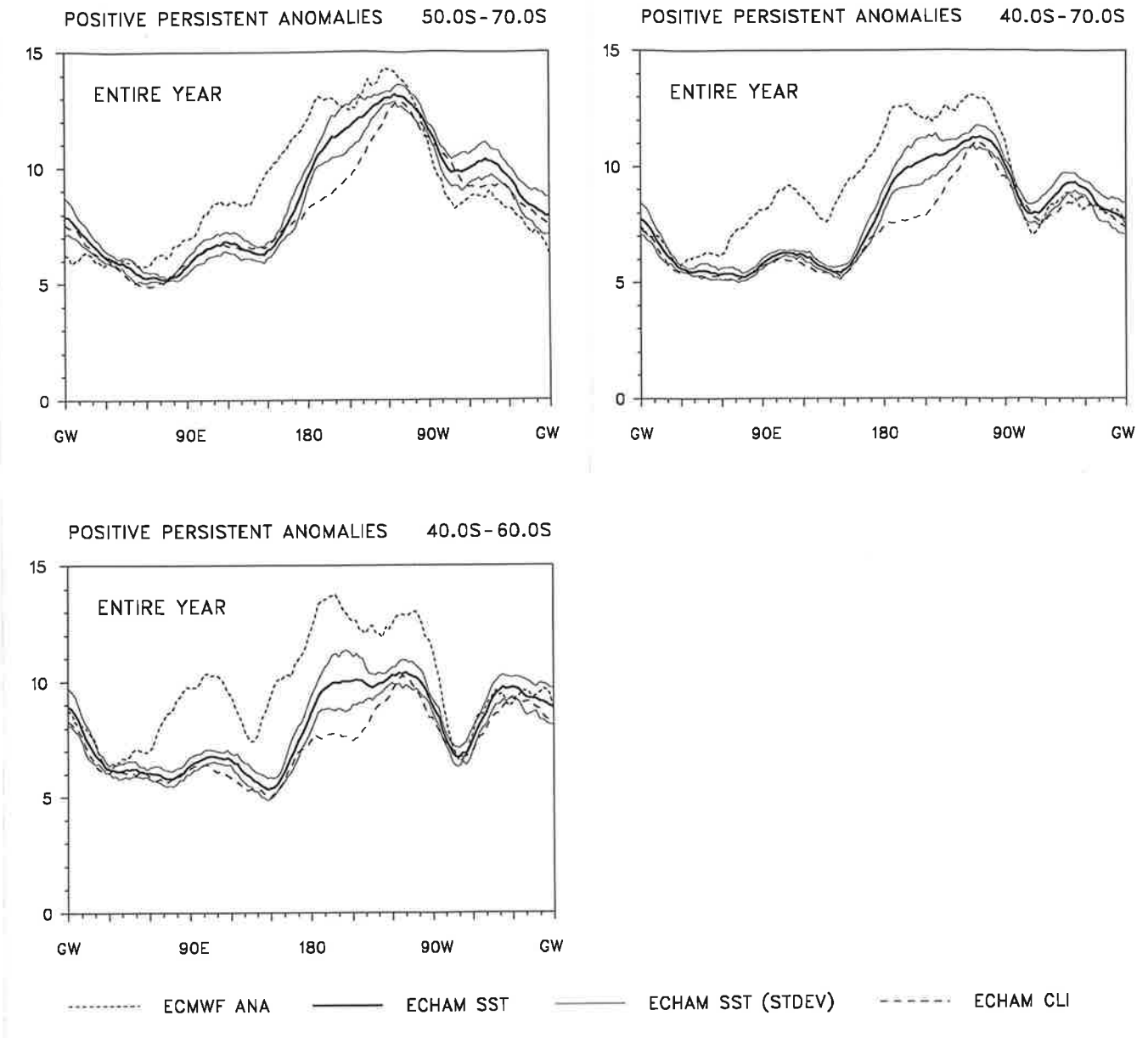

Fig. 4.2.29. Relative occurrence of positive persistent anomalies in the 500 hPa geopotential height field obtained from the the ECMWF analyses and the two sets of simulations performed with ECHAM3 as a function of longitude for different zones. The mean value obtained from the simulations with varying Sea Surface Temperatures is given by the heavy solid line, the light solid lines represent this mean value with the standard deviation of the five individual simulations added and subtracted, respectively. The mean value obtained from the simulations with fixed Sea Surface Temperatures is indicated by long dashes, that derived from the analyses by short dashes. Units are %.

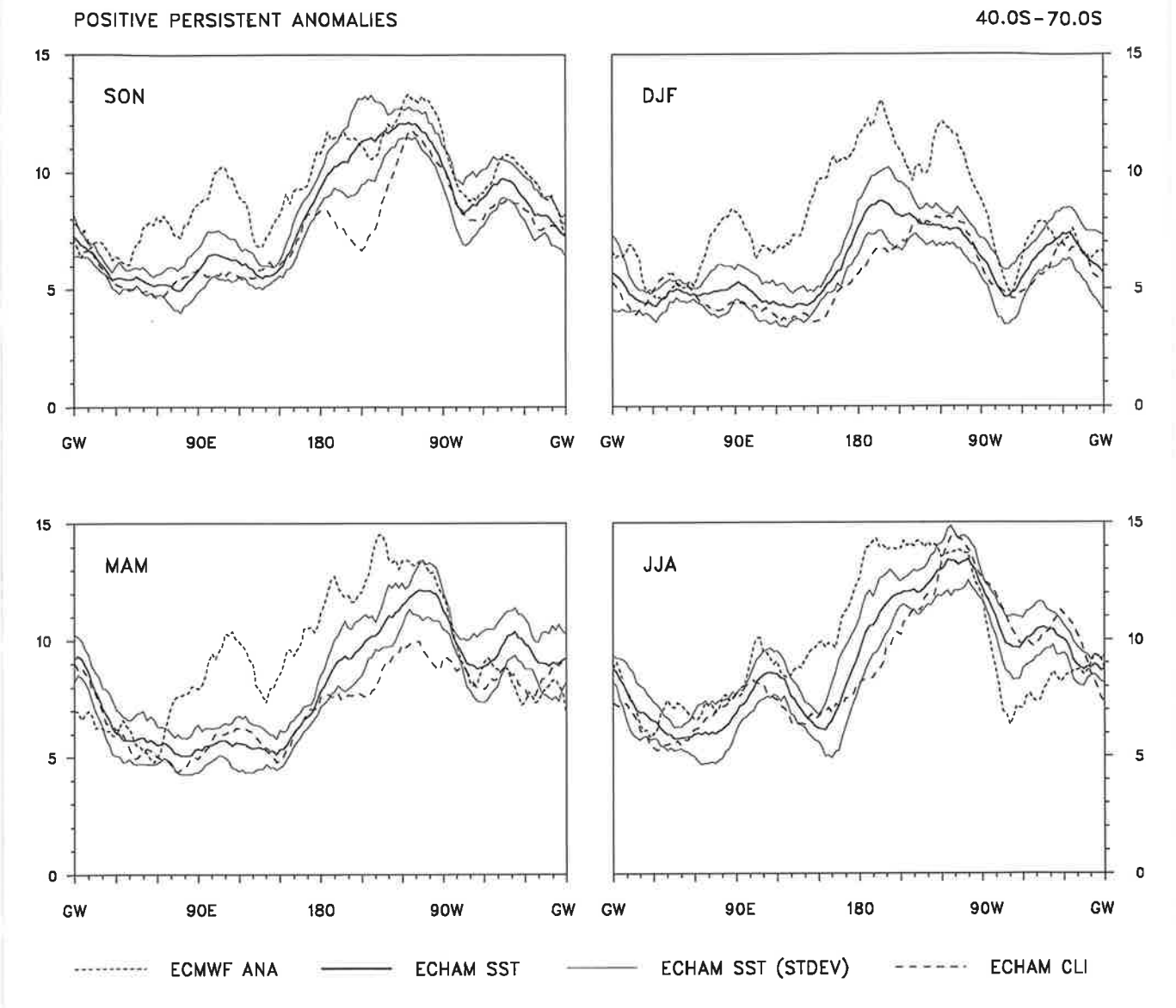

Fig. 4.2.30. As Fig. 4.2.29 for the zone beteeen 40° and 70°S distinguishing between seasons.

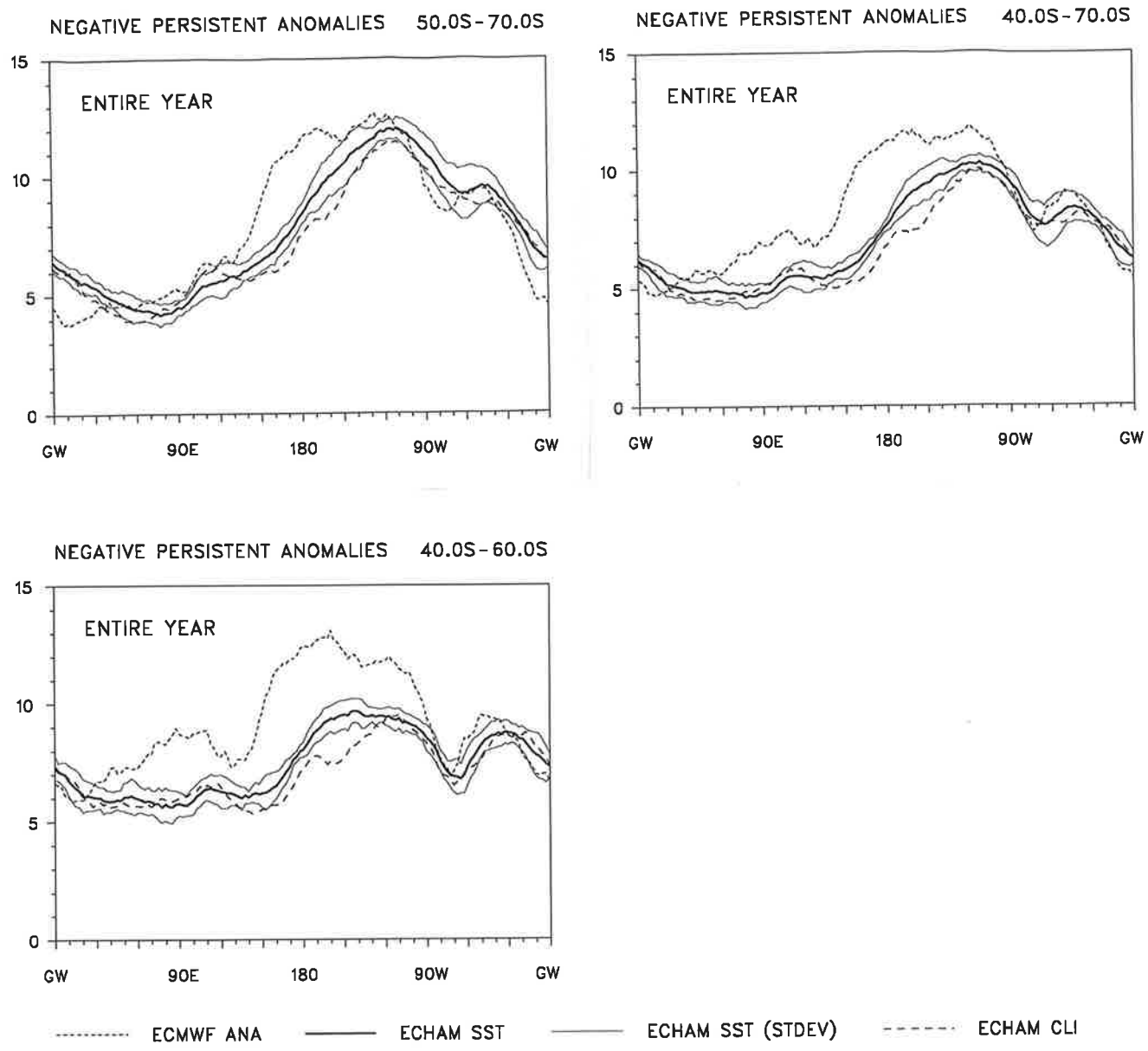

Fig. 4.2.31. As Fig. 4.2.29 but for the negative persistent anomalies.

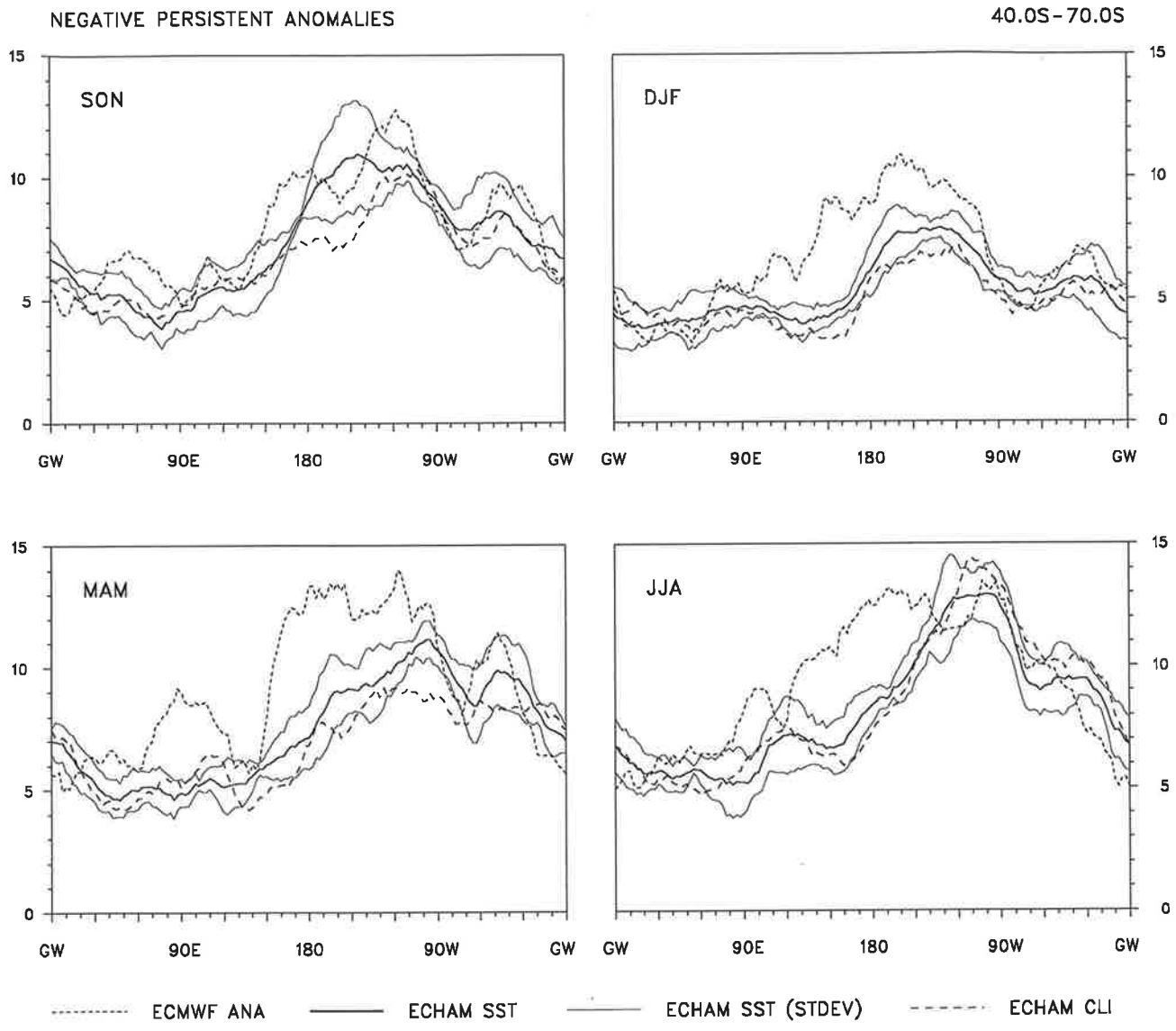

Fig. 4.2.32. As Fig. 4.2.31 for the zone beteeen 40° and 70°S distinguishing between seasons.

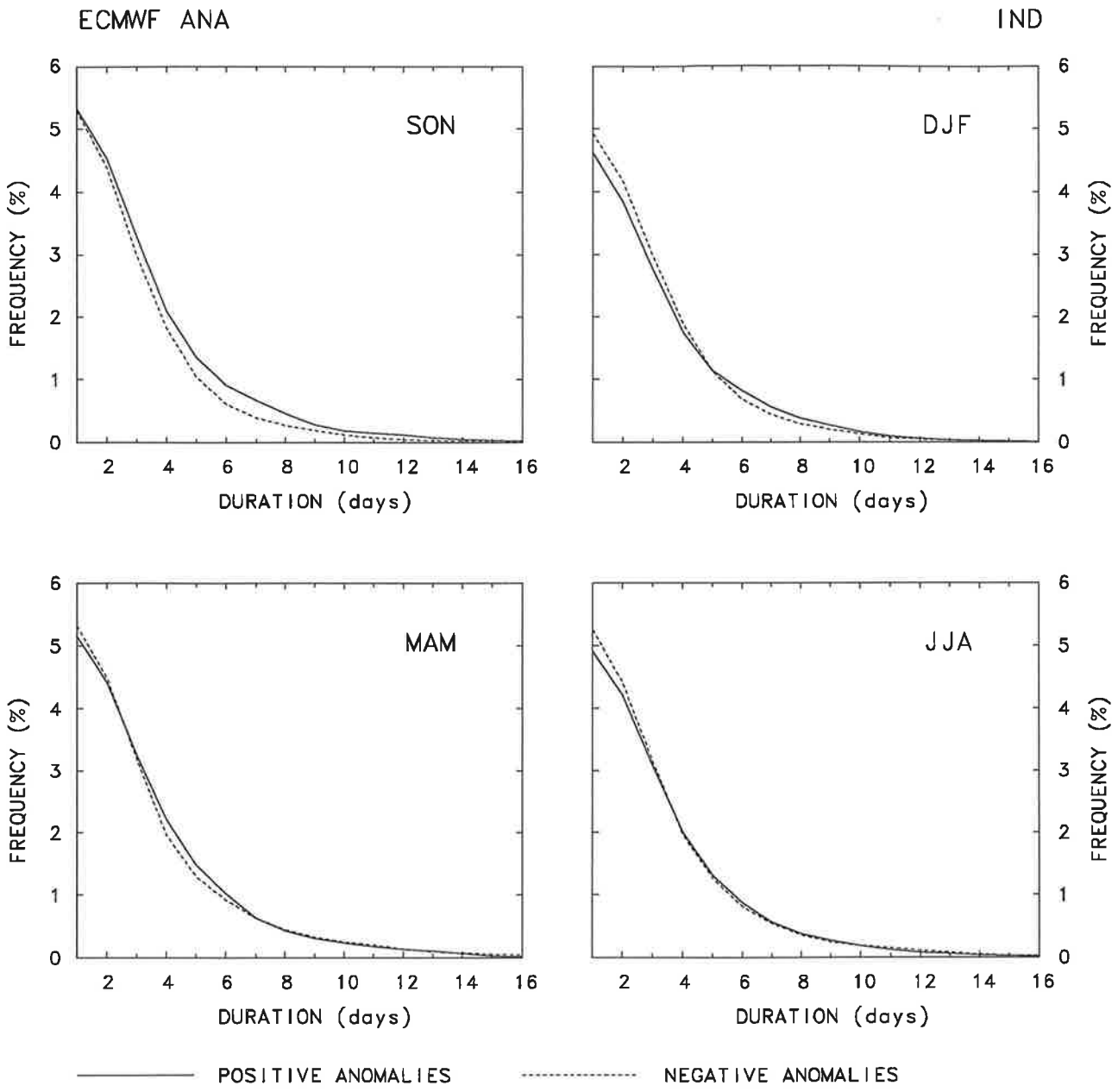

Fig. 4.2.33. Relative occurrence of anomalies in the 500 hPa geopotential height field obtained from the the ECMWF analyses as a function of their lifetime for the Indian Ocean (see text for details) distinguishing between seasons. The solid line represents the positive and the dashed line the negative anomalies.

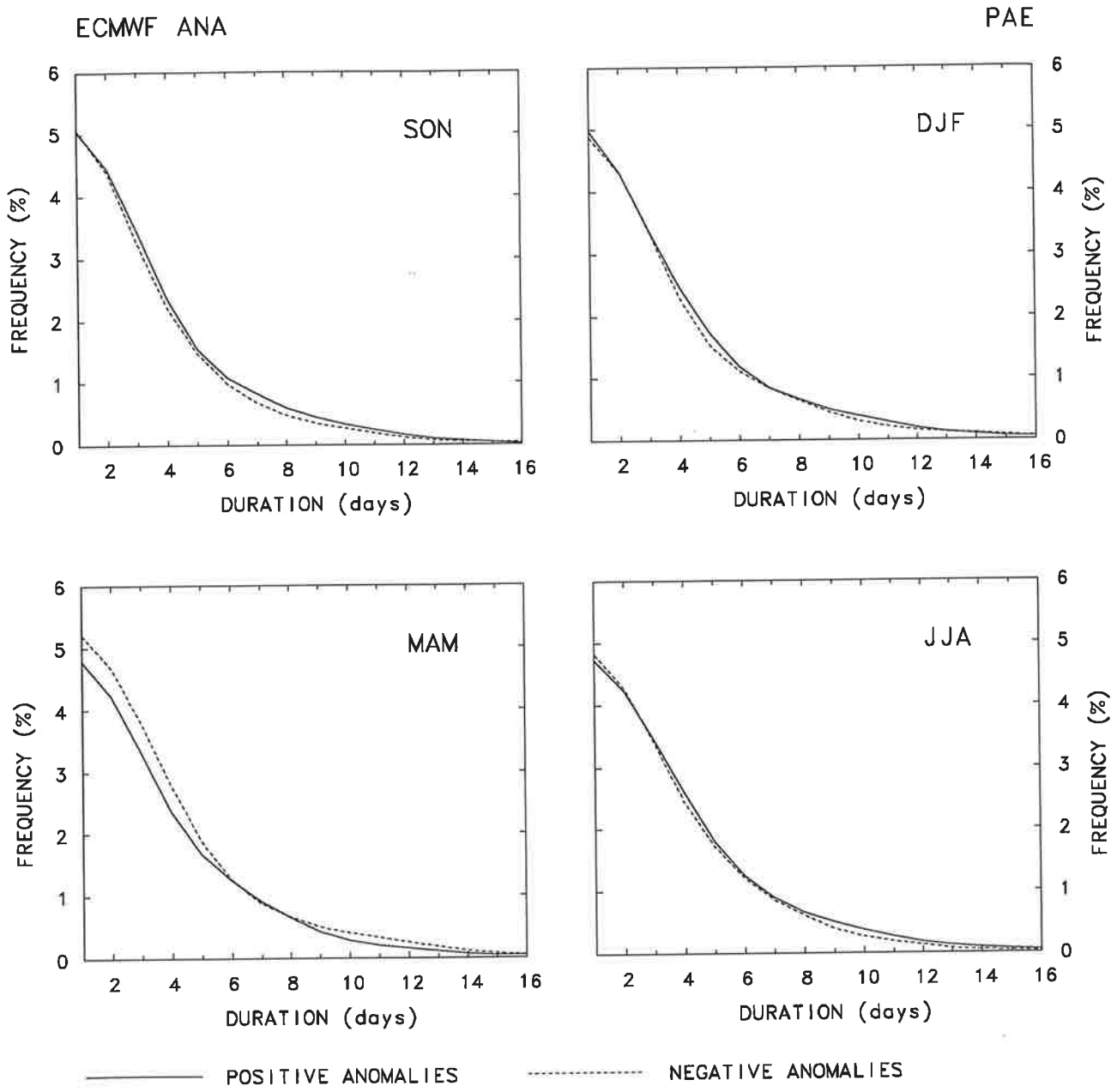

Fig. 4.2.34. As Fig. 4.2.33 but for the eastern Pacific Ocean.

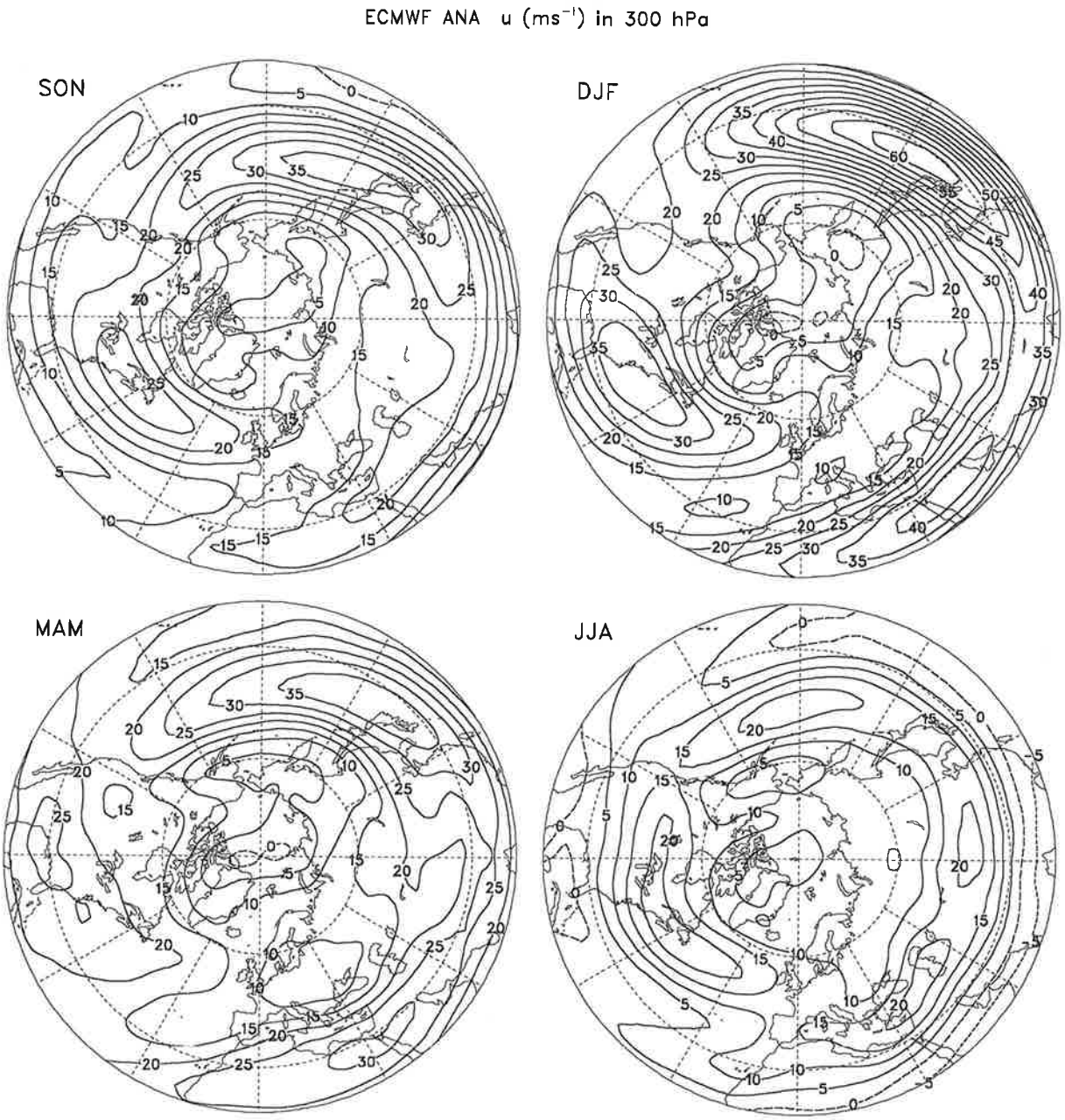

Fig. 4.3.1. Climatological mean zonal wind component at 300 hPa obtained from the ECMWF analyses distinguishing between seasons. Positive values (solid contour lines) indicate westerly, negative ones (dashed contour lines) indicate easterly winds. Units are m/s, the contour interval is 5 m/s.

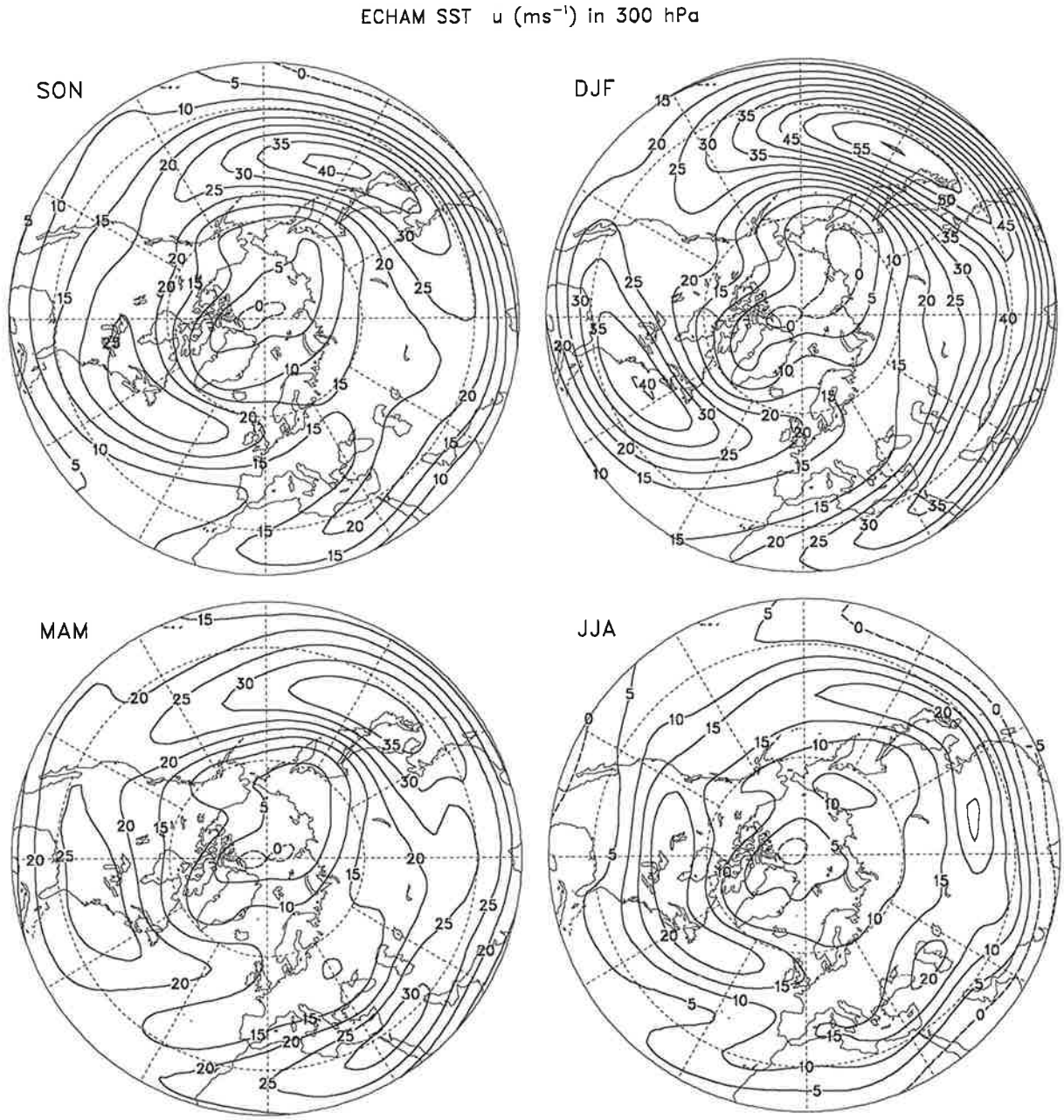

Fig. 4.3.2. As Fig. 4.3.1 but for the simulations performed with ECHAM3 with varying Sea Surface Temperatures as boundary forcing.

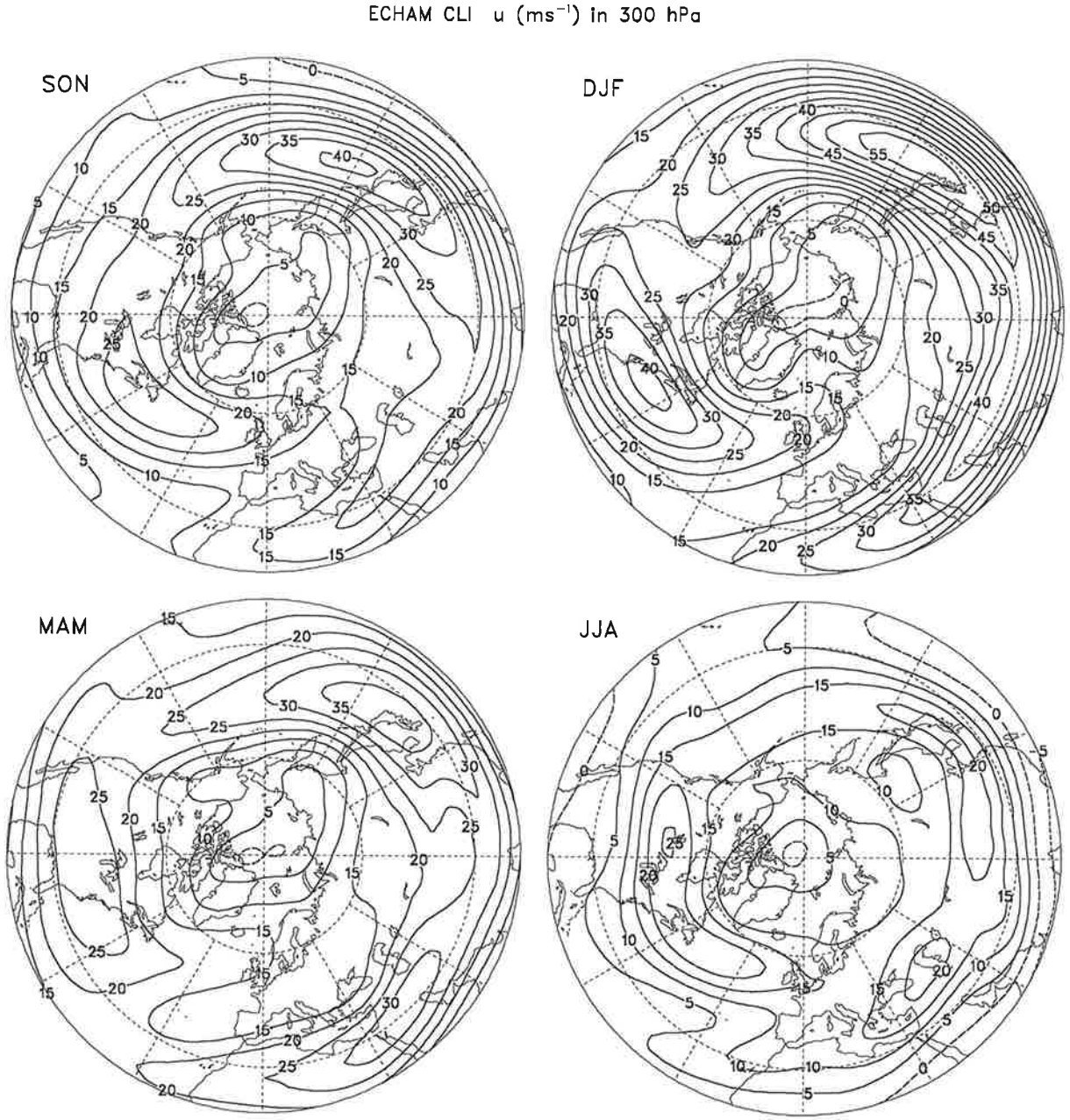

Fig. 4.3.3. As Fig. 4.3.1 but for the simulations performed with ECHAM3 with fixed Sea Surface Temperatures as boundary forcing.

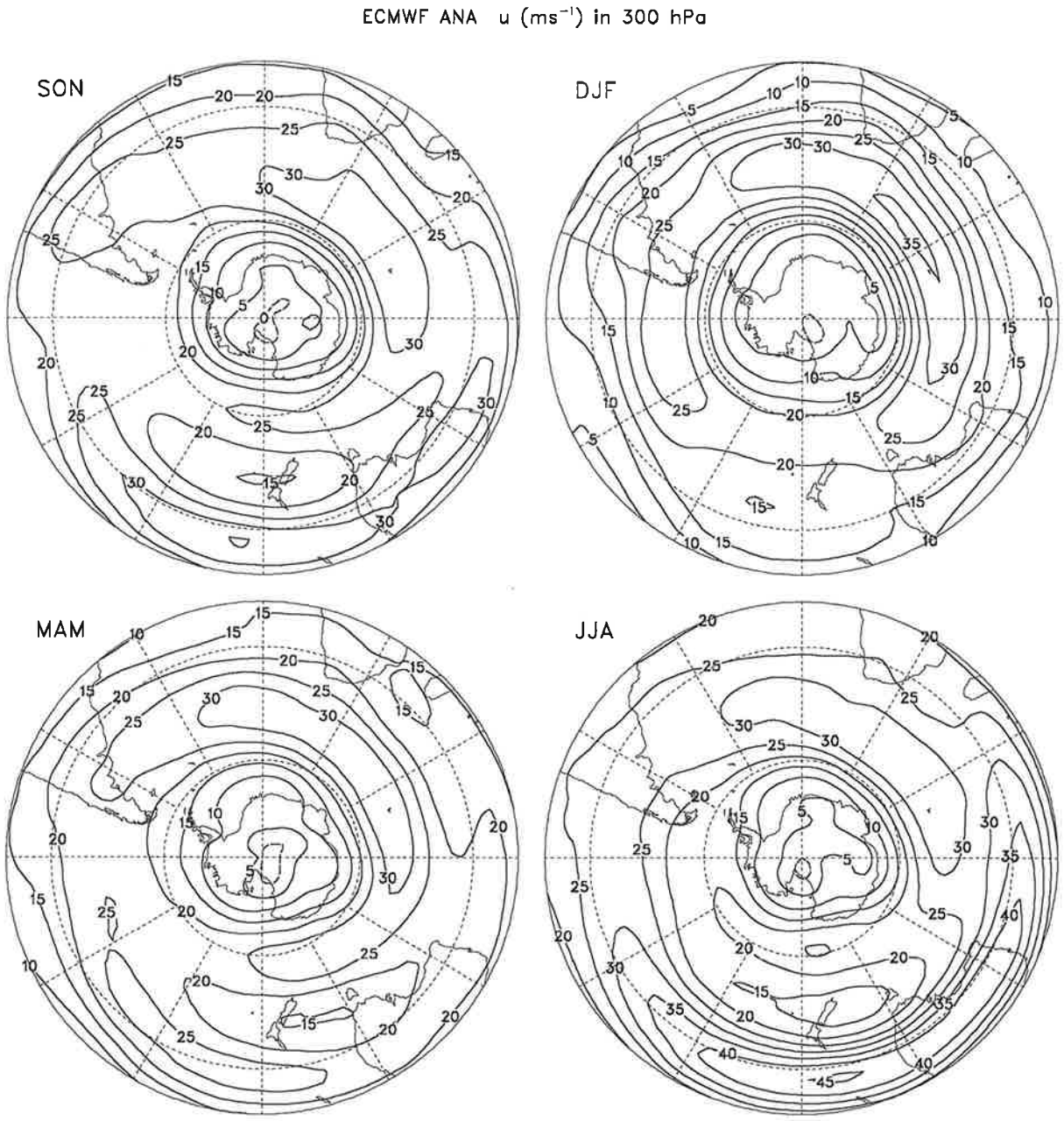

Fig. 4.3.4. Climatological mean zonal wind component at 300 hPa obtained from the ECMWF analyses distinguishing between seasons. Positive values (solid contour lines) indicate westerly, negative ones (dashed contour lines) indicate easterly winds. Units are m/s, the contour interval is 5 m/s.

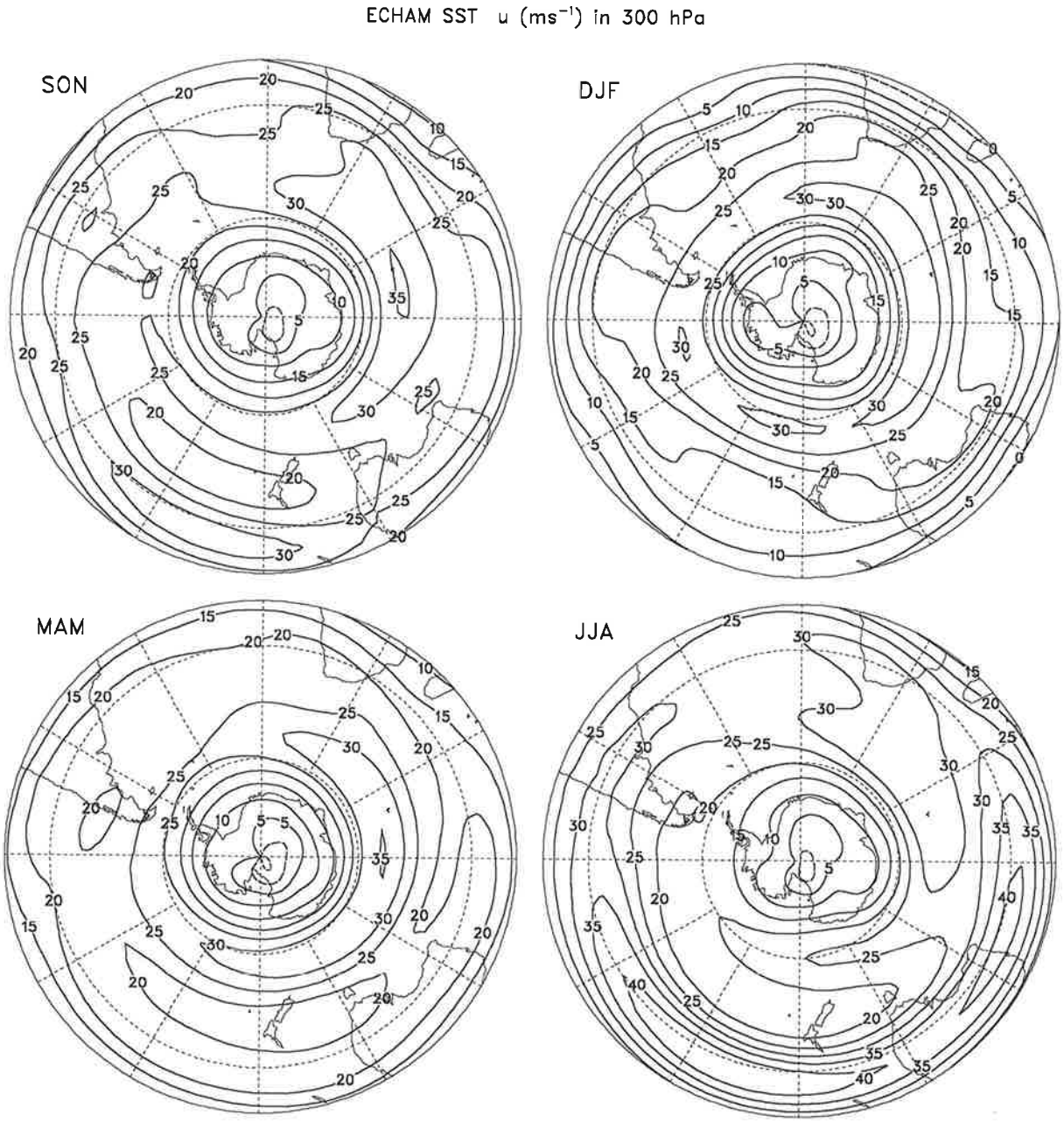

Fig. 4.3.5. As Fig. 4.3.4 but for the simulations performed with ECHAM3 with varying Sea Surface Temperatures as boundary forcing.

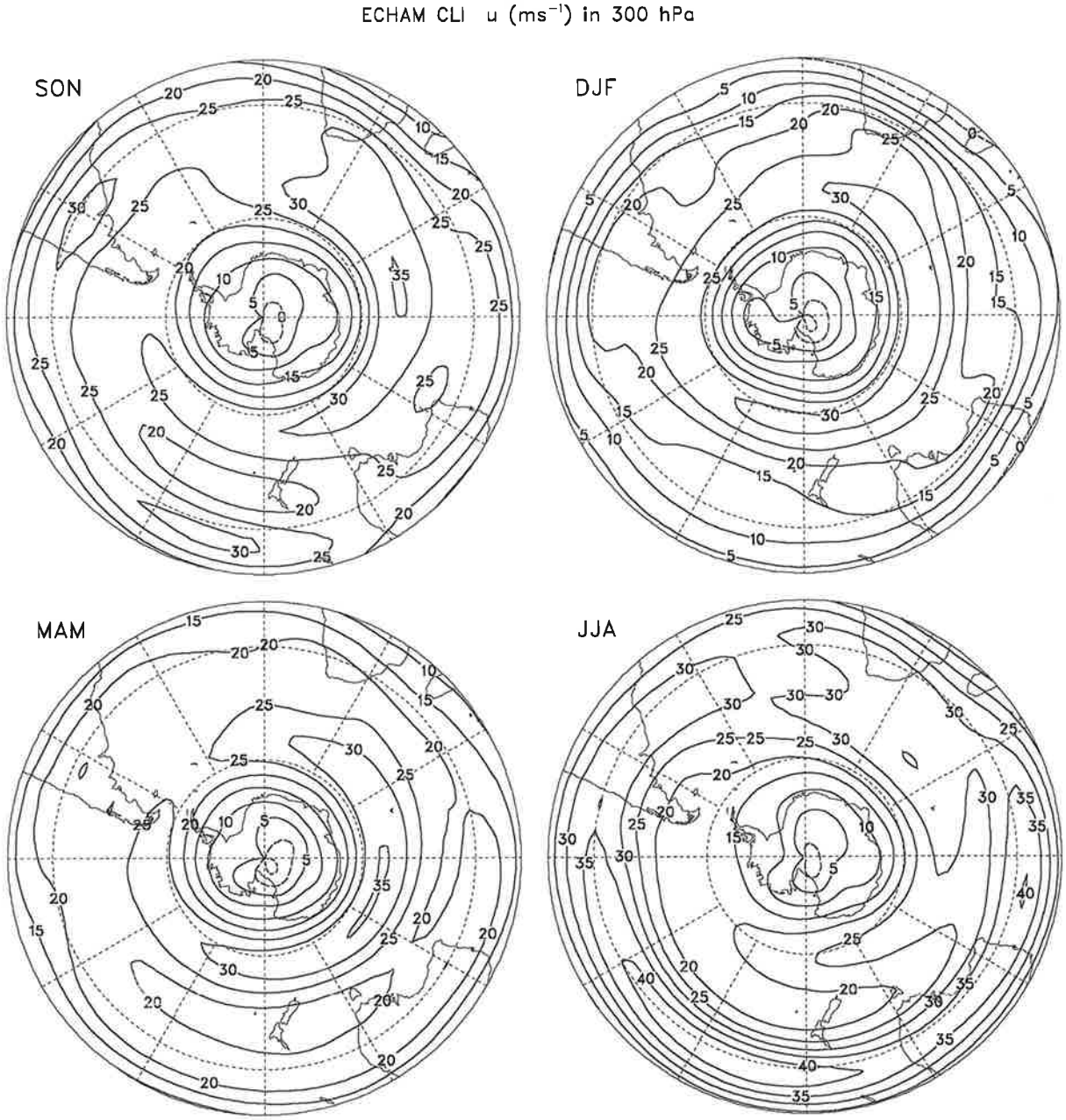

Fig. 4.3.6. As Fig. 4.3.4 but for the simulations performed with ECHAM3 with fixed Sea Surface Temperatures as boundary forcing.

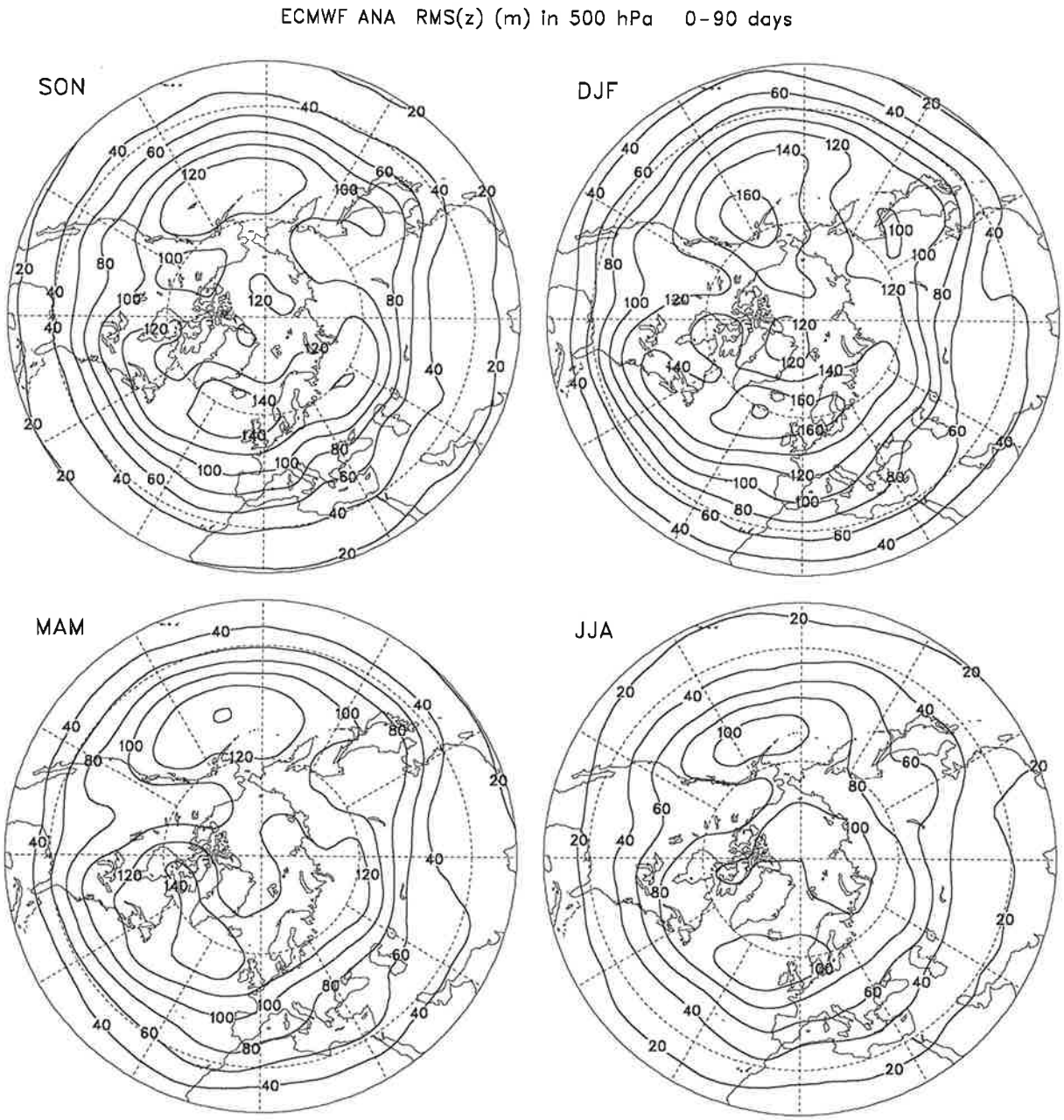

Fig. 4.4.1. RMS of the 500 hPa geopotential height field due to unfiltered transient fluctuations obtained from the ECMWF analyses distinguishing between seasons. Units are m, the contour interval is 20 m.

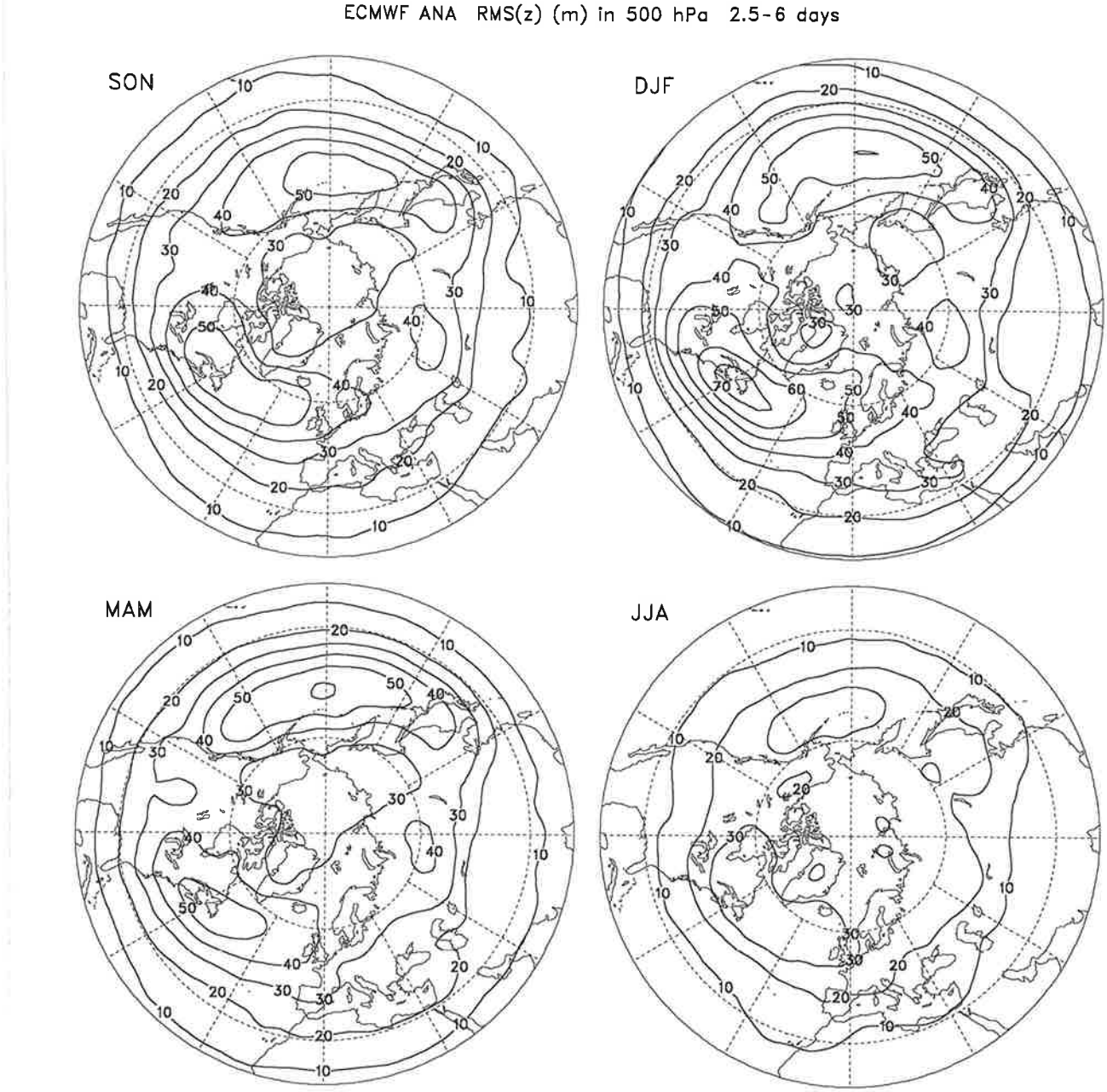

Fig. 4.4.2. As Fig. 4.4.1 but for the band-pass filtered transient fluctuations. The contour interval is 10 m.

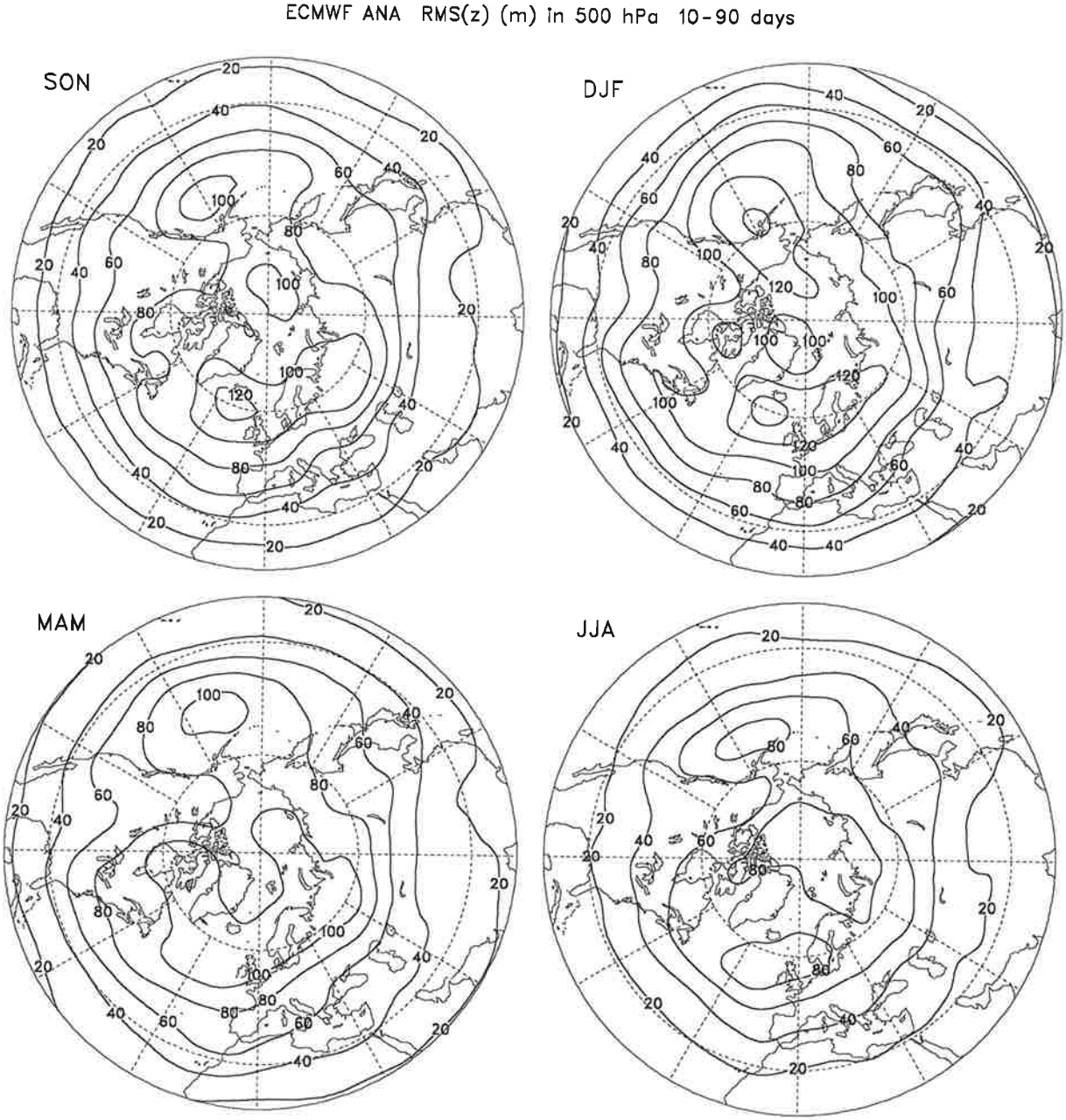

Fig. 4.4.3. As Fig. 4.4.1 but for the low-pass filtered transient fluctuations.

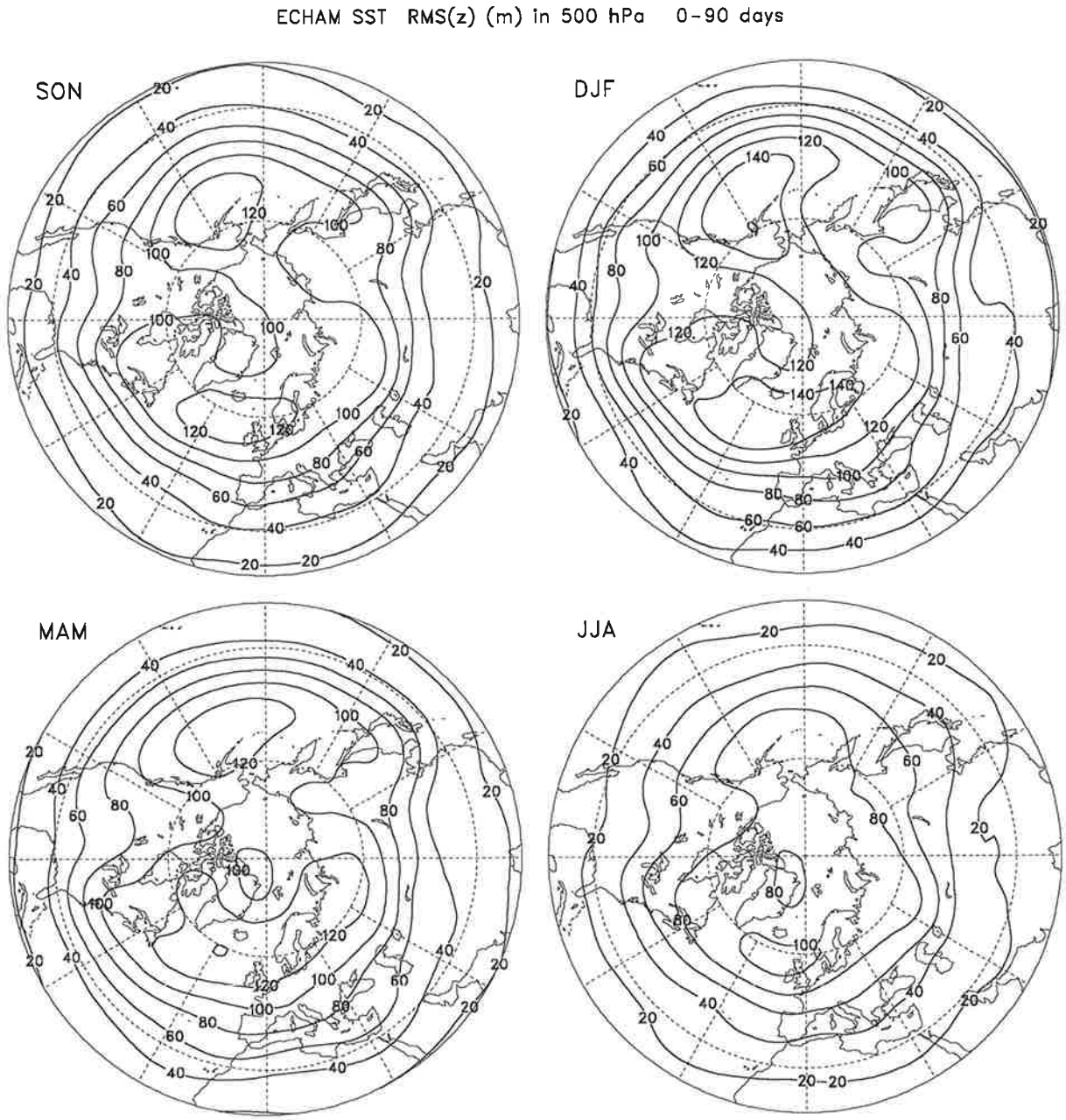

Fig. 4.4.4. As Fig. 4.4.1 but for the simulations performed with ECHAM3 with varying Sea Surface Temperatures as boundary forcing.

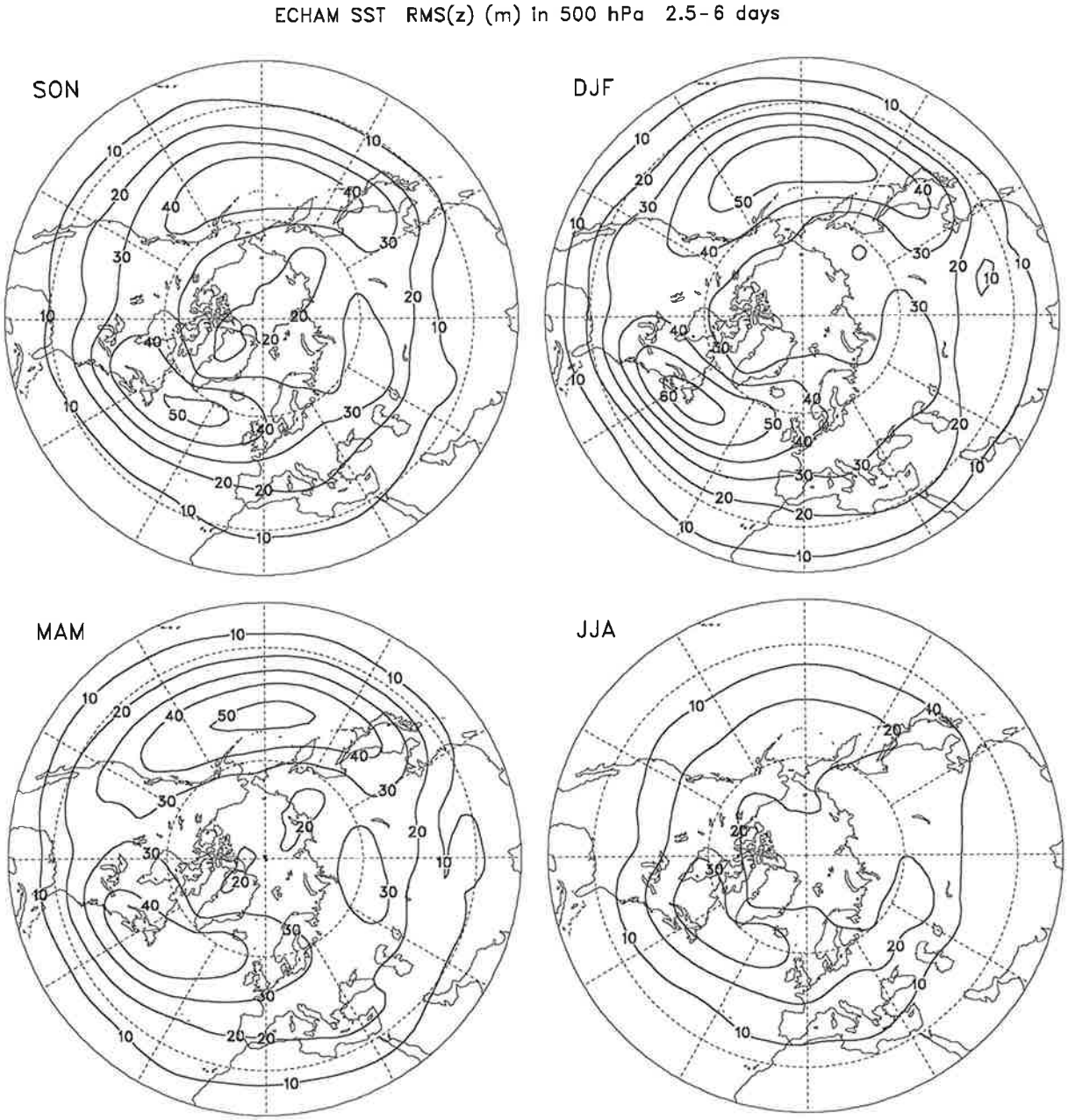

Fig. 4.4.5. As Fig. 4.4.4 but for the band-pass filtered transient fluctuations. The contour interval is 10 m.

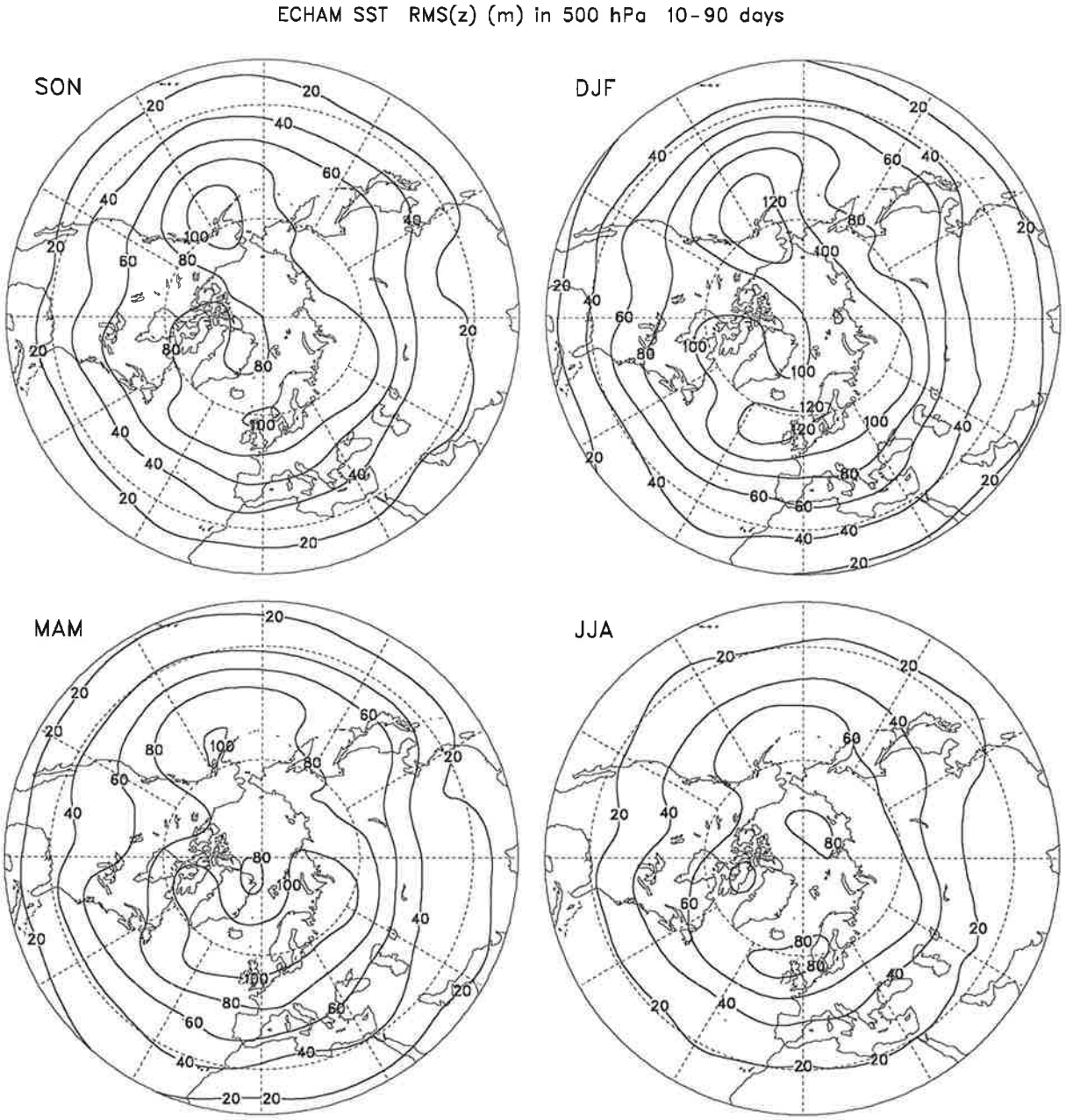

Fig. 4.4.6. As Fig. 4.4.4 but for the low-pass filtered transient fluctuations.

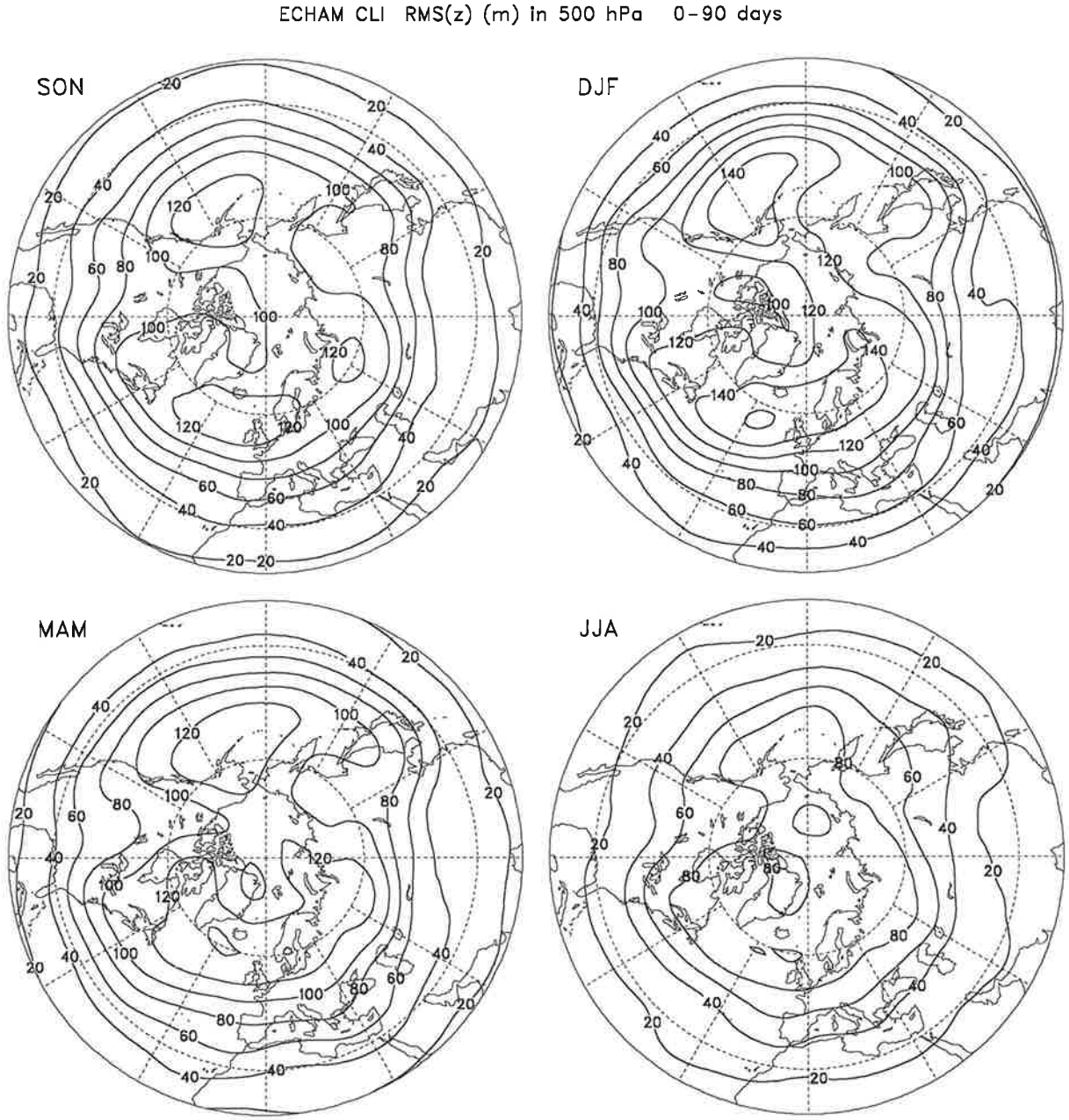

Fig. 4.4.7. As Fig. 4.4.1 but for the simulations performed with ECHAM3 with fixed Sea Surface Temperatures as boundary forcing.

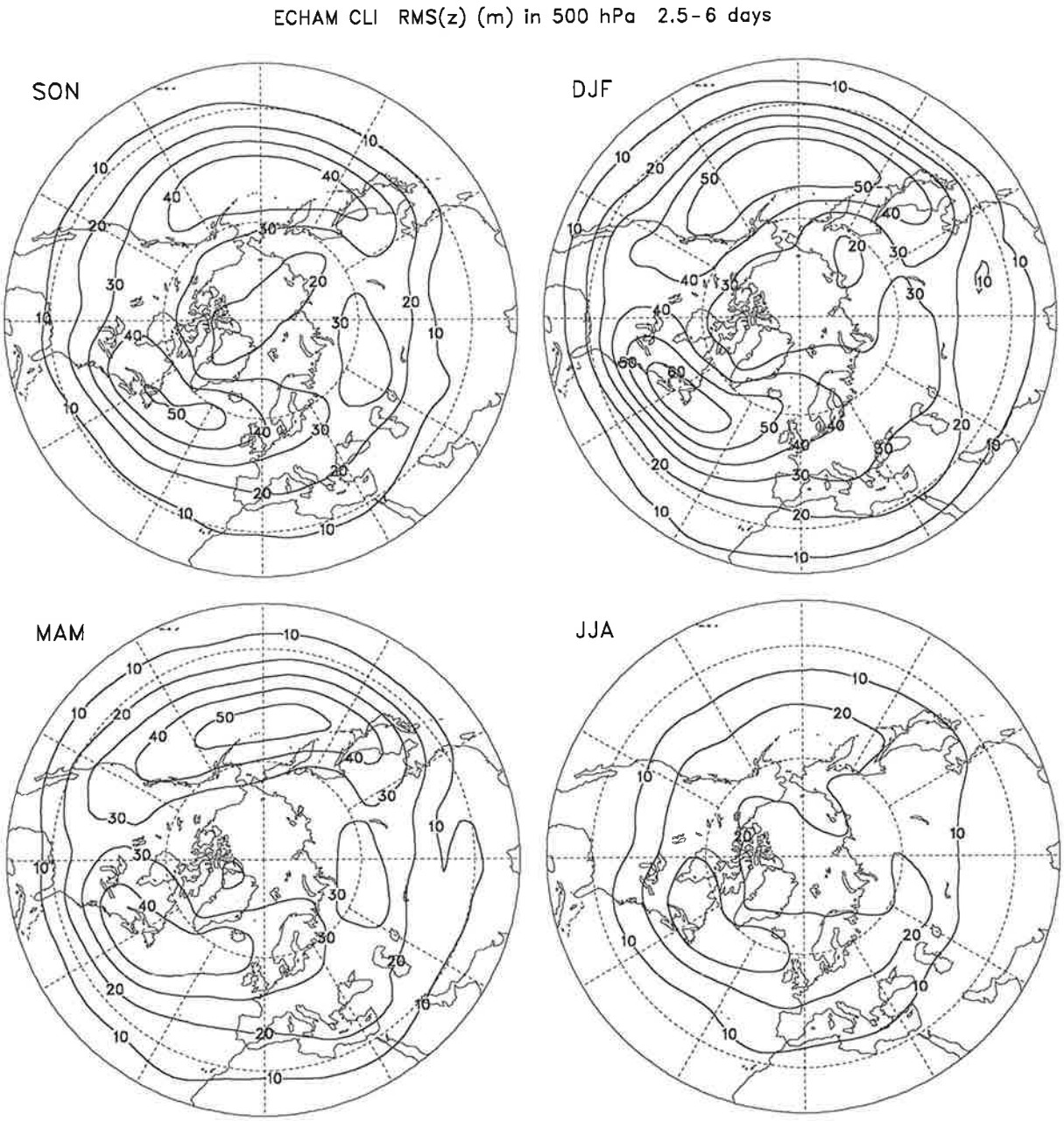

Fig. 4.4.8. As Fig. 4.4.7 but for the band-pass filtered transient fluctuations. The contour interval is 10 m.

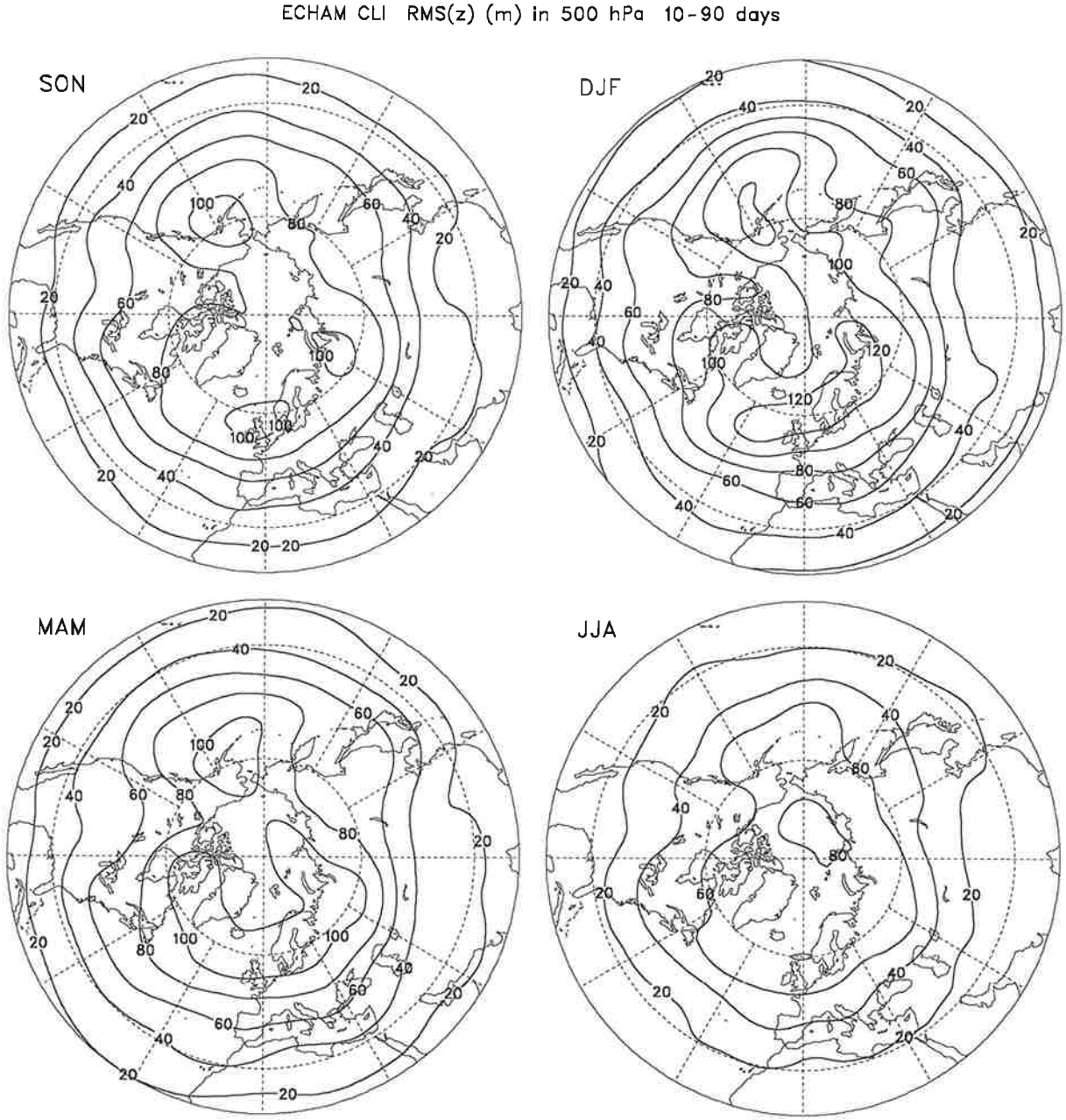

Fig. 4.4.9. As Fig. 4.4.7 but for the low-pass filtered transient fluctuations.

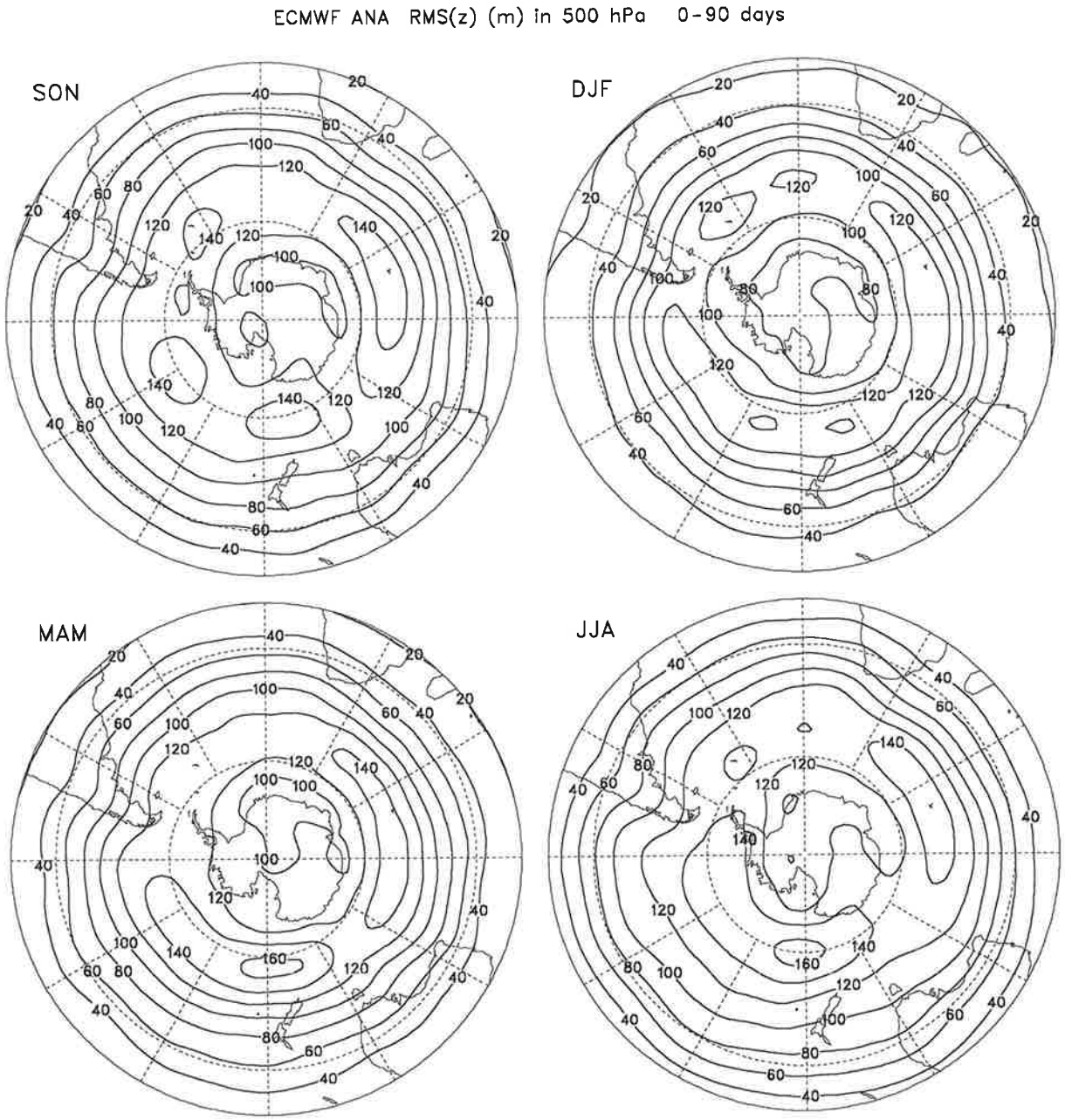

Fig. 4.4.10. RMS of the 500 hPa geopotential height field due to unfiltered transient fluctuations obtained from the ECMWF analyses distinguishing between seasons. Units are m, the contour interval is 20 m.

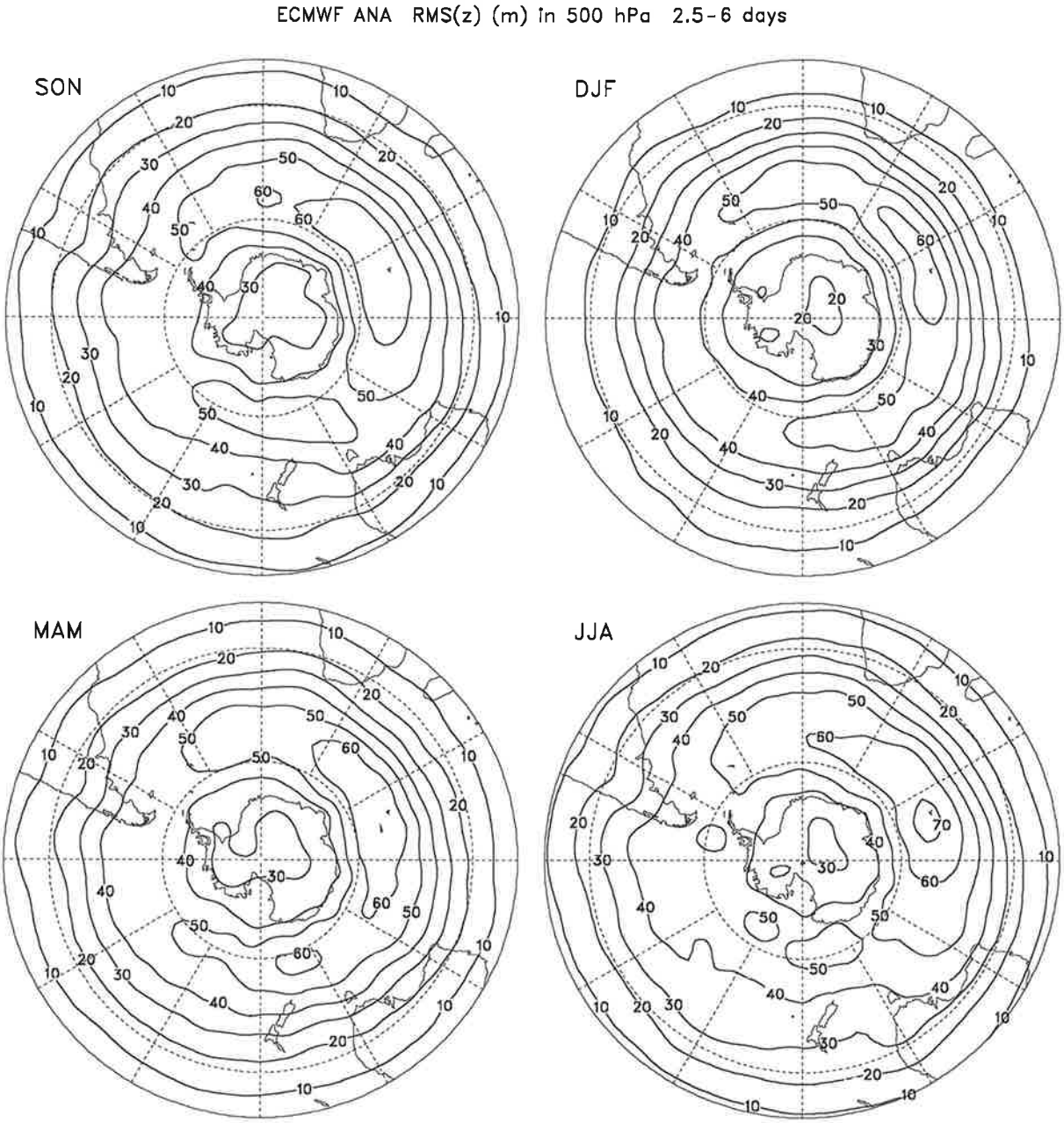

Fig. 4.4.11. As Fig. 4.4.10 but for the band-pass filtered transient fluctuations. The contour interval is 10 m.

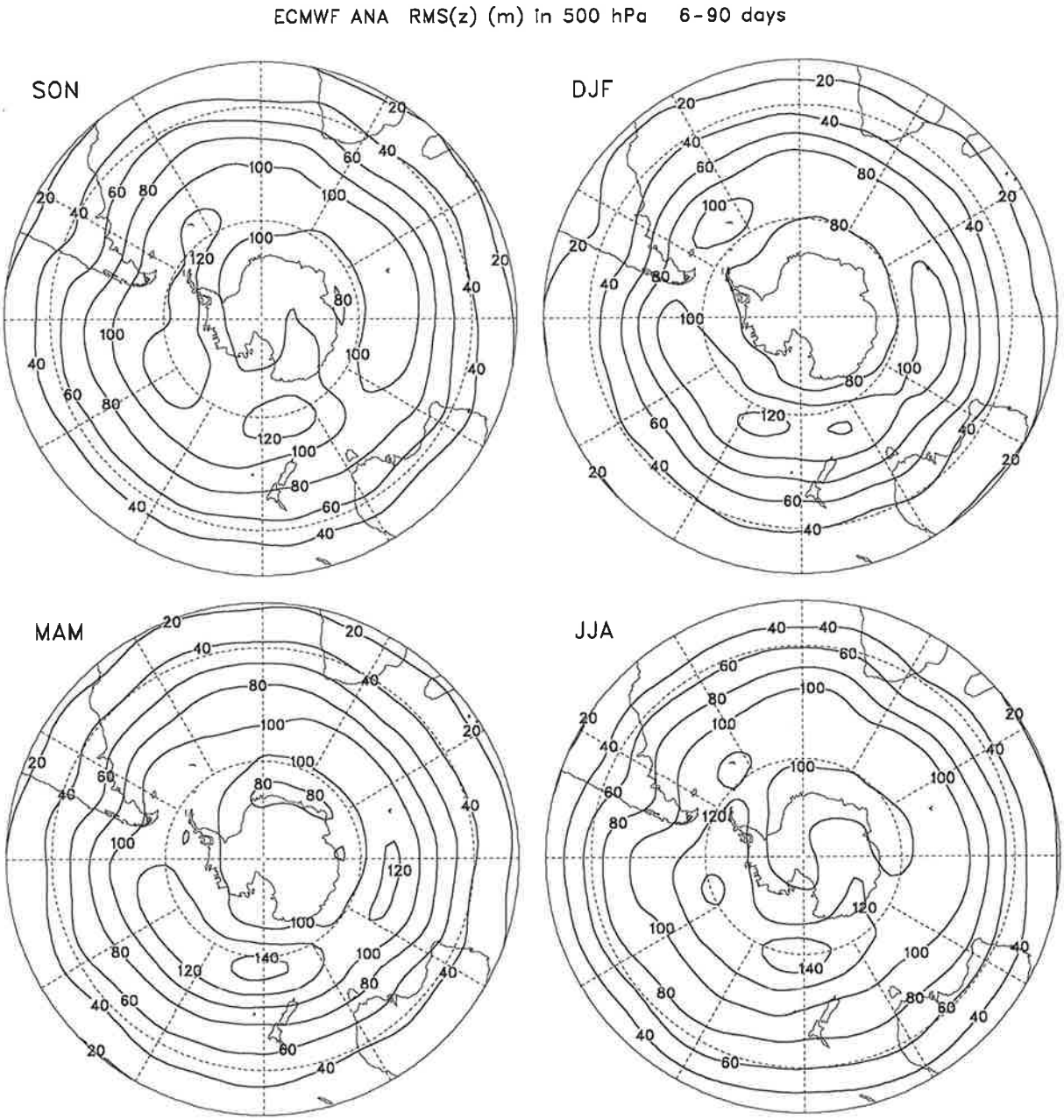

Fig. 4.4.12. As Fig. 4.4.10 but for the low-pass filtered transient fluctuations.

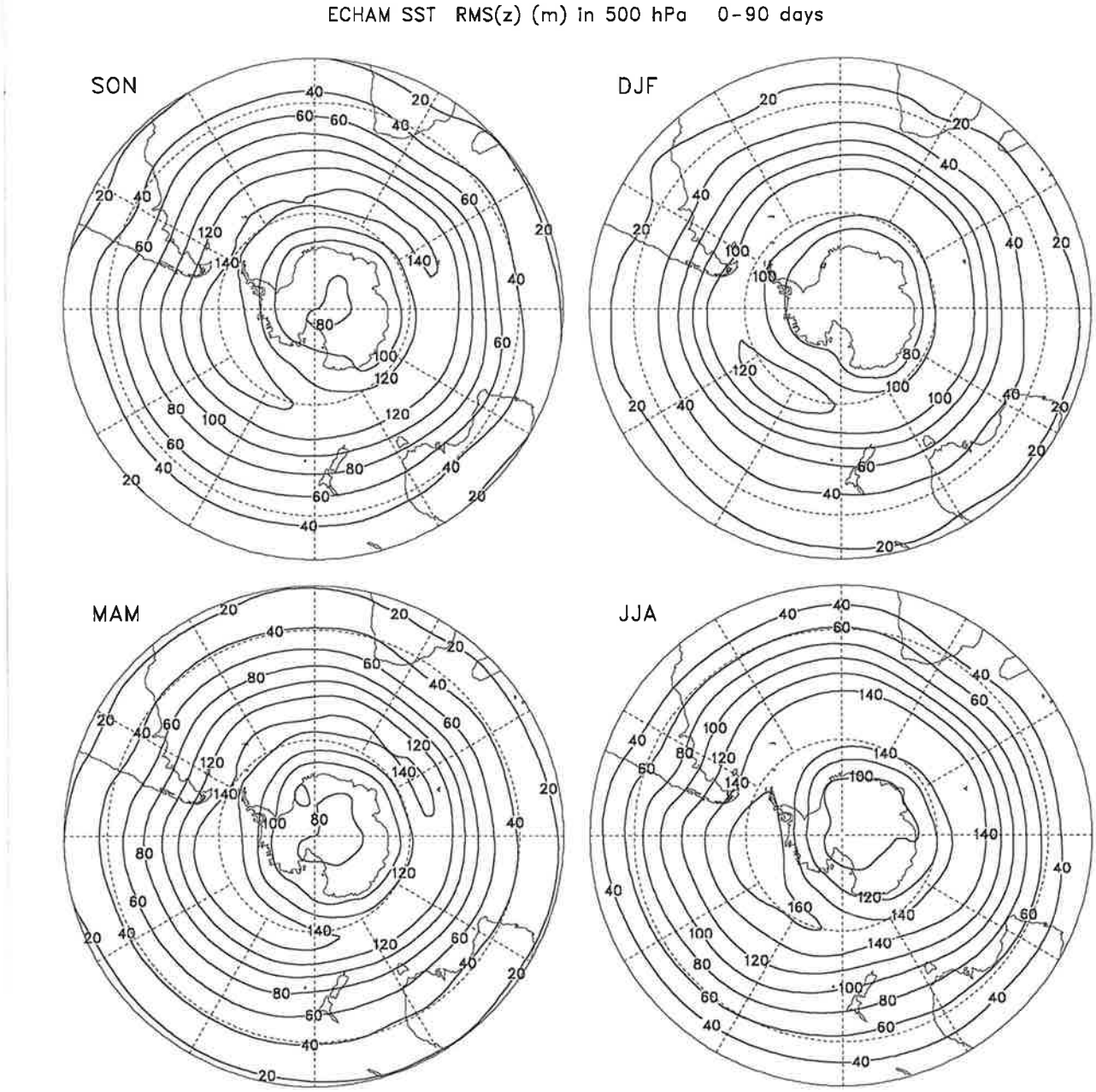

Fig. 4.4.13. As Fig. 4.4.10 but for the simulations performed with ECHAM3 with varying Sea Surface Temperatures as boundary forcing.

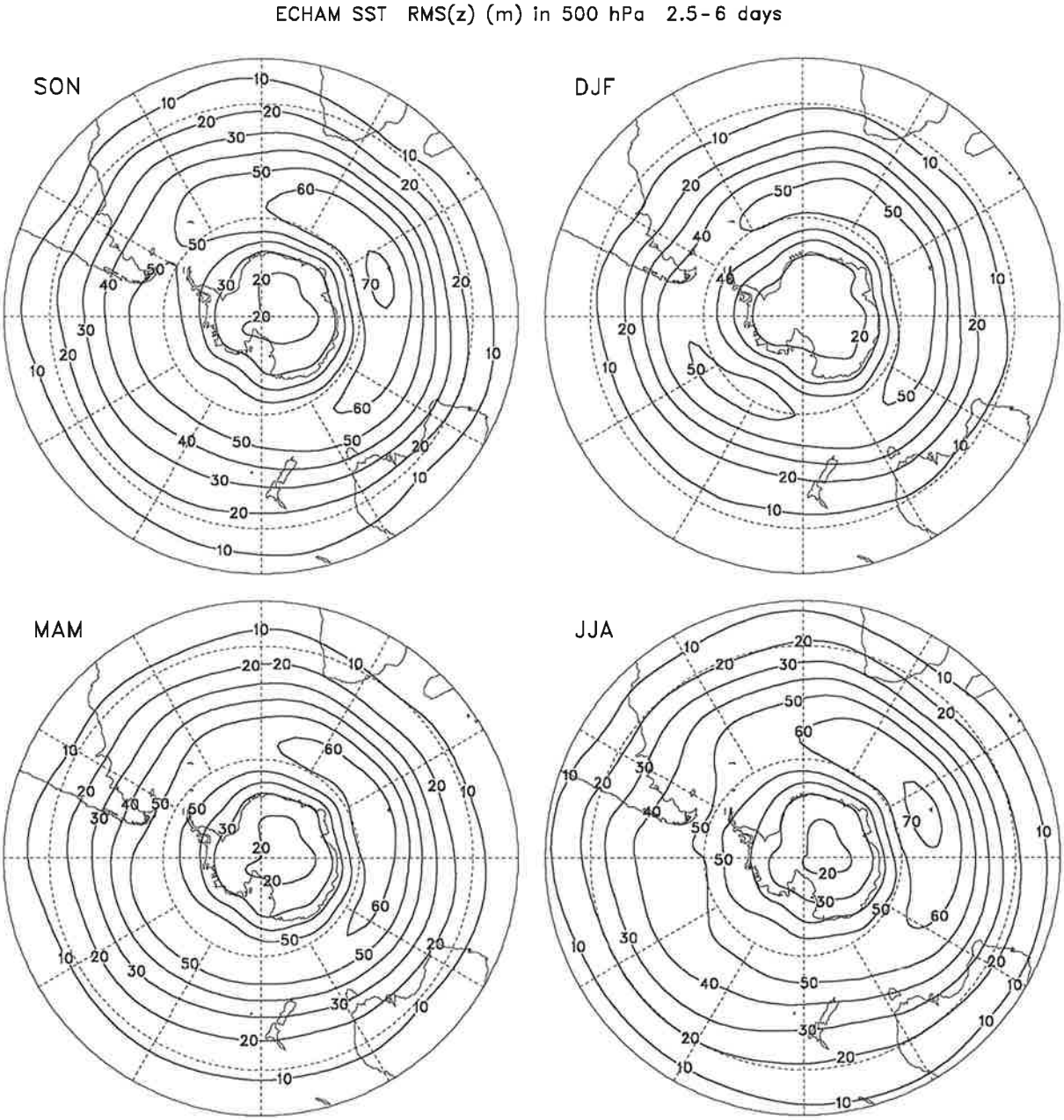

Fig. 4.4.14. As Fig. 4.4.13 but for the band-pass filtered transient fluctuations. The contour interval is 10 m.

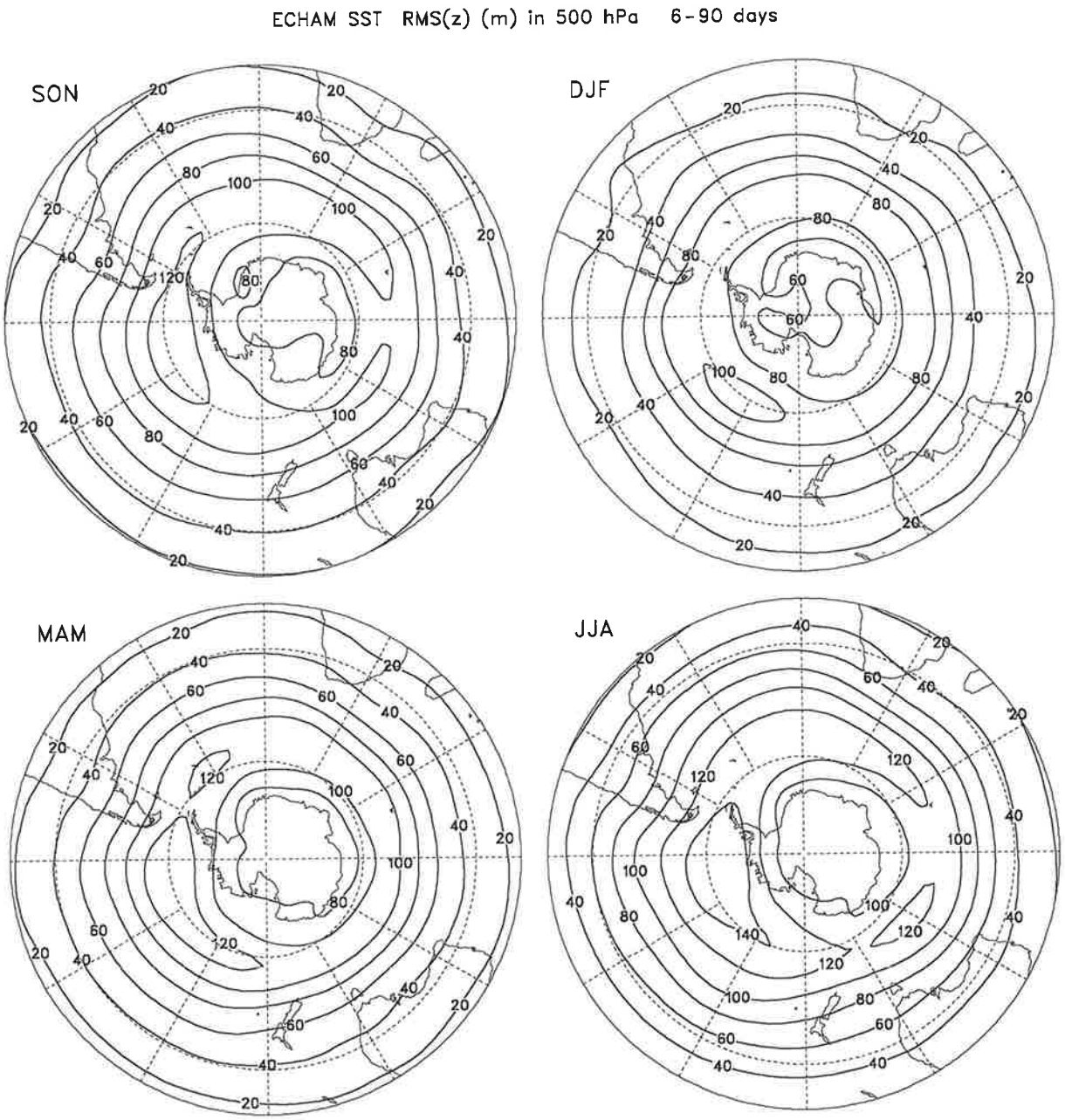

Fig. 4.4.15. As Fig. 4.4.13 but for the low-pass filtered transient fluctuations.

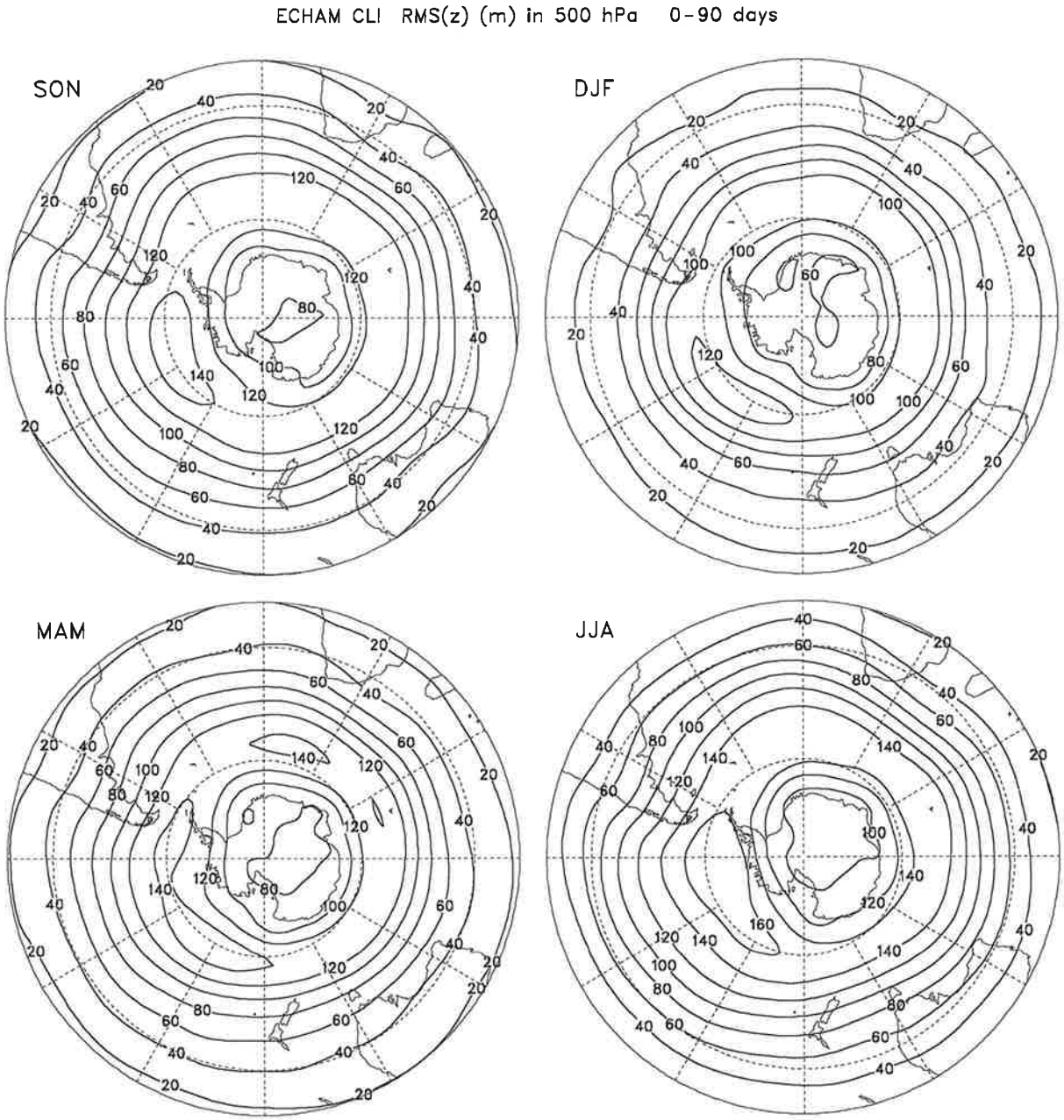

Fig. 4.4.16. As Fig. 4.4.10 but for the simulations performed with ECHAM3 with fixed Sea Surface Temperatures as boundary forcing.

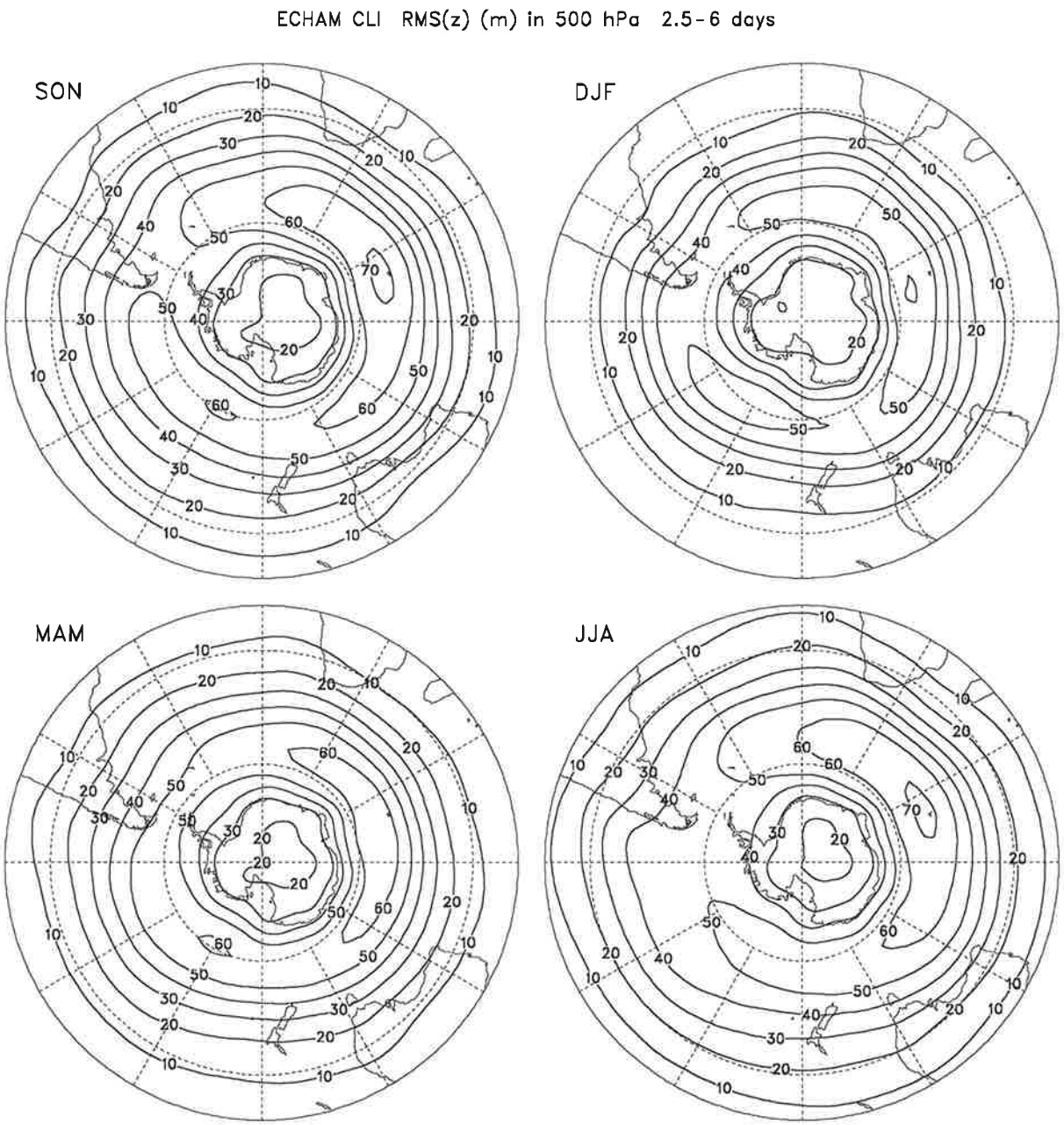

Fig. 4.4.17. As Fig. 4.4.16 but for the band-pass filtered transient fluctuations. The contour interval is 10 m.

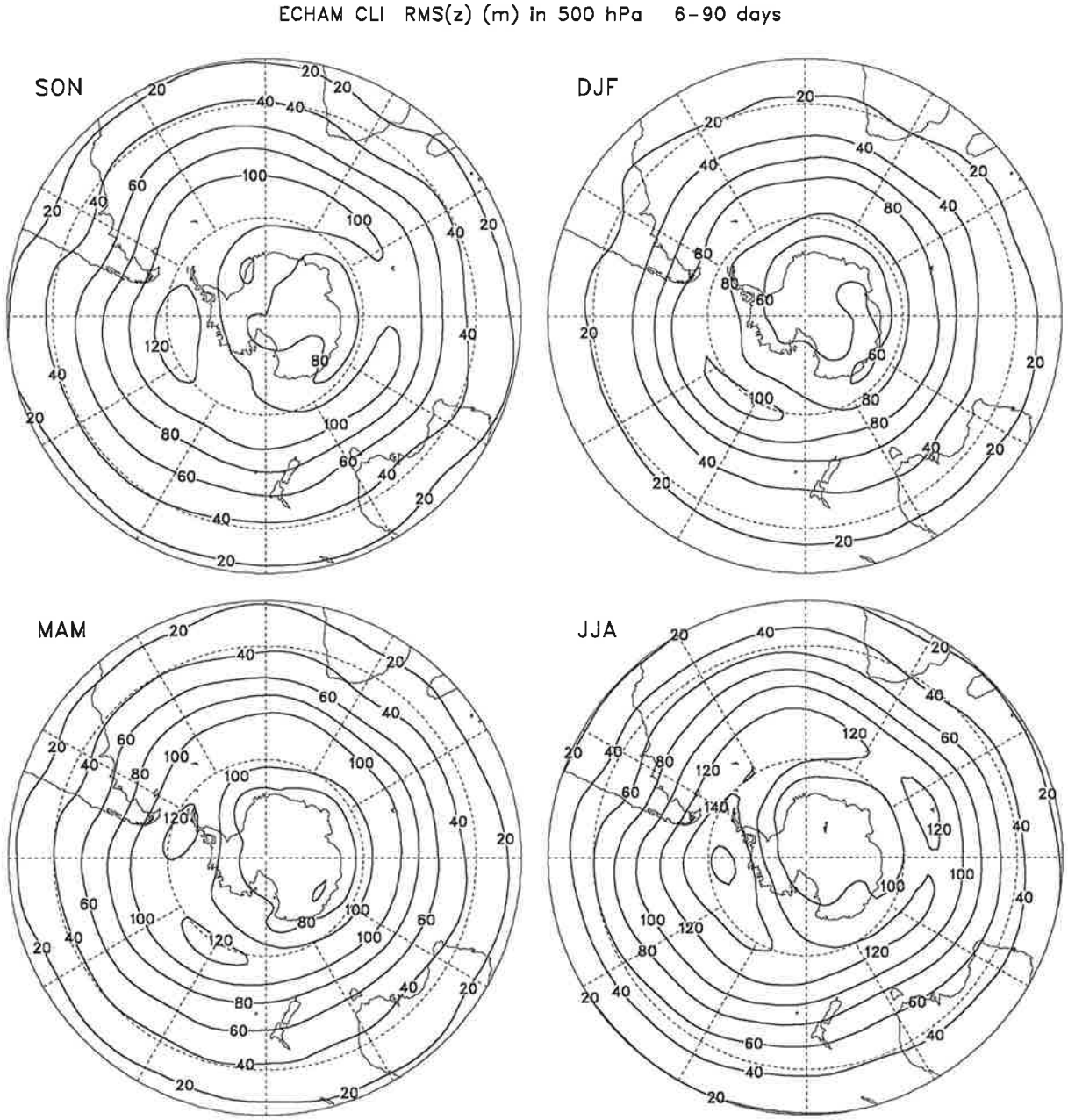

Fig. 4.4.18. As Fig. 4.4.16 but for the low-pass filtered transient fluctuations.

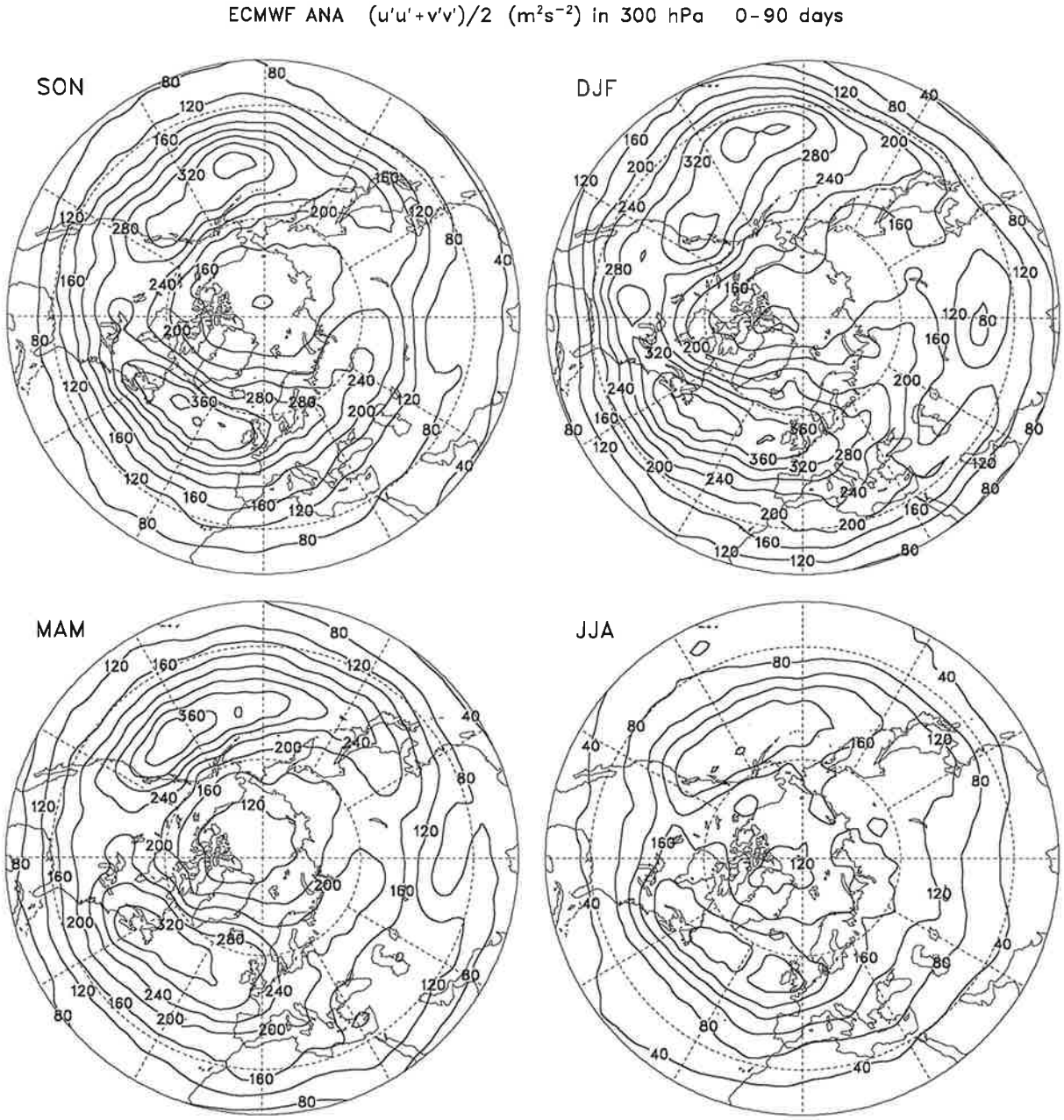

Fig. 4.4.19. Eddy kinetic energy at 300 hPa due to unfiltered transient fluctuations obtained from the ECMWF analyses distinguishing between seasons. Units are m^2/s^2, the contour interval is 40 m^2/s^2.

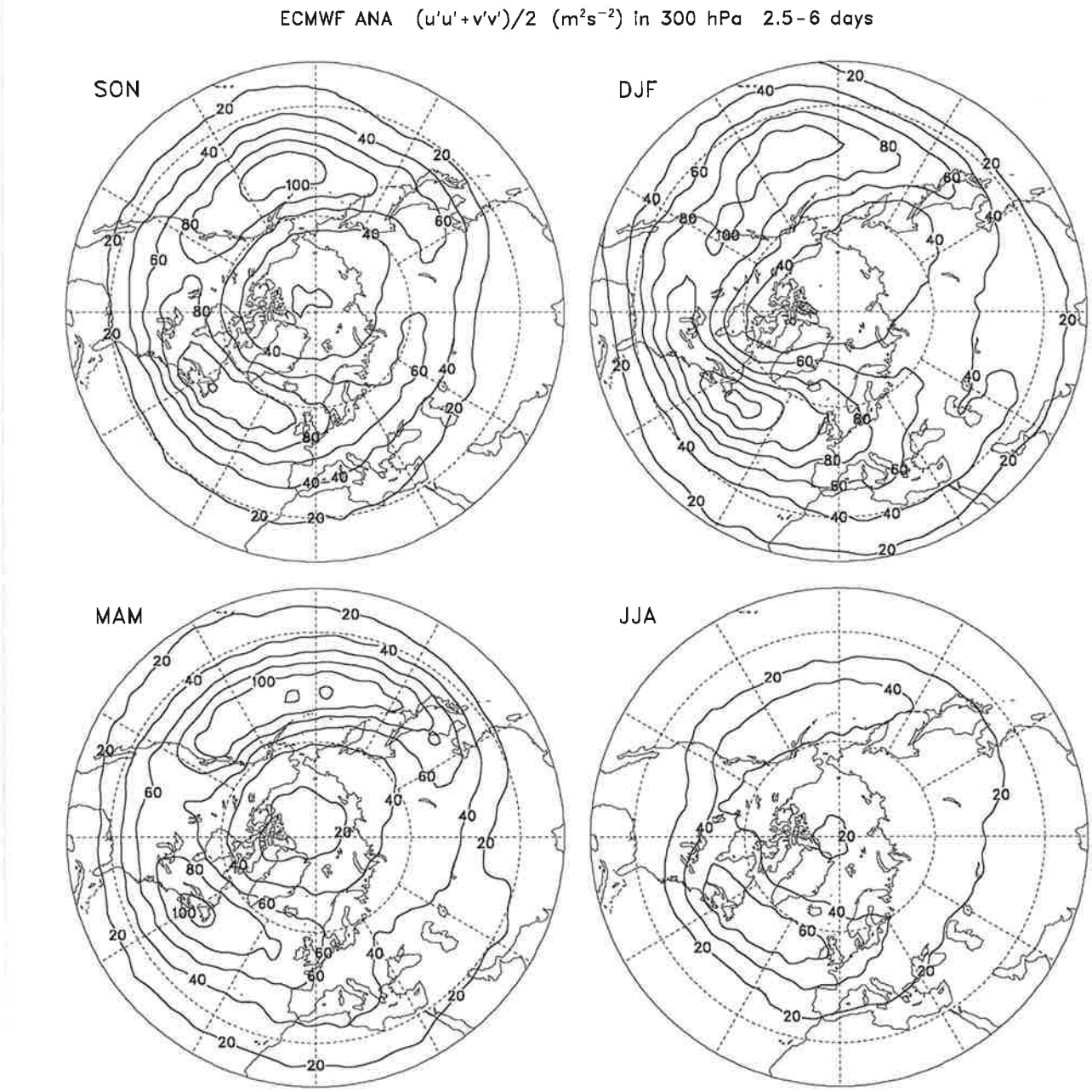

Fig. 4.4.20. As Fig. 4.4.19 but for the band-pass filtered transient fluctuations. The contour interval is 20 m^2/s^2.

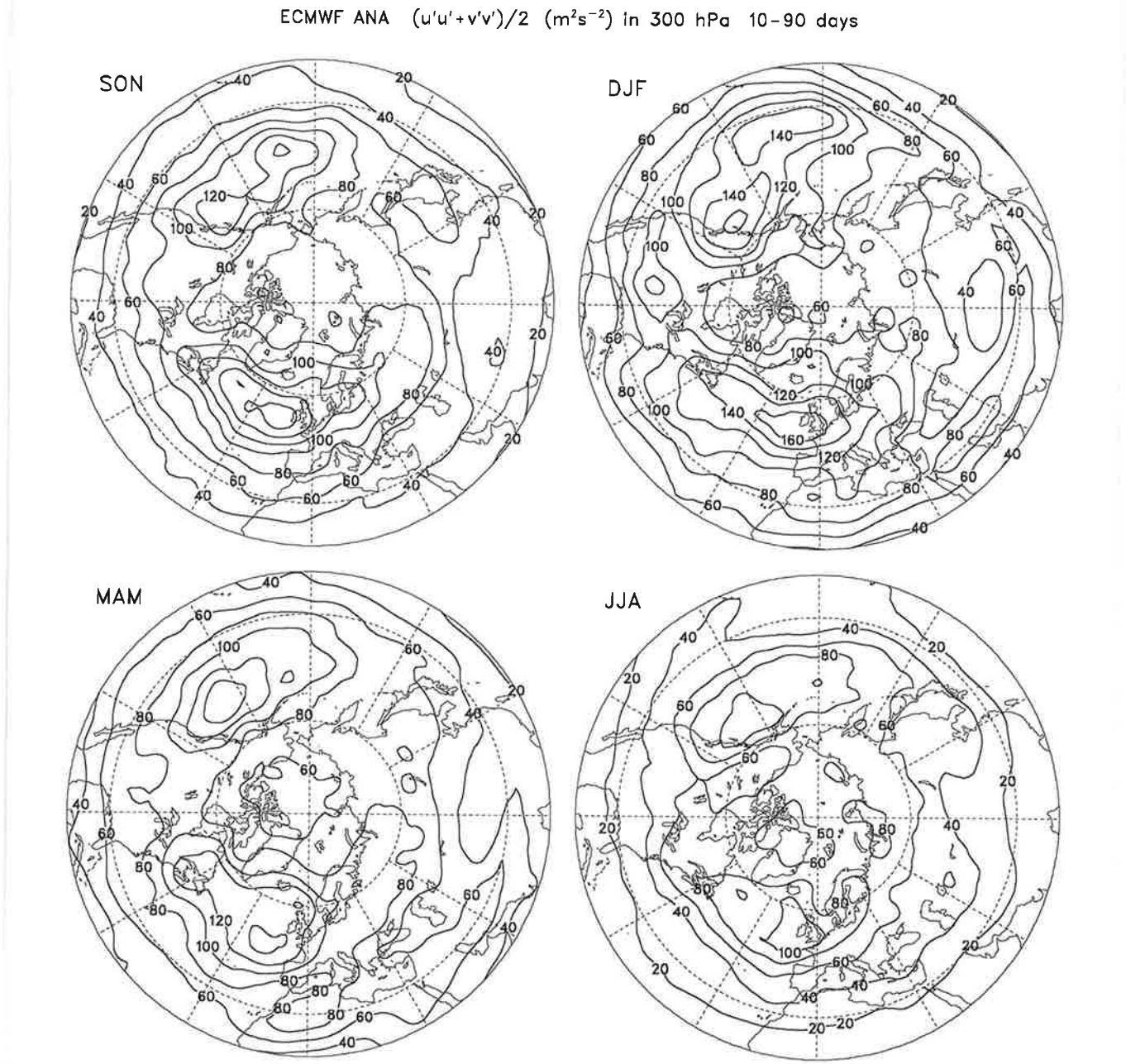

Fig. 4.4.21. As Fig. 4.4.19 but for the low-pass filtered transient fluctuations.

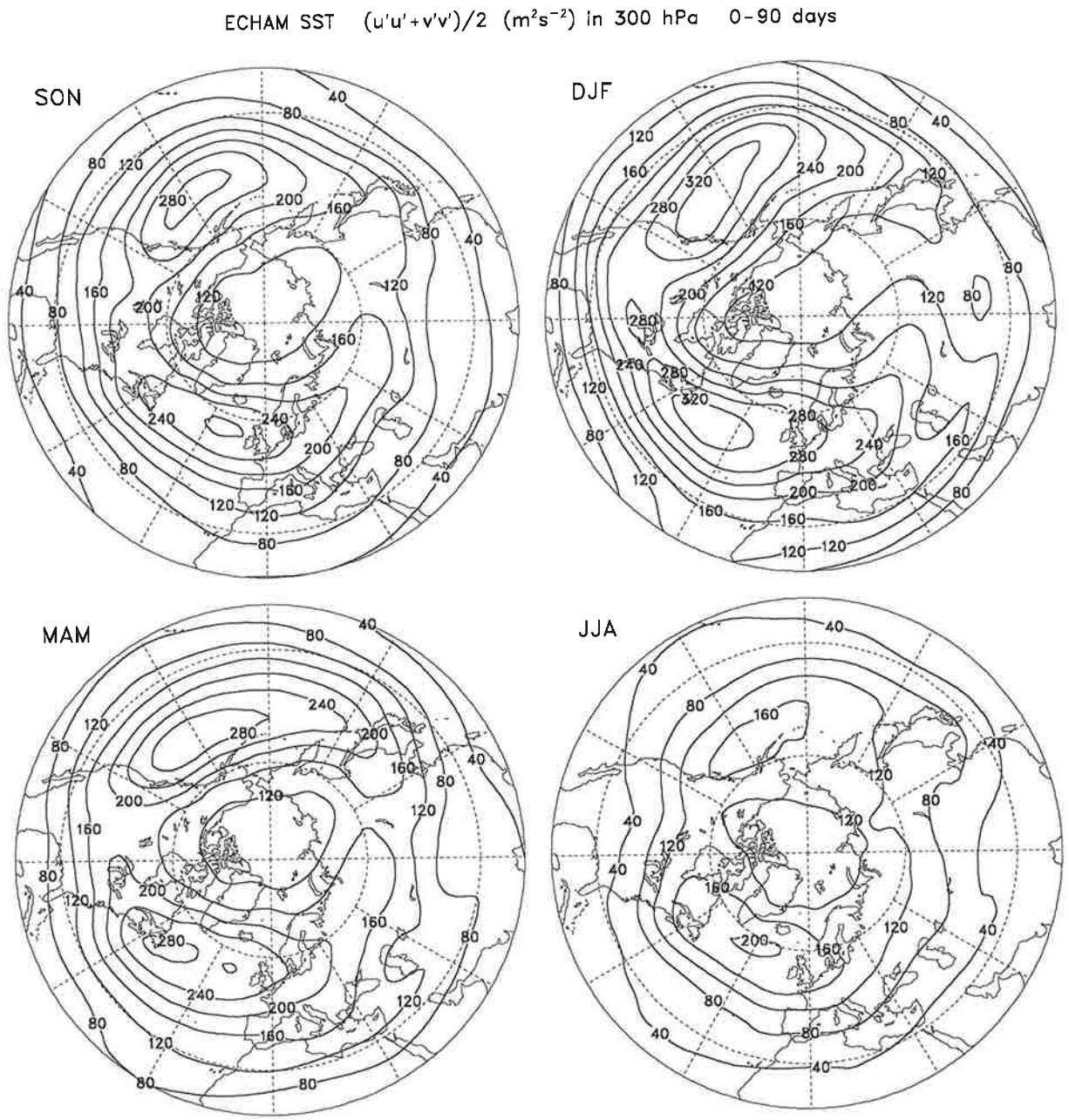

Fig. 4.4.22. As Fig. 4.4.19 but for the simulations performed with ECHAM3 with varying Sea Surface Temperatures as boundary forcing.

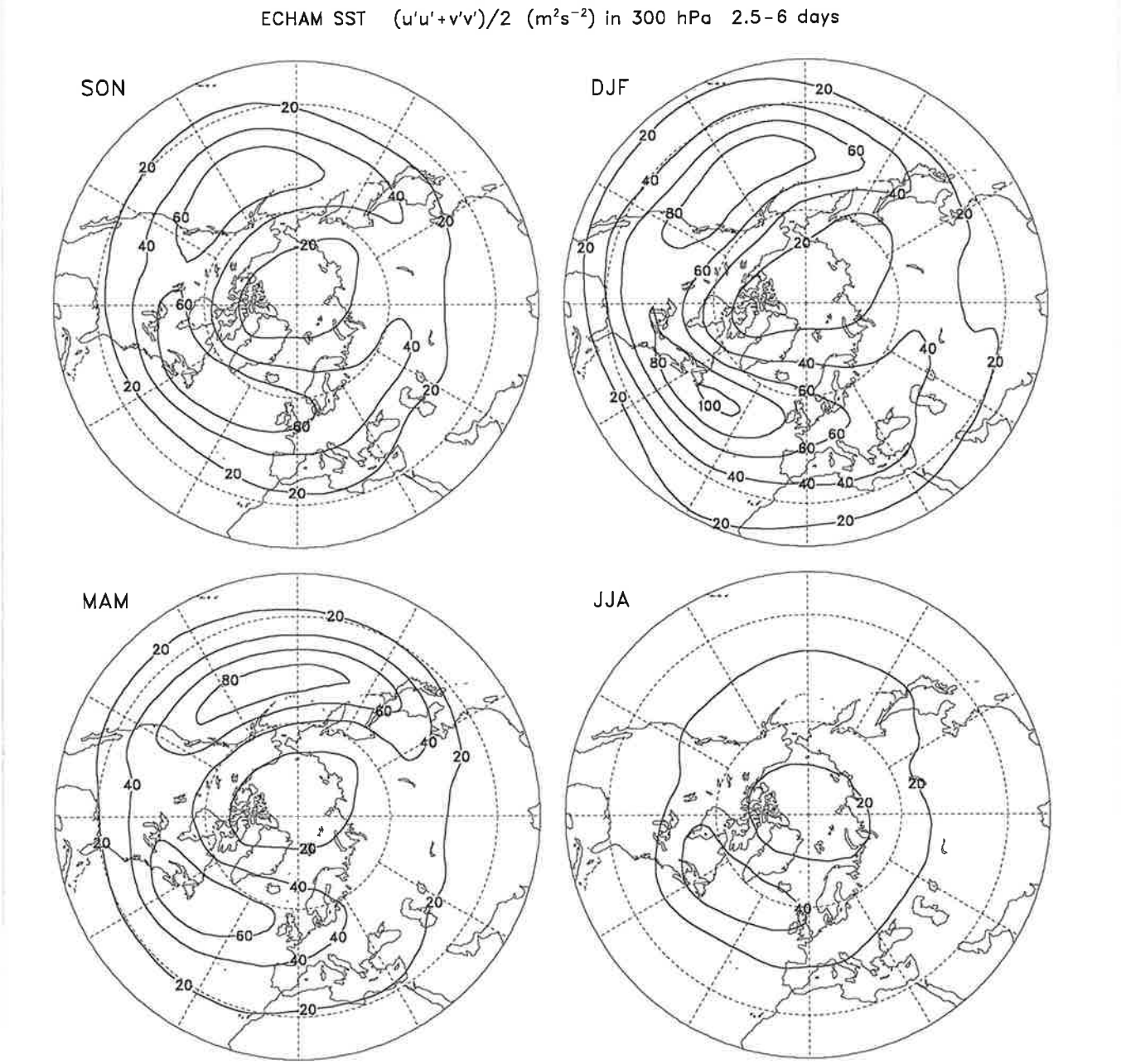

Fig. 4.4.23. As Fig. 4.4.22 but for the band-pass filtered transient fluctuations. The contour interval is 20 m^2/s^2.

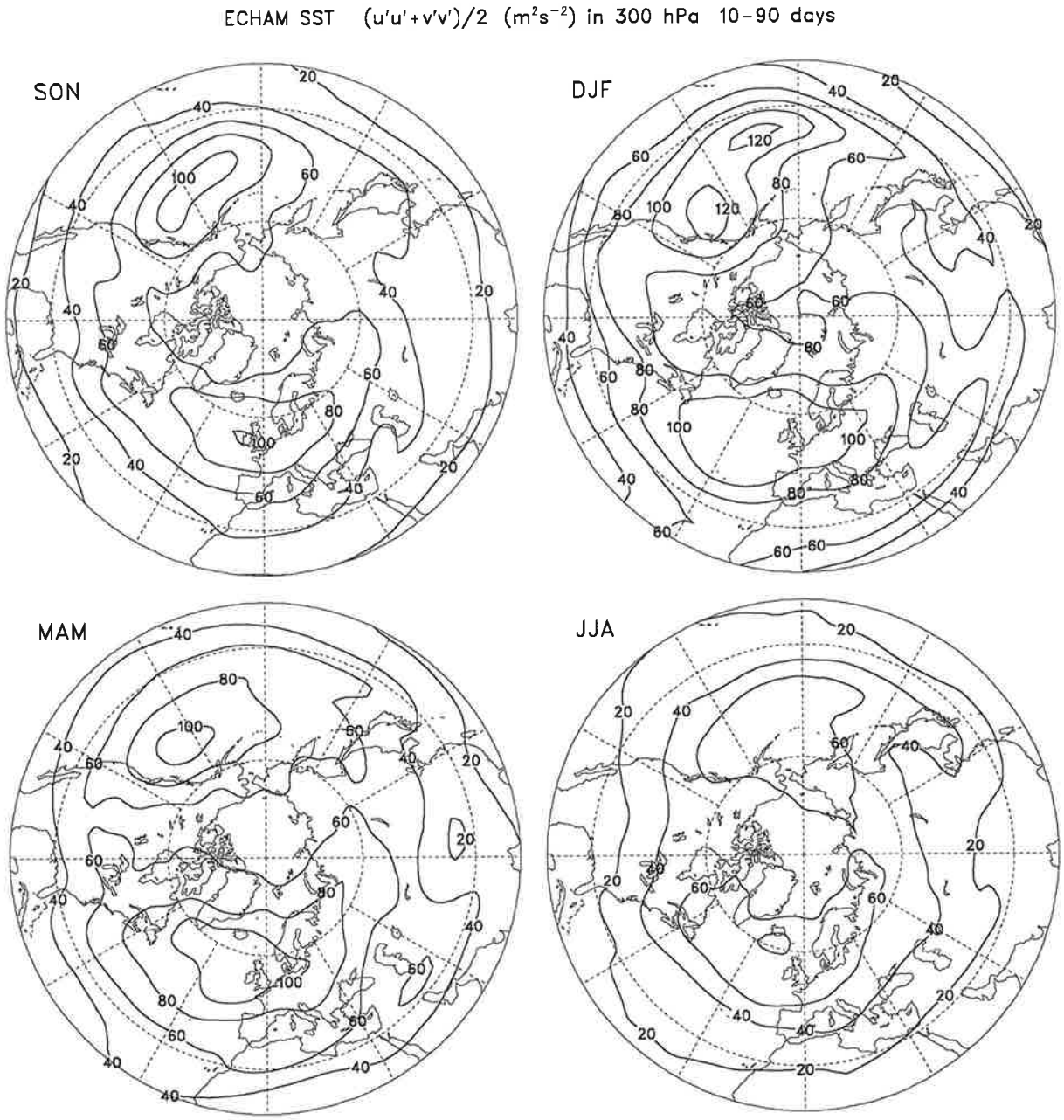

Fig. 4.4.24. As Fig. 4.4.22 but for the low-pass filtered transient fluctuations.

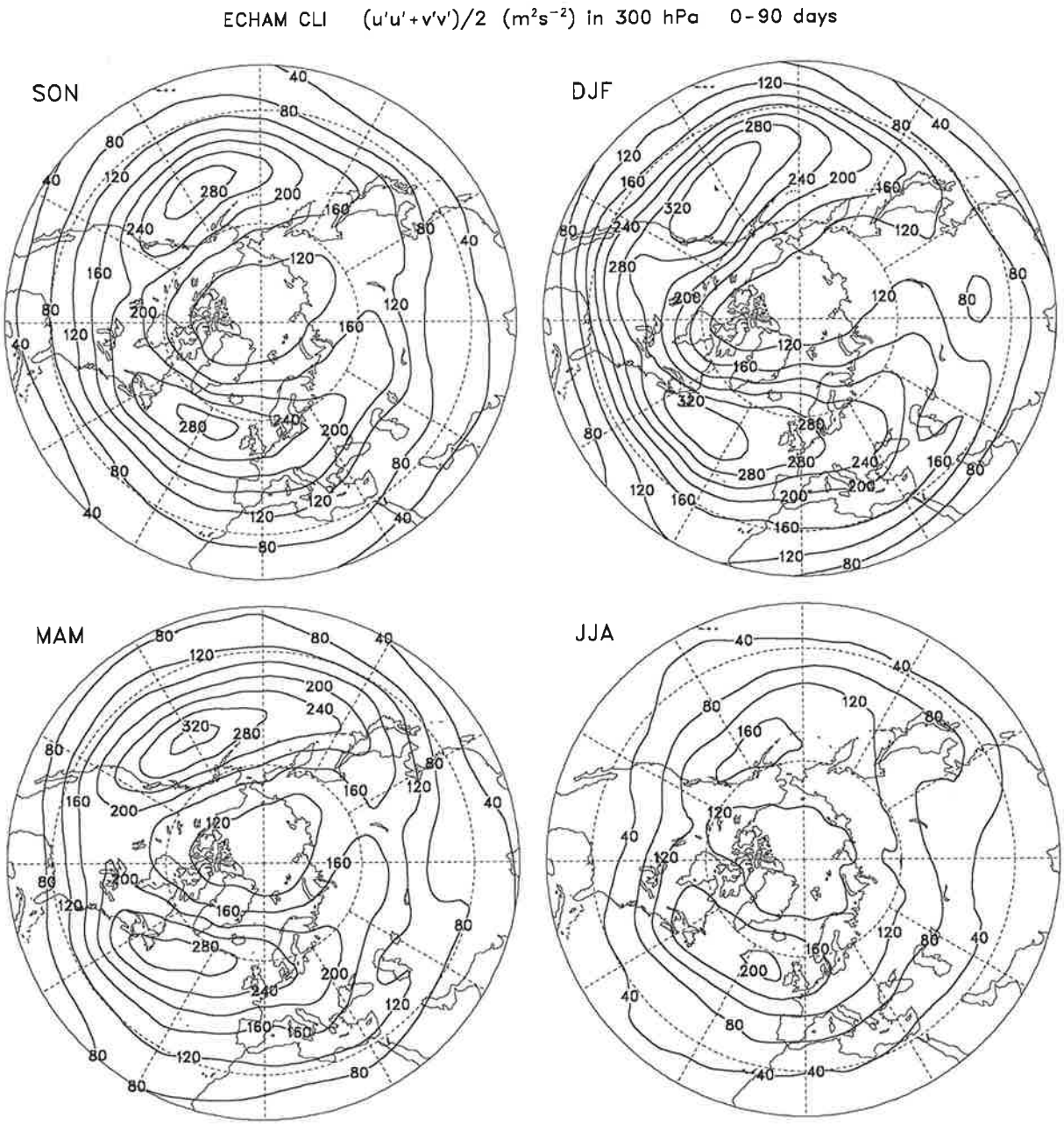

Fig. 4.4.25. As Fig. 4.4.19 but for the simulations performed with ECHAM3 with fixed Sea Surface Temperatures as boundary forcing.

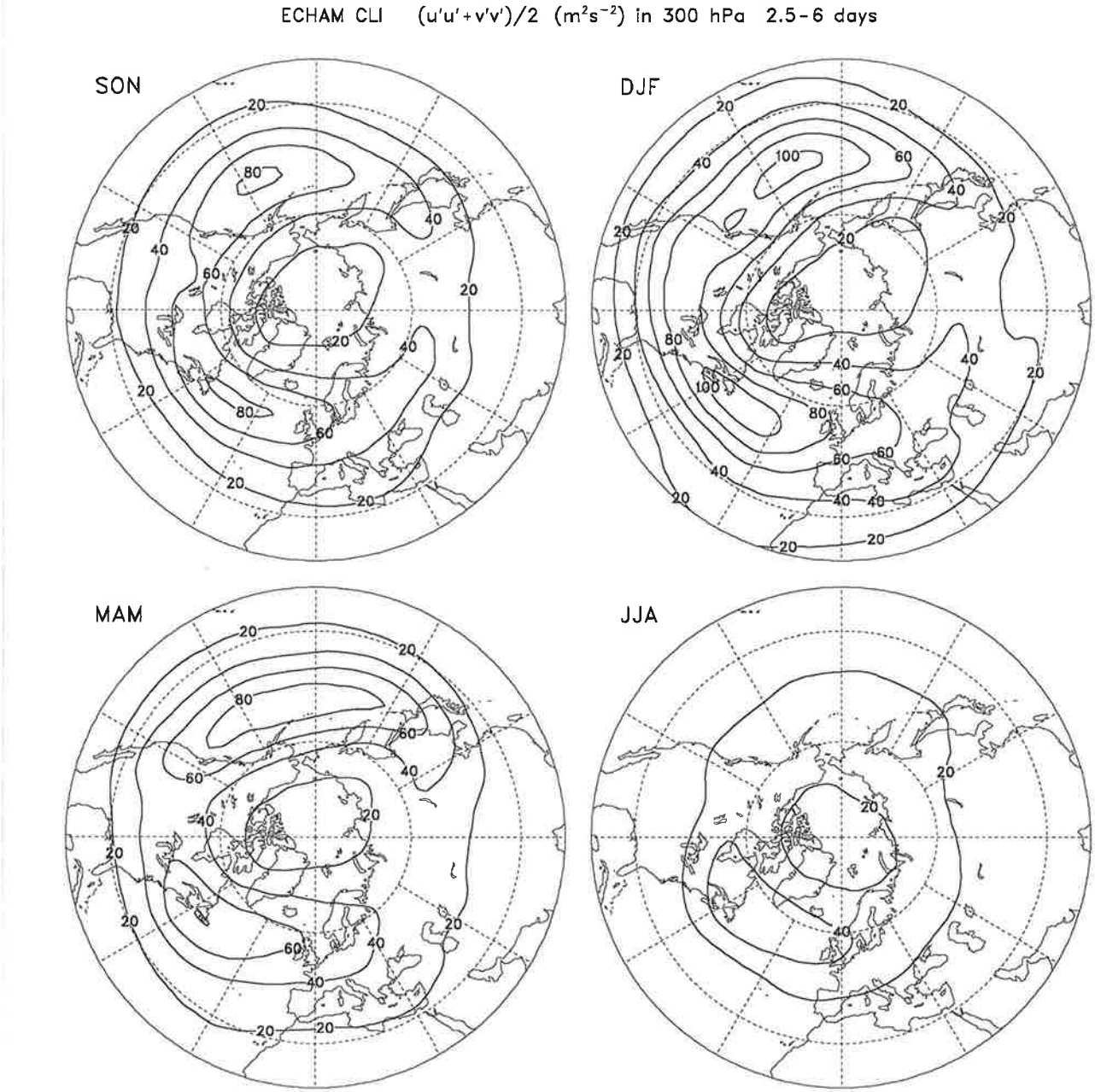

Fig. 4.4.26. As Fig. 4.4.25 but for the band-pass filtered transient fluctuations. The contour interval is 20 m^2/s^2.

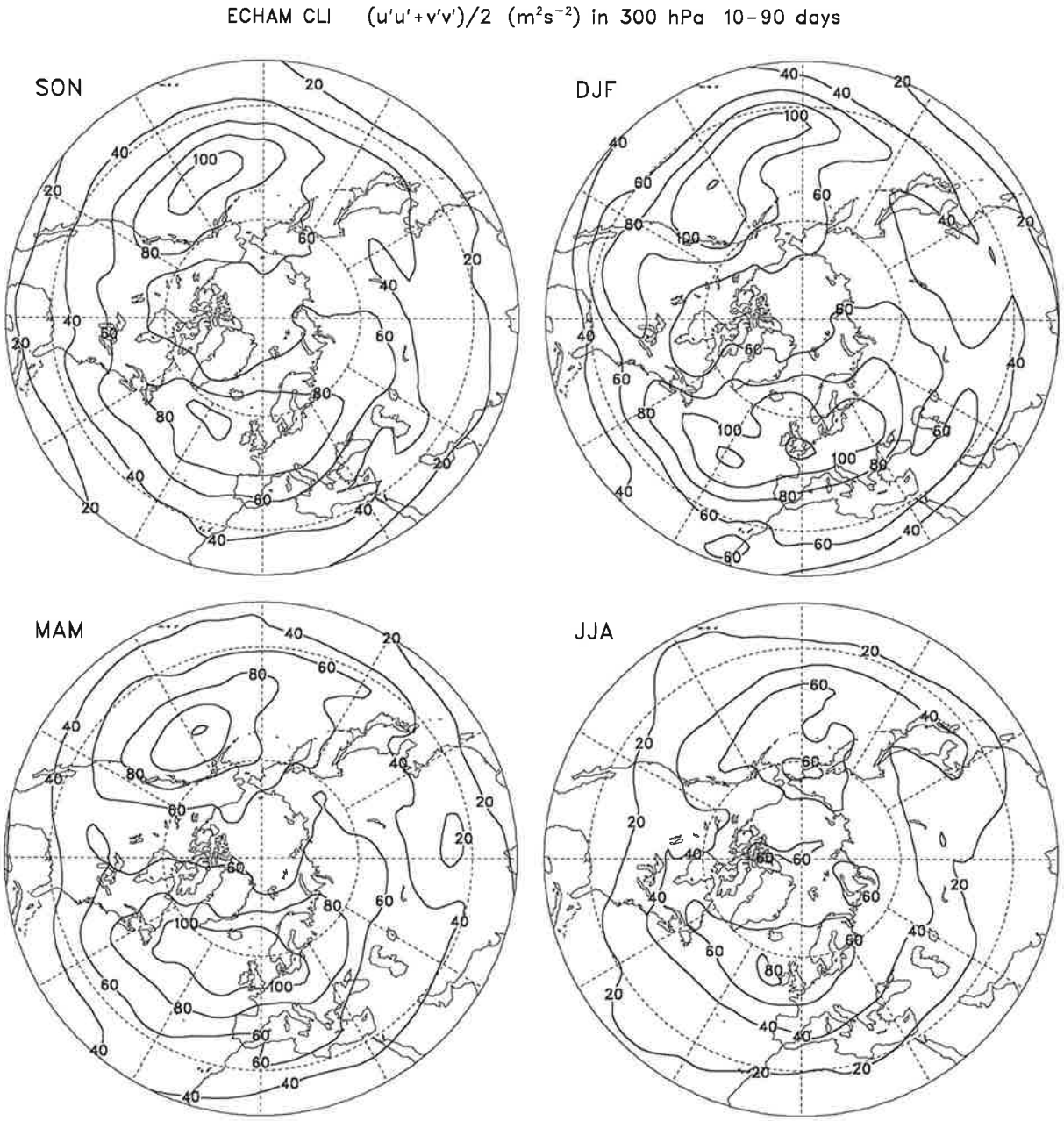

Fig. 4.4.27. As Fig. 4.4.25 but for the low-pass filtered transient fluctuations.

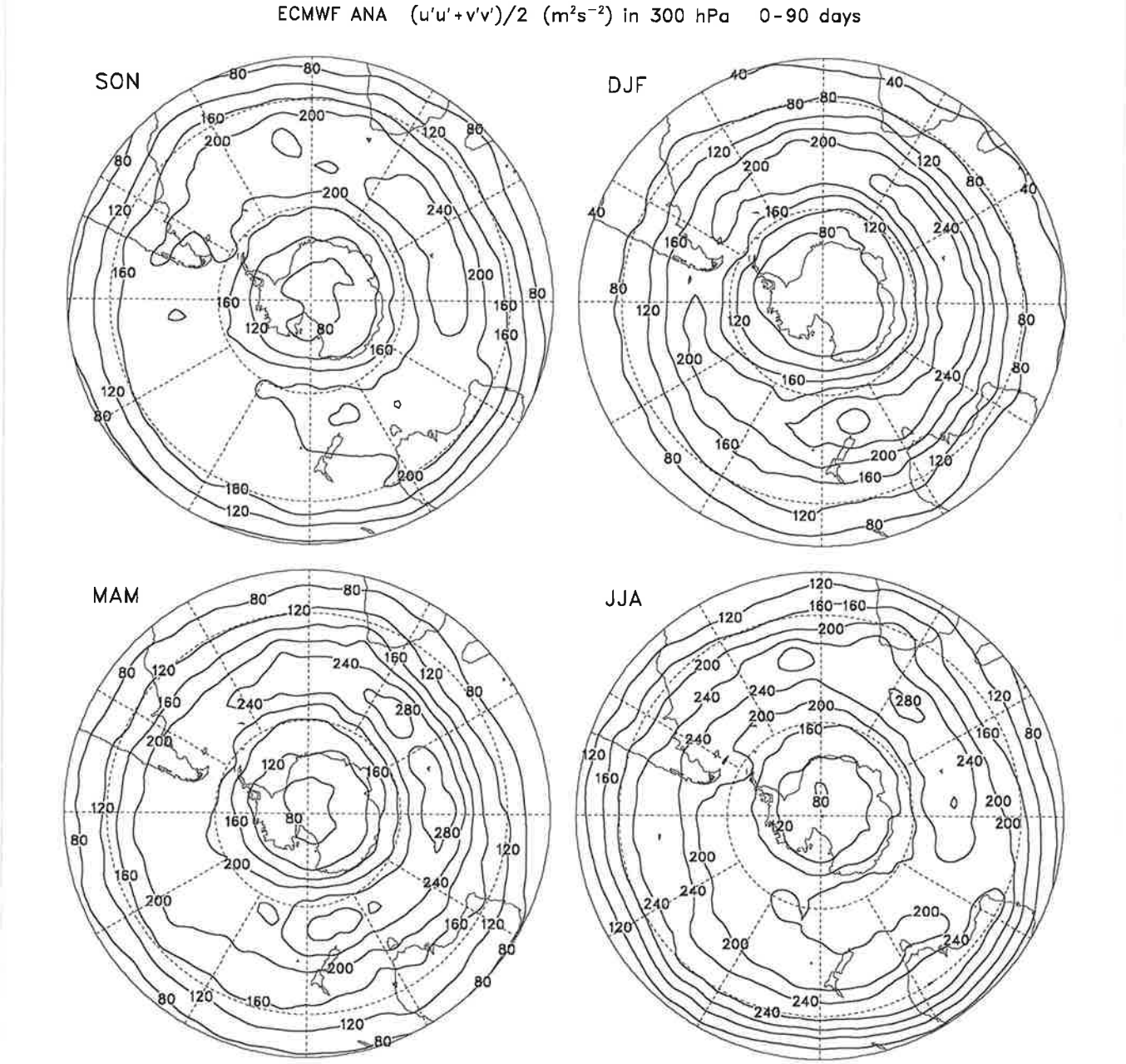

Fig. 4.4.28. Eddy kinetic energy at 300 hPa due to unfiltered transient fluctuations obtained from the ECMWF analyses distinguishing between seasons. Units are m^2/s^2, the contour interval is 40 m^2/s^2.

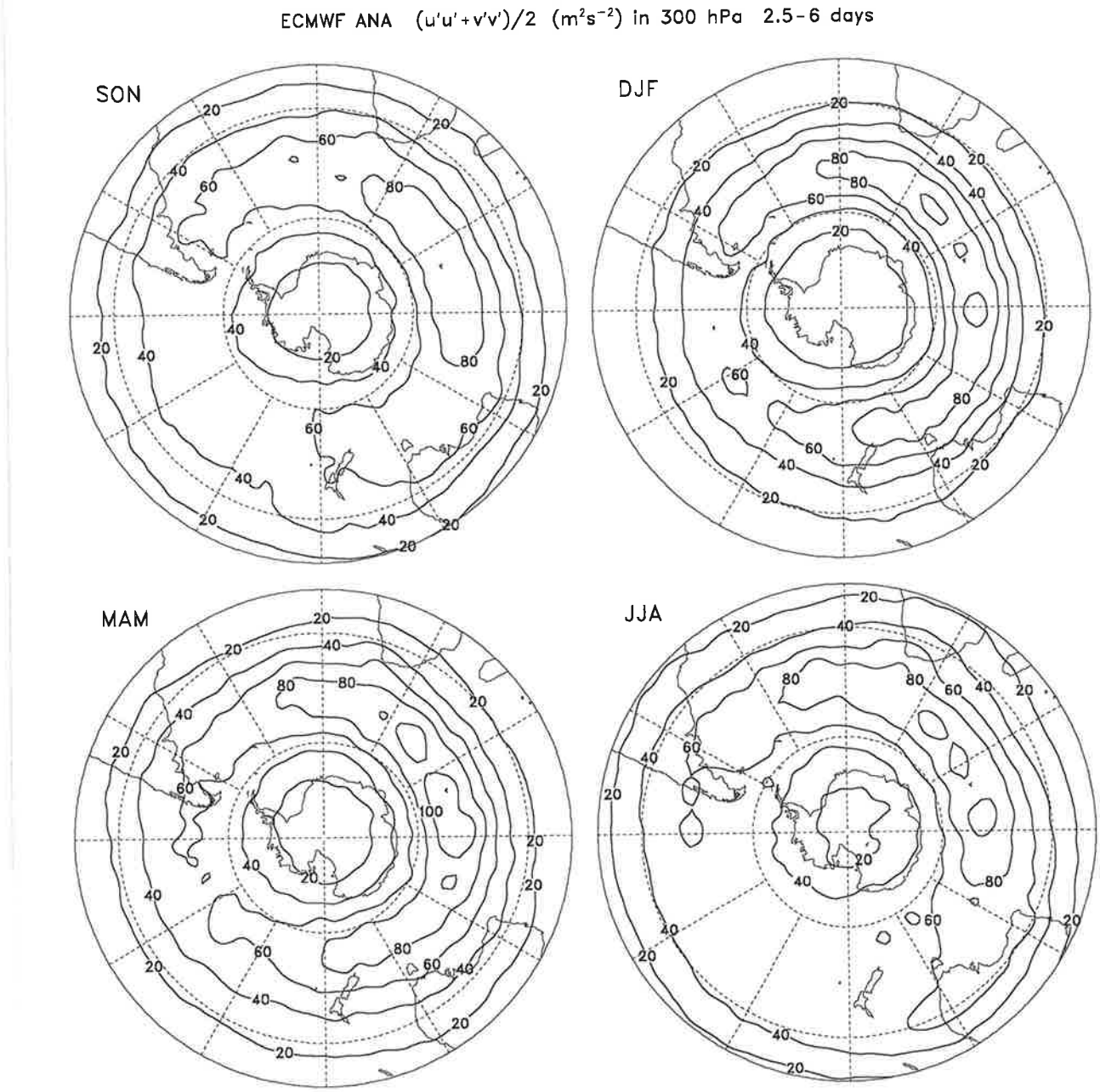

Fig. 4.4.29. As Fig. 4.4.28 but for the band-pass filtered transient fluctuations. The contour interval is 20 m^2/s^2.

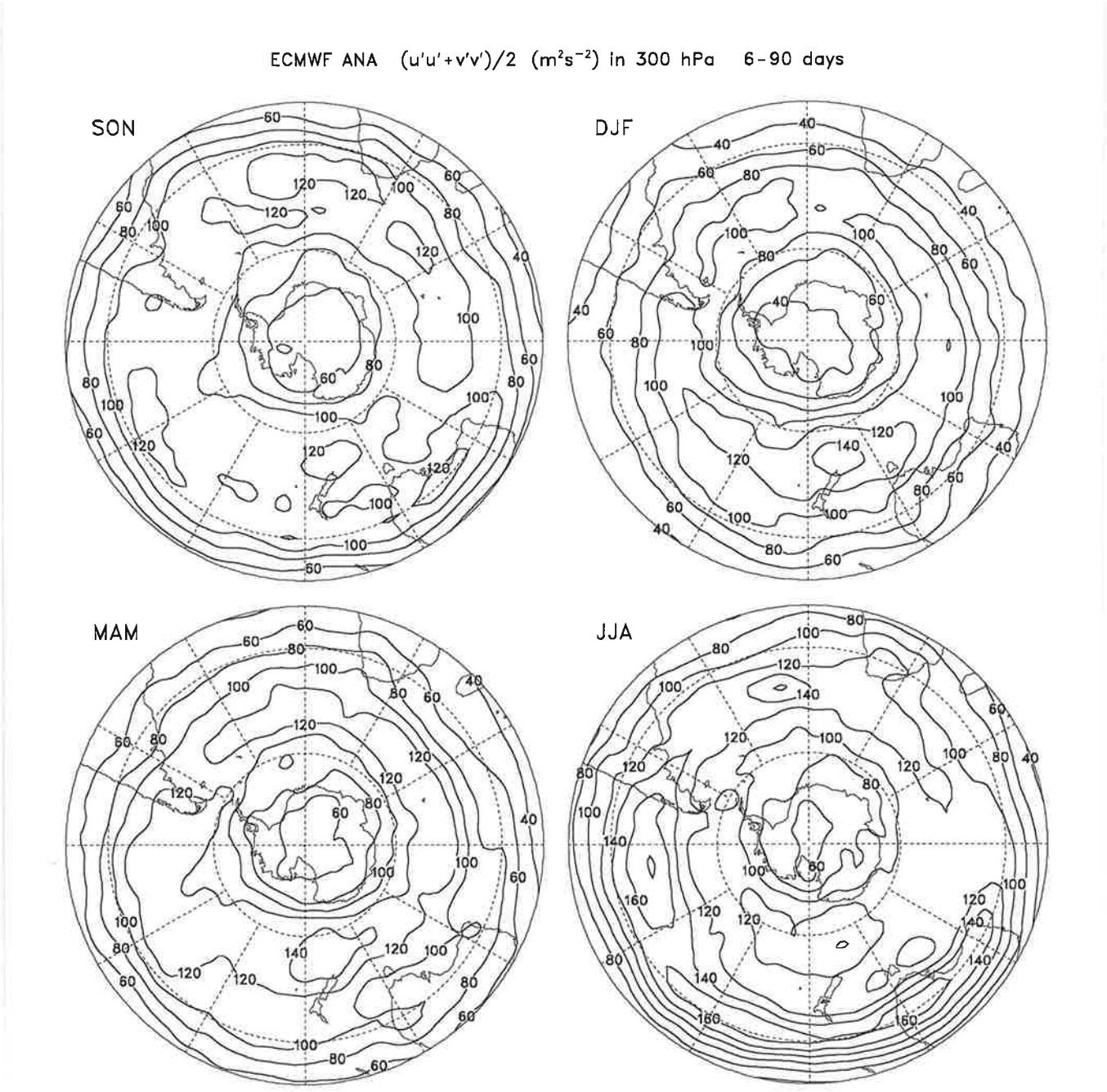

Fig. 4.4.30. As Fig. 4.4.28 but for the low-pass filtered transient fluctuations. The contour interval is 20 m^2/s^2.

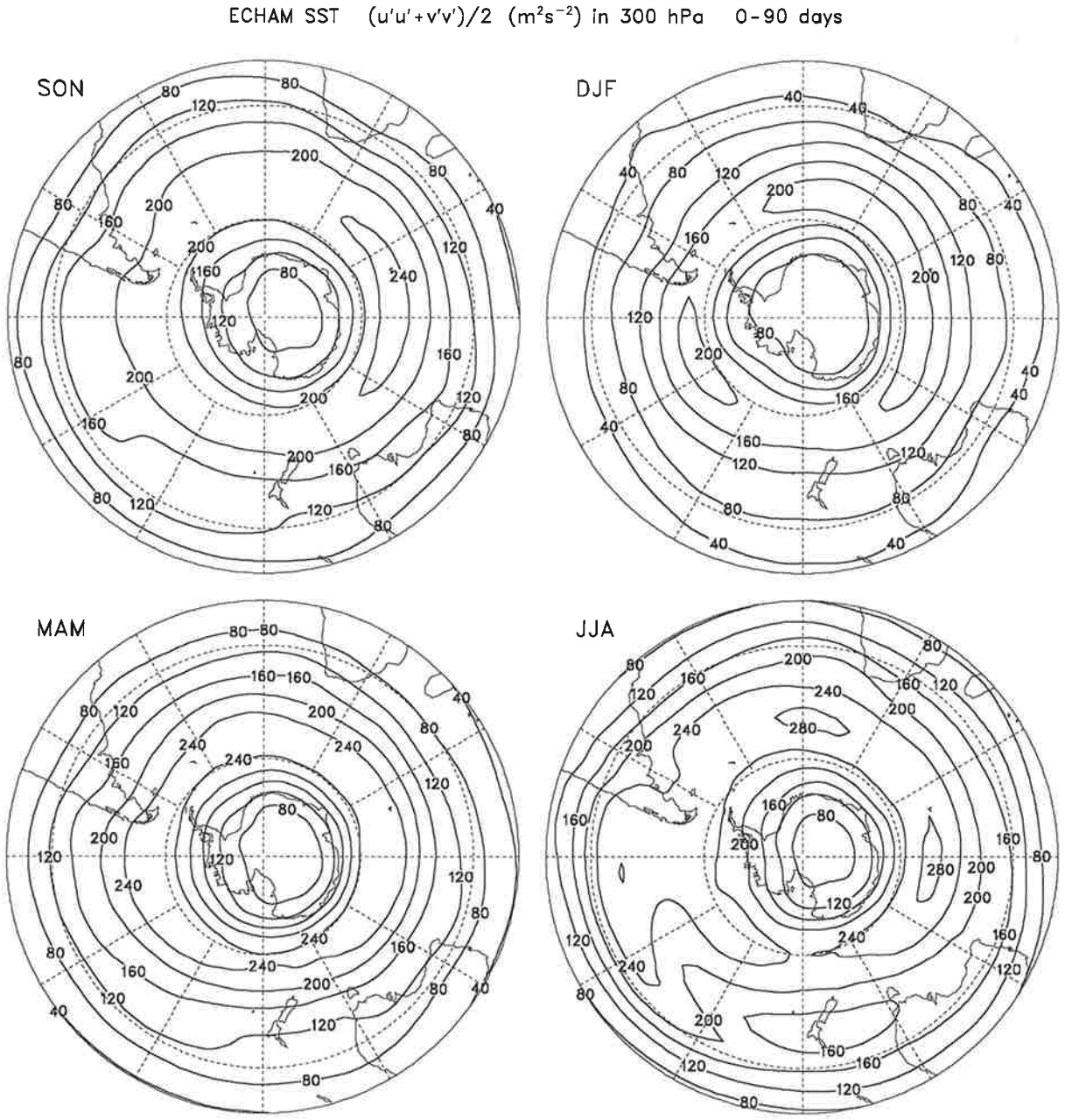

Fig. 4.4.31. As Fig. 4.4.28 but for the simulations performed with ECHAM3 with varying Sea Surface Temperatures as boundary forcing.

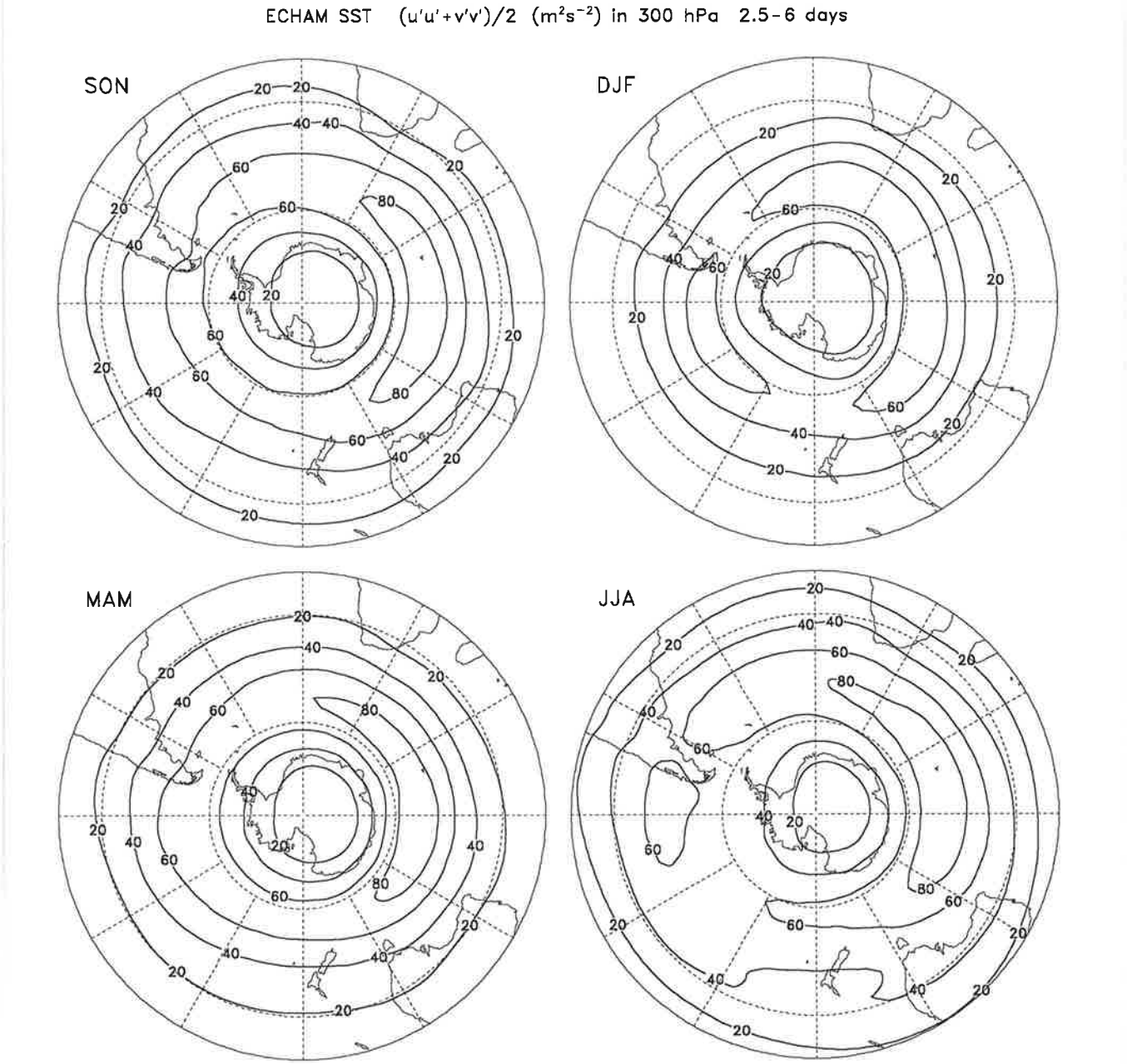

Fig. 4.4.32. As Fig. 4.4.31 but for the band-pass filtered transient fluctuations. The contour interval is 20 m^2/s^2.

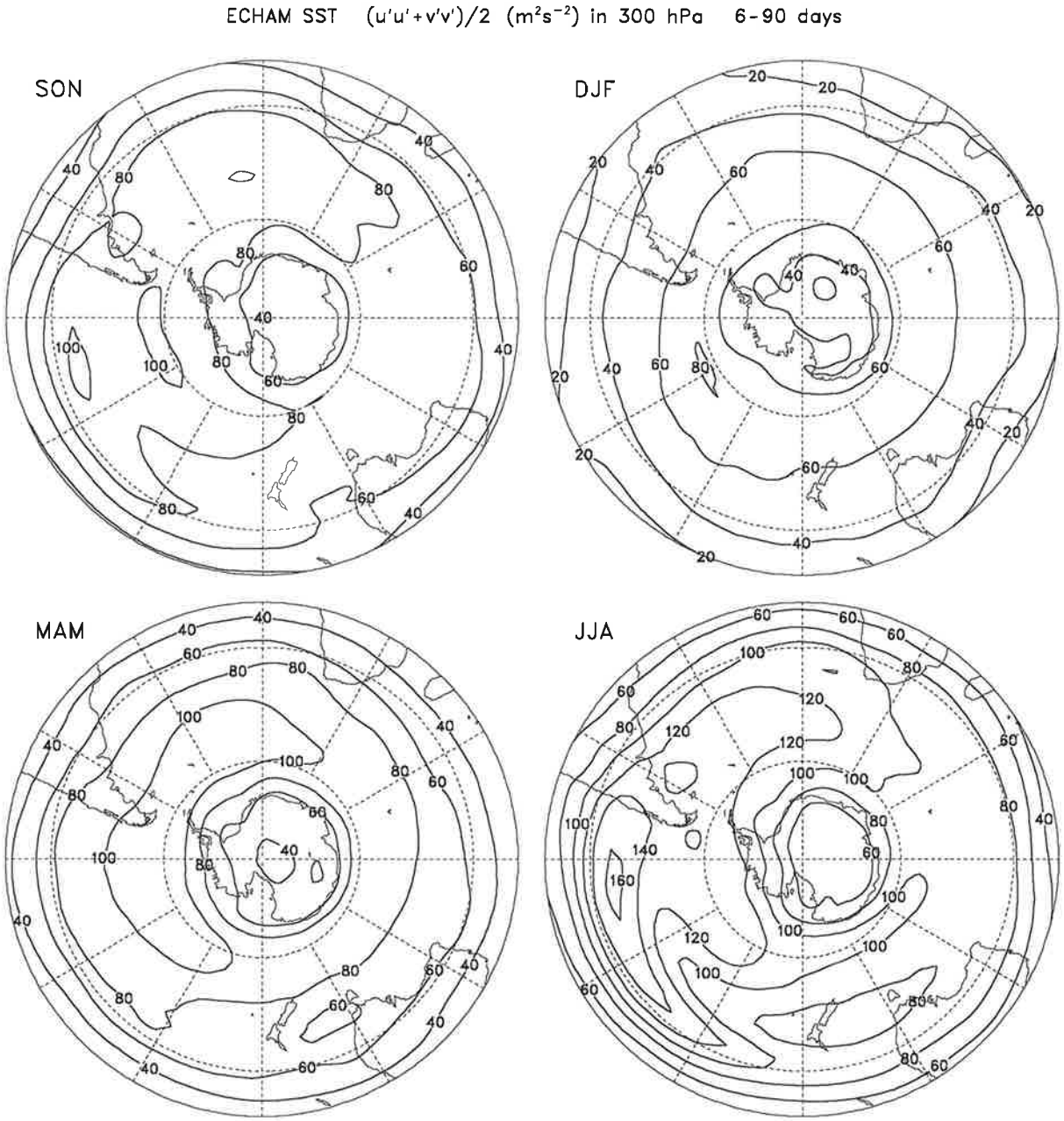

Fig. 4.4.33. As Fig. 4.4.31 but for the low-pass filtered transient fluctuations. The contour interval is 20 m^2/s^2.

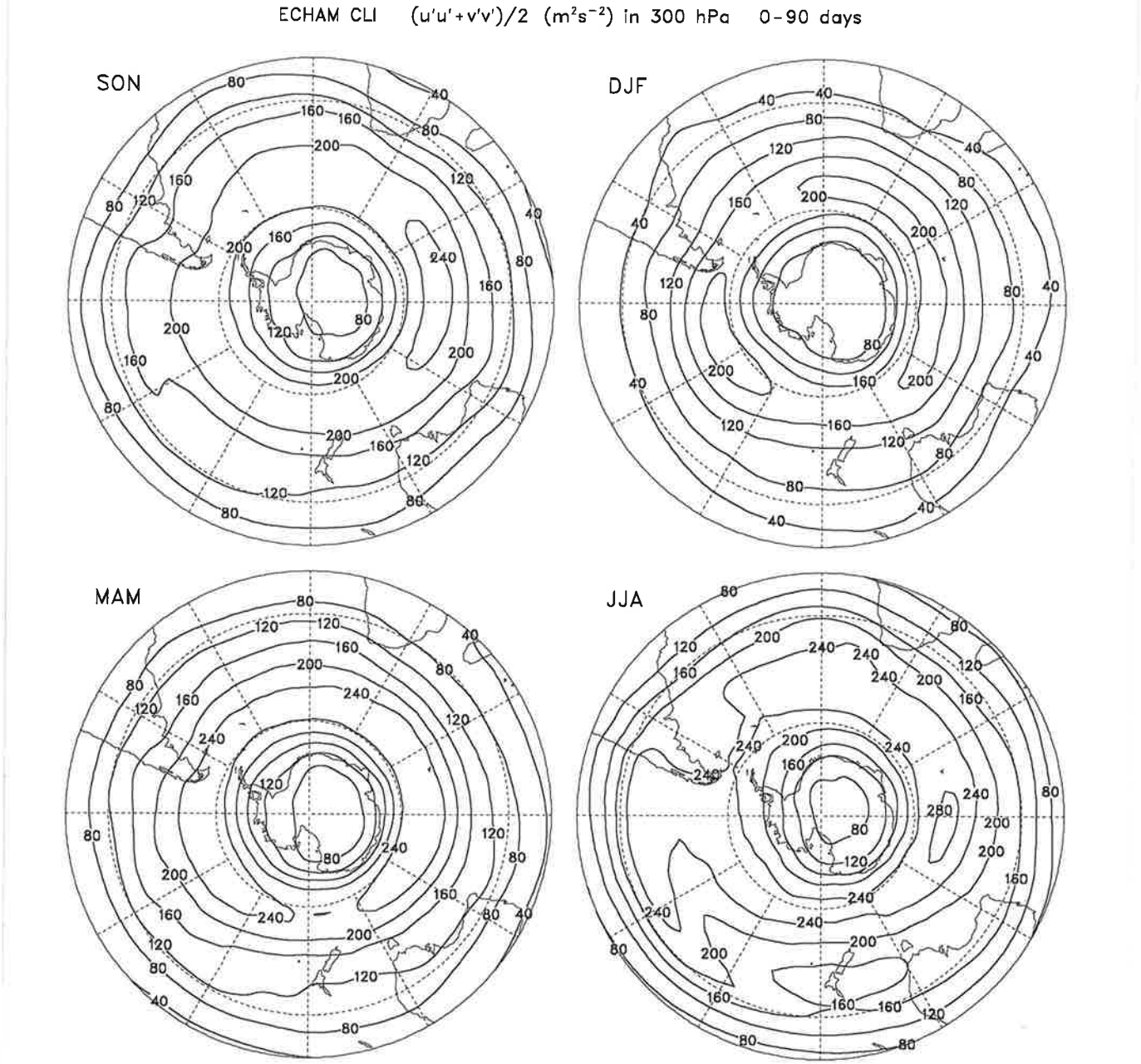

Fig. 4.4.34. As Fig. 4.4.28 but for the simulations performed with ECHAM3 with fixed Sea Surface Temperatures as boundary forcing.

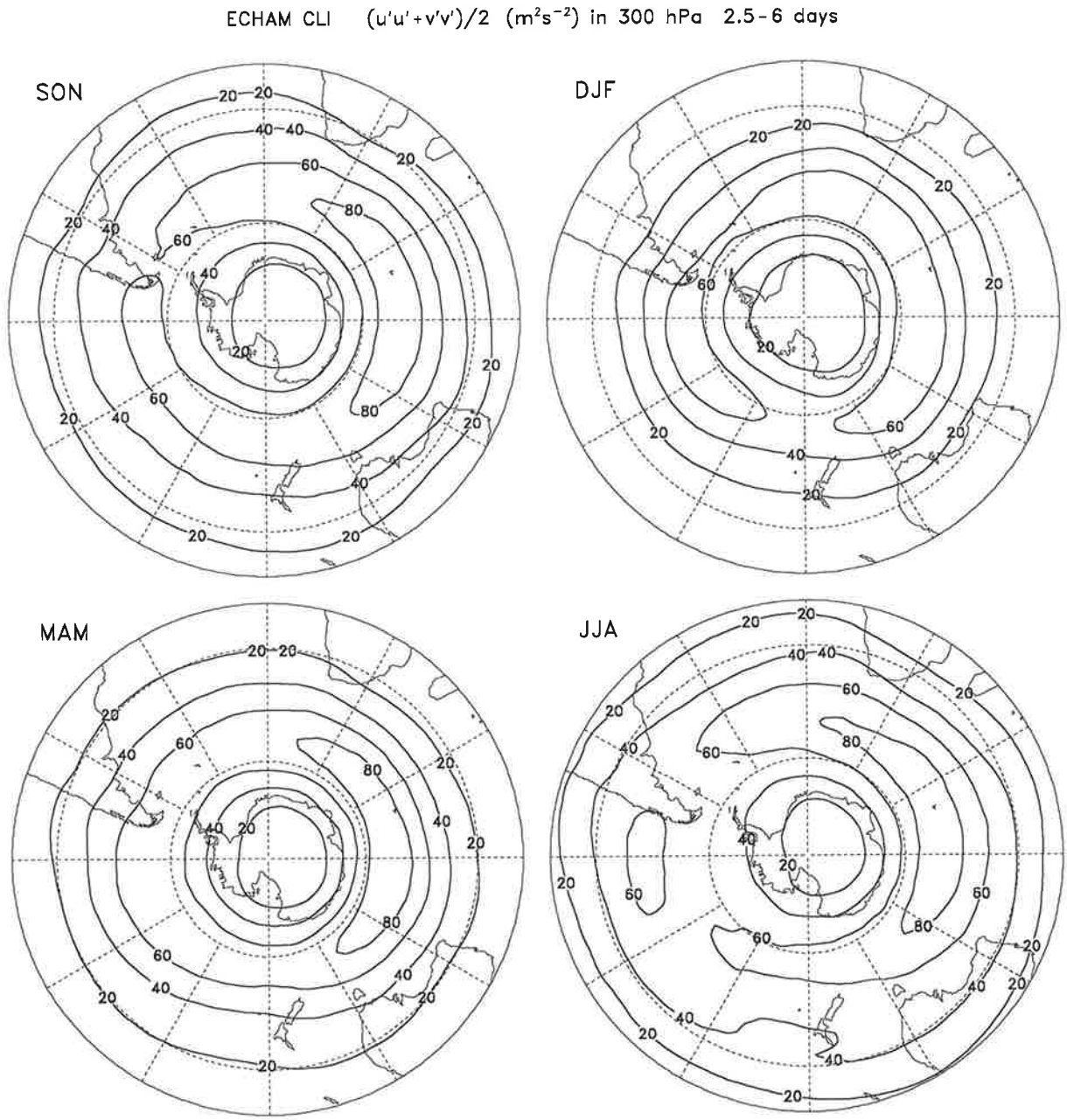

Fig. 4.4.35. As Fig. 4.4.34 but for the band-pass filtered transient fluctuations. The contour interval is 20 m^2/s^2.

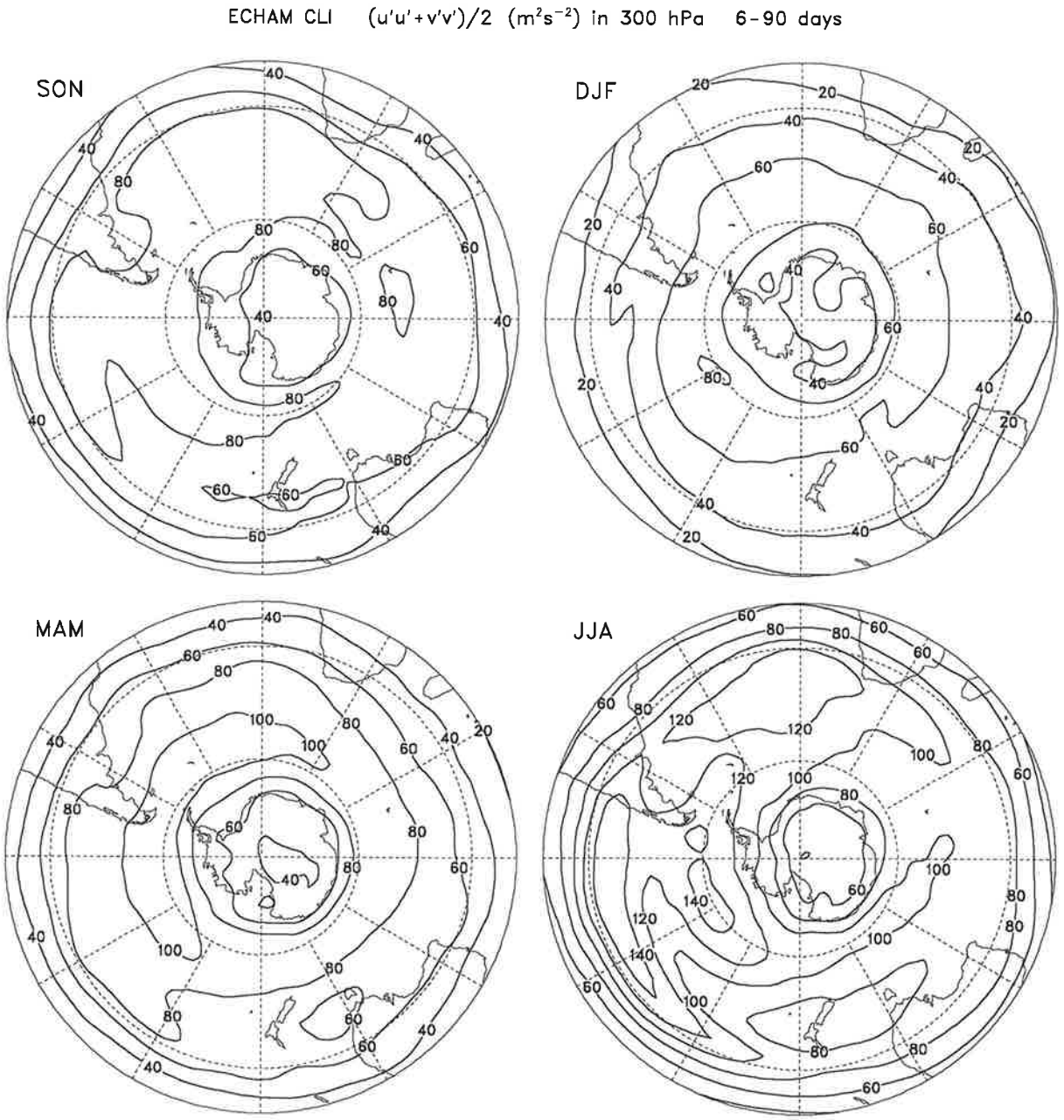

Fig. 4.4.36. As Fig. 4.4.34 but for the low-pass filtered transient fluctuations. The contour interval is 20 m^2/s^2.

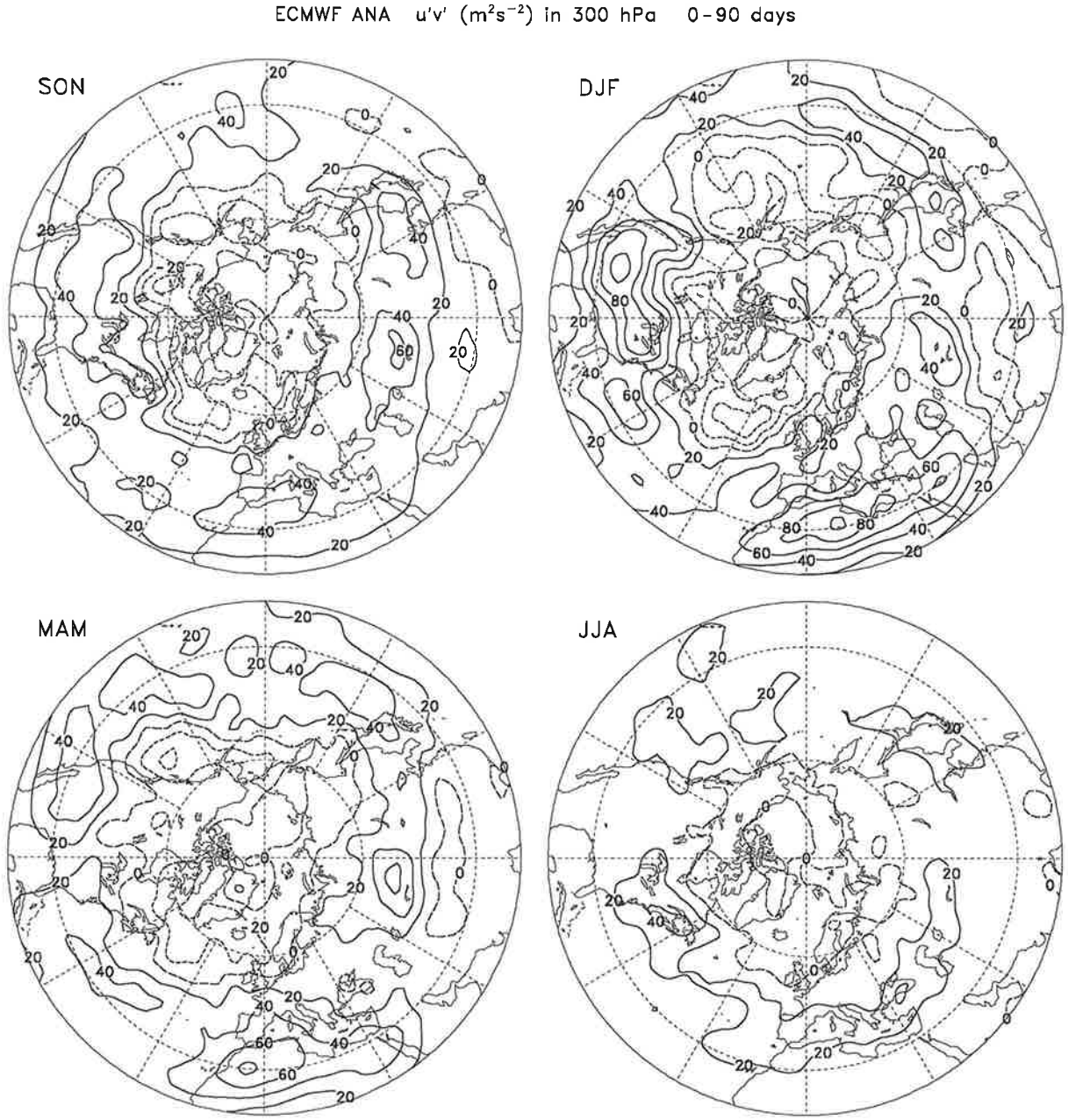

Fig. 4.4.37. Meridional transport of westerly momentum at 300 hPa due to unfiltered transient fluctuations obtained from the ECMWF analyses distinguishing between seasons. Positive values (solid contour lines) indicate poleward, negative ones (dashed contour lines) indicate equatorward momentum fluxes. Units are m^2/s^2, the contour interval is 20 m^2/s^2.

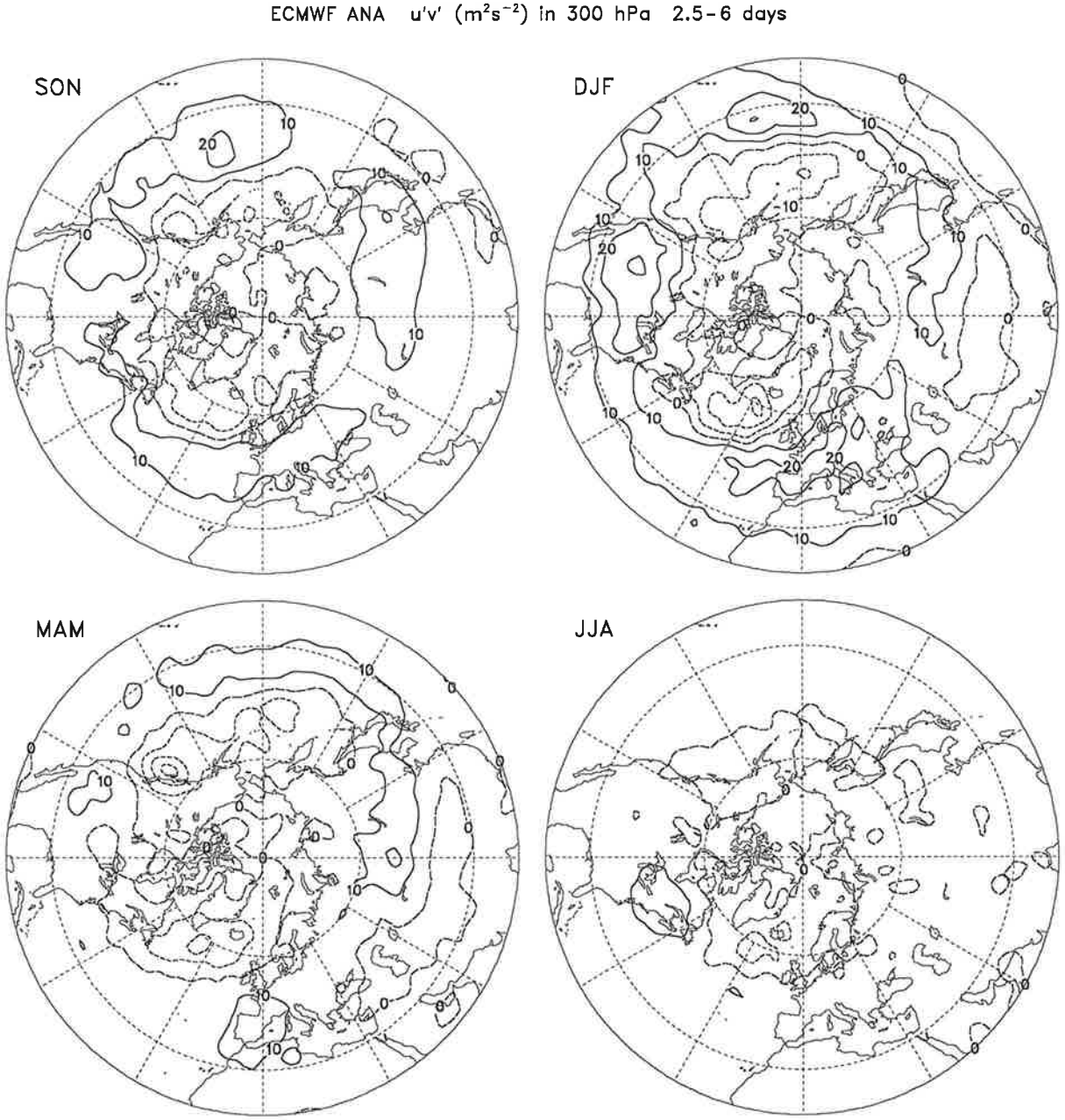

Fig. 4.4.38. As Fig. 4.4.37 but for the band-pass filtered transient fluctuations. The contour interval is 10 m^2/s^2.

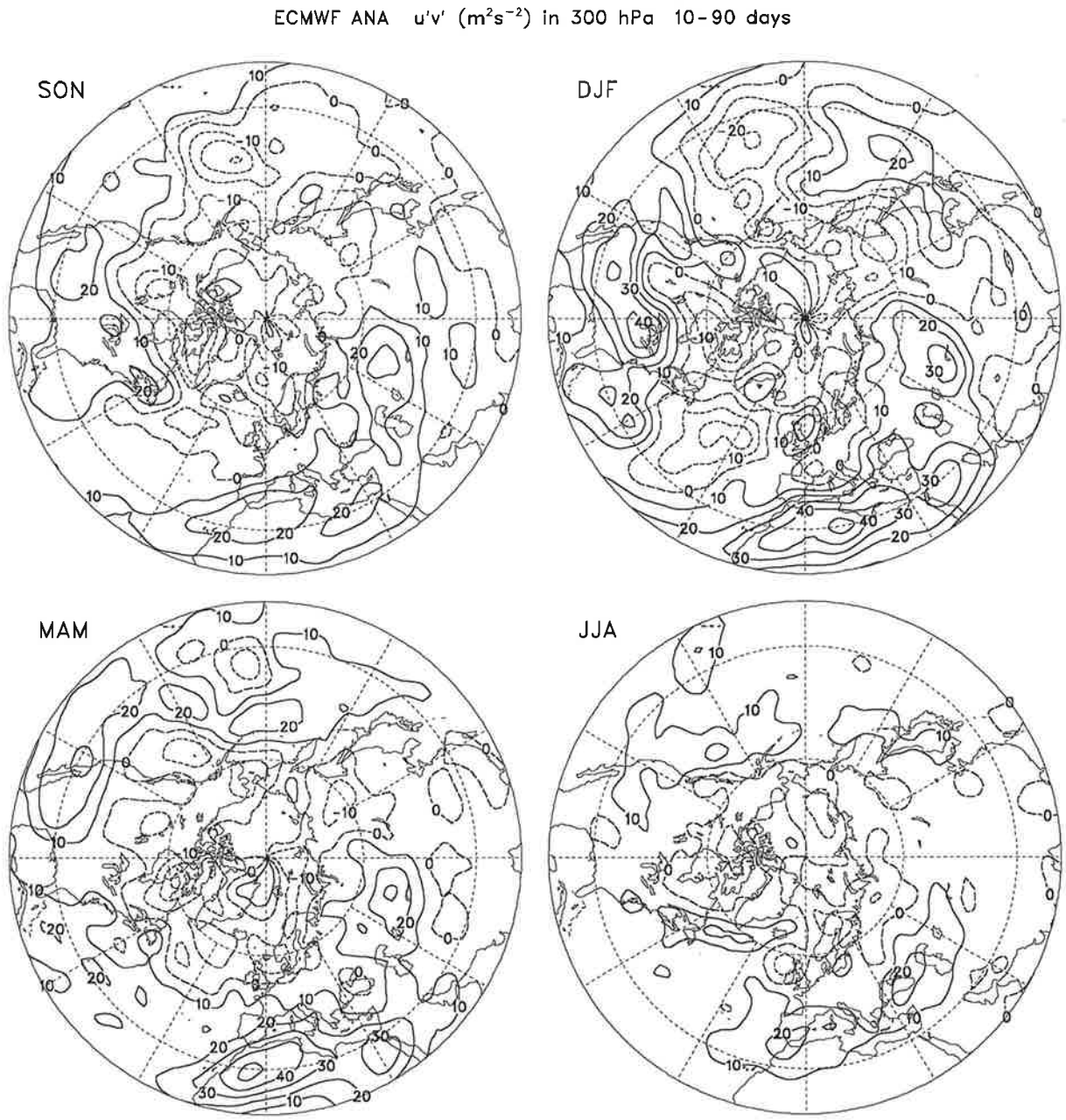

Fig. 4.4.39. As Fig. 4.4.37 but for the low-pass filtered transient fluctuations. The contour interval is 10 m^2/s^2.

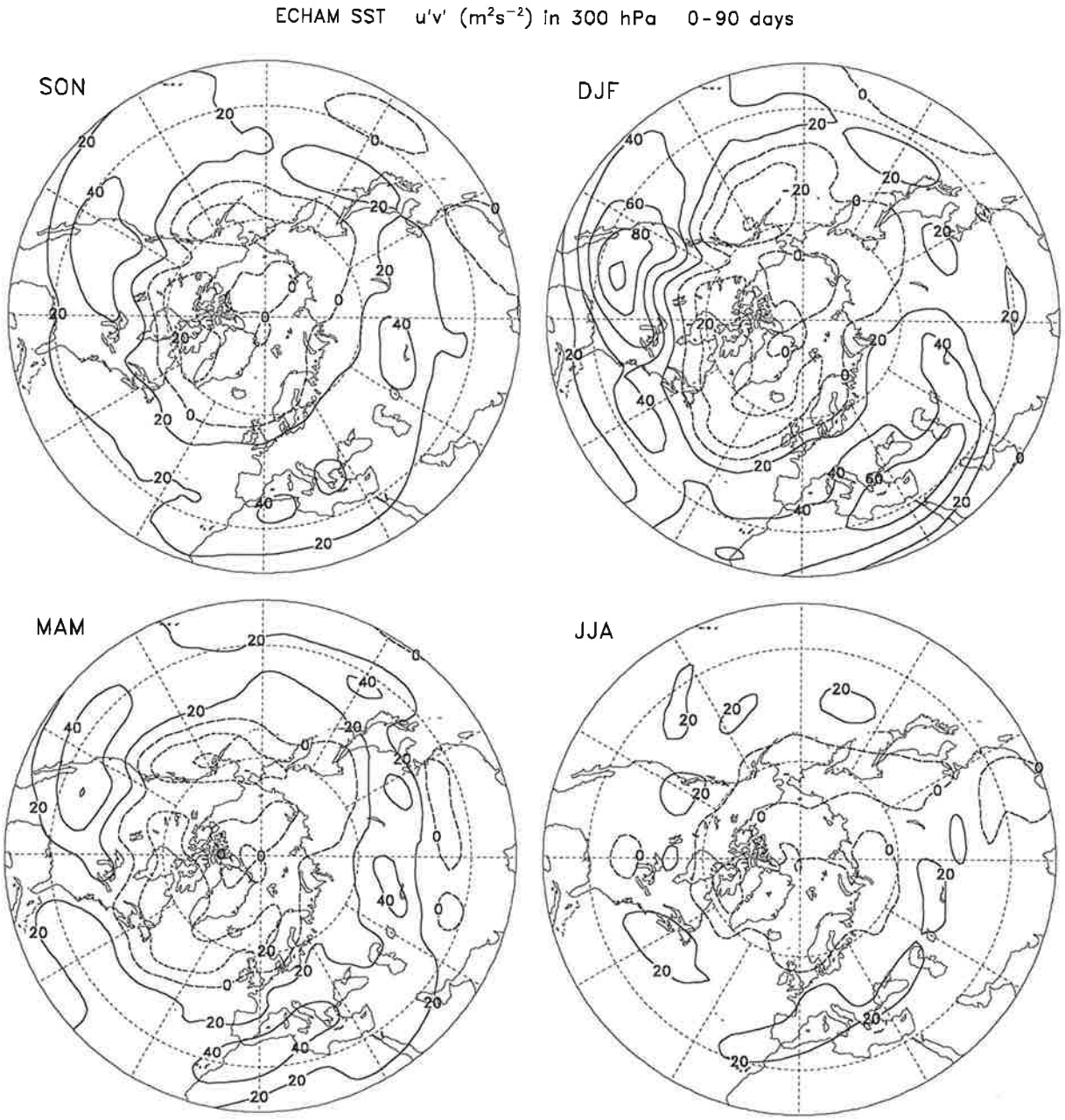

Fig. 4.4.40. As Fig. 4.4.37 but for the simulations performed with ECHAM3 with varying Sea Surface Temperatures as boundary forcing.

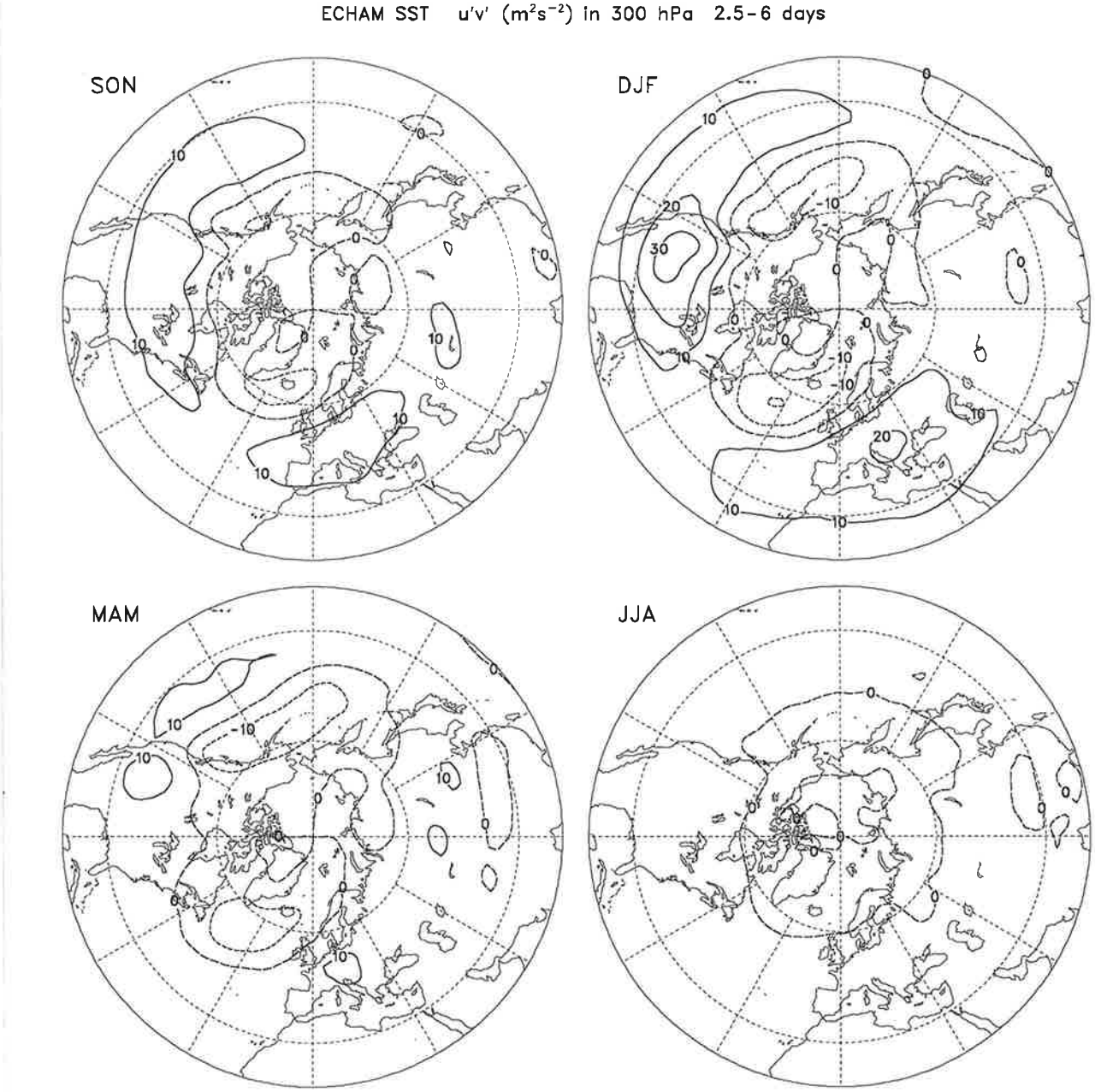

Fig. 4.4.41. As Fig. 4.4.40 but for the band-pass filtered transient fluctuations. The contour interval is 10 m^2/s^2.

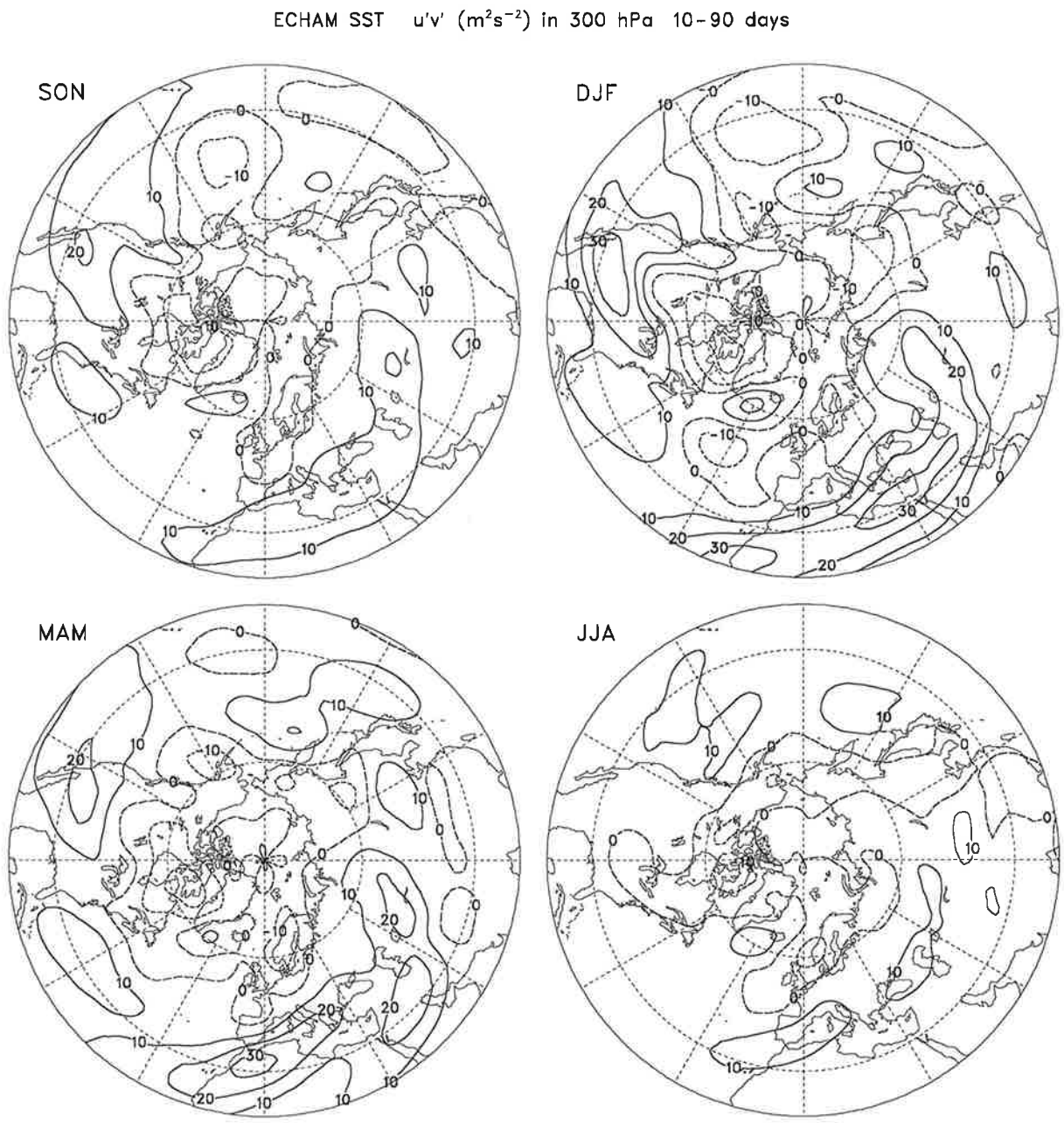

Fig. 4.4.42. As Fig. 4.4.40 but for the low-pass filtered transient fluctuations. The contour interval is 10 m^2/s^2.

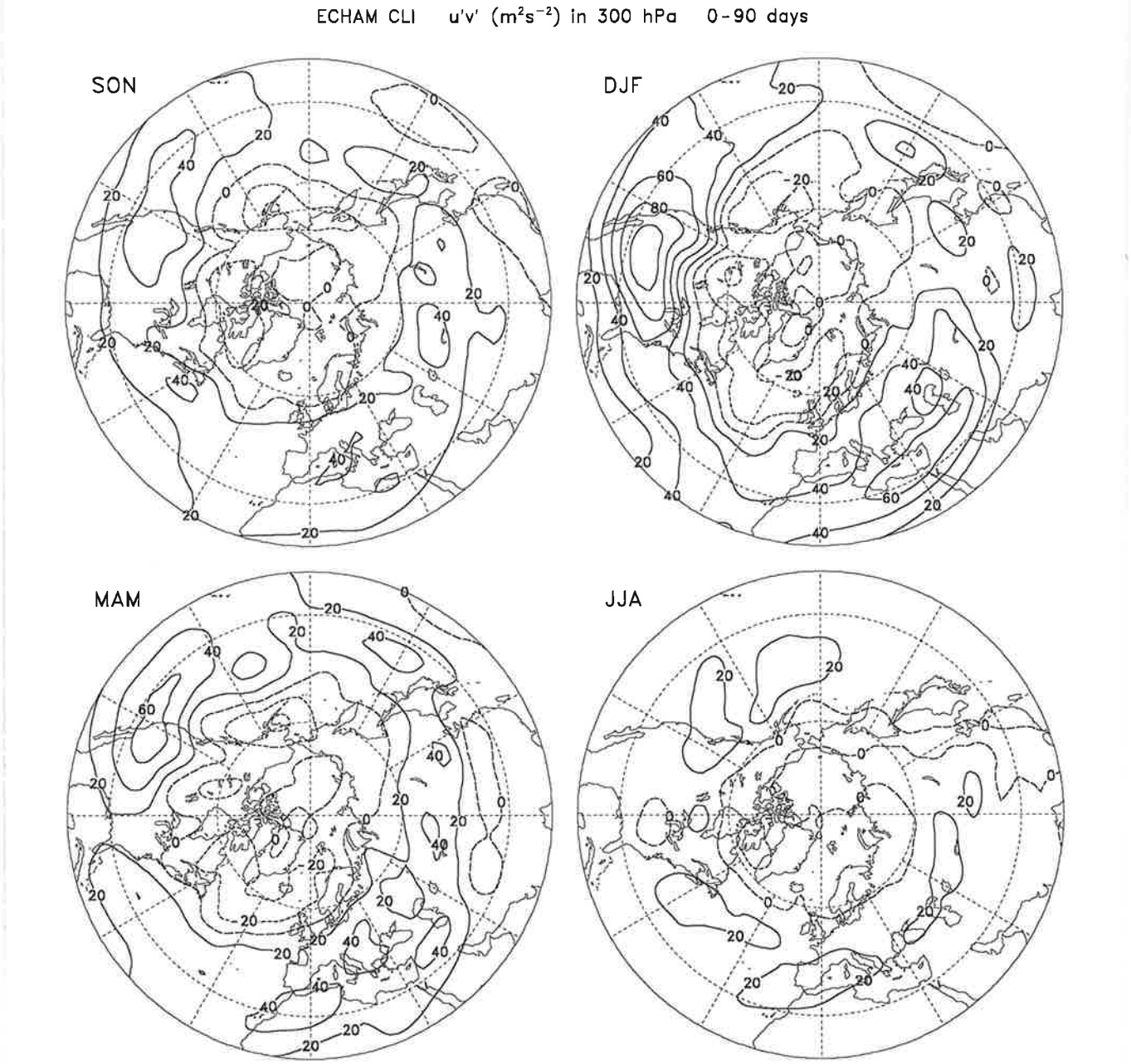

Fig. 4.4.43. As Fig. 4.4.37 but for the simulations performed with ECHAM3 with fixed Sea Surface Temperatures as boundary forcing.

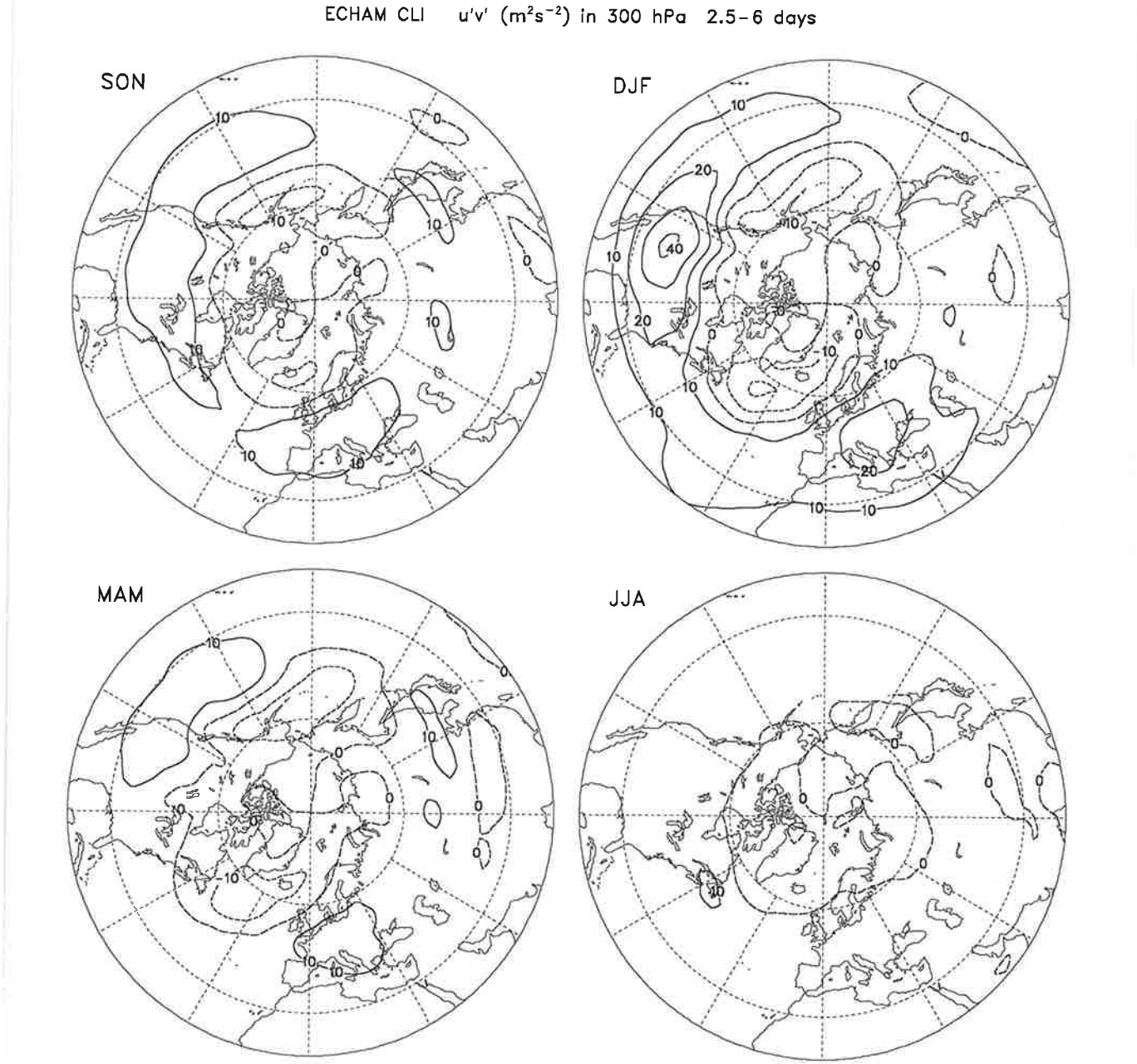

Fig. 4.4.44. As Fig. 4.4.43 but for the band-pass filtered transient fluctuations. The contour interval is 10 m^2/s^2.

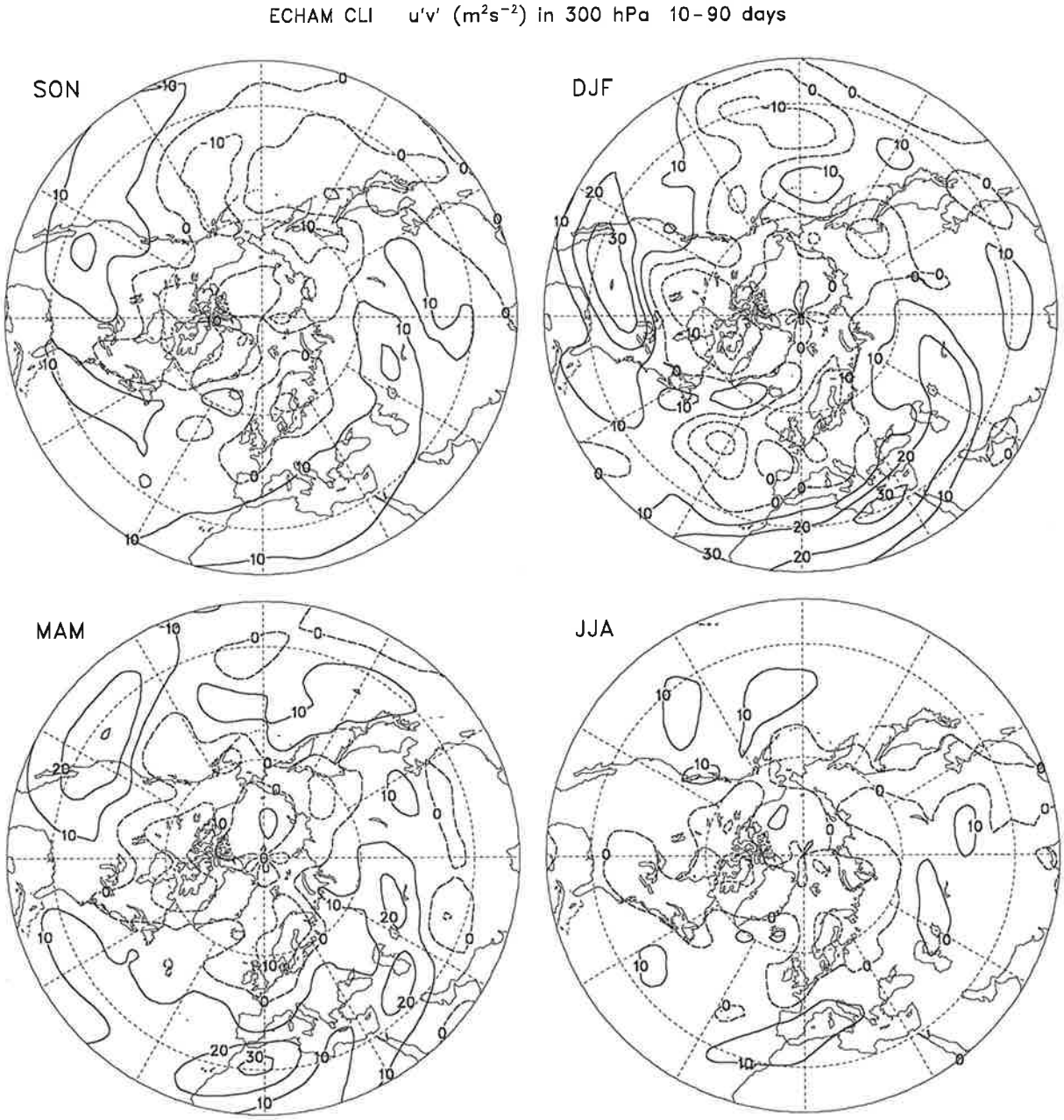

Fig. 4.4.45. As Fig. 4.4.43 but for the low-pass filtered transient fluctuations. The contour interval is 10 m^2/s^2.

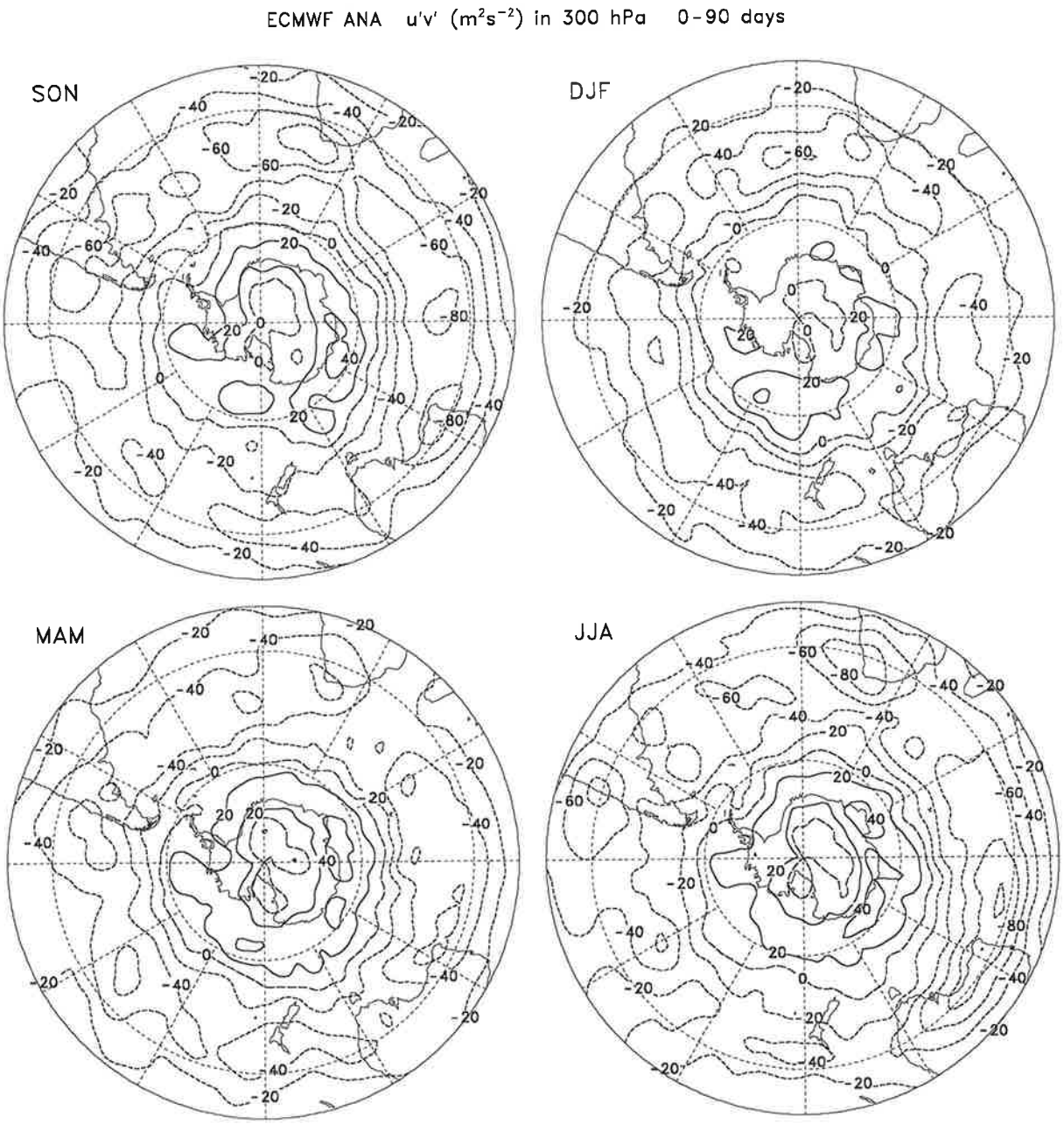

Fig. 4.4.46. Meridional transport of westerly momentum at 300 hPa due to unfiltered transient fluctuations obtained from the ECMWF analyses distinguishing between seasons. Negative values (dashed contour lines) indicate poleward, positive ones (solid contour lines) indicate equatorward momentum fluxes. Units are m^2/s^2, the contour interval is 20 m^2/s^2.

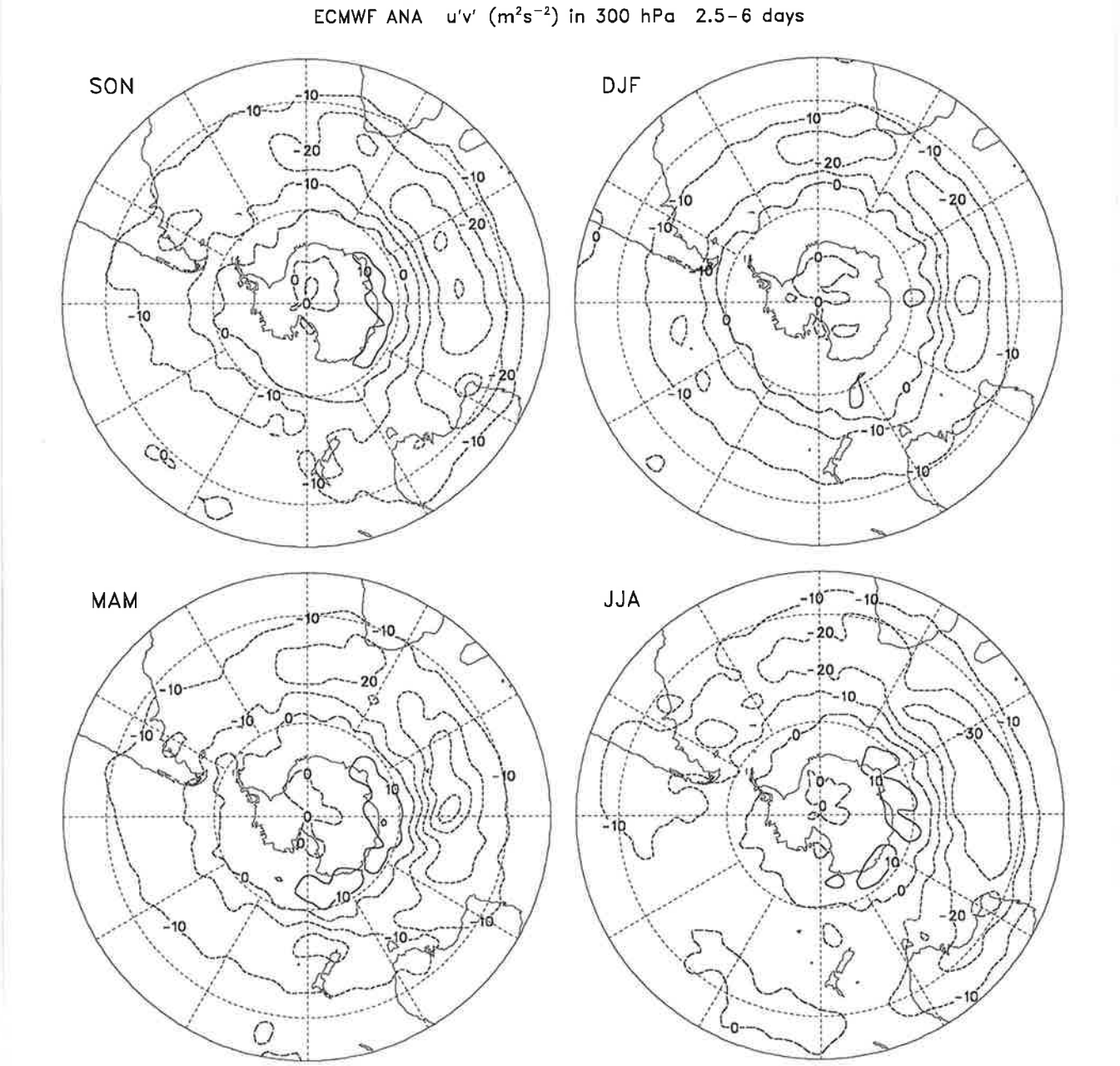

Fig. 4.4.47. As Fig. 4.4.46 but for the band-pass filtered transient fluctuations. The contour interval is 10 m^2/s^2.

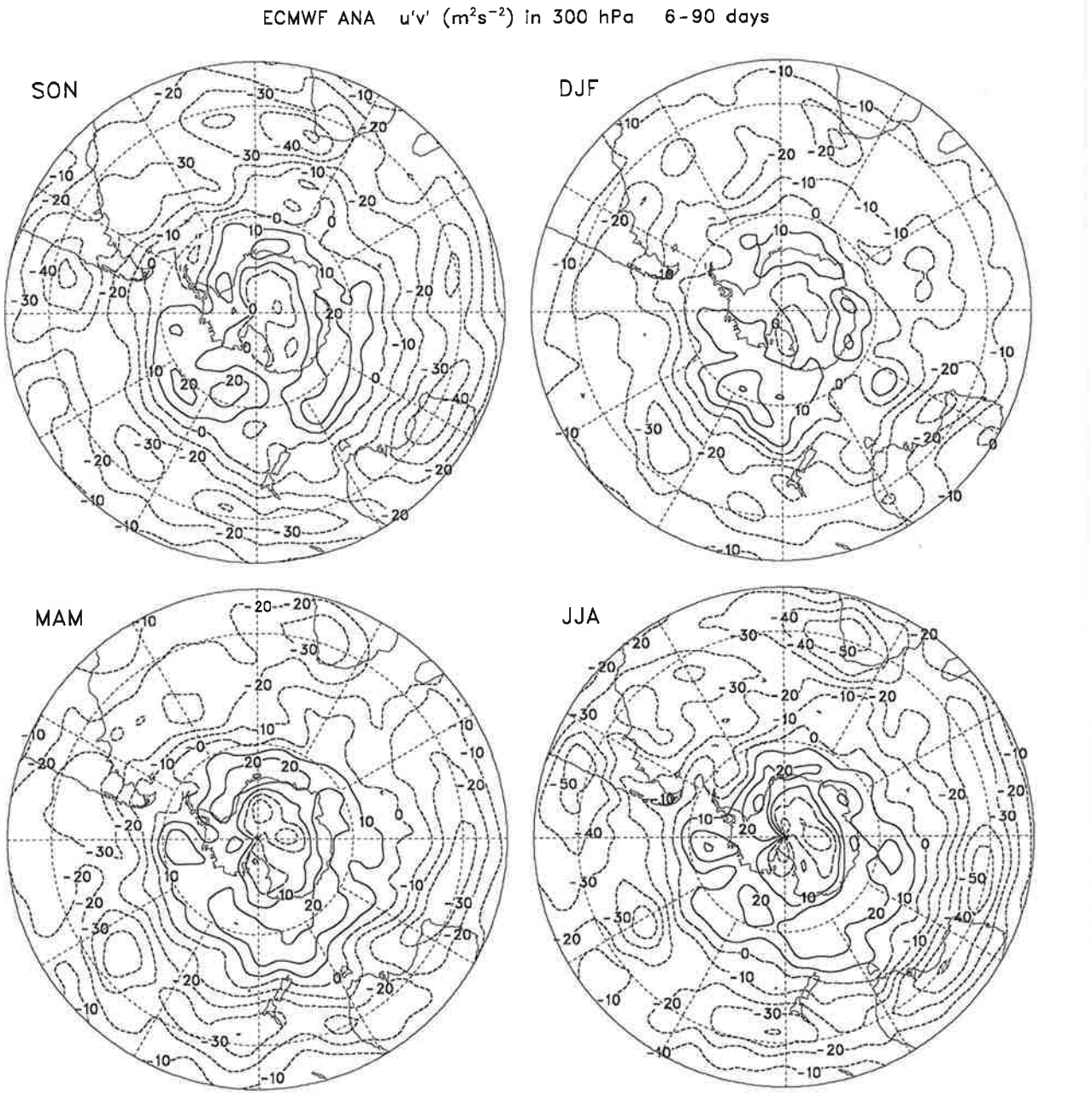

Fig. 4.4.48. As Fig. 4.4.46 but for the low-pass filtered transient fluctuations. The contour interval is 10 m^2/s^2.

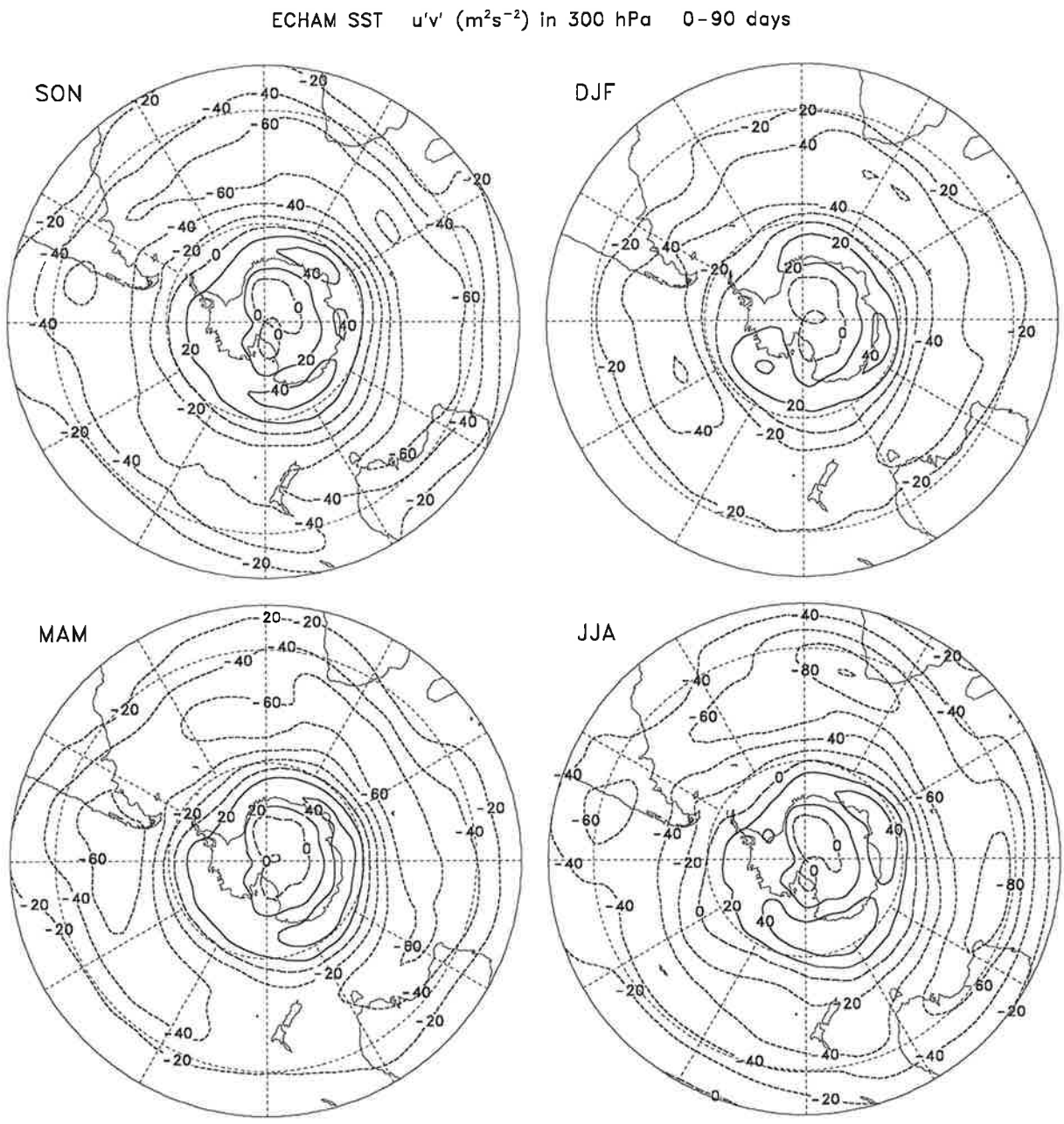

Fig. 4.4.49. As Fig. 4.4.46 but for the simulations performed with ECHAM3 with varying Sea Surface Temperatures as boundary forcing.

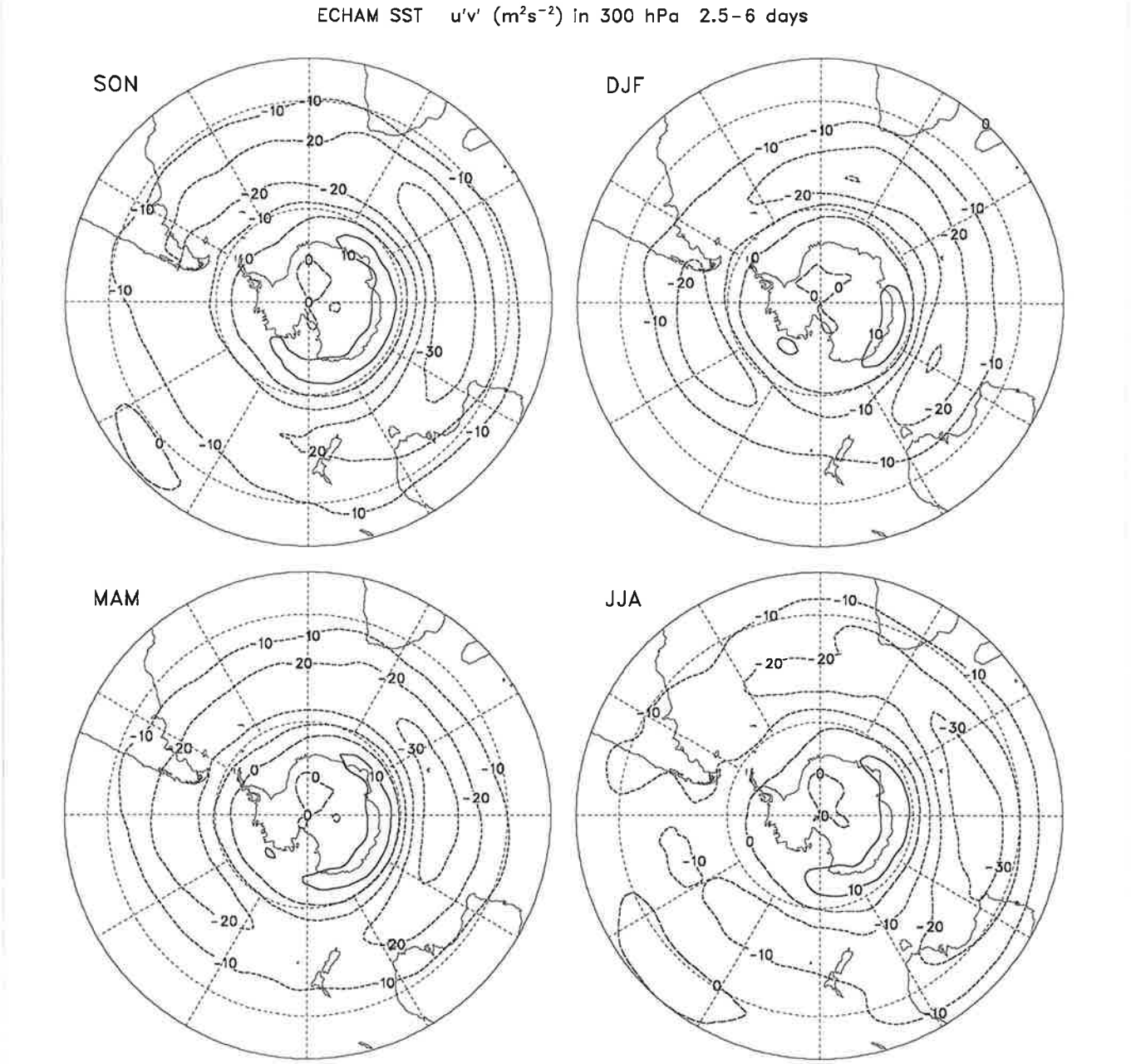

Fig. 4.4.50. As Fig. 4.4.49 but for the band-pass filtered transient fluctuations. The contour interval is 10 m^2/s^2.

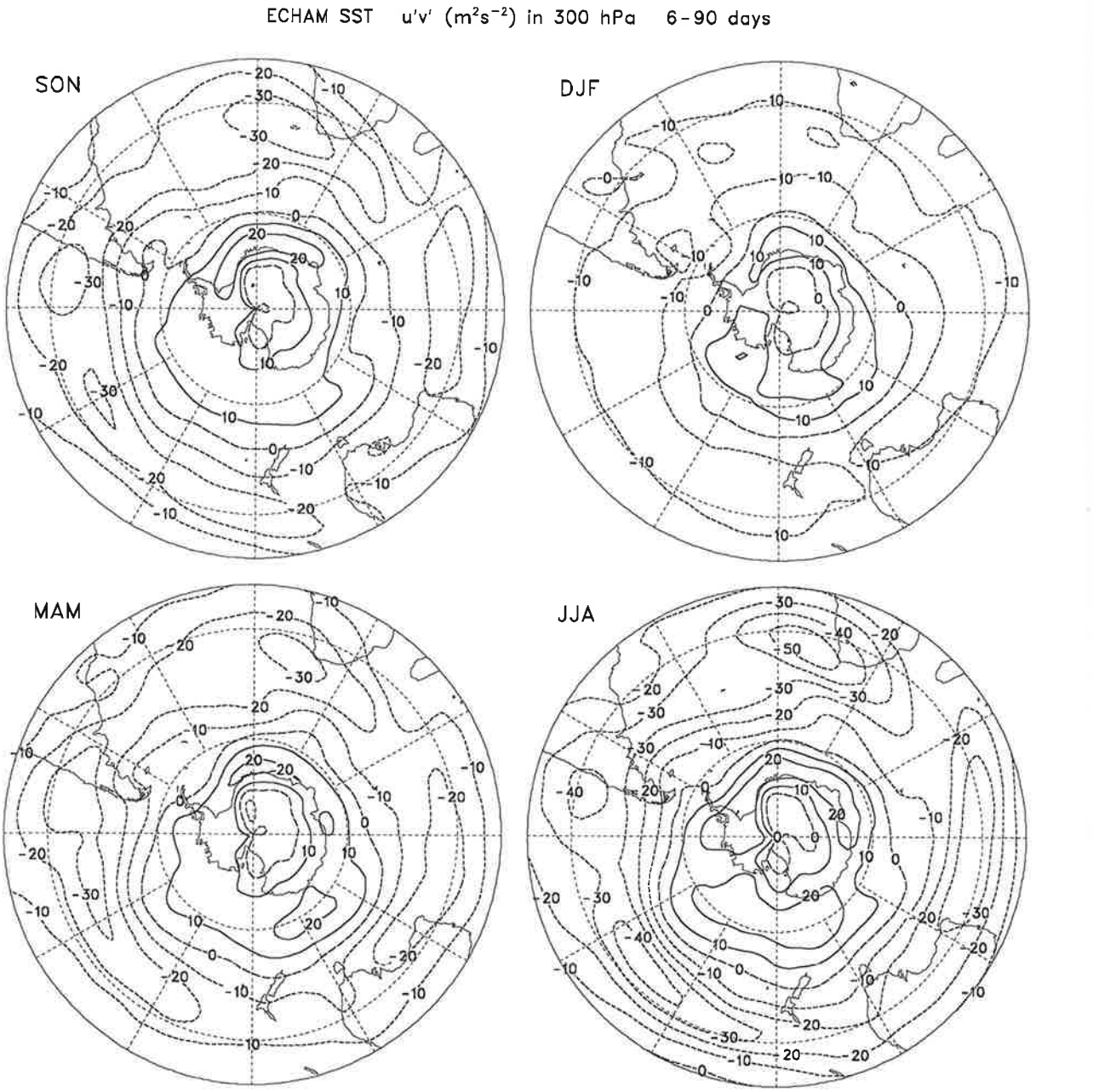

Fig. 4.4.51. As Fig. 4.4.49 but for the low-pass filtered transient fluctuations. The contour interval is 10 m^2/s^2.

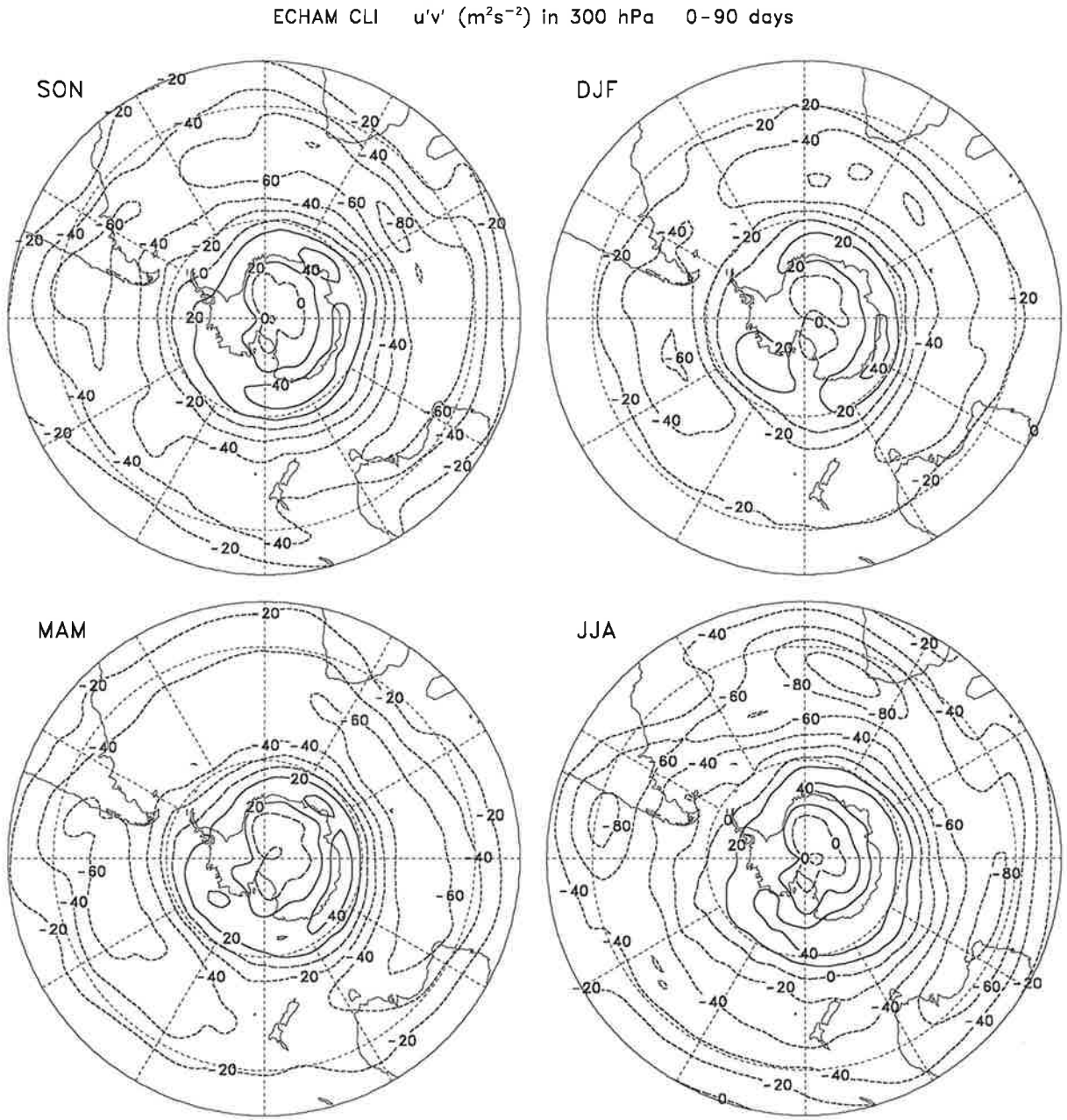

Fig. 4.4.52. As Fig. 4.4.46 but for the simulations performed with ECHAM3 with fixed Sea Surface Temperatures as boundary forcing.

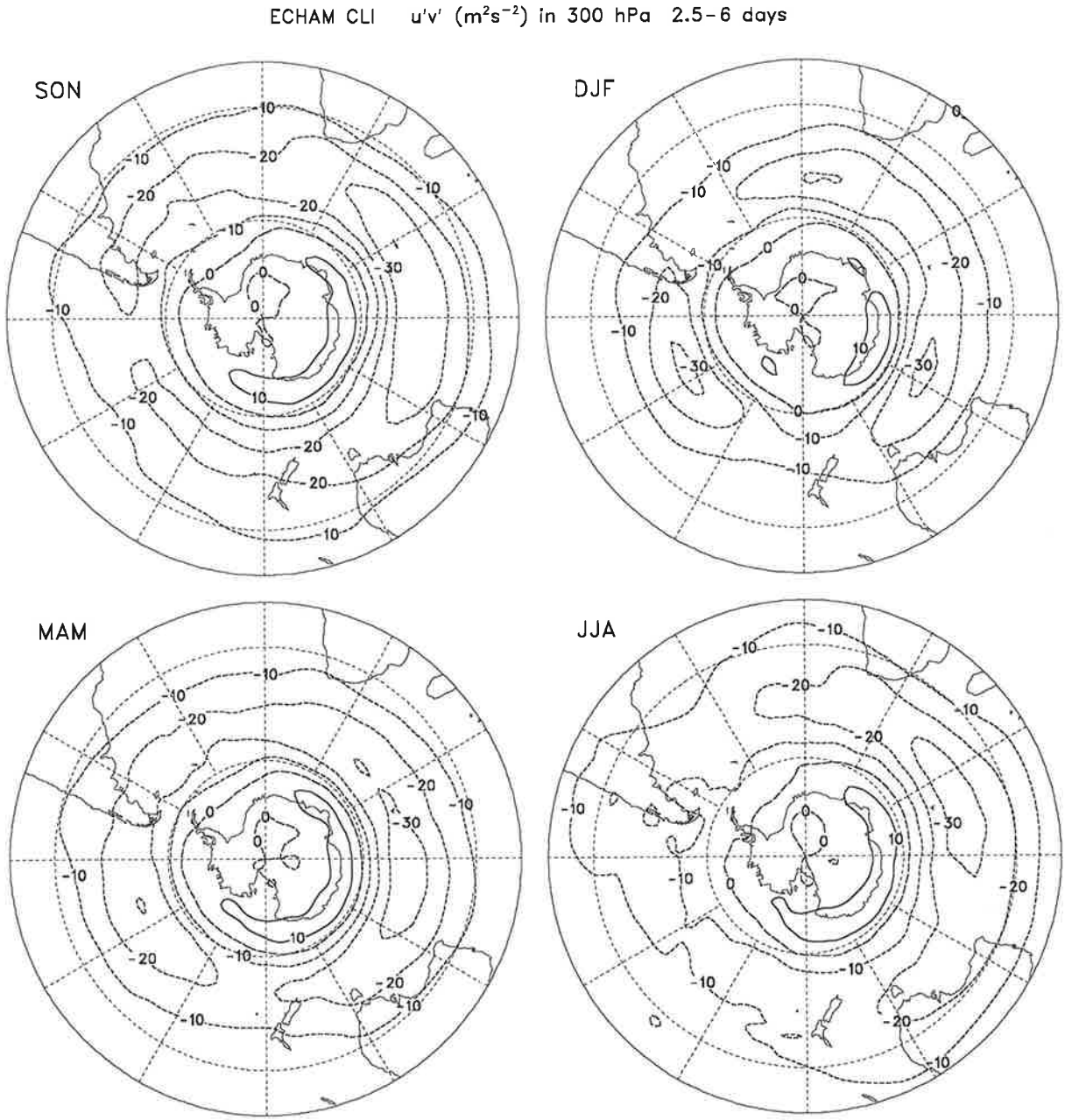

Fig. 4.4.53. As Fig. 4.4.52 but for the band-pass filtered transient fluctuations. The contour interval is 10 m^2/s^2.

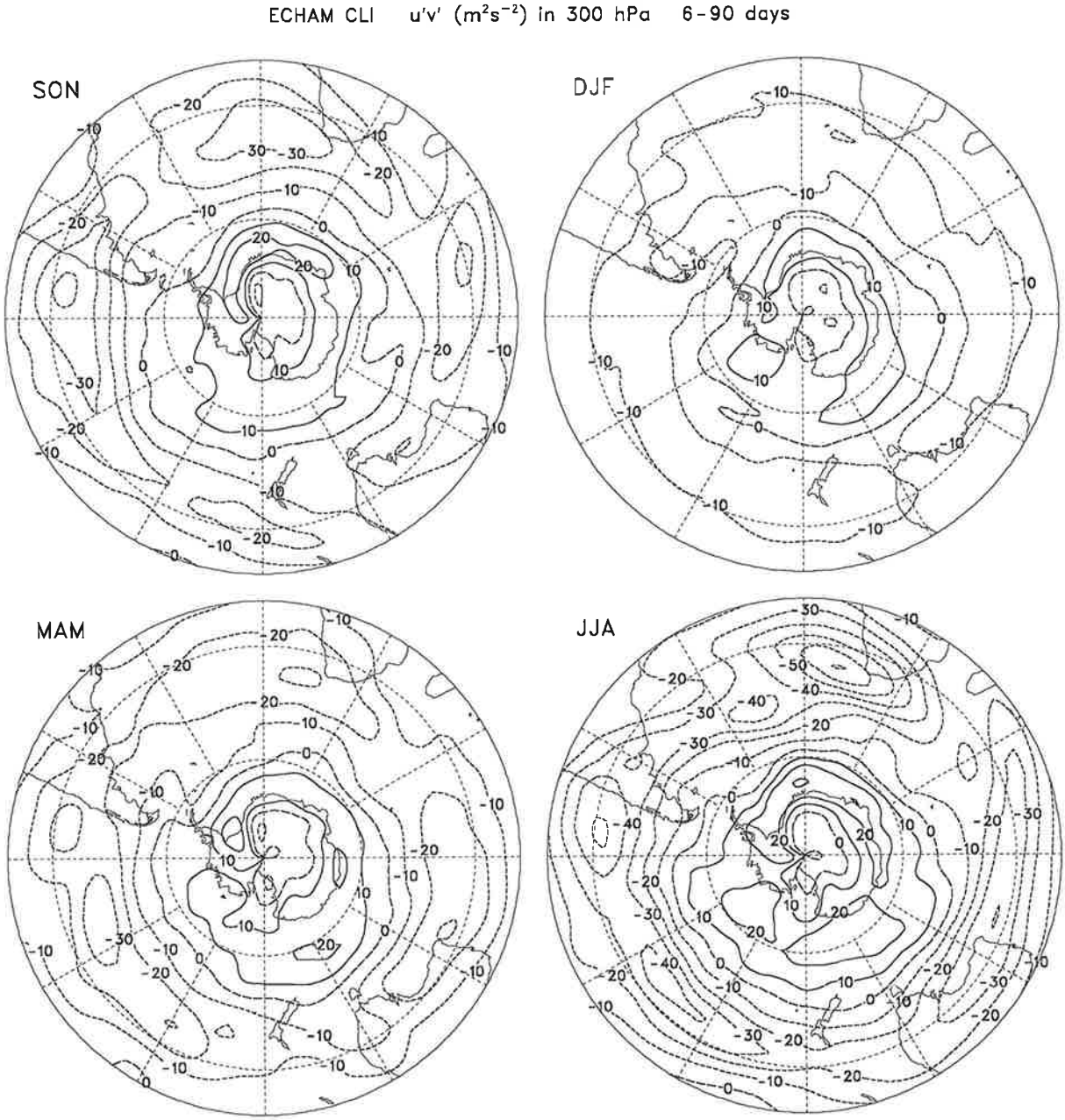

Fig. 4.4.54. As Fig. 4.4.52 but for the low-pass filtered transient fluctuations. The contour interval is 10 m^2/s^2.

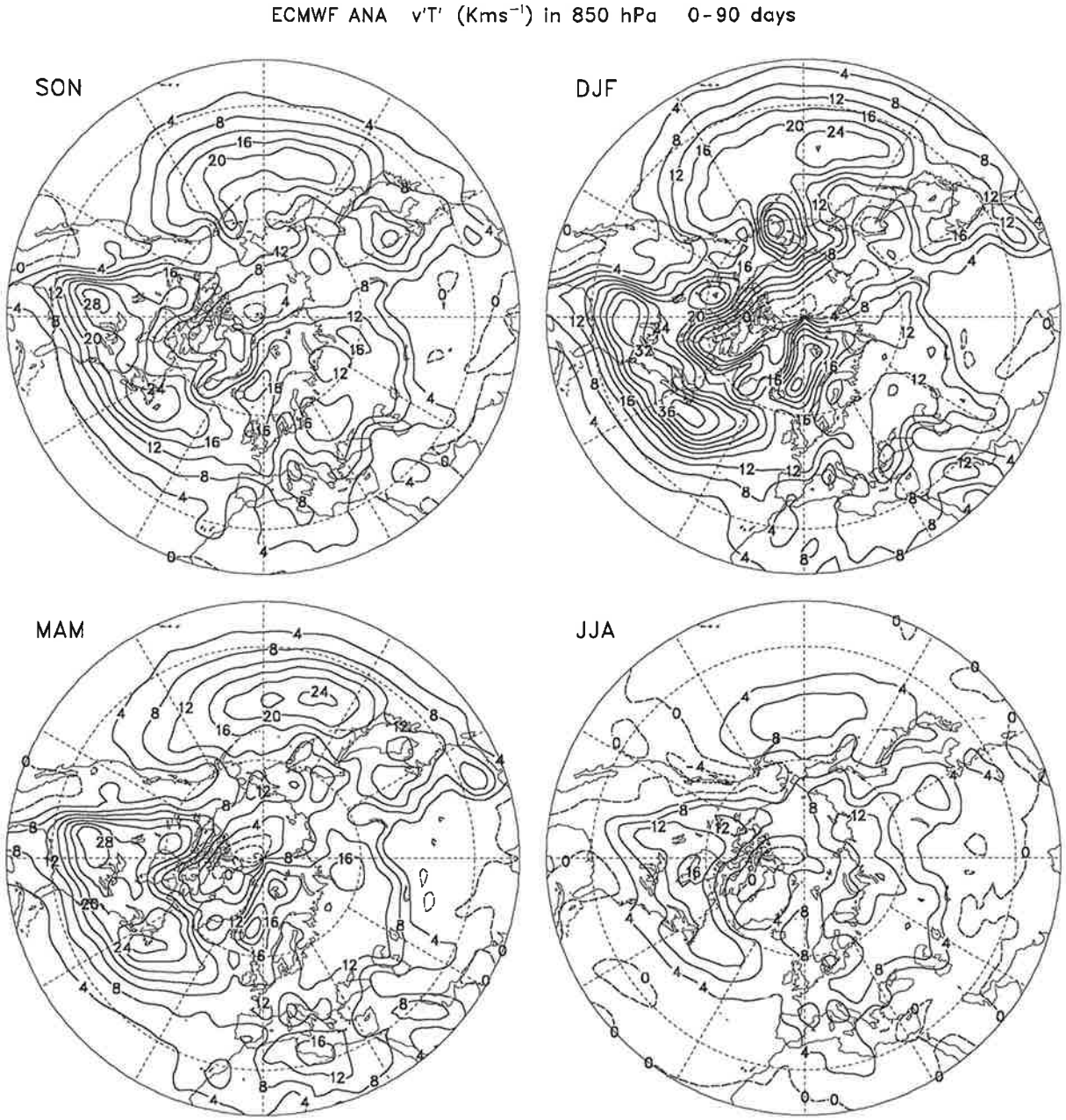

Fig. 4.4.55. Meridional transport of sensible heat at 850 hPa due to unfiltered transient fluctuations obtained from the ECMWF analyses distinguishing between seasons. Positive values (solid contour lines) indicate poleward, negative ones (dashed contour lines) indicate equatorward momentum fluxes. Units are Km/s, the contour interval is 4 Km/s.

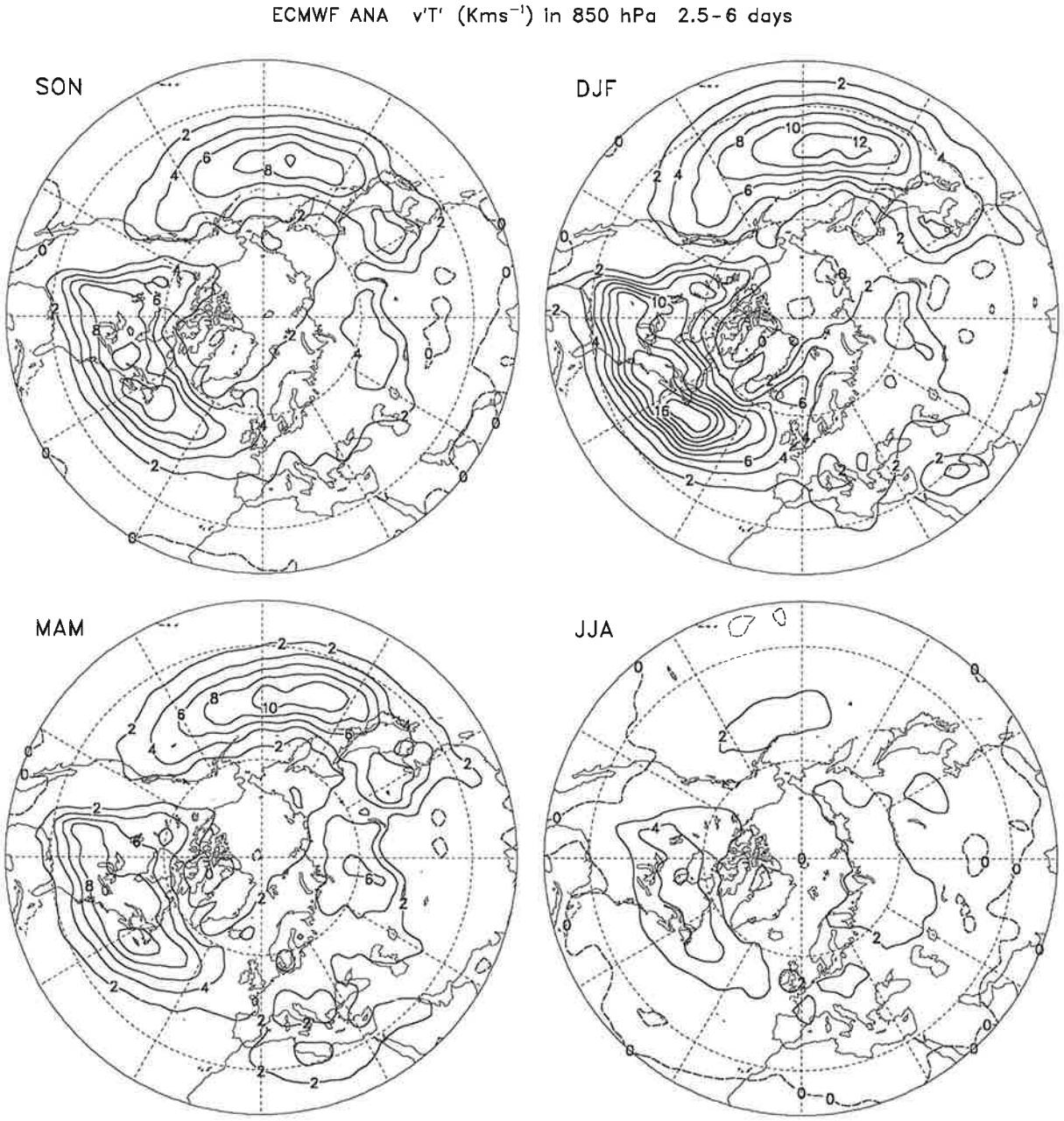

Fig. 4.4.56. As Fig. 4.4.55 but for the band-pass filtered transient fluctuations. The contour interval is 2 Km/s.

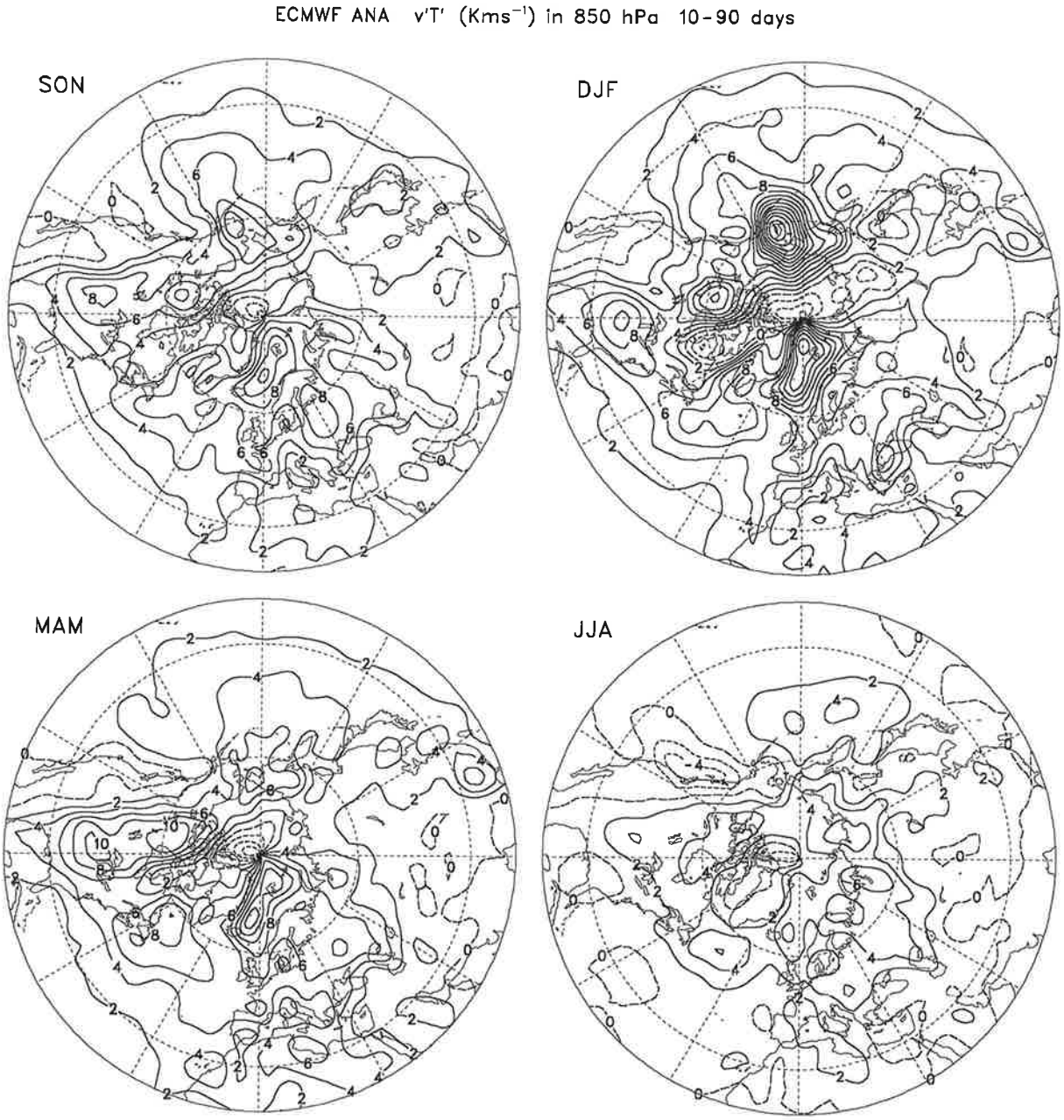

Fig. 4.4.57. As Fig. 4.4.55 but for the low-pass filtered transient fluctuations. The contour interval is 2 Km/s.

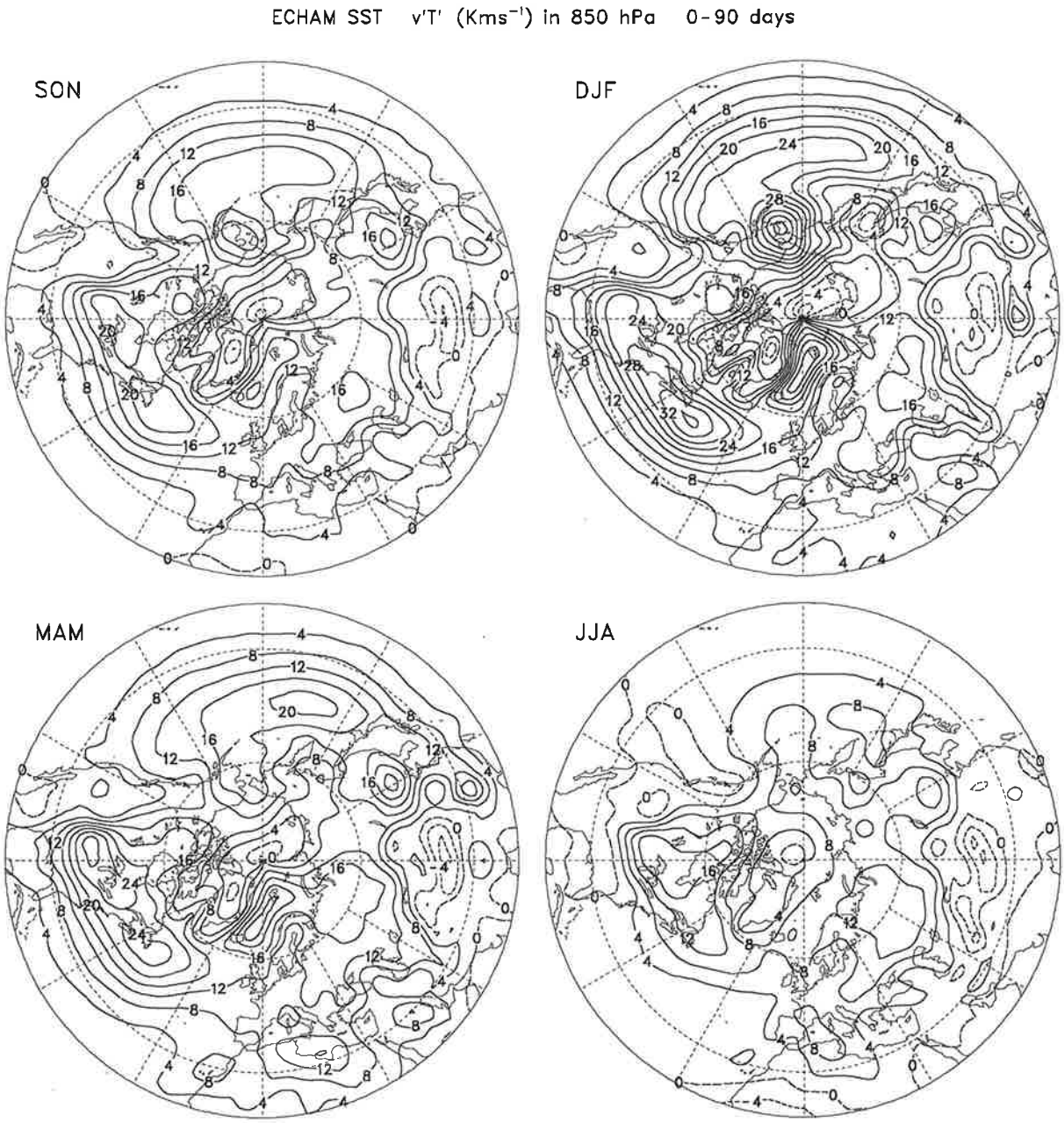

Fig. 4.4.58. As Fig. 4.4.55 but for the simulations performed with ECHAM3 with varying Sea Surface Temperatures as boundary forcing.

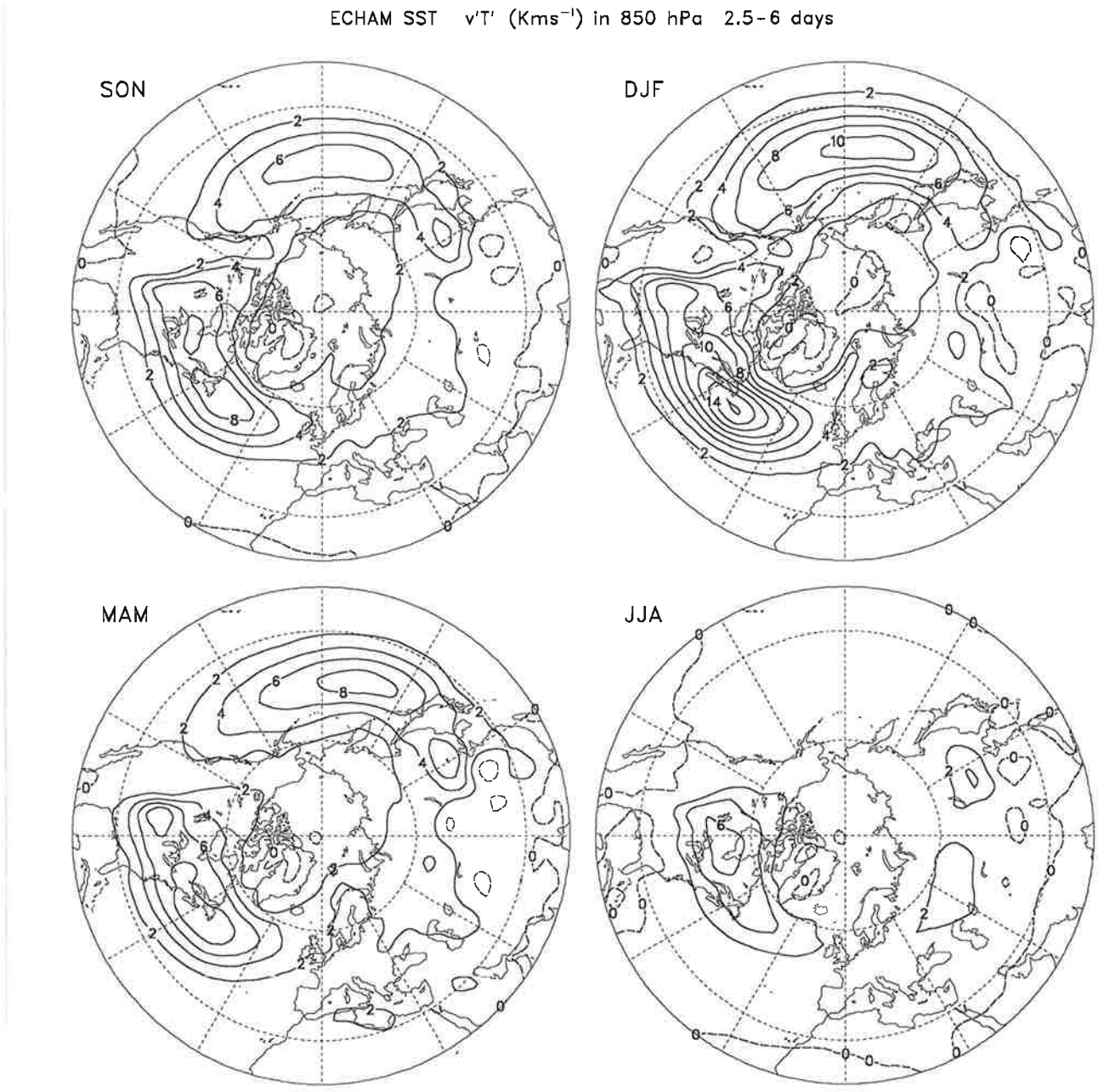

Fig. 4.4.59. As Fig. 4.4.58 but for the band-pass filtered transient fluctuations. The contour interval is 2 Km/s.

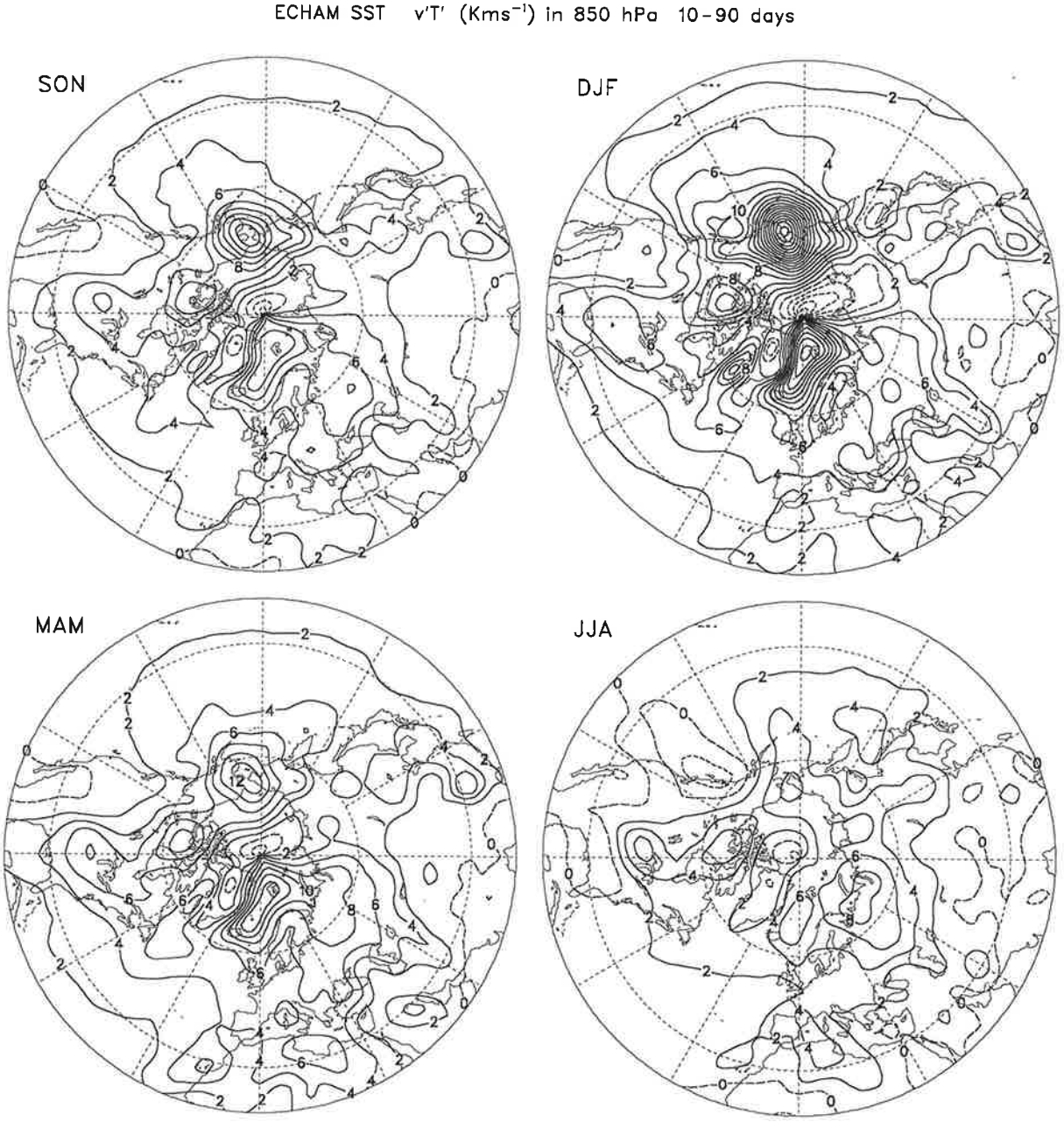

Fig. 4.4.60. As Fig. 4.4.58 but for the low-pass filtered transient fluctuations. The contour interval is 2 Km/s.

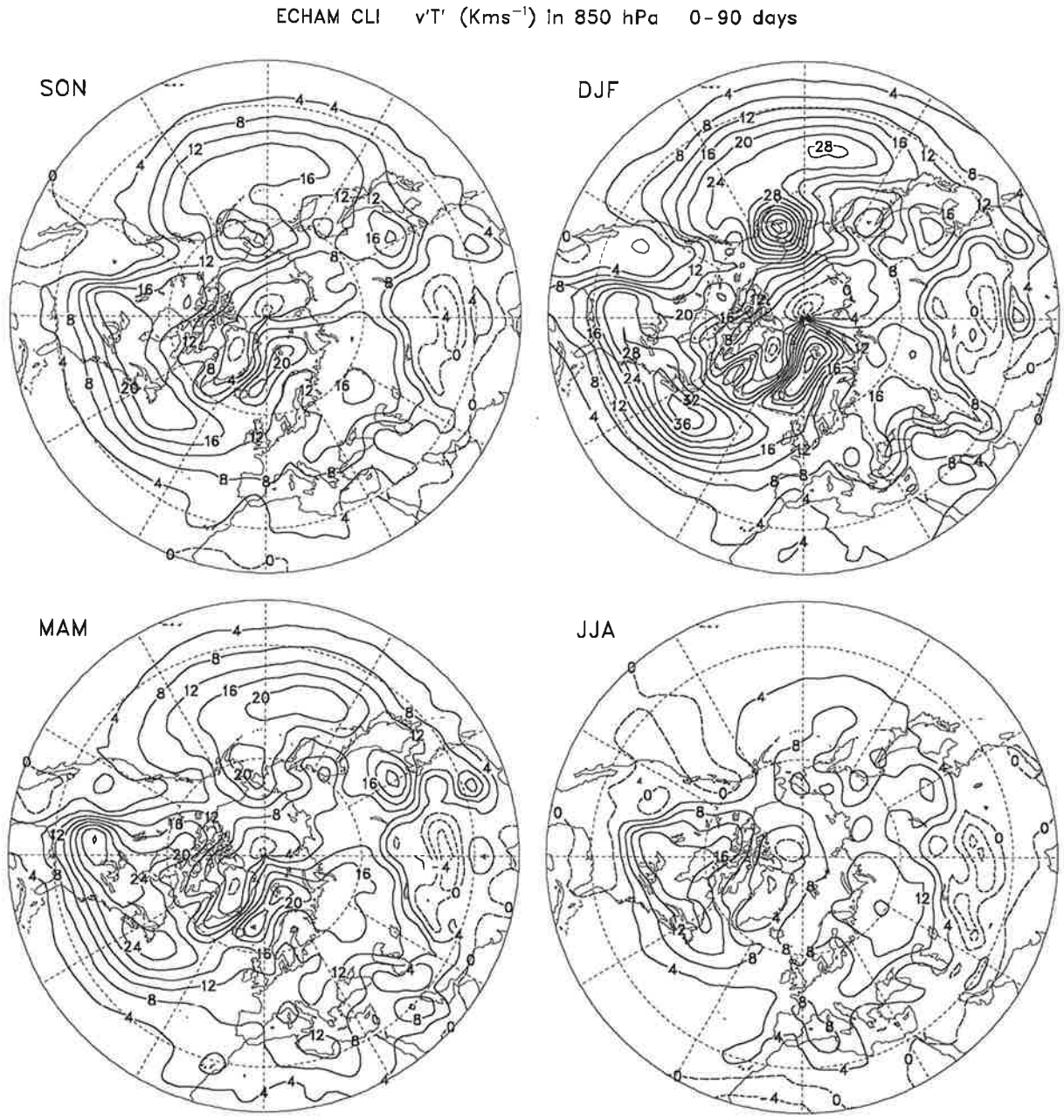

Fig. 4.4.61. As Fig. 4.4.55 but for the simulations performed with ECHAM3 with fixed Sea Surface Temperatures as boundary forcing.

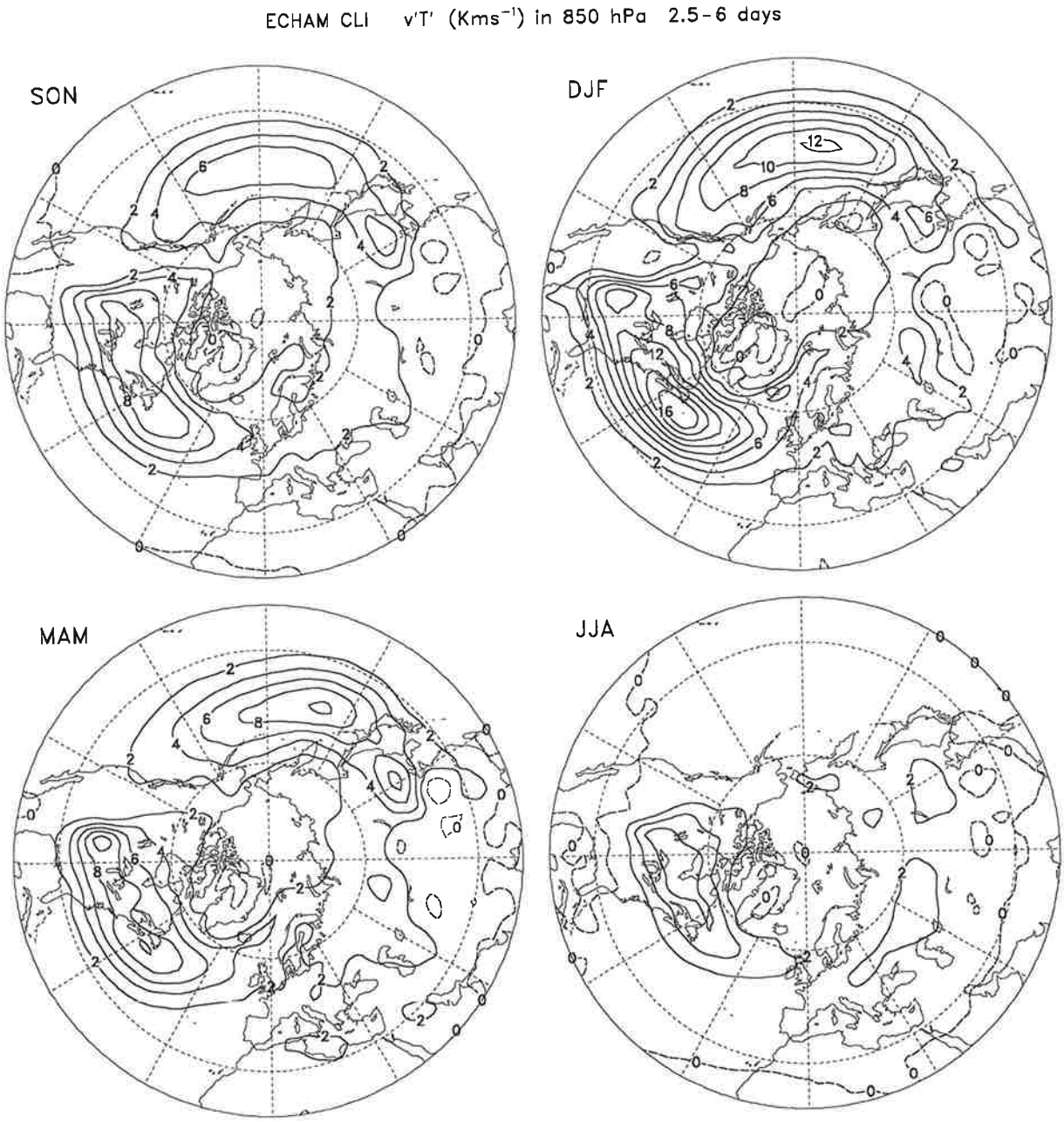

Fig. 4.4.62. As Fig. 4.4.61 but for the band-pass filtered transient fluctuations. The contour interval is 2 Km/s.

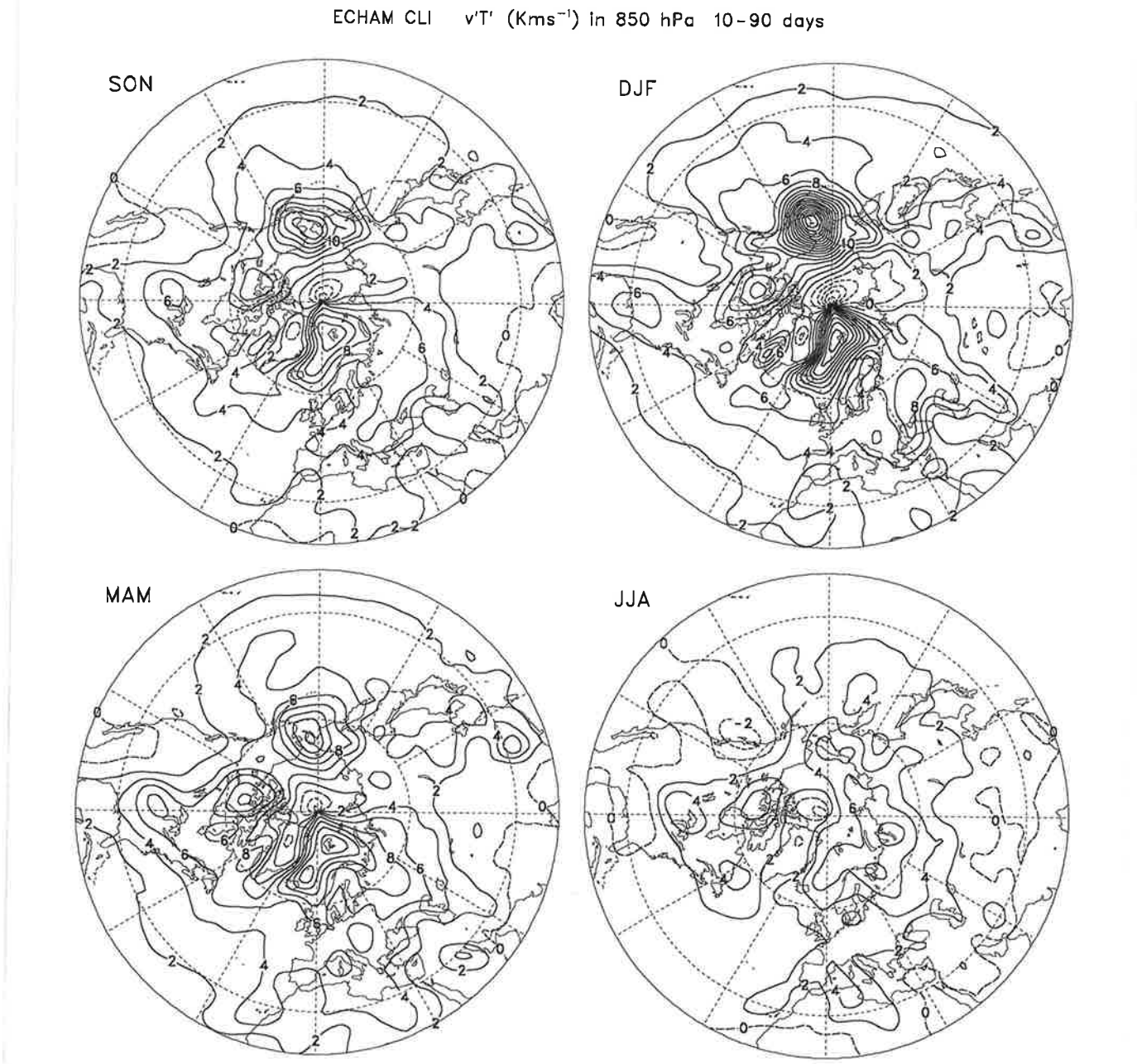

Fig. 4.4.63. As Fig. 4.4.61 but for the low-pass filtered transient fluctuations. The contour interval is 2 Km/s.

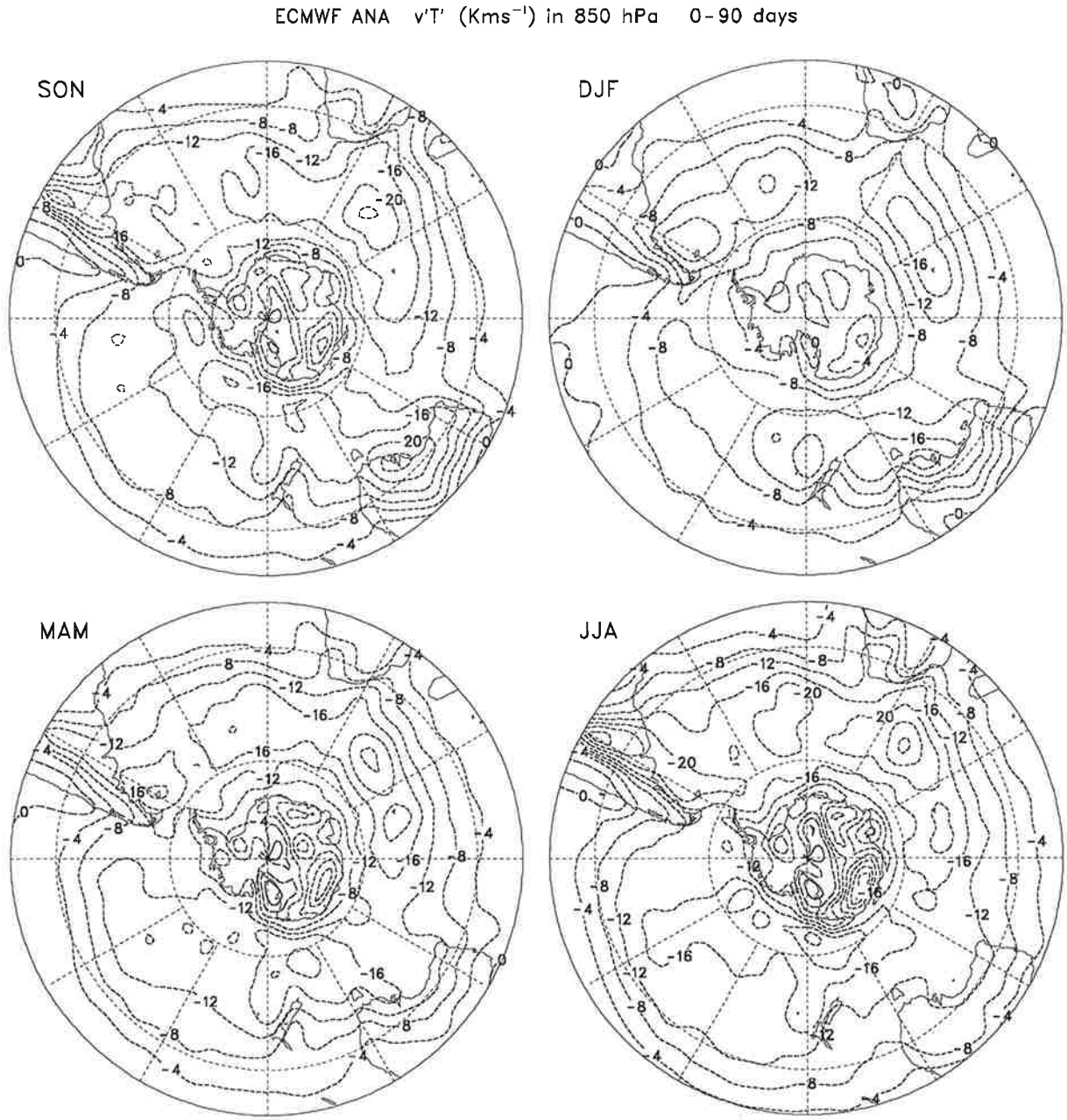

Fig. 4.4.64. Meridional transport of sensible heat at 850 hPa due to unfiltered transient fluctuations obtained from the ECMWF analyses distinguishing between seasons. Negative values (dashed contour lines) indicate poleward, positive ones (solid contour lines) indicate equatorward momentum fluxes. Units are Km/s, the contour interval is 4 Km/s.

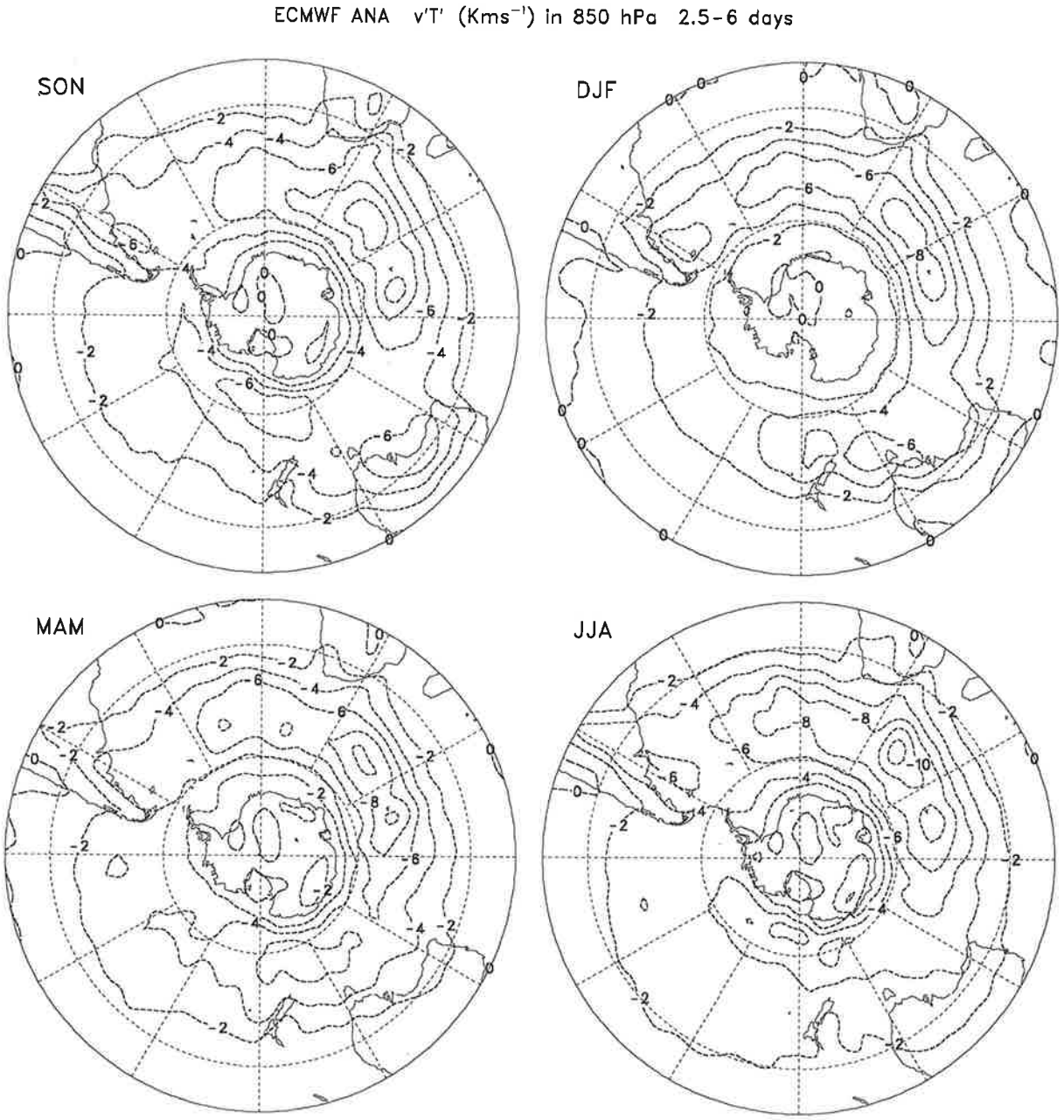

Fig. 4.4.65. As Fig. 4.4.64 but for the band-pass filtered transient fluctuations. The contour interval is 2 Km/s.

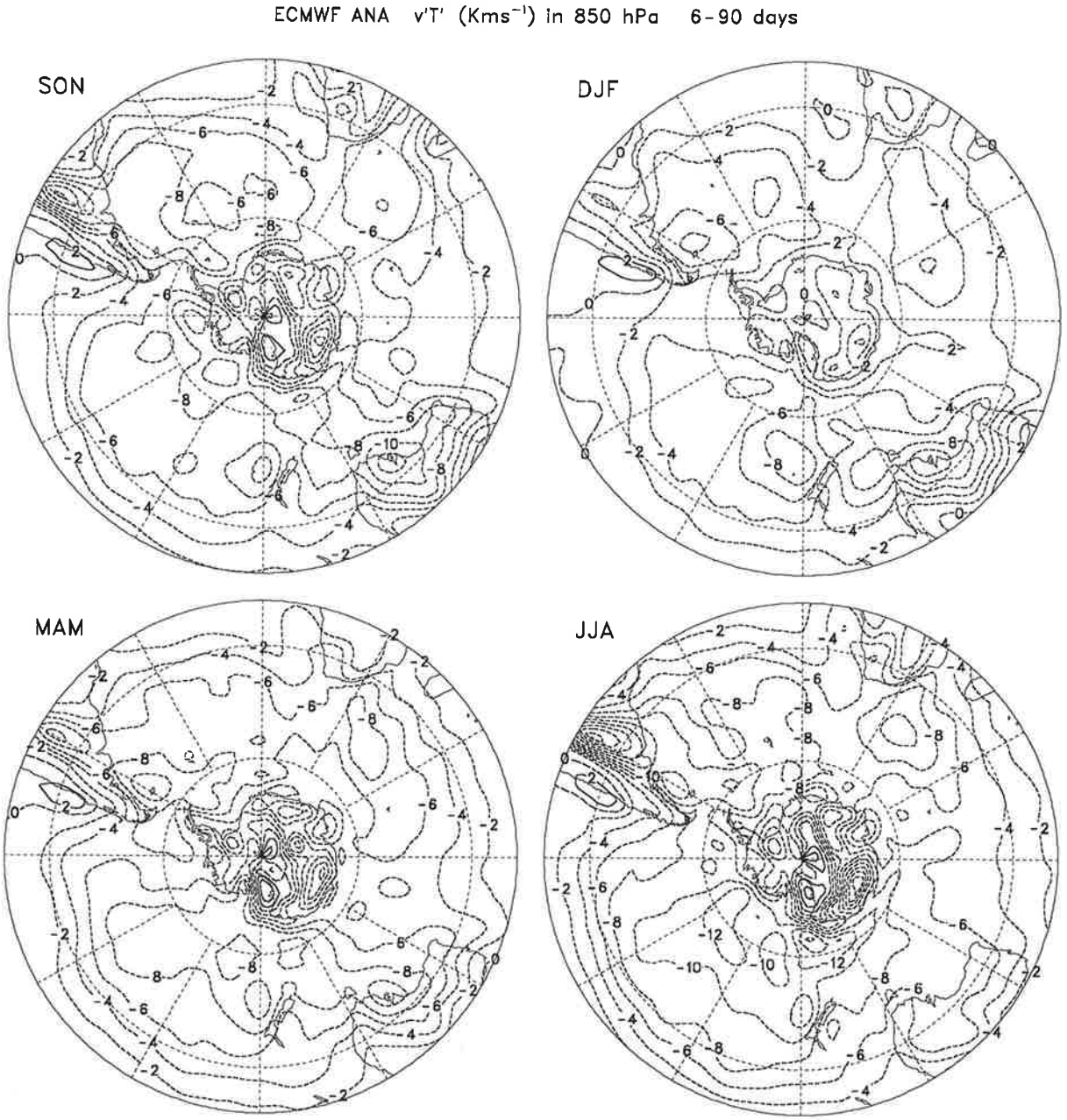

Fig. 4.4.66. As Fig. 4.4.64 but for the low-pass filtered transient fluctuations. The contour interval is 2 Km/s.

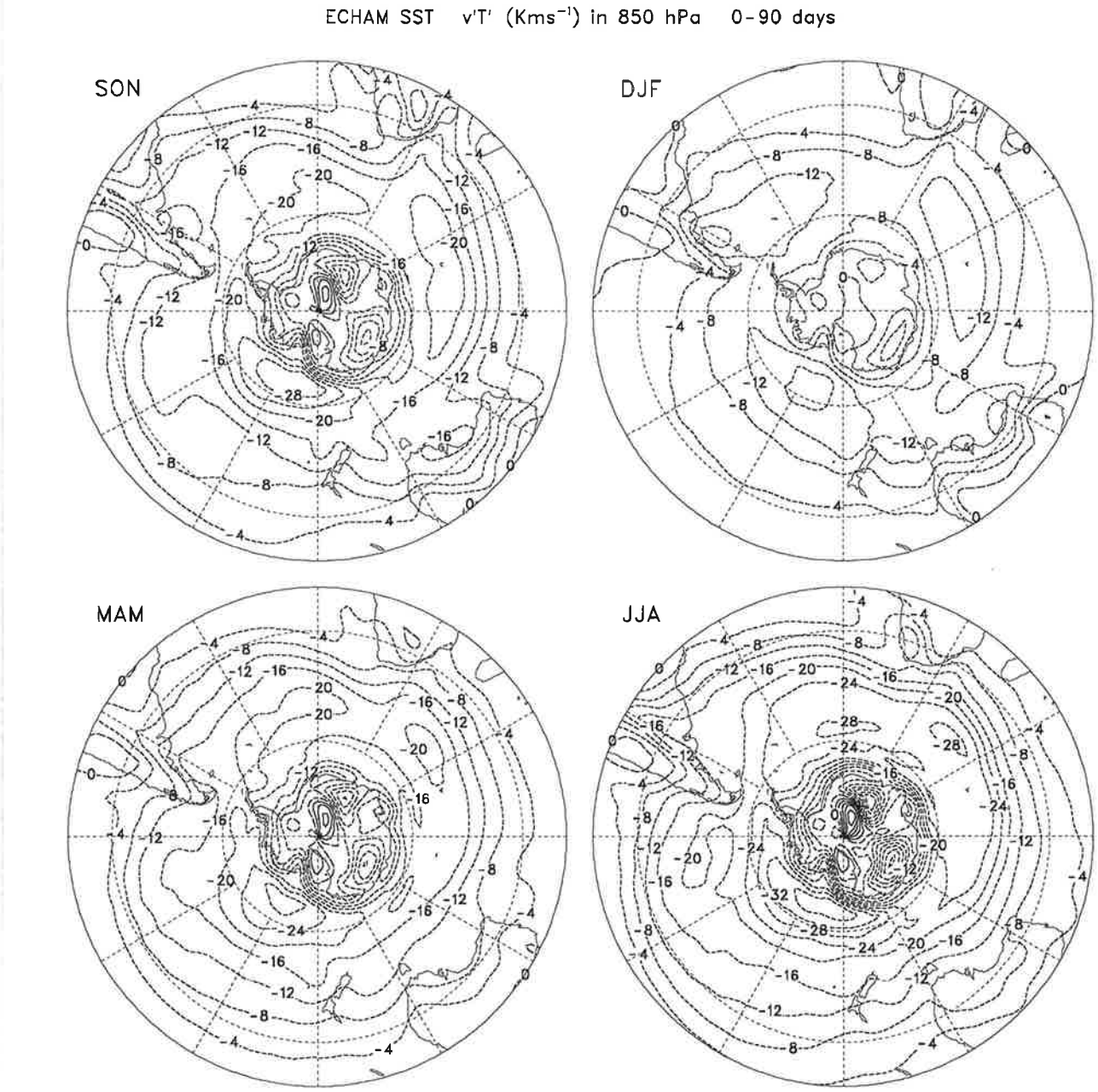

Fig. 4.4.67. As Fig. 4.4.64 but for the simulations performed with ECHAM3 with varying Sea Surface Temperatures as boundary forcing.

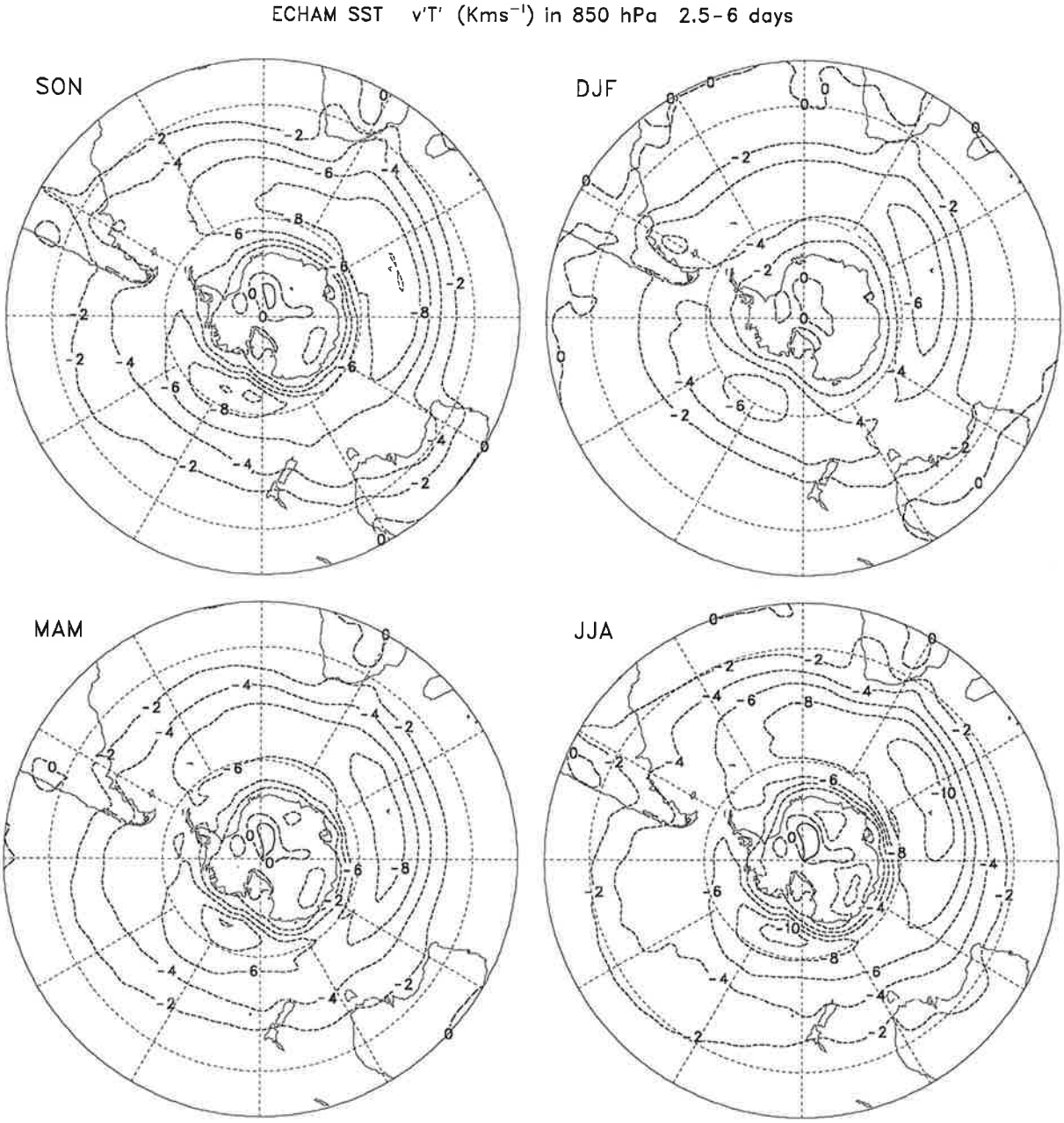

Fig. 4.4.68. As Fig. 4.4.67 but for the band-pass filtered transient fluctuations. The contour interval is 2 Km/s.

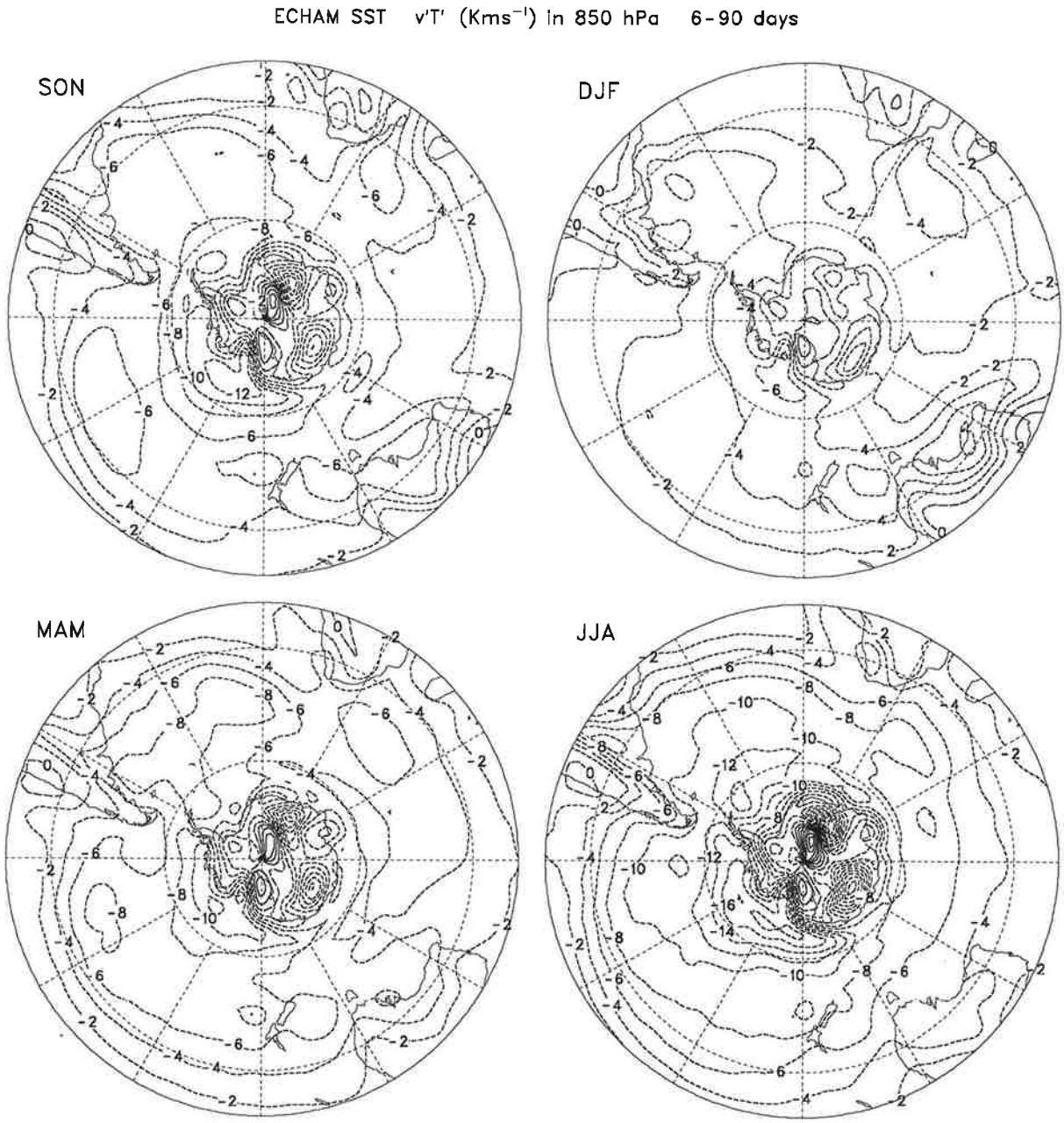

Fig. 4.4.69. As Fig. 4.4.67 but for the low-pass filtered transient fluctuations. The contour interval is 2 Km/s.

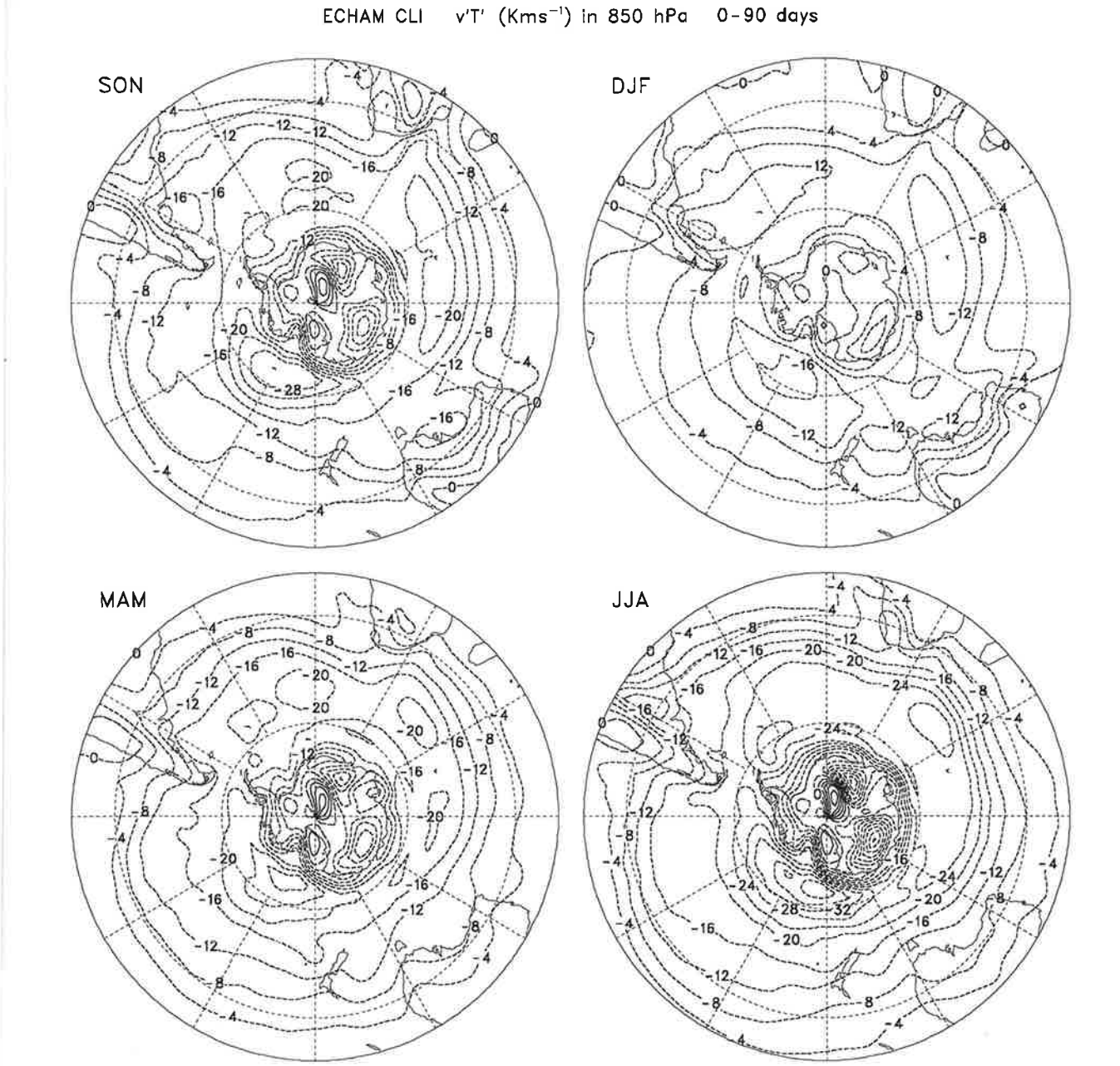

Fig. 4.4.70. As Fig. 4.4.64 but for the simulations performed with ECHAM3 with fixed Sea Surface Temperatures as boundary forcing.

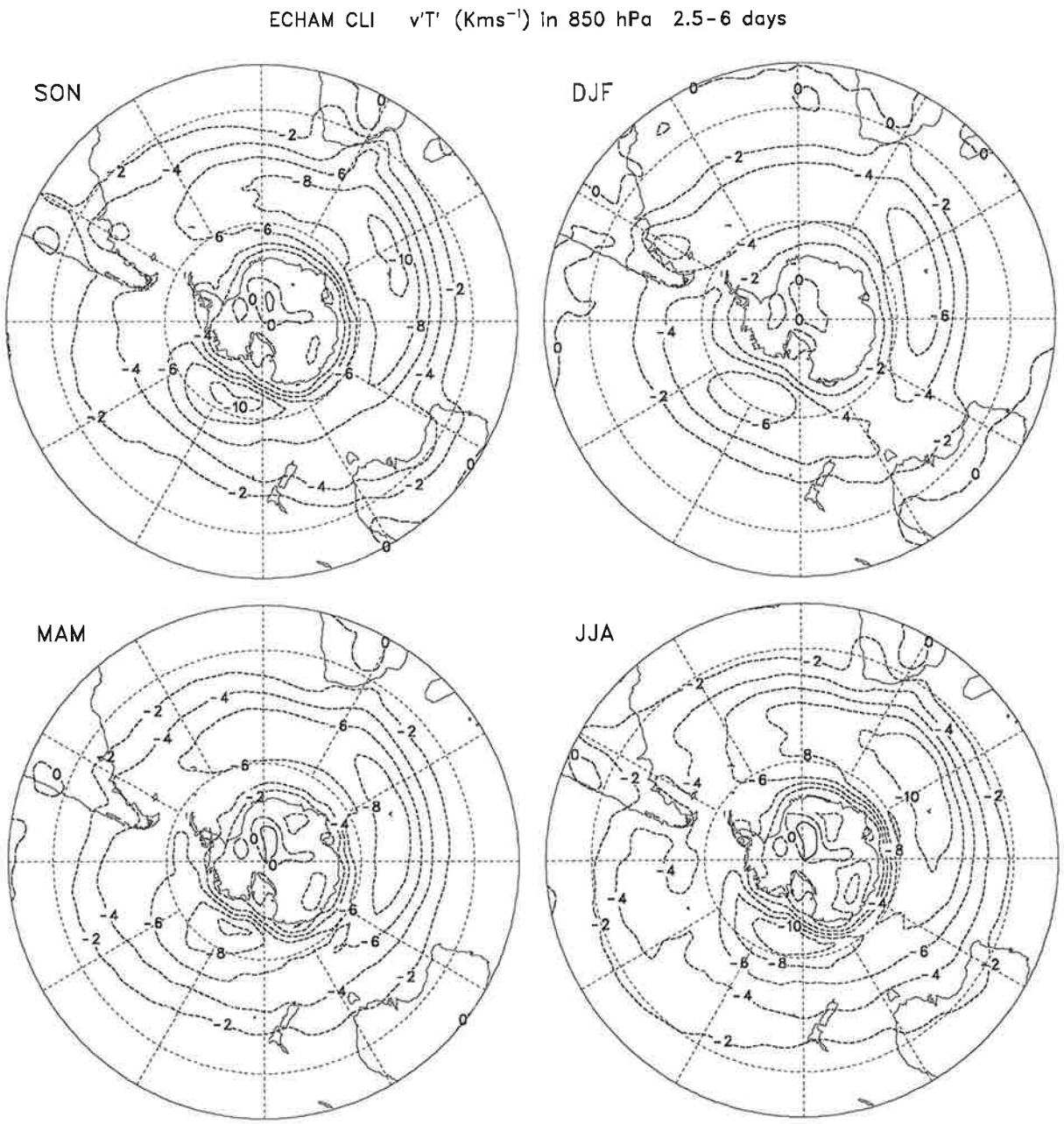

Fig. 4.4.71. As Fig. 4.4.70 but for the band-pass filtered transient fluctuations. The contour interval is 2 Km/s.

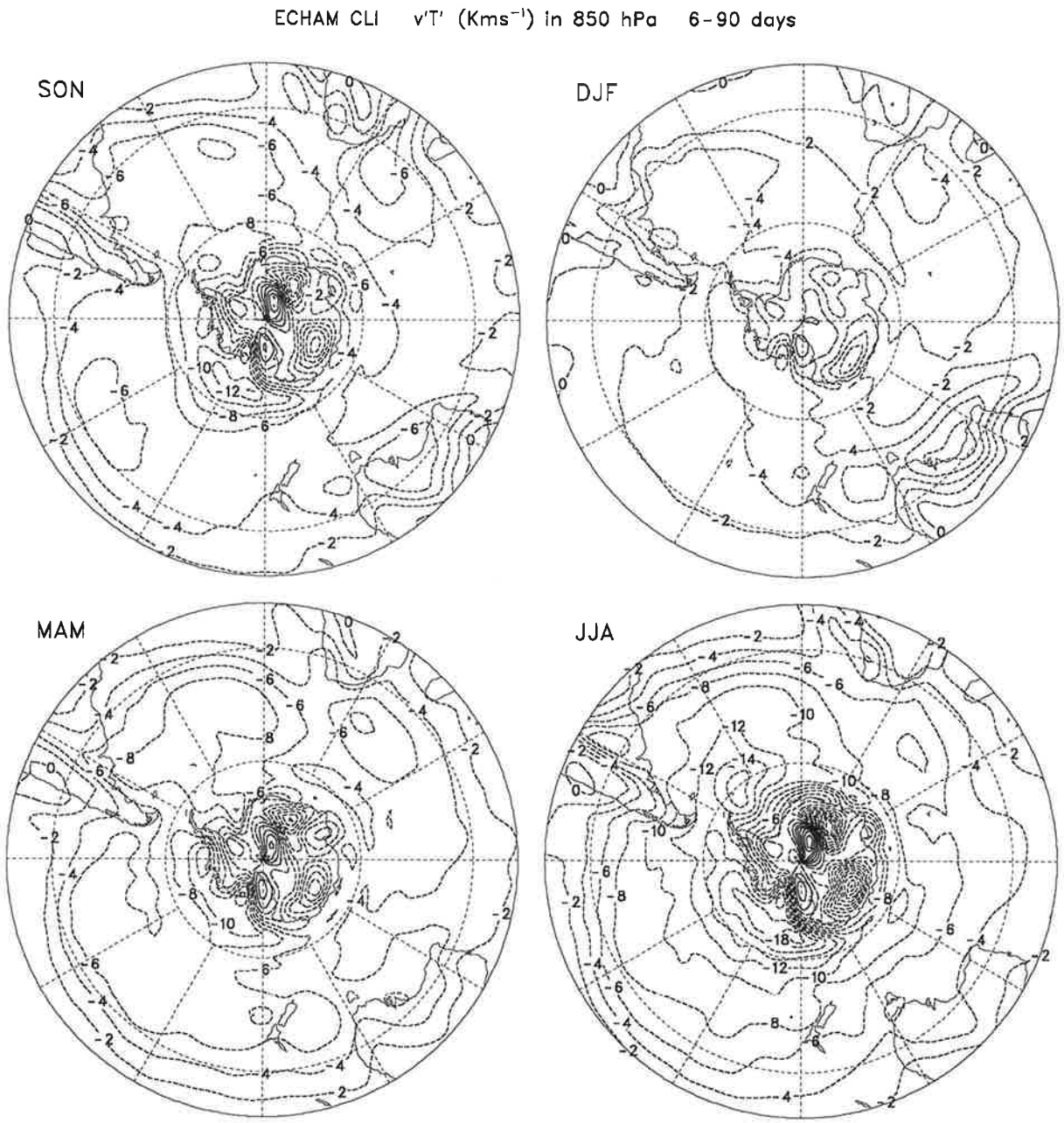

Fig. 4.4.72. As Fig. 4.4.70 but for the low-pass filtered transient fluctuations. The contour interval is 2 Km/s.